UC San Diego

UC San Diego Electronic Theses and Dissertations

Title

Experimental and Numerical Simulation of Seismically Isolated Critical Facilities under Extreme Seismic Loading

Permalink

https://escholarship.org/uc/item/95p2s301

Author

Sarebanha, Alireza

Publication Date

2018

Peer reviewed|Thesis/dissertation

eScholarship.org Powered by the California Digital Library
University of California

UNIVERSITY OF CALIFORNIA, SAN DIEGO

Experimental and Numerical Simulation of Seismically Isolated Critical Facilities under Extreme Seismic Loading

A dissertation submitted in partial satisfaction of the
requirements for the degree
Doctor of Philosophy

in

Structural Engineering

by

Alireza Sarebanha

Committee in charge:

Professor Gilberto Mosqueda, Chair
Professor Raymond de Callafon
Professor Hyonny Kim
Professor Pui-Shum Shing
Professor Chia-Ming Uang

2018

Copyright
Alireza Sarebanha, 2018
All rights reserved.

The Dissertation of Alireza Sarebanha is approved, and it is acceptable in quality and form for publication on microfilm and electronically:

_____

_____

_____

_____

_____

Chair

University of California, San Diego

2018

DEDICATION

To the people of Bam.

It was a cold Friday morning in December 2003 and I remember it like it was few days ago. A magnitude 6.6 earthquake struck Bam and took almost 26,000 lives while left thousands of families with the grief of their loved ones and a country to sorrow. I was a teenager back then with dreams of shaping a better world. It keeps happening and we do our best to learn from each one of them and get ready and be prepared for the next one.

2004: Indonesia; 2005: Indonesia, Pakistan; 2006: Peru, Indonesia; 2008: China; 2009: Indonesia; 2010: Haiti, Chile; 2011: Japan; 2013: Pakistan; 2014: China; 2015: Nepal; 2016: Ecuador; 2017: Mexico, Kermanshah (Iran)…

We came a long way to get where we are now but we can do better than this.

We should do better than this.

TABLE OF CONTENTS

Signature Page……..……...……....iii

Dedication…….. iv

Table of Contents……..……...v

List of Figures……..…...……x

List of Tables……..……...…….……xvii

Acknowledgements……..……xix

Vita……...……...xxii

Publications……... ……. xxii

Abstract of The Dissertation xxv

Chapter 1 Introduction 1

1-1 Seismic Risk of Critical Facilities.....1

1-2 Seismic Isolation in Nuclear Power Plants 2

1-3 Research Objective and Scope.....3

1-4 Overview of the Dissertation 5

Chapter 2 Background and Literature Review.....8

2-1 Seismic Isolation.....8

2-1-1 Seismic Isolation in NPP 9

2-1-2 Experimental Testing of Isolated Structures.....11

2-2 Hybrid Simulation.....13

2-2-1 Real-time Hybrid Simulation.....15

2-3 Structural Pounding and Moat Wall Impact 15
2-3-1 Experimental studies 16
2-3-2 Analytical and Numerical Studies 22
2-3-3 Passive earth pressure load-deflection 24
Chapter 3 Adaptation of The Caltrans SRMD Test Facility for Hybrid Simulation 33
3-1 Introduction 33
3-2 Description of The SRMD Testing Facility 33
3-3 Development of Hybrid Simulation Capabilities 37
3-3-1 Hybrid Simulation Hardware Configuration 37
3-3-2 Hybrid Simulation Software Configuration 42
3-4 Implementation of Digital Communication Network using SCRAMNet+ 47
3-5 Delay Compensation 51
3-5-1 Constant Delay for each DOF 52
3-5-2 Feed-forward Control 54
3-5-3 Adaptive Time Series (ATS) Compensator 55
3-6 Rate and Accuracy of Hybrid Tests 58
3-7 Compensation for Friction and Inertia Forces 64
3-7-1 Model 1: Empirical Model for Inertia and Friction Forces of the SRMD 64
3-7-2 Model 2: Inertia and Friction Force model using System Identification Techniques 68
3-8 Preparation for Hybrid Simulation Test 72
3-8-1 Limiter Settings for Magnitude and Rate 72
3-8-2 Initial Offset due to Drifting 73

3-8-3 Special Setting for Testing of Triple Friction Pendulum Bearings....74
3-9 Summary of Hybrid Infrastructure....76
3-10 Conclusions....78
Chapter 4 Hybrid Simulation of Seismically Isolated Nuclear Power Plant using Full-Scale Bearing....82
4-1 Introduction....82
4-2 Analytical Model of Seismically Isolated Nuclear Power Plant....83
4-2-1 Different Models of the Isolation System....84
4-3 Different Types of Bearings....86
4-3-1 Test Specimens: LPRB....86
4-4 Test Setup Configuration....89
4-4-1 Recorded Data and Instrumentations....90
4-4-2 Data acquisition systems....93
Chapter 5 Seismic Response of NPP Isolated with LPRB....96
5-1 Introduction....96
5-2 Hybrid Simulation Test Plan....97
5-3 Results of Hybrid Simulation with LPRB....102
5-3-1 Comparison of 1-D and 2-D Horizontal Inputs....102
5-3-2 Influence of Test Rate....111
5-3-3 Influence of Vertical Excitation....123
5-3-4 Variation due to Different Bearing Discretization Models....127
5-3-5 Bearing Failure Test....133
5-4 Conclusion....135

Chapter 6 Seismic Response of Base Isolated Nuclear Power Plants Considering Impact to Moat Walls....138
6-1 Introduction....138
6-2 Simplified Model of Nuclear Power Plant....139
6-3 Moat Wall Model....141
6-3-1 Moat wall....144
6-3-2 Soil Model....145
6-3-3 Impact Model....149
6-3-4 Sensitivity Analysis....152
6-4 Parametric Study....156
6-4-1 Ground Motions (GM):....157
6-4-2 Intensity Level (IL):....157
6-4-3 Clearance to Stop (CS):....158
6-4-4 Bearing Properties:....159
6-4-5 Case Studies Considered....160
6-5 Compiled Results....161
6-5-1 Variability on the moat wall and backfill soil properties....165
6-6 Comparison between fixed-base and Isolated NPP with and without Moat wall impact....170
6-7 Summary and Conclusion....172
Chapter 7 Advanced Modeling of Seismically Isolated Nuclear Power Plant with Impact to Moat Walls....177
7-1 Introduction....177

7-2 Nuclear Power Plant Model 178
7-2-1 Modeling of Moat Wall and Backfill Soil 179
7-3 Numerical Simulations 184
7-3-1 Sample Results 185
7-3-2 Torsional Effects 191
7-4 Parametric Study using ANT Model 194
7-4-1 Parameters Considered 195
7-4-2 Results 196
7-5 Relations between impact response measures 200
7-5-1 Strength of Moat Wall and Backfill Soil 201
7-5-2 Estimation of Penetration 202
7-6 Summary 205
Chapter 8 Summary and Conclusion 208
8-1 Summary of research work performed 208
8-2 Novel contributions to knowledge 209
8-3 Recommendation for future research work 212

LIST OF FIGURES

Figure 2-1 Principle of seismic isolation [2].....9

Figure 2-2 Different types of seismic isolation system 11

Figure 2-3 Apparatus for dynamic impact experiments [50].....17

Figure 2-4 Overall view of test structure with reference frame [52] 18

Figure 2-5 Setup of (a) the impact experiment and (b) shaking table test [54] 19

Figure 2-6 Shake table test setup for moat wall impact testing [55] 20

Figure 2-7 Schematic of new impact element [56].....20

Figure 2-8 Full Scale Base Isolated Building Specimen [14].....21

Figure 2-9 Damage after pounding to BW40: (a) without rubber blocks under Takatori 90% (b) with rubber blocks under Takatori 65% [14].....21

Figure 2-10 Different Impact Model [49].....23

Figure 2-11 Test arrangement for passive pressure load tests [69] 24

Figure 2-12 Schematic elevation view of passive earth pressure experiment with instrumentation layout [73] 26

Figure 3-1 SRMD testing facility: (a) overview and (b) installed bearing 34

Figure 3-2 SRMD plan view [1] 35

Figure 3-3 Hybrid simulation testing configuration 38

Figure 3-4 Hybrid Controller configuration using dSpace 39

Figure 3-5 Analog signal conditioning for the feedback signal.....41

Figure 3-6 Noise in the feedback signal from the SRMD 41

Figure 3-7 Hybrid simulation configuration.....42

Figure 3-8 Predictor-corrector algorithm in Stateflow [12].....46

Figure 3-9 Hybrid simulation hardware configuration using SCRAMNet+ and xPC.....47

Figure 3-10 SCRAMNet+ serial ring network at the SRMD laboratory.....48

Figure 3-11 SRMD SCRAMNet+ readout map. 50

Figure 3-12 Hybrid Controller configuration in Simulink using SCRAMNET+ and xPC Target51

Figure 3-13 Delay model in Simulink 53

Figure 3-14 Tracking signal for delay: (a) no FF and (b) with FF 54

Figure 3-15 Adaptive change of ATS compensator gains during a hybrid simulation 57

Figure 3-16 Command signals and corresponding experimental error indicators (with FF and no ATS) – Run # 8 – 2D – real-time.....59

Figure 3-17 Command signals and corresponding experimental error indicators (with FF and ATS) – Run # 42 – 2D – real-time.....60

Figure 3-18 Command signals and corresponding experimental error indicators – Run # 166 – 3D – 2x slower.....62

Figure 3-19 Command signals and corresponding experimental error indicators – Run # 157 – 3D – real-time 63

Figure 3-20 Friction force for different instantaneous velocity values.....65

Figure 3-21 Machine contact surfaces: (a) and (b) vertical actuators; (c) and (d) outriggers 68

Figure 3-22 Model schematic to correct for friction, inertia and offset using friction model 71

Figure 3-23 Sample correction of feedback forces (longitudinal direction).....71

Figure 3-24 Applying the limits on the command signals.....73

Figure 3-25 Optional observers available in the SRMD controller 75

Figure 3-26 Schematic of the test set-up using SCRAMNet+ and xPC Target.....77

Figure 4-1 Perspective overview of APR1400 nuclear power plant – courtesy of KEPCO E&C 83

Figure 4-2 Different ANT models: (a) One-bearing equivalent (b) five-bearing equivalent and (c) 486 bearing model in OpenSees [1] 84

Figure 4-3 LPRB specifications provided by Unison eTech 87

Figure 4-4 LPRB lateral quality control test and design envelope 88

Figure 4-5 LPRB axial quality control test 89

Figure 4-6 Overview of the typical test set-up....90

Figure 4-7 Vertical displacement of the SRMD and LVDTs 93

Figure 4-8 LVDTs used to measure vertical deformation of the bearings 93

Figure 5-1 Superstructure result output locations....102

Figure 5-2 Comparison of bearing response to 1-D and 2-D analyses (real-time)....104

Figure 5-3 Comparison of bearing response to 1-D and 2-D analyses (real-time)....104

Figure 5-4 Response spectra comparison of 1-D and 2-D analyses (real-time) 106

Figure 5-5 Fourier amplitude of displacement error in Run 38 and 42 107

Figure 5-6 Comparison of bearing response to 1-D and 2-D analyses (2x slower)....108

Figure 5-7 Response spectra comparison of 1-D and 2-D analyses (2x slower)....110

Figure 5-8 Comparison of bearing response to test rate (1-D) 112

Figure 5-9 Response spectra comparison to test rate (1-D)....113

Figure 5-10 Fourier amplitude of displacement error (top) and normalized tracking indicator (bottom) in run 38 (a) and run 55 (b)....114

Figure 5-11 Comparison of bearing response to test rate (2-D) 116

Figure 5-12 Response spectra comparison to test rate (2-D) 118

Figure 5-13 Fourier amplitude of displacement error (top) and normalized tracking indicator (bottom) in run 42 (a) and 56 (b) 119

Figure 5-14 Comparison of bearing response to test rate (3-D) 120

Figure 5-15 Response spectra comparison to test rate (3-D) 122

Figure 5-16 Comparison of bearing response to a ground motion with and without vertical excitation (2x vs. 10x slower) 124

Figure 5-17 Response spectra comparison to a ground motion with and without vertical excitation (2x vs. 10x slower) 126

Figure 5-18 Comparison of bearing responses to bearing layout discretization (2-D) 128

Figure 5-19 Response spectra comparison to bearing layout discretization (2-D) 130

Figure 5-20 Comparison of bearing responses to bearing layout discretization (3-D) 132

Figure 5-21 Response spectra comparison to bearing layout discretization (3-D) 133

Figure 5-22 Bearing hysteretic response during failure test of UET-2: Run 183 with 16,259 kN axial load 134

Figure 5-23 Failure of the LPRB (UET-2): (a) deformed bearing under 400% shear strain, (b) ruptured bearing 134

Figure 6-1 Lumped mass model for RCB 140

Figure 6-2 Schematic view of NPP with moat wall and backfill soil 142

Figure 6-3 Slab and moat wall deformed shape modeled in LS-Dyna (a and b), and proposed macro model to capture impact in OpenSees (c) 144

Figure 6-4 Moment rotation for 0.3048 m (1 ft.) width of the wall 145

Figure 6-5 (a) Maximum stiffness and (b) ultimate force for HFD model (Soil type: T2) 147

Figure 6-6 Calculation of corresponding ultimate forces for soil spring 148

Figure 6-7 Dynamic soil mass consideration - (a) passive failure plane and (b) 0.609m assumed thickness for soil mass 149

Figure 6-8 Contact force-penetration relation for Hertz, Hertz Damped model and Impact material in OpenSees 151

Figure 6-9 Displacement time histories of the NPP isolation system (a) and acceleration time histories at ground level (b) during and after impact for various impact stiffness values 153

Figure 6-10 Floor response spectra at ground level for various impact stiffness values.....154

Figure 6-11 Displacement time histories of the base mat of NPP (a) and acceleration time histories at ground level (b)for different assumed for various moat wall and backfill soil mass values.....155

Figure 6-12 Floor response spectra at ground level for various moat wall and backfill soil mass values 156

Figure 6-13 Spectral acceleration (5% damping) for different GMs – 0.5g PGA.....158

Figure 6-14 GM 5: Loma Prieta, CS: 300 % (0.672 m), IL: 1.0 g, NV, K2/K1 ratio = 0.1 (Case 25) (a) base displacement time history, (b) acceleration at ground level, (c) isolator hysteresis, (d) floor response spectral acceleration at ground level (e) hertz impact force, and (f) backfill soil force-deformation 162

Figure 6-15 Impact cases for different GM Intensity Levels and bearing properties.....163

Figure 6-16 Displacement demand normalized by clearance to stop 164

Figure 6-17 Maximum positive and negative acceleration at ground level.....165

Figure 6-18 Variability in Displacement Demand ratios and Absolute Acceleration at ground level (GM4).....167

Figure 6-19 Floor response spectra along the height of NPP – IL=1.0g – GM3 – No Moat Wall - LB – Config. 3 - K2/K1=0.1 (a) and K2/K1=0.01 (b) 168

Figure 6-20 Max. spectral acceleration for intensity level 1.0 g – LB – K2/K1=0.1 169

Figure 6-21 Max. spectral acceleration for intensity level 1.0 g – LB – K2/K1=0.01 169

Figure 6-22 Isolator displacement time history 170

Figure 6-23 Floor response spectra at ground level assuming different intensity level for fixed based NPP vs. isolated NPP with and without a moat wall 171

Figure 7-1 NPP and moat wall node coordinates.....179

Figure 7-2 Implementation of the impact macro model 180

Figure 7-3 Impact force – deformation (indentation) for different scale factors on penalty stiffness using LS-dyna – impact velocity: 0.4572 m/s (1.5 ft./sec).....182

Figure 7-4 Impact force – deformation (indentation) using LS-Dyna, Hertz Damped Model and OpenSees Impact Material 184

Figure 7-5 ANT Model plane view.....185

Figure 7-6 Response to 2-D Loma Prieta at 1.0g: (a and b) bearing hysteresis, (c) bearings orbits, and (d) shear interactions.....186

Figure 7-7 Response to 2-D Loma Prieta at 1.0g: (a) base displacement, (b) impact force deformation, (c) moat wall shear force time history, (d) moment rotation of rotational spring, (e) backfill soil force deformation 188

Figure 7-8 Response to 2-D Loma Prieta at 1.0g: total impact force, moat wall base shear, and backfill soil force time history on (a) north and (b) west side of NPP 189

Figure 7-9 Location along elevations of RCB selected to examine floor response spectra 190

Figure 7-10 Floor response acceleration for RCB at different elevations for fixed-based and isolated NPP with and without moat wall to 2-D Loma Prieta at 1.0g.....191

Figure 7-11 Bearings displacements for model with and without torsion, IL:1.0 g – 1-D excitation - Loma Prieta.....192

Figure 7-12 Impact, moat wall base shear and backfill soil force comparison for model with and without torsion, IL:1.0 g – 1-D excitation - Loma Prieta 193

Figure 7-13 Floor response acceleration for RCB at different elevations for model with and without torsion, IL:1.0 g – 1-D excitation – Loma Prieta.....193

Figure 7-14 Displacement demand over clearance to stop ratio, IL=0.75 g.....197

Figure 7-15 Displacement demand over clearance to stop ratio, IL=1.0 g.....198

Figure 7-16 Relative acceleration at elev. 47.5 m, IL=0.75 g 199

Figure 7-17 Relative acceleration at elev. 47.5 m, IL=1.0 g 200

Figure 7-18 Relationships between different impact response parameters 201

Figure 7-19 Shear strength of the moat wall using plastic design 202

Figure 7-20 Shear strength of the moat wall using plastic design 203

Figure 7-21 Measured and predicted penetrations for different impact velocities 204

LIST OF TABLES

Table 3-1 Testing machine technical specification [1] 35

Table 3-2 Voltage conversion units for different channels 39

Table 3-3 Signal calibration for longitudinal displacement 41

Table 3-4 SCRAMNet+ memory map 49

Table 3-5 ATS coefficients setup 56

Table 3-6 Approximate friction force versus instantaneous velocity 66

Table 3-7 Parameters calculated for resisting force correction 70

Table 3-8 Magnitude limits for different degrees of freedom 72

Table 4-1 Modal frequencies of the isolated NPP model 84

Table 4-2 Summary of design properties of the isolation bearings 86

Table 4-3 LPRB design properties 87

Table 4-4 Updated bearing properties prior to hybrid tests 89

Table 4-5 Typically recorded channel list 92

Table 5-1 Hybrid simulation tests conducted on LPRB bearings (Unison eTech) 98

Table 5-2 Matrix of run numbers for hybrid simulation comparisons 101

Table 6-1 Modal frequencies for isolated simplified NPP (2-D) 140

Table 6-2 Properties of the entire isolation system using Lead Rubber Bearings (LRB) 140

Table 6-3 Calculated parameters for unit width soil springs in OpenSees 148

Table 6-4 Ground motions used in simulations 157

Table 6-5 Different case considered for Clearance to Stop (CS) 158

Table 6-6 Calculated bounded properties using property modification factors.....159

Table 6-7 Cases considered in parametric study.....160

Table 6-8 Multiplier on moat wall and soil properties for different configurations.....166

Table 7-1 Bilinear bearing model parameters for individual isolators in ANT model.....179

Table 7-2 Fitted Hertz Stiffness for different scale factors in contact springs 183

Table 7-3 Different case considered for Clearance to Stop (CS).....195

Table 7-4 Cases considered for parametric study.....195

ACKNOWLEDGEMENTS

I am incredibly grateful to have had the opportunity to work with some remarkable individual during my PhD studies. These amazing people have shaped both my intellectual and personal development in many ways.

First and foremost, I would like to express my deepest gratitude to my advisor, Professor Gilberto Mosqueda for his guidance, support, and friendship. His advice and confidence in me has had an immeasurable impact on my personal and scientific development.

I would also like to express my gratitude to Professor Stephen Mahin. It has been a true privilege for me to collaborate with him, have helpful discussions, and receive insightful feedbacks to complete and improve this dissertation. We all miss him a lot. I would like to especially thank Dr. Andreas Schellenberg for being an exemplary role model and mentor and hopefully a lifelong friend. Also, I would like to thank Dr. Matthew Schoettler for his indispensable contribution in our joint research program.

Special thanks must go to Danny Innamorato, Edward Stovin, Dr. Gianmario Benzoni for their assistance in making these experiments happen. I am so thankful of my UCSD Structural Engineering family particularly Yvonne Wollmann for her kindness and endless support. I would like to extend my gratitude to Mr. Brad Theon, Dr. Armin Masroor, Dr. M Javad Hashemi, and Dr. Hamed Ebrahimian for their guidance and friendship. Also, kudos to my fellow teammates in UCSD Triathlon Team for making my last two years in UCSD an incredible experience.

My amazing friends: Masoud, Payam, Bahar, Nojan, Mojgan, Milad, Parham, Arman, Elina, and Negin. Thank you for always being there for me. I am so lucky to have beautiful people like you in my life.

I would like to thank my parents, Hamideh and Reza, and my sister Sanaz for their unconditional love and support. I owe them everything and their encouragement is the driving force in my life.

And finally, Maryam. You brought shine to my life and cheered me on every step of the way. Your endless patience and support helped me get through tough times and kept me motivated. Thank you for being a great companion throughout this journey.

Chapter 3, 4 and 5, in part, are reprint of the material as it appears in "Hybrid Simulation of Seismic Isolation Systems Applied to an APR-1400 Nuclear Power Plant", Schellenberg, A. H., Sarebanha, A., Schoettler, M. J., Mosqueda, G., Benzoni, G., and Mahin, S. A., *Technical Report PEER 2015/05*, "Hybrid Simulation of Seismic Isolation Systems applied to an Archetype Nuclear Test (ANT) Power Plant under Design Level Excitation", Schellenberg, A. H., Sarebanha, A., Schoettler, M. J., Shao, B., Mosqueda, G., and Mahin, S. A. *PEER Technical Report 2016, and* "Hybrid Simulation of Full Scale Seismic Isolation Bearing using the Caltrans SRMD Test Facility", Sarebanha, A., Schellenberg, A., Schoettler, M., Mosqueda, G., Mahin, S., 16th World Conference on Earthquake Engineering, Santiago, Chile (2017). The dissertation author was a primary investigator and author of these reports and papers.

Chapter 6, in part, is a reprint of the material as it appears in "Seismic response of base isolated nuclear power plants considering impact to moat walls", Sarebanha, A., Mosqueda, G., Kim, M. K., and Kim, J. H., *Nuclear Engineering and Design*, 328(2018), 58-72. The dissertation author was the primary investigator and author of this paper.

Chapter 7, in part, is a reprint of the material as it appears in “Modeling of moat wall compliance during impact in seismically isolated nuclear power plants”, Sarebanha, A., Mosqueda, G., Kim M. K. and Kim J. H., *Transactions, 24th International Conference on Structural Mechanics in Reactor Technology (SMiRT-24, 2017)*. The dissertation author was the primary investigator and author of this paper.

Research documented in Chapters 3, 4 and 5 of this dissertation was supported by the KEPCO E&C. Research works presented in Chapters 6 and 7 was supported by the National Research Foundation of Korea (NRF) grant funded by the Korea government (MSIP) (No. 2017M2A8A4014829.

VITA

2010 Bachelor of Science, Sharif University of Technology

2012 Master of Science, The State University of New York, University at Buffalo

2018 Doctor of Philosophy, University of California, San Diego

PUBLICATIONS

Journal Papers:

Sarebanha, A., Mosqueda, G., Kim, M. K., and Kim, J. H. (2018): "Seismic response of base isolated nuclear power plants considering impact to moat walls." *Nuclear Engineering and Design*, 328, 58-72.

Sarebanha, A., Schellenberg, A., Schoettler, M., Mosqueda, G., and Mahin, S. (2018): "Hybrid Simulation of Seismic Isolation System Using Caltrans Seismic Response Modification Device Test System." (*in preparation*).

Sarebanha, A., Mosqueda, G., Kim, M. K., and Kim, J. H. (2018). "Advanced Modeling of Seismically Isolated Nuclear Power Plant with Impact to Moat Walls." (*in preparation*).

Slovenec, D., Sarebanha, A., Pollino, M., Mosqueda, G., and Qu, B. (2017): "Hybrid Testing of the Stiff Rocking Core Seismic Rehabilitation Technique." *Journal of Structural Engineering*, 143 (9), 04017083.

Conference Papers:

Sarebanha, A., Mosqueda, G., Kim, M. K., Kim, J. H. (2017). "Effect of Moat Wall Impact on the Seismic Response of Base Isolated Nuclear Power Plants.", *16th World Conference on Earthquake Engineering*, Santiago, Chile.

Sarebanha, A., Schellenberg, A., Schoettler, M., Mosqueda, G., Mahin, S. (2017). "Hybrid Simulation of Full Scale Seismic Isolation Bearing using the Caltrans SRMD Test Facility.", *16th World Conference on Earthquake Engineering,* Santiago, Chile.

Sarebanha, A., Mosqueda, G., Kim M. K. and Kim J. H. (2017): "Modeling of moat wall compliance during impact in seismically isolated nuclear power plants" *Transactions, 24th International Conference on Structural Mechanics in Reactor Technology (SMiRT-24).*

Sarebanha A., Schellenberg A., Schoettler M., Mosqueda G., Mahin S. (2017): "Dynamic 3-D testing of seismic isolation bearing under large earthquakes using hybrid simulation," *7th International Conference on Experimental Vibration Analysis for Civil Engineering Structures*, San Diego, CA.

Sarebanha A., Schellenberg A., Schoettler M., Mosqueda G., Mahin S. (2018): "Seismic Response of Isolated Nuclear Power Plants using Hybrid Simulation." *Proceedings of the 11th National Conference in Earthquake Engineering*, Earthquake Engineering Research Institute, Los Angeles, CA.

Hughes P., Sarebanha A., Mosqueda G. (2018): "Finite element analysis of moat wall pounding in base-isolated buildings." *Proceedings of the 11th National Conference in Earthquake Engineering*, Earthquake Engineering Research Institute, Los Angeles, CA.

Montijo A., Sarebanha A., Mosqueda G., (2018): "Design Considerations for Tolerance in end connections of Viscous Damping Devices," 11NCEE., *Proceedings of the 11th National Conference in Earthquake Engineering*, Earthquake Engineering Research Institute, Los Angeles, CA.

Slovenec, D., Sarebanha, A., Sabzehzar, S., Pollino, M., Mosqueda, G., and Qu, B. (2015). "Experimental Testing of Sub-standard Multi-story Steel Braced Frames Rehabilitated using a Stiff Rocking Core and Steel Yielding Links", *ASCE Structures Congress,* Portland, OR.

Pollino, M., Sabzehzar, S., Mosqueda, G., Sarebanha, A., and Qu, B. (2014). "Hybrid Simulation of Steel Buildings with Stiff Rocking Cores for Improved Seismic Drift Distribution.",

Proceedings of the 10th National Conference on Earthquake Engineering, Anchorage, Earthquake Engineering Research Institute, AK, 2014.

Technical Reports:

Schellenberg, A. H., Sarebanha, A., Schoettler, M. J., Shao, B., Mosqueda, G., and Mahin, S. A. (2016): "Hybrid Simulation of Seismic Isolation Systems applied to an Archetype Nuclear Test (ANT) Power Plant under Design Level Excitation." *Technical Report.* Pacific Earthquake Engineering Research Center, University of California, Berkeley, Berkeley, CA.

Schellenberg, A. H., Sarebanha, A., Schoettler, M. J., Mosqueda, G., Benzoni, G., and Mahin, S. A. (2015): "Hybrid Simulation of Seismic Isolation Systems Applied to an APR-1400 Nuclear Power Plant." *Technical Report PEER 2015/05* Pacific Earthquake Engineering Research Center, University of California, Berkeley

Sarebanha, A., Mosqueda, G., and Uang, C. M. (2015): "Experimental Evaluation of Damper Frames with Displacements Amplification Mechanisms", *Technical Report: TR-15/02*, Department of Structural Engineering, University of California, San Diego.

ABSTRACT OF THE DISSERTATION

Experimental and Numerical Simulation of Seismically Isolated Critical Facilities under Extreme Seismic Loading

by

Alireza Sarebanha

Doctor of Philosophy in Structural Engineering

University of California, San Diego, 2018

Professor Gilberto Mosqueda, Chair

Seismic isolation can be an effective strategy to protect critical facilities including Nuclear Power Plants (NPPs) from the damaging effects of horizontal earthquake ground shaking. For critical facilities, the isolation system should demonstrate a high-confidence of low-probability of failure at the design level and the load carrying capacities should be maintained under beyond design earthquake shaking (BDBE). Experimental evaluation of seismic isolation bearings is important to fully understand their behavior and capacity for reliable performance. Safety mechanisms such as a stop can be imposed to prevent excessive displacement of the

isolation system under BDBE, however, this raises concerns for detrimental effects of pounding against a stop or moat wall. Methods of analysis are presented in this dissertation to evaluate both seismic isolation system behavior under extreme earthquakes and the potential effects of pounding by imposing displacement restraints.

The dynamic response of an isolated NPP depends on the combined characteristics of the ground motion, bearings, and structure while the seismic isolation bearings themselves can exhibit complex nonlinear behavior that depends on several factors, including the scale size, axial load, temperature, and rate of loading especially under strong earthquake shaking. With a specific interest on the in-structure response of seismically isolated NPPs, hybrid simulation is shown to be a viable approach to examine bearing behavior at full scale under realistic earthquake loading. The adaptation of a full-scale bearing test machine (SRMD testing facility at UC San Diego) and developed toolsets for the implementation of fast hybrid simulation to study the dynamic response of base isolated NPP using full scale lead plug rubber bearings under realistic earthquake loading conditions are presented. Results from these tests validate the effectiveness of seismic isolation technology for application in nuclear facilities and provide valuable data towards improving numerical models of seismic isolation bearings.

In a seismically isolated NPP, a surrounding moat wall can function as a stop to limit isolation system displacements and prevent bearing failure for beyond design basis shaking. Impact of isolated structures against a moat wall is of concern due to potential amplification of superstructure response. A moat wall model able to capture impact forces is proposed and used in numerical simulations to capture the effects of impact on the response of seismically isolated NPPs. Variable clearance to the stop and a range of properties for the impact model, moat wall and isolation system are considered to identify parameters that influence the response. Results

indicate that large NPP plants as considered here can have significant penetration into the moat wall, not fully limiting displacements in the isolation system, while causing considerable increases in accelerations throughout the NPP. A simplified methodology to estimate impact response parameters including penetration is proposed towards developing design tools that consider these effects.

Chapter 1 Introduction

1-1 Seismic Risk of Critical Facilities

Critical facilities are all manmade structures that, because of their function, size, service area, or uniqueness, have the potential to cause serious bodily harm, extensive property damage, or disruption of vital socioeconomic activities if they are destroyed, damaged, or if their functionality is impaired [1]. Among the critical facilities, nuclear facilities pose a potential nuclear hazard to workers, the public, and/or the environment and must comply with stringent government regulations.

General design criteria for nuclear facilities require that structures and components important to safety withstand environmental hazards, including earthquake, without losing the capacity to perform their safety functions. In term of seismic design, specific provisions are required and detailed seismic hazard evaluation must be developed to ensure that these facilities have a very low probability of unacceptable seismic performance to prevent catastrophic events.

1-2 Seismic Isolation in Nuclear Power Plants

Seismic isolation can be an effective strategy to protect critical facilities including Nuclear Power Plants (NPPs) from the damaging effects of horizontal earthquake shaking. Seismic isolation is typically achieved by installing a layer of flexible bearings at the base of the structure with a horizontal clearance or a moat at the basement level. Application of seismic isolation to NPPs has been considered since the early 1980's with potential benefits including simplification of seismic design, enhanced safety margin, and facilitated standardization [2-4].

Even though seismic isolation is a relatively mature technology, to date there are still very limited applications (only France and South Africa) to nuclear related structures. Seismically isolated NPPs include the Curas NPP in France and Koeberg NPP in South Africa. Recent studies seeking to expand applications are focused towards identifying and addressing technical challenges as well as concerns related to application of seismic isolation in NPPs. In the US, recent code developments (ASCE 4-16, NUREG) provide regulatory guidance on the use of seismic isolation technology and define minimum performance expectations and associated acceptance criteria for isolation system, superstructure, foundation, umbilical lines and stop/moat for seismically isolated NPP and safety related nuclear structures [5, 6]. The isolation system should demonstrate a high-confidence of low-probability of failure at the design level and the load carrying capacities should be maintained under beyond design earthquake shaking while excessive displacement which may result failure of isolators should be precluded using a stop.

1-3 Research Objective and Scope

The goal of this study is to experimentally and numerically assess the effectiveness of seismic isolation for applications in NPP considering beyond design earthquake shaking. In particular, this study experimentally examines seismic isolation bearing behavior to large displacements using hybrid simulation and for the first time address the seismic response on isolated NPP considering moat wall pounding under extreme earthquake excitations.

The dynamic response of an isolated NPP depends on the combined characteristics of the ground motion, bearings, and structure while the seismic isolation bearings themselves can exhibit complex nonlinear behavior that depends on several factors, including the scale size, axial load, temperature, and rate of loading especially under strong earthquake shaking. This complex behavior provides some uncertainty concerning the nonlinear seismic response of isolated structures and requires detailed experimental investigations to fully characterize such behavior. Therefore, component tests of individual bearings and realistic full-scale system level tests capturing the interaction with the superstructure are both essential towards fully characterizing and understanding the behavior of an isolated system for the validation of numerical models that can be used to examine their behavior under a wider range of conditions. Because laboratory facilities exist to test full-scale seismic isolation bearings under prescribed displacement or loading protocols at appropriate rates and the linear elastic superstructure can be modelled reliably in a finite element software, hybrid simulation provides a unique opportunity to experimentally assess the behavior of base isolated NPP using full scale bearings. System level testing of full scale bearings for application in NPP would be prohibitive on a shake table due to the gravity weight required on the bearings.

The increased flexibility at the base and resulting elongation of the natural vibration period of the structure provided by the isolation system leads to significant reductions in forces and acceleration transmitted to the structure above the isolation level at the expense of displacements concentrated in the isolation system. Displacement demands can be large at sites of moderate to high seismic hazard and can be accommodated by a horizontal clearance or moat at the isolation level, typically located in the basement of a structure. A surrounding moat wall can function as a stop to limit isolation system displacements and prevent bearing failure for beyond design basis shaking. However, impact of the isolated structure against the moat wall is of concern due to potential amplification in response of the superstructure. Design guidelines aim to prevent impact by specifying a required minimum clearance to stop with a low annual frequency of exceedance. A clearance to stop below the required value can be justified through analysis considering impact to the moat wall or stop. However, little guidance is available on how to model impact to the moat wall and resulting effects on the NPP superstructure.

The specific objectives of this research are:

- Experimentally assess the dynamic response of a seismically isolated NPP under realistic earthquake excitation using hybrid simulation
- Investigate the effects of different numerical models, seismic isolator bearings and earthquake excitation scenarios to evaluate seismic response of isolated NPP
- Propose a new impact macro element to simulate pounding of base isolated NPP and a moat wall with backfill soil
- Study the response of base isolated NPP pounding to a moat wall

- Conduct sensitivity study and parametric analysis to examine the importance of different modeling and design parameters and their effects of the seismic response of isolated NPP considering impact
- Compare response of fixed base and base isolated NPP with and without moat wall

1-4 Overview of the Dissertation

The presentation of this research work has been divided into eight chapters, the contents of which are outlined below.

Chapter 2 presents an overview of seismic isolation and its application in NPPs, experimental testing using hybrid simulation and moat wall pounding in isolated structures. Past research on the development of hybrid simulation and moat wall impact model are presented and the effort performed by researchers in the fields are summarized.

Chapter 3 describes the adaptation of a full-scale bearing test machine (SRMD testing facility at UC San Diego) to conduct real-time or near real-time hybrid simulations to study the dynamic response of isolated structures under realistic earthquake loading conditions. This chapter also describes challenges encountered in achieving reliable simulation results for these large scale dynamic tests such as compensation and correction for delay, inertia forces, and friction forces in the experimental setup.

Chapter 4 describes different components of hybrid simulation testing of seismically isolated NPP conducted at SRMD testing facility as part of this research program including analytical models, physical specimens, test setup configuration and different instrumentations

used to experimentally asses the seismic performance of seismically isolated NPP under different level of earthquake shakings.

In chapter 5, a summary of results from hybrid simulation tests conducted on seismically isolated NPP using full scale lead plug rubber bearings under different loading scenarios are provided. The complex nonlinear behavior of the seismic isolation bearings (i.e. vertical-horizontal coupling due to overturning or 3-D seismic excitation) is captured experimentally and its interaction with the numerical model of the superstructure is studied to evaluate system level and in-structure response.

In Chapter 6, a new moat wall model for impact simulation is proposed to capture the impact forces and the effects of impact on the response of seismically isolated NPPs. The moat wall model is added to simplified isolated plant model and used in parametric studies with different modeling and design properties such as a range of properties of impact model, moat wall and isolation system and variable clearance to the stop to identify parameters that influence the response.

In Chapter 7, additional studies were conducted with more refined structural model of NPP based on the APR 1400 in an effort to more accurately assess the seismic response of base isolated NPPs under uni- and bi-directional horizontal excitations considering moat wall impact using the proposed moat wall impact model in Chapter 6. Results for impact response parameters including penetration depth, impact velocities, and forces are examined and a simplified methodology to estimate these parameters is proposed.

Finally, chapter 8 summarizes the research work performed in this dissertation, emphasizes the main original contributions and findings of the research work, and provides recommendations for future research.

References

[1] FEMA (2007): Design Guide for Improving Critical Facility Safety from Flooding and High Winds: Providing Protection to People and Buildings. FEMA 543.

[2] Tajirian, F. F., Kelly, J. M., and Aiken, I. D. (1990): Seismic Isolation of Advanced Nuclear Power Stations. Earthquake Spectra, 6 (2), 371-401.

[3] Buckle, I. G., and Mayes, R. L. (1990): Seismic Isolation: History, Application, and Performance - A World View. Earthquake Spectra, 6 (2), 161-201.

[4] Bhatti, M. A., Ciampi, V., Kelly, J. M., and Pister, K. S. (1982): An earthquake isolation system for steam generators in nuclear power plants. Nuclear Engineering and Design, 73 (3), 229-252.

[5] ASCE (2017): Seismic analysis of safety-related nuclear structures, ASCE/SEI Standard 4. Reston, VA.

[6] United States Nuclear Regulatory Commission (USNRC) (forthcoming): Technical considerations for seismic isolation of nuclear facilities. NUREG-** Washington DC.

Chapter 2 Background and Literature Review

Technical background and literature review of seismic isolation and its application in NPPs, experimental testing using hybrid simulation, and structural pounding in isolated structures are presented. Past researcher efforts on the development of hybrid simulation and moat wall impact model are summarized here.

2-1 Seismic Isolation

Seismic isolation presents an effective strategy to protect structures from the damaging effects of horizontal earthquake shaking. This technique reduces the seismic forces by changing the stiffness and damping of the structure at the expense of increasing the relative displacement between the structure and its foundation in comparison to a non-isolated structure (Figure 2-1). The reduced demands in the superstructure above minimize the likelihood of the damage to structural and non-structural component of the structure [1]. Increasing damping in the isolation system by using devices such as viscous dampers together with the isolators could be considered to reduce the large displacement demand.

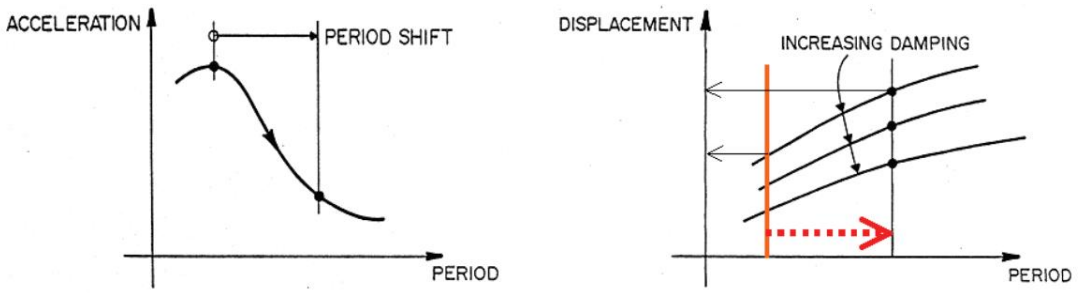

Figure 2-1 Principle of seismic isolation [2]

Unlike traditional design strategies which requires additional strength and ductility in the structure to resist seismic forces, typically the design of an isolated structure is such that the structure above the isolation plane remains essentially elastic while the isolation system exhibits nonlinear hysteretic behavior that localizes large deformations and provides energy dissipation.

The concept of seismic isolation traces back to more than a century ago, but it has been only in the last three-four decades that the technology matured to have engineered structures designed and built using this earthquake protective strategy. In 1985, the first seismically isolated building in the US was constructed, the Foothill Communities Law and Justice Center in Rancho Cucamonga. Since then, construction of seismically isolated building has increased with an almost exponential rate in Japan and China while in the US seismic isolation has remained mainly for critical and civil structures as well as essential and public building such as hospitals, city halls or emergency response centers [1].

2-1-1 Seismic Isolation in NPP

Application of seismic isolation to NPPs has been considered since the early 1980's with potential benefits including simplification of seismic design, enhanced safety margin, and facilitated standardization [3]. Although seismic isolation is a relatively mature technology, to

date there are very few applications to nuclear related structures. The Curas NPP in France and Koeberg NPP in South Africa equipped with synthetic rubber (neoprene) bearings and flats slider in some installation are the only two base isolated NPPs and both were designed and constructed in late 1970s and mid-1980s. Two experimental and research reactors equipped with seismic isolators, Jules Horowiz Reactor (JHR) and International Thermonuclear Experimental Reactor (ITER), are under construction and are considered as the modern application of seismic isolation in the nuclear industry [4].

There are different reasons associated with the limited applications of seismic isolation in the nuclear industry such as limited construction of new plants in the past 30 years and a lack of guidelines, codes and standards for the analysis, design and construction of isolation systems specific to nuclear structures [5]. In the US, recent code developments (ASCE 4-16 [5], and NUREG [6]) provide regulatory guidance on the use of seismic isolation technology and define minimum performance expectations and associated acceptance criteria for isolation system, superstructure, foundation, umbilical lines and stop/moat for seismically isolated NPP and safety related nuclear structures. The isolation system should demonstrate a high-confidence of low-probability of failure at the design level and the load carrying capacities should be maintained under beyond design earthquake shaking while excessive displacement of the isolation system should be precluded using a stop.

A variety of seismic isolation bearings have been developed and implemented around the world. In the US, three types of isolators have been qualified for the use in safety-related nuclear structures and NPPs: low damping (natural) rubber isolators, lead-rubber (natural) isolators, and friction pendulum sliding isolators [6], shown in Figure 2-2. Per ASCE 4, use of other types of

isolators and isolation system for the safety-related nuclear structures that are qualified (per ASCE 4-16 Sec. 12.1) may be acceptable in the future.

a) Lead rubber bearing

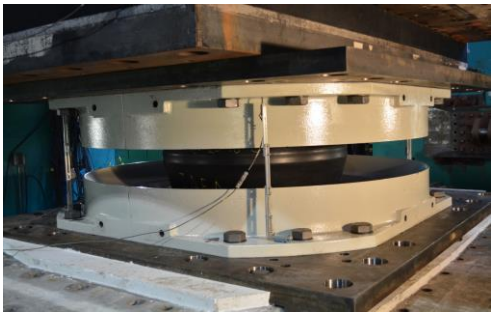

b) Triple Friction Pendulum bearing

Figure 2-2 Different types of seismic isolation system

2-1-2 Experimental Testing of Isolated Structures

The dynamic response of an isolated structure depends on the combined characteristics of the ground motion, bearings, and structure. This complex behavior provides some uncertainty concerning the nonlinear seismic response of isolated structures and requires detailed experimental investigations to fully characterize such behavior [2]. Especially under strong earthquake shaking, seismic isolation bearings can exhibit complex nonlinear behavior that is dependent on several factors, including the size scale, axial load, temperature, and rate of loading.

Full scale component tests of individual bearings and system level tests capturing the interaction with the superstructure are essential towards fully characterizing and understanding the bearing behavior. The use of reduced-scale test specimens reduces the confidence that can be placed in this technology, and uncertainties about the realism of test results complicates validation of numerical models and understanding of the behavior of an isolated system under extreme loading conditions.

In component (characterization) tests, the test specimen is subjected to a pre-described history of displacement and loading. Results from these tests are important to develop verified and validated numerical models capable of predicting accurate dynamic response of different types of bearings specially for application in nuclear industry [5]. In the US, different design codes such as ASCE 7 (buildings), AASHTO (bridges), ASCE 4 (safety-related nuclear structures), NUREG (NPPs) require a number of full scale prototype and production tests under specified loading protocols for each type of seismic isolator used in the isolation system to ensure reliable and consistent performance of these components [6-9].

While the standard prototype tests are necessary to characterize the response of seismic isolators, these tests are not sufficient to verify the adequacy of analytical models and more realistic dynamic testing is required to capture the system level dynamic response of the isolation system for which shake table and hybrid simulation tests could be considered.

Full scale shake table testing is considered to be the most realistic method to experimentally asses the dynamic response of structural systems. Only a few system level tests have been conducted on full-scale isolated building structures using shake tables [10-14]. Unfortunately, full scale testing of bearings for application in nuclear facilities would be prohibitive on a shake table due to the size and load limitations.

Hybrid simulations at real-time or near real-time rates can be an efficient and economical approach for testing seismically isolated structures. Laboratory facilities exist to test full-scale seismic isolation bearings under prescribed displacement or load protocols, and the supported structure is expected to remain essentially within the elastic range of response and can be accurately modeled. Thus, hybrid simulation provides a unique opportunity to assess experimentally the dynamic behavior of base isolated NPPs, using full scale bearings.

2-2 Hybrid Simulation

Hybrid simulation, formerly also called the psedudo-dynamic test method, is a well-established method of testing which combines analytical and experimental modeling approaches to investigate the behavior of a structural system. This method seamlessly combines experimental substructures representing critical components that exhibit complex nonlinear behavior and analytical models of the remainder of the structural system with more predictable behavior. Some of the most important advantages of this testing technique are:

- Wide variety of loading conditions including both dynamic (seismic, wind, blast, wave, and traffic) and static loading (gravity, prestress)
- Large scale experimental testing through substructuring
- Ability to capture time-dependent behaviors with real-time hybrid simulation
- Possibility to conduct geographically distributed testing

Several research studies initiated the development of the hybrid simulation testing in the late 1960s and early 1970s. The first major publication was by Takanshi et al. which proposed the hybrid simulation testing method as an alternative to shake table tests [15]. The advancement in hybrid simulation to develop a faster and more reliable test method ties closely to developments in the field of control and high-performance computing. Developments in hybrid simulation include variety of areas such as suitable integration algorithm to ensure stability in iterations with experimental substructures, experimental errors, continuous testing and delay compensations, real-time testing, substructuring techniques, and geographically distributed hybrid simulation testing [16].

There have been many efforts to develop stable, efficient and accurate integration algorithm to be used in hybrid simulation [17-21]. Implicit Newmark with fixed number of iteration (iterative) and the operator-splitting (non-iterative) integrations schemes are among widely used methods for hybrid simulation. Study by Del Carpio et al. examines the performance of different integration methods for hybrid simulation through collapse using large scale physical substructures and highly nonlinear numerical models [22].

With regards to experimental error, studies by Shing and Mahin, Nakashima et al, Thewalt and Mahin in late 1980s and 1990s [17, 23, 24] provided significant contribution to identifying and determining the experimental errors and the rate of loading effects. More recent studies provided detailed explanations and summaries on errors in hybrid simulations, including errors based on modeling, implementation techniques, and the experimental setup as well as error indicators for hybrid simulation tests [25-28].

Continuous testing is essential to have an accurate and reliable hybrid simulation in comparison to conventional pseudo-dynamic testing method that the load is applied using ramp-hold procedure. The two reasons that make it essential are force relaxation in the hold period and non-deterministic command generation from the analytical model while the control system of the actuator system requires commands in a determinist rates. Different predictor-corrector command generation as well as delay compensation schemes were developed by different researchers to improve stability [29-36]. Schellenberg et al. compiled a range of new and improved Predictor-Corrector algorithms to develop a common framework for conducting hybrid simulation across various laboratories and computing environments, the Open-source Framework for Experimental Setup and Control [37-39] . OpenFresco was used in hybrid simulation tests as part of this research program and a brief summary is presented in Chapter 3.

2-2-1 Real-time Hybrid Simulation

Real-time hybrid simulation has been proposed for testing structures that can exhibit significant rate of loading effects and need to capture strain-rate, damping and inertial effects. Seismic isolation bearings have demonstrated path-dependent behavior with degradation parameters that depend on the rate of loading, number of cycles and scale size of the bearings and required testing in real-time or near real-time to fully capture the true response behavior of isolators.

In a real-time hybrid simulation test, velocities are controlled as well as displacement for the experimental portion therefore damping, inertia, and any other strain rate effects can be measured accurately from the physical specimen. The first application of hybrid simulation for real-time testing was implemented by Nakashima et al. to a SDOF system using a dynamic actuator and a digital servo-mechanism (replacing the analogue one) to ensure accurate displacement and velocity control [31].

Recent development in delay compensation techniques and direct time integration schemes were able to reduce instability issues and improve testing accuracy in real-time hybrid simulation [32, 34, 36, 40-44]. Real-time hybrid simulations have been successfully used to investigate the dynamic behavior of structure with rate-dependent devices [35, 45-47].

2-3 Structural Pounding and Moat Wall Impact

Earthquake induced pounding between adjacent structures of building and highway bridges has been a major cause of structural and nonstructural seismic damage in past earthquakes. Pounding damage in buildings has been widely reported in most major earthquakes.

In the 1985 Mexico City Earthquake, over 40% of the 330 severely damaged or collapsed building were reported to be caused by structural pounding [48]. A few cases of pounding have been reported in base isolated buildings [49].

In a base isolated structure, the increased flexibility at the base leads to significant reductions in forces and acceleration transmitted to the structure above the isolation level at the expense of displacements concentrated in the isolation system. A surrounding moat wall with its backfill soil can function as a stop to limit isolation system displacements and prevent bearing failure for beyond design basis shaking. However, impact of the isolated structure against the moat wall is of concern due to potential amplification in response of the superstructure. An overview of research to study structural pounding, moat wall impact and passive response of backfill soil are presented here.

2-3-1 Experimental studies

A number of tests have been conducted to study response of structures considering pounding and assess the validity of different impact theories, and accuracy of the assumed models. van Mier et al. studied concrete-to-concrete impacts between breakwater armor elements through a series of dynamic experiments for different impact velocities, concrete quality, mass of the striker elements and contact surface geometries [50]. The testing apparatus consisted of a prestressed concrete pile (with cross section of 250 mm ^{2} and length of 20 m) and different shape and weight strikers (Figure 2-3). Different contact geometries of the striker and the target surface were considered in these tests such as: spherical, conical, truncated conical, corrugated geometries. van Mier et al. concluded that the choice of contact surface geometry had a significant influence on the load-time response of the impact. A simple elastoplastic contact

model was developed to predict the pressure time history of the contact zone based on the contact stiffness, critical stress and size of the contact surface and the unloading stiffness.

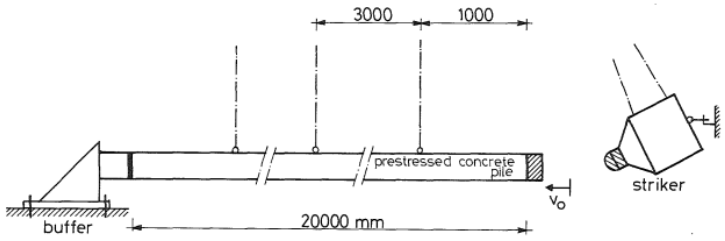

Figure 2-3 Apparatus for dynamic impact experiments [50]

Filiatrault et al conducted a series of shake table tests of pounding between adjacent three- and eight- story single-bay steel framed model structure [51]. Experimental results from these tests were compared to numerical predictions using elastic gap elements. Accurate displacement and impact forces were estimated from the analytical model.

In an effort to investigate further the pounding phenomenon of adjacent building during earthquake, Papadrakakis et al. performed two series of shake table tests using two, two-story reinforced concrete building frames; one designed to be more flexible to the other (Figure 2-4) [52]. In the first series of tests, the test structures were placed with an adequate gap to avoid pounding. The same tests were repeated with zero gap separation and pounding was induced. The acceleration response of structure considering pounding showed a dramatic increase up to six time with respect to tests without pounding. Also, it was shown that an analytical approach based on Lagrange multiplier method could be a reliable tool to model pounding between adjacent buildings.

Figure 2-4 Overall view of test structure with reference frame [52]

Goldsmith reported results of experimental tests on collision between spheres, impact of spheres on plates and impact tests on elastic bars and beams. Goldsmith proposed the stiffness parameter of the Hertz impact model to be a function elastic properties and geometry of the two colliding bodies [53].

Jankowski performed two sets of experimental tests to determine the range of the coefficient of restitution and the impact stiffness parameter between steel, concrete, timber and ceramics (Figure 2-5) [54]. The first set of experiments was conducted by dropping balls (ball diameters between 21 and 128 mm) of different masses on a rigid surface of the same material, whereas the second sets used a small shaking table to focus on pounding-involved structural response of two tower models. The results of the impact experiment showed that the value of the coefficient of restitution depends substantially on the prior-impact velocity and the material of colliding elements. Based on the results of the shaking table experiment, Jankowski concluded that structural pounding may cause considerable amplification of the response by structural

pounding and there is a substantial influence of the material used for colliding elements on the behavior of structures during earthquake.

(a) (b)

Figure 2-5 Setup of (a) the impact experiment and (b) shaking table test [54]

Masroor and Mosqueda conducted a series of shake table tests to assess performance of limit states of seismically isolated buildings under strong ground motion considering moat wall pounding using a ¼ scale three storey intermediate moment resisting frame, friction pendulum bearing and a moat wall model (Figure 2-6) [55]. Different moat wall models including a rigid triangle steel stop and a concrete wall with various thickness with backfill soil were considered. The test results indicate that the contact forces were largely dependent on the provided gap displacement, impact velocity, and wall flexibility. Masroor and Mosqueda proposed a new impact model that consider both local deformation and the vibration aspects of impact (Figure 2-7) [56]. It was shown that the proposed impact element was able to accurately capture the observed response in experiments and the effects of impact on superstructure response.

Figure 2-6 Shake table test setup for moat wall impact testing [55]

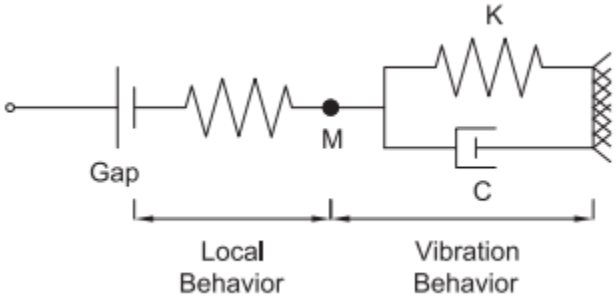

Figure 2-7 Schematic of new impact element [56]

More recently, Sasaki et al. conducted full-scale shake table experiments of base-isolated building to evaluate the increase in the floor response acceleration due to pounding to moat wall [14]. The specimen was an isolated four-story RC building with rubber and sliding bearings as well as steel U-shaped and oil dampers for the isolation system (Figure 2-8). Two different thicknesses for the reinforced concrete moat wall were considered, 200 (BW20) and 400 mm (BW40). To evaluate functionality after pounding under strong motion, several furniture pieces were also installed to represent different occupancies such as school class room, medical rooms, server room and etc. Different pounding condition were considered by varying provided

clearance and using rubber blocks to mitigate the impact shock. Based on provided results, the rubber blocks were able to mitigate the floor acceleration due to impact while there was still an increase in the floor acceleration which caused non-structural damages.

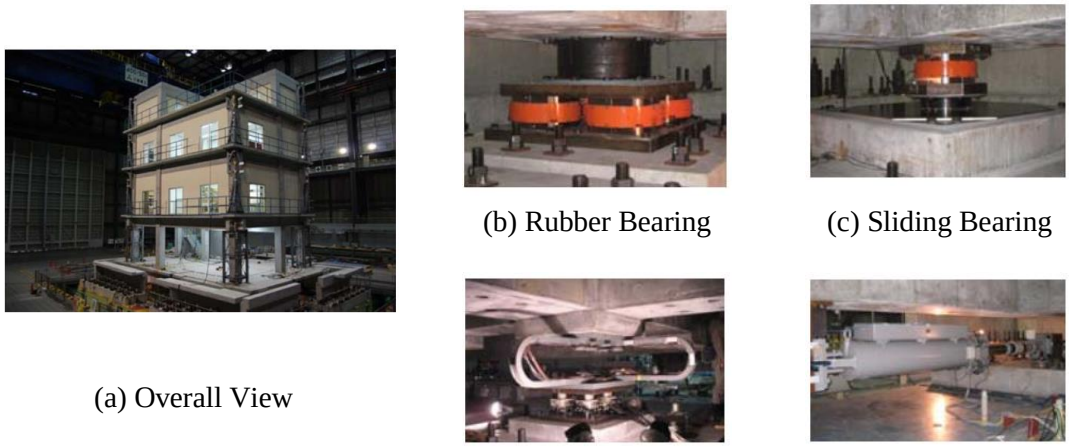

(a) Overall View

(b) Rubber Bearing

(c) Sliding Bearing

(d) U-Shaped Steel Damper

(e) Oil Damper

Figure 2-8 Full Scale Base Isolated Building Specimen [14]

(a)

(b)

Figure 2-9 Damage after pounding to BW40: (a) without rubber blocks under Takatori 90% (b) with rubber blocks under Takatori 65% [14]

2-3-2 Analytical and Numerical Studies

A variety of impact models for modeling the dynamic response of structures were developed by researcher to analyze the dynamic properties of structure considering pounding effects. Two main modeling techniques are the stereomechanical approach and the contact element approach. The classical theory of impact, called stereomechanical approach, assumes that the impact is instantaneous and the laws of momentum and energy conservation are used to determine the post-impact velocities of the colliding bodies [53, 57, 58]. Energy loss during impact is accounted in this approach by using coefficient of restitution (e). This approach has been used to model structural pounding by several researchers [59, 60]. This approach lacks the ability to account for duration, impact forces, and local deformation (indentation) at the contact point and these assumptions limit its application to capture impact response of structural pounding accurately [49].

Alternatively, the contact element approach is a force-based approach to model the impact and it uses combination of springs and dashpots to represent the impact force-deformation behavior. Several linear and non-linear impact contact elements have been developed including linear spring element, Kelvin-Voigt element, the Hertz contact element and the Hertz damped elements (Figure 2-10).

The simplest one is the linear spring model which uses a linear spring to model the impact force and the energy dissipation during impact is ignored in this model [61], see Figure 2-10a. To overcome this limitation, the Kelvin model represented by a linear spring in combination with a damper is proposed and used in some studies [62, 63]. In this model, the damping coefficient can be related to the coefficient of restitution which describe the energy loss

during impact [63]. This model exhibits an initial jump of the impact force upon the impact and also results in tensile force acting on bodies just before separation (Figure 2-10b). A minor adjustment is proposed by Komodoromos et al [64], modified Kelvin-Voigt element, to avoid the tensile impact force before at the end of restitution period.

Results from some impact experimental tests showed that the energy is mainly dissipated within the approach period of impact and the Hertz model can adequately predict the impact behavior [53]. The Hertz contact law was originally proposed for static contact of two bodies and the contact force is based on the relative indentation of two bodies considering their elastic properties and geometry. The original model does not capture the energy dissipation during impact and to overcome this limitation the Hertz damped model in conjugation with a non-linear damper was proposed and adopted by several researchers to study structural pounding [56, 57, 65-68].

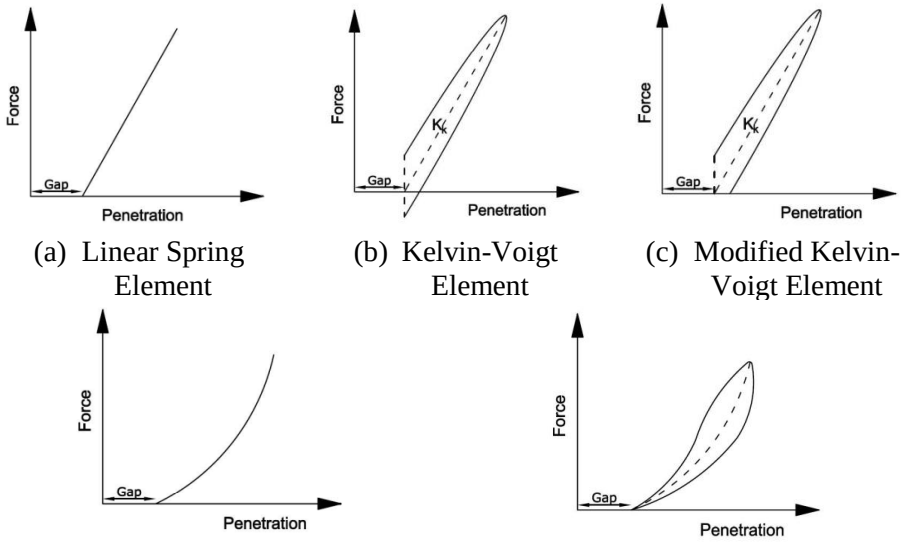

(a) Linear Spring Element (b) Kelvin-Voigt Element (c) Modified Kelvin-Voigt Element

(d) Hertz element (e) Hertz Damped Element

Figure 2-10 Different Impact Model [49]

2-3-3 Passive earth pressure load-deflection

Past numerical studies and experimental tests on bridge abutments with backfill soil were found to be relevant to modeling the backfill soil used in proposed impact macro elements in Chapter 6. Extensive experimental works including several large scale tests associated with passive earth pressure and load-deflection curve were performed by different researchers over the past years.

Duncan and Mokwa performed two passive pressure tests on a 1.1 meter high, 1.9 meter long, 0.9 meter wide anchor block considering using two different backfill soils [69]. In these tests, load was applied incrementally and each load was maintained for about 1 min before applying the next load. Based on results from those tests, it was shown the hyperbolic model provides a good approximate of the passive load-deflection curve.

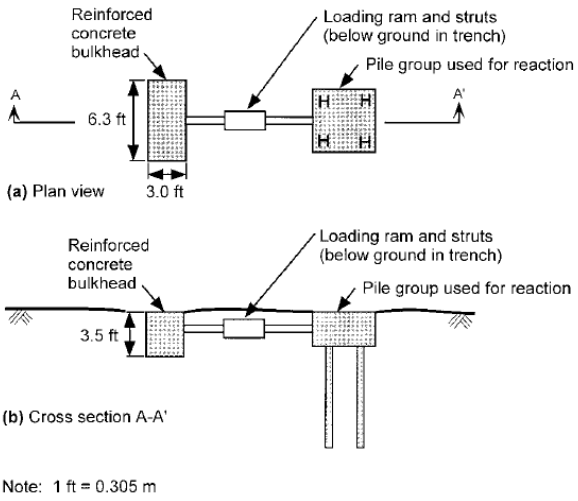

Figure 2-11 Test arrangement for passive pressure load tests [69]

Cole and Rollins performed a series of full-scale tests on a 1.1 meter high, 5.2 meter long and 3.1 meter wide pile cap under cyclic loading using four different soils [70]. From these tests, Cole and Rollins concluded that the hyperbolic model proposed by Duncan and Mokwa [69]

provided the best agreement with the measured load-deflection behavior for monotonic loading and the Log Spiral theory with correction for 3D effects provided the best estimate of the ultimate passive pressure.

Lemnitzer et al. [71] performed a series of full-scale cyclic tests of a 1.7 meter high abutment backwall with well graded silty sand (SW-SM) backfill by using diagonal and lateral loading system to provide a purely horizontal translation of the backwall and not allowed to displace vertically. Lemnitzer et al. concluded that the ultimate passive strength was estimated accurately by the Log Spiral method and a method of slices approach and the shape of measured load-deflection behavior was well estimated with the hyperbolic curves.

In 2009, Wilson performed two large scale static experiments on a 1.68 meter high, 2.87 meter width test wall using a 2.54 meter high, 6.7 meter long and 2.9 meter wide soil container filled with the backfill material consisted of sand with non-plastic silt (about 7%) and fine gravel (less than 7%) [72]. Two static passive earth pressure tests were conducted to measure the passive load-displacement behavior. Lateral load was applied to the vertical reinforced concrete wall section, which displaces freely along with the adjacent backfill in the horizontal and vertical directions. Results from FE simulations conducted by Wilson using hyperbolic model provided a good agreement between experimental data and simulated results. The FE model was later employed to investigate the passive force-displacement response, per meter of wall with, for four considered backfills over a range of wall heights (1 to 5 m). Hyperbolic model approximation was reported for 32 different combination and can be used to represent passive earth pressure load-displacement response in pushover and dynamic simulation.

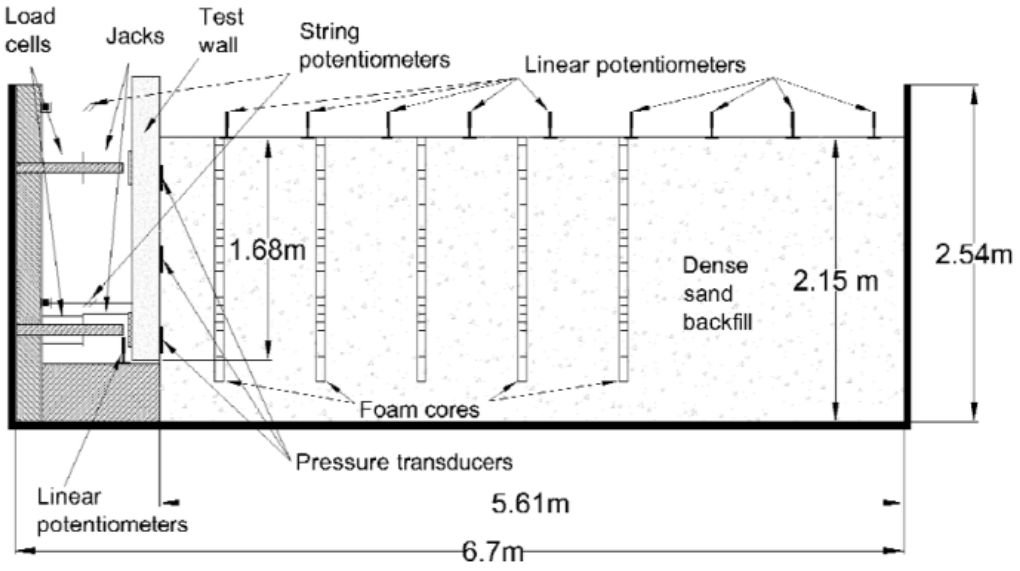

Figure 2-12 Schematic elevation view of passive earth pressure experiment with instrumentation layout [73]

Experimental studies described above have provided valuable new insight, but cover only a limited range of backfill soil types, wall heights (up to 2.3 meters) and wall configurations. A majority of these experimental studies on retaining walls were conducted under static loading condition in an effort to develop the load-deflection curve and measure the peak passive resistance of the backfill soil. In these tests, retaining walls were loaded using static actuators to mostly displace the retaining walls in horizontal direction with the base of the wall free to displace and/or rotate which have different boundary conditions for the application to moat walls considered here. Even though the described studies may not be a perfect match to the case of moat wall pounding, these studies were found relevant to modeling thee backfill soil for this study.

References

[1] Warn, G. P., and Ryan, K. L. (2012): A Review of Seismic Isolation for Buildings: Historical Development and Research Needs. Buildings, 2 (3), 300.

[2] Constantinou, M. C., Whittaker, A. S., Kalpakidis, Y., Fenz, D. M., and Warn, G. P. (2007): Performance of seismic isolation hardware under service and seismic loading. MCEER-07-0012Multidisciplinary Center for Earthquake Engineering Research, Buffalo, NY

[3] Tajirian, F. F., Kelly, J. M., and Aiken, I. D. (1990): Seismic Isolation of Advanced Nuclear Power Stations. Earthquake Spectra, 6 (2), 371-401.

[4] Lo Frano, R., and Forasassi, G. (2010): Isolation systems influence in the seismic loading propagation analysis applied to an innovative near term reactor. Nuclear Engineering and Design, 240 (10), 3539-3549.

[5] Whittaker, A. S., Kumar, M., and Kumar, M. (2014): Seismic Isolation of Nuclear Power Plants. Nuclear Engineering and Technology, 46 (5), 569-580.

[6] ASCE (2017): Seismic analysis of safety-related nuclear structures, ASCE/SEI Standard 4. Reston, VA.

[7] USNRC (forthcoming): Technical considerations for seismic isolation of nuclear facilities. NUREG-** Washington DC.

[8] AASHTO (2017): LRFD Bridge Design Specifications Washington, D.C.

[9] ASCE (2017): ASCE Minimum Design Loads and Associated Criteria for Buildings and Other Structures, ASCE/SEI Standard 7. Reston, VA.

[10] Sato, E., Furukawa, S., Kakehi, A., and Nakashima, M. (2011): Full-scale shaking table test for examination of safety and functionality of base-isolated medical facilities. Earthquake Engineering & Structural Dynamics, 40 (13), 1435-1453.

[11] Dao, N. D., Ryan, K. L., Sato, E., and Sasaki, T. (2013): Predicting the displacement of triple pendulum™ bearings in a full-scale shaking experiment using a three-dimensional element. Earthquake Engineering & Structural Dynamics, 42 (11), 1677-1695.

[12] Furukawa, S., Sato, E., Shi, Y., Becker, T., and Nakashima, M. (2013): Full-scale shaking table test of a base-isolated medical facility subjected to vertical motions. Earthquake Engineering & Structural Dynamics, 42 (13), 1931-1949.

[13] Chen, M. C., Pantoli, E., Wang, X., Astroza, R., Ebrahimian, H., Hutchinson, T. C., Conte, J. P., Restrepo, J. I., Marin, C., Walsh, K. D., Bachman, R. E., Hoehler, M. S., Englekirk, R., and Faghihi, M. (2016): Full-Scale Structural and Nonstructural Building System Performance during Earthquakes: Part I – Specimen Description, Test Protocol, and Structural Response. Earthquake Spectra, 32 (2), 737-770.

[14] Sasaki, T., Sato, E., Fukuyama, K., and Kajiwara, K. (2017): Enhancement of Base-isolation based on E-Defense Full-Scale Shake Table Experiments: Dynamic Response of Base-Isolated Building under Impact due to Pounding. 16WCEE, Santiago, Chile.

[15] Takanashi, K., Udagawa, K., Seki, M., Okada, T., and Tanaka, H. (1975): Non-linear earthquake response analysis of structures by a computer-actuator online system. Transations of the Architectural Institute of Japan, 229, 77–83.

[16] Hashemi, M. J. (2013): Collapse simulation of multi-story buildings through hybrid testing with substructuring techniques.Ph.D. dissertation, Dept. of Civil and Environmental Engineering, The State University of New York, Univeristy at Buffalo, Buffalo, NY.

[17] Shing, P., and Mahin, S. A. (1984): Pseudodynamic test method for seismic performance evaluation: theory and implementation. EERC ReportUBC/EERC-84

[18] Shing, P.-S. B., Vannan, M. T., and Cater, E. (1991): Implicit time integration for pseudodynamic tests. Earthquake Engineering & Structural Dynamics, 20 (6), 551-576.

[19] Ghaboussi, J., Yun, G. J., and Hashash, Y. M. A. (2006): A novel predictor–corrector algorithm for sub-structure pseudo-dynamic testing. Earthquake Engineering & Structural Dynamics, 35 (4), 453-476.

[20] Ahmadizadeh, M., and Mosqueda, G. (2008): Hybrid Simulation with Improved Operator-Splitting Integration Using Experimental Tangent Stiffness Matrix Estimation. Journal of Structural Engineering, 134 (12), 1829-1838.

[21] Chen, C., Ricles, J. M., Marullo, T. M., and Mercan, O. (2009): Real-time hybrid testing using the unconditionally stable explicit CR integration algorithm. Earthquake Engineering & Structural Dynamics, 38 (1), 23-44.

[22] Del Carpio R., M., Hashemi, M. J., and Mosqueda, G. (2017): Evaluation of integration methods for hybrid simulation of complex structural systems through collapse. Earthquake Engineering and Engineering Vibration, 16 (4), 745-759.

[23] Nakashima, M. (1983): Stability and accuracy of integration techniques in pseudo-dynamic testing. Technical Report No. 105Building Research Institute, Ministry of Construction, Japan

[24] Thewalt, C. R., and Mahin, S. A. (1995): Non-planar pseudodynamic testing. Earthquake Engineering & Structural Dynamics, 24 (5), 733-746.

[25] Mosqueda, G. (2003): Continuous hybrid simulation with geographically distributed substructures.Ph.D. dissertation.

[26] Mosqueda, G., and Mahin, S. A. (2005): Implementation and accuracy of continuous hybrid simulation with geographically distributed substructures.

[27] Mercan, O. (2007): Analytical and experimental studies on large scale real-time pseudodynamic testing.Ph.D. dissertation, Dept. of Civil and Environmental Engineering, Lehigh Univ., Bethlehem, Pa.

[28] Ahmadizadeh, M., and Mosqueda, G. (2009): Online energy-based error indicator for the assessment of numerical and experimental errors in a hybrid simulation. Engineering Structures, 31 (9), 1987-1996.

[29] Agrawal, A. K., and Yang, J. N. (2000): Compensation of time-delay for control of civil engineering structures. Earthquake Engng. Struct. Dyn.,, 29 (37-62).

[30] Takanashi, K., and Ohi, K. (1983): Earthquake response analysis of steel structures by rapid computer-actuator on-line system. Earthquake Resistant Strcutre Research Center (ERS), Inst. of Indusctrial Sci. University of Tokyo.

[31] Nakashima, M., and Masaoka, N. (1999): Real-time on-line test for MDOF systems. Earthquake Engng. Struct. Dyn., 28, 393–420.

[32] Horiuchi, T., and Konno, T. (2001): A new method for compensating actuator delay in real–time hybrid experiments. Philosophical Transactions of the Royal Society of London. Series A: Mathematical, Physical and Engineering Sciences, 359 (1786), 1893-1909.

[33] Magonette, G. (2001): Development and application of large-scale continuous pseudo-dynamic testing techniques. Phil. Trans. R. Soc. Lond., 359, 1771-1799.

[34] Ahmadizadeh, M., Mosqueda, G., and Reinhorn, A. M. (2008): Compensation of actuator delay and dynamics for real-time hybrid structural simulation. Earthquake Engineering & Structural Dynamics, 37 (1), 21-42.

[35] Carrion, J. E., Spencer, B. F., and Phillips, B. M. (2009): Real-time hybrid simulation for structural control performance assessment. Earthquake Engineering and Engineering Vibration, 8 (4), 481-492.

[36] Chae, Y., Kazemibidokhti, K., and Ricles, J. M. (2013): Adaptive time series compensator for delay compensation of servo-hydraulic actuator systems for real-time hybrid simulation. Earthquake Engineering & Structural Dynamics, 42 (11), 1697-1715.

[37] OpenFresco (2014): Open-source framework for experimental setup and control (Version 2.7) [computer software] <available at: http://openfresco.berkeley.edu/>.

[38] Schellenberg, A. H., Mahin, S. A., and Fenves, G. L. (2009): Advanced Implementation of Hybrid Simulation. Technical Report PEER 2009/104 Pacific Earthquake Engineering Research Center, University of California, Berkeley, Berkeley, CA.

[39] Fenves, A. S. S. A. M. a. G. L. (2007): A Software Framework for Hybrid Simulation of Large Structural Systems. Structural Engineering Research Frontiers.

[40] Darby, A. P., Blakeborough, A., and Williams, M. S. (1999): Real-Time Substructure Tests Using Hydraulic Actuator. Journal of Engineering Mechanics, 125 (10), 1133-1139.

[41] Darby, A. P., Blakeborough, A., and Williams, M. S. (2001): Improved control algorithm for real-time substructure testing. Earthquake Engineering & Structural Dynamics, 30 (3), 431-448.

[42] Bonelli, A., Bursi, O. S., He, L., Magonette, G., and Pegon, P. (2008): Convergence analysis of a parallel interfield method for heterogeneous simulations with dynamic substructuring. International Journal for Numerical Methods in Engineering, 75 (7), 800-825.

[43] Gao, X., Castaneda, N., and Dyke, S. J. (2013): Real time hybrid simulation: from dynamic system, motion control to experimental error. Earthquake Engineering & Structural Dynamics, 42 (6), 815-832.

[44] Shao, X., Reinhorn, A. M., and Sivaselvan, M. V. (2011): Real-Time Hybrid Simulation Using Shake Tables and Dynamic Actuators. Journal of Structural Engineering, 137 (7), 748-760.

[45] Wu, B., Wang, Q., Benson Shing, P., and Ou, J. (2007): Equivalent force control method for generalized real-time substructure testing with implicit integration. Earthquake Engineering & Structural Dynamics, 36 (9), 1127-1149.

[46] Karavasilis, T. L., Ricles, J. M., Sause, R., and Chen, C. (2011): Experimental evaluation of the seismic performance of steel MRFs with compressed elastomer dampers using large-scale real-time hybrid simulation. Engineering Structures, 33 (6), 1859-1869.

[47] Chen, C., Ricles, J. M., and Guo, T. (2012): Improved Adaptive Inverse Compensation Technique for Real-Time Hybrid Simulation. Journal of Engineering Mechanics, 138 (12), 1432-1446.

[48] Rosenblueth, E., and Meli, R. (1986): The 1985 Earthquake: Causes and Effects in Mexico City. Concrete International, 8, 23-24.

[49] Masroor Shalmani, A. (2013): Seismic response of base isolated buildings considering pounding to moat walls. PhD Dissertation Ph.D., State University of New York at Buffalo.

[50] Mier, J. G. M. v., Pruijssers, A. F., Reinhardt, H. W., and Monnier, T. (1991): Load-Time Response of Colliding Concrete Bodies. Journal of Structural Engineering, 117 (2), 354-374.

[51] Filiatrault, A., Wagner, P., and Cherry, S. (1995): Analytical prediction of experimental building pounding. Earthquake Engineering & Structural Dynamics, 24 (8), 1131-1154.

[52] Papadrakakis, M., and Mouzakis, H. P. (1995): Earthquake simulator testing of pounding between adjacent buildings. Earthquake Engineering & Structural Dynamics, 24 (6), 811-834.

[53] Goldsmith, W. (2001): Impact: The Theory and Physical Behavior of Colliding Solids. Dover Publication, New York.

[54] Jankowski, R. (2010): Experimental study on earthquake-induced pounding between structural elements made of different building materials. Earthquake Engineering & Structural Dynamics, 39 (3), 343-354.

[55] Masroor, A., and Mosqueda, G. (2012): Experimental simulation of base-isolated buildings pounding against moat wall and effects on superstructure response. Earthquake Engineering & Structural Dynamics, 41 (14), 2093-2109.

[56] Masroor, A., and Mosqueda, G. (2013): Impact model for simulation of base isolated buildings impacting flexible moat walls. Earthquake Engineering & Structural Dynamics, 42 (3), 357-376.

[57] Muthukumar, S., and DesRoches, R. (2006): A Hertz contact model with non-linear damping for pounding simulation. Earthquake Engineering & Structural Dynamics, 35 (7), 811-828.

[58] X., G. A., and H., L. (2008): Pounding reduction of highway bridges with pounding effect by using magnetorheological dampers under earthquake excitations. Advances in Structural Engineering, 11 (3), 317-334.

[59] Papadrakakis, M., Mouzakis, H., Plevris, N., and Bitzarakis, S. (1991): A lagrange multiplier solution method for pounding of buildings during earthquakes. Earthquake Engineering & Structural Dynamics, 20 (11), 981-998.

[60] Malhotra, P. K. (1998): Dynamics of Seismic Pounding at Expansion Joints of Concrete Bridges. Journal of Engineering Mechanics, 124 (7), 794-802.

[61] Maison, B. F., and Kasai, K. (1990): Analysis for a Type of Structural Pounding. Journal of Structural Engineering, 116 (4), 957-977.

[62] Wolf, J. P., and Skrikerud, P. E. (1980): Mutual pounding of adjacent structures during earthquakes. Nuclear Engineering and Design, 57 (2), 253-275.

[63] Anagnostopoulos, S. A. (1988): Pounding of buildings in series during earthquakes. Earthquake Engineering & Structural Dynamics, 16 (3), 443-456.

[64] Komodromos, P., Polycarpou, P. C., Papaloizou, L., and Phocas, M. C. (2007): Response of seismically isolated buildings considering poundings. Earthquake Engineering & Structural Dynamics, 36 (12), 1605-1622.

[65] Jing, H.-S., and Young, M. (1991): Impact interactions between two vibration systems under random excitation. Earthquake Engineering & Structural Dynamics, 20 (7), 667-681.

[66] Davis, R. O. (1992): Pounding of buildings modelled by an impact oscillator. Earthquake Engineering & Structural Dynamics, 21 (3), 253-274.

[67] Pantelides, C. P., and Ma, X. (1998): Linear and nonlinear pounding of structural systems. Computers & Structures, 66 (1), 79-92.

[68] Chau, K. T., and Wei, X. X. (2001): Pounding of structures modelled as non-linear impacts of two oscillators. Earthquake Engineering & Structural Dynamics, 30 (5), 633-651.

[69] Duncan, J. M., and Mokwa, R. L. (2001): Passive Earth Pressures: Theories and Tests. Journal of Geotechnical and Geoenvironmental Engineering, 127 (3).

[70] Cole, R. T., and Rollins, K. M. (2006): Passive Earth Pressure Mobilization during Cyclic Loading. Journal of Geotechnical and Geoenvironmental Engineering, 132 (9).

[71] Lemnitzer, A., Ahlberg, E. R., Nigbor, R. L., Shamsabadi, A., Wallace, J. W., and Stewart, J. P. (2009): Lateral Performance of Full-Scale Bridge Abutment Wall with Granular Backfill. Journal of Geotechnical and Geoenvironmental Engineering, 135 (4).

[72] Wilson, P. (2009): Large scale passive force-displacement and dynamic earth pressure experiments and simulations. Ph.D. Dissertation, University of California, San Diego.

[73] Wilson, P., and Elgamal, A. (2010): Large-Scale Passive Earth Pressure Load-Displacement Tests and Numerical Simulation. Journal of Geotechnical and Geoenvironmental Engineering, 136 (12), 1634-1643.

Chapter 3 Adaptation of The Caltrans SRMD Test Facility for Hybrid Simulation

3-1 Introduction

This chapter describes the adaptation of a full-scale bearing test machine to conduct real-time or near real-time hybrid simulations to study the dynamic response of isolated structures under realistic earthquake excitations. This chapter also describes challenges encountered in achieving reliable simulation results for the large scale dynamic tests presented in this dissertation. In particular, algorithms for delay compensation and correction of feedback forces to remove inherent inertia and friction forces in the experimental setup were developed.

3-2 Description of The SRMD Testing Facility

The Seismic Response Modification Device (SRMD) testing facility at UCSD was designed for real-time 6-DOF dynamic characterizations of full-scale bearing devices and

dampers using predefined loading protocols. The facility shown in Figure 3-1 was developed jointly by the California Department of Transportation (Caltrans), the Department of Structural Engineering at UCSD, and MTS Corporation in 1999. This facility was primarily designed to apply large displacement demands on bearings and dampers at relatively high velocity with a high loading capacity. For example, the machine's axial load capacity of 53,400 kN is well above the design gravity load and anticipated axial load demand induced by overturning moment for most applications of seismic isolation. A summary of the machine's capacities is given in Table 3-1.

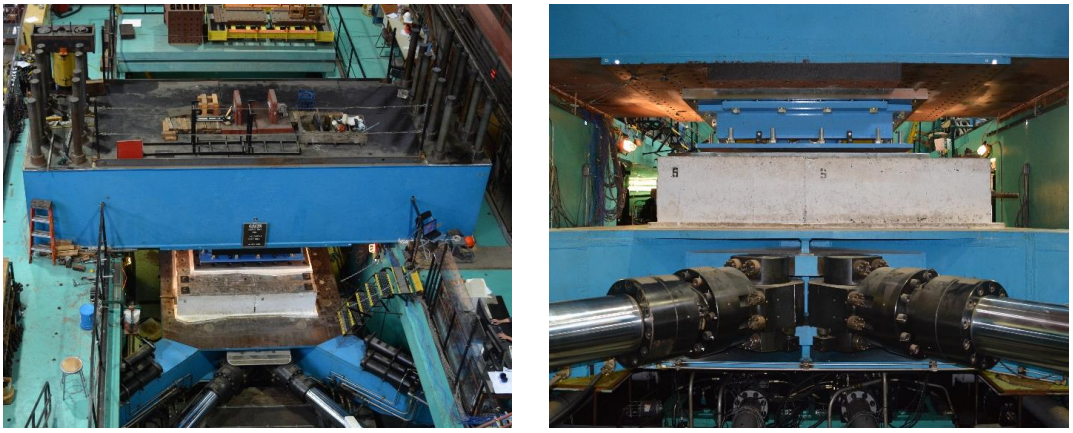

(a) (b)

Figure 3-1 SRMD testing facility: (a) overview and (b) installed bearing

The moving platen of the SRMD is contained within a self-reacting prestressed concrete reaction box. Four horizontal actuators control the longitudinal and lateral displacements of the 3,658 mm wide by 4,750 mm long platen. The platen slides over four hydrostatic low friction bearings that control the vertical movement of the platen (Figure 3-2). For improved stability, the platen is connected to four steel outrigger arms, each supported by a pair (i.e., upper and lower) of low friction sliding bearing actuators to control the vertical and rotational motions of the platen. A removable steel cross beam is used to restrain the top of the bearing sitting on the

platen and subject to desired multi-axis loading The installation was updated in 2003 with a digital tri-variable controller and a digital off-line simulation for performance prediction and to operate in “shaking table” mode.

Table 3-1 Testing machine technical specification [1]

Component	***Capacity***	***Accuracy of application***	***Accuracy of readout***
Vertical force	53,400 kN	±5%	0.5% full range
Longitudinal force	8900 kN		1.0% full range
Lateral force	4450 kN		1.0% full range
Vertical displacement	±0.127 m	±2%	1.0% full range
Longitudinal displacement	±1.22 m	±2%	1.0% full range
Lateral displacement	±0.61 m	±2%	1.0% full range
Vertical velocity	±254 mm/sec	±10%	
Longitudinal velocity	±1,778 mm/sec	±10%	
Lateral velocity	±762 mm/sec	±10%	
Rotation (roll, pitch, and yaw)	±2°		

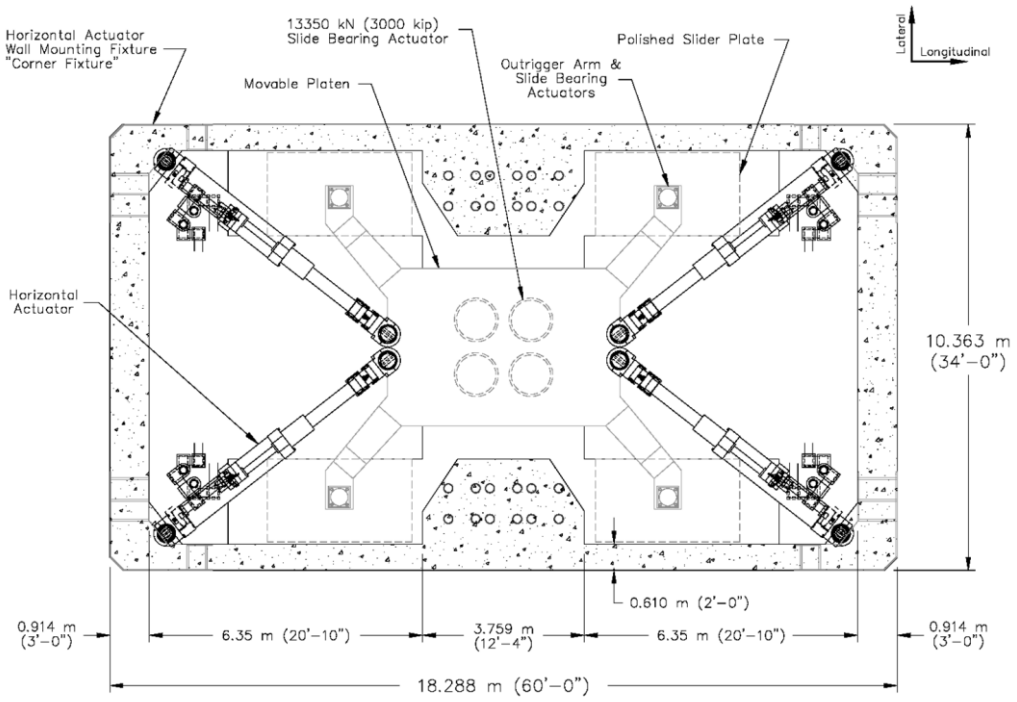

Figure 3-2 SRMD plan view [1]

The SRMD is a six-DOF table system governed by movements of its collective actuators. The six controllable DOFs are: longitudinal, lateral, vertical, roll, pitch and yaw. The primary vertical control mode is displacement, while force is applied and controlled through an integrator dominated control loop. The vertical force on a test bearing is controlled through this cascade control loop to enable force control mode.

Each actuator is controlled using multi-stage proportional and integral closed-loop control systems, where the inner loop controls the poppet valves and the outer loop controls actuator displacements. Four-stage poppet valve assemblies are used in place of more traditional multi-stage servo-valves typically used in structural testing. These valves are able to achieve the high volume of oil flow needed to facilitate the fast movement of these actuators, at the expense of less control accuracy. This can be of particular concern for hybrid simulation because displacement control errors can propagate through the numerical model and potentially lead to instability. However, careful control and compensation of these errors can produce reliable simulation results as will be demonstrated here.

To expand the capabilities of the SRMD to meet the needs of this research program, the testing facility was adapted for hybrid simulation in past few years. In 2014, the testing facility was adapted for quasi-static hybrid simulation by utilizing existing external analog input channels as command signals [2, 3]. More recently, an upgrade to provide complete digital communication was implemented in an effort to enable real-time hybrid simulation.

3-3 Development of Hybrid Simulation Capabilities

While the SRMD was not originally designed with the intent of conducting hybrid simulations, it includes different software and hardware components that allow for this adaptation. Even though the implementation discussed herein is for the SRMD, the challenges addressed can be faced by researchers attempting real-time hybrid simulations of large scale structures under multiple components of excitation. The tests reported are unique in terms of the scale of the structures examined, the multiple components of loads and displacements applied on the experimental subassembly, and the large number of degrees of freedom in the numerical models.

3-3-1 Hybrid Simulation Hardware Configuration

Hybrid simulation requires that customizable hardware components communicate between the computational driver, which solves the equation of motion for the complete hybrid numerical and experimental model, and the controller in the laboratory loading the experimental subassembly. Figure 3-3 illustrates the implementation of the hybrid setup on top of the SRMD conventional control configuration. The architecture includes a computational driver, the SRMD with MTS feed-back control system, and a real-time Digital Signal Processor [4] to communicate between the digital computers and the analog input/output of the SRMD control system. The SRMD controller is used in a manner similar to conventional cyclic dynamic testing except that instead of providing a predefined loading signal, the longitudinal and lateral displacement commands and the vertical force command are external reference signals being computed by the hybrid model as the simulation progresses. In its original configuration, the SRMD control system could only receive and send signals through analog input/output channels [2].

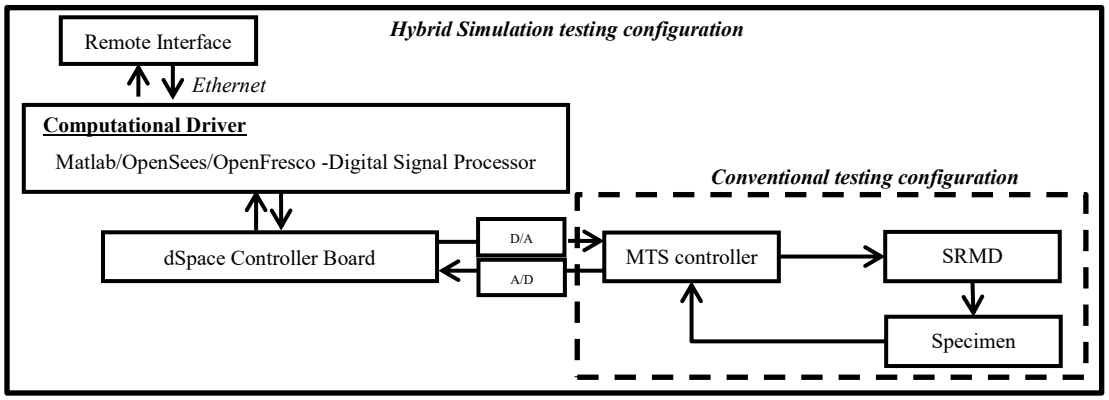

Figure 3-3 Hybrid simulation testing configuration

The real time digital signal processor used in the test set-up consisted of a dSpace ACE 1104 hardware kit [4]. The ACE 1104 hardware kit consists of a DSP processor on a PCI card with a connector panel with 16 BNC connectors. The connector panel has eight ADC inputs (Analog to Digital Converters), four with 16-bit resolution and four with 12-bit resolution, and eight DAC outputs (Digital to Analog Converters) with 16-bit resolution via BNC connectors. The dSpace DSP is used for signal generation; and it is set to sends commands and receives feedbacks at 1000 Hz (1 millisecond), which is identical to the rate of operation of the SRMD controller. With the Real-Time Interface (RTI) software, Simulink models can be run on the DS 1104 R&D Controller Board. Also, users are able to configure all I/O graphically, insert the blocks into a Simulink block diagram, and generate the model code via Simulink Coder (formerly Real-Time Workshop). The real-time model is then compiled, downloaded, and started automatically, thus reducing implementation time to a minimum.

During a hybrid simulation test, the numerical model calculates the command signals for the SRMD controller. These numerical values need to be converted to corresponding voltage through different gains based on the settings in the controller, shown schematically in Figure 3-4. The dSpace controller board (DS1104) has a ±10 volts input and output voltage range, which is

the same as the MTS controller voltage range in the SRMD. The dSpace command signals were calibrated to the same volt-displacement/force ratio as the command displacement/force of the SRMD facility for each DOF.

Table 3-2 shows D/A and A/D channels of the dSpace controller board connected to the MTS controller. Based on the output voltage and the resolution of each channel, the noise level for each DOF can be calculated. The SRMD machine internal units are *U.S. ton* (ton short) for force, *inch* for displacement, and *degree* for rotational DOF. Unit conversions from the hybrid model using [*kip, ft.*, and *rad*] to the SRMD machine units of [*ton, in.*, and *deg.*] are performed through scale factors that can be specified for the experimental set-up in OpenFresco (discussed later).

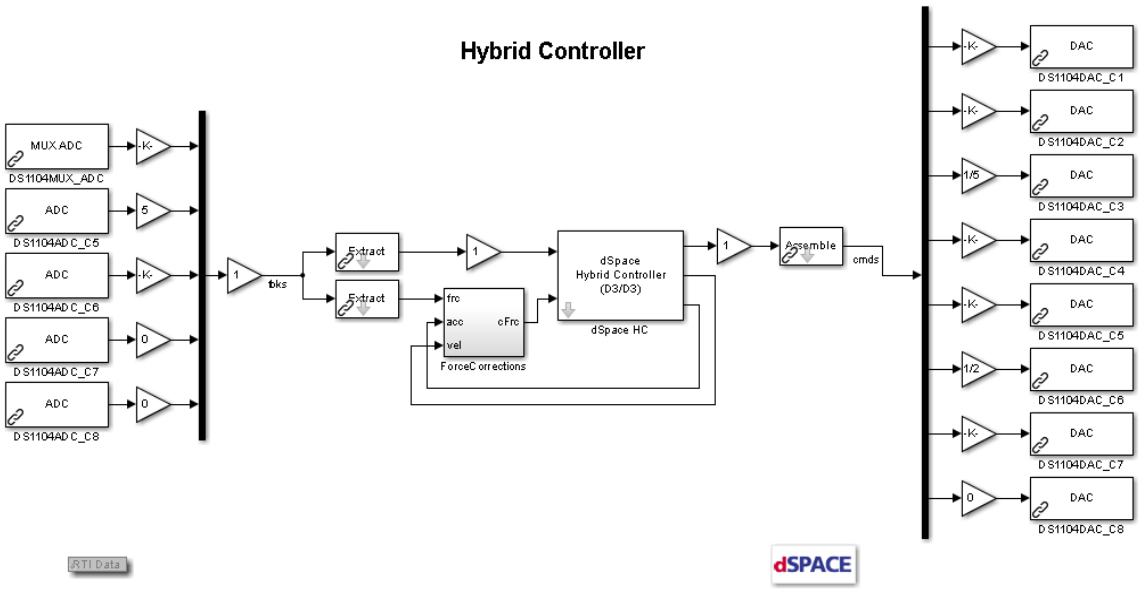

Figure 3-4 Hybrid Controller configuration using dSpace

To fine tune the command and feedback signal communication, further signal calibrations were performed based on a linear fit on each DOF calculated from Eq. 3-1. This calibration, which did not need the machine hydraulics powered on, was done by comparing values for each DOF from the SRMD controller and the dSpace control desk experiment.

Table 3-2 Voltage conversion units for different channels

Feedback (ADC)	***Conversion***	***Reference (DAC)***	***Conversion***
Longitudinal displacement	1219.2	Longitudinal displacement	1/1219.2
Longitudinal force (kN)	21016.8	Lateral displacement	1/609.6
Lateral displacement	609.6	Vertical displacement	1/127
Lateral force (kN)	16418.9	Roll (°)	1/2.25
Vertical displacement	127	Pitch (°)	1/2.25
Vertical force (kN)	70977.8	Yaw (°)	1/2
-	-	Vertical force (kN)	1/70977.8

Calibration points were selected at zero, ± half span and ± full span for longitudinal, lateral, roll, pitch, and yaw. For compression force, points were checked for five different values. Linear regression was applied [Eq. 3-1] and proper gain value [Eq. 3-2] and required offset voltage [Eq. 3-3] were added to command reference signals sent to and feedback coming from the MTS Controller. Table 3-3 is an example of the values obtained for the longitudinal displacement DOF.

$$\text{Linear fit: } y = ax + b \tag{3-1}$$

where *x* and *y* are dSpace and SRMD readings; and

$$Gain = {}^{1}/_{a} \tag{3-2}$$

$$Offset = -{}^{b}/_{a} \times 10\ volts \tag{3-3}$$

Sending feedback from the SRMD to the computational driver requires extracting signals in analog form using D/A (digital to analog) converters that are built into the SRMD. This D/A conversion introduced noise spikes in the feedback signal received by dSpace, which was resolved by adding signal conditioners (analog conditioning); see Figure 3-5. These spikes in the

feedback signals were also observed through an oscilloscope, which was used to verify that the analog output was noisy and related to the output generated by the SRMD (Figure 3-6). Digital filtering was another option to remove those glitches in the feedback signal. Using moving median and moving average digital filters within the Simulink model helped to remove some of these glitches but did not completely remove their effect.

Table 3-3 Signal calibration for longitudinal displacement

Long. displacement			
Before calibration		After calibration	
SRMD	dSpace	SRMD	dSpace
-609.27	-609.85	-609.27	-609.35
-304.42	-304.55	-305.26	-305.44
-0.71	-0.51	-0.71	-0.79
303.91	304.29	303.56	303.86
608.46	609.60	609.02	608.89

offset	-0.00167
gain	0.99872

Figure 3-5 Analog signal conditioning for the feedback signal

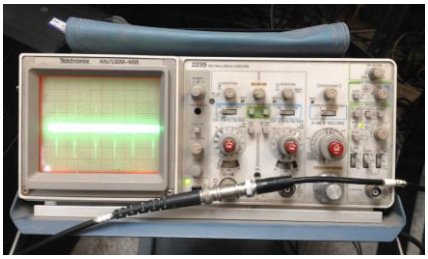

Figure 3-6 Noise in the feedback signal from the SRMD

3-3-2 Hybrid Simulation Software Configuration

The complex models utilized in the hybrid simulation presented here require integrated software components running on the hardware presented in the previous section. In general, a fast computational driver to solve the equations of motion of the hybrid model using direct integration algorithms needs to communicate with the laboratory's controllers through a middleware that bridges numerical and physical portions of the hybrid simulation testing system (Figure 3-7). These software components communicate with each other throughout the test. The key software components for a hybrid simulation as implemented at the SRMD facility for this test series are described below. Several improvements and additions that were specifically developed for this project include the deployment of multi-processor computational driver software and updated OpenFresco middleware software.

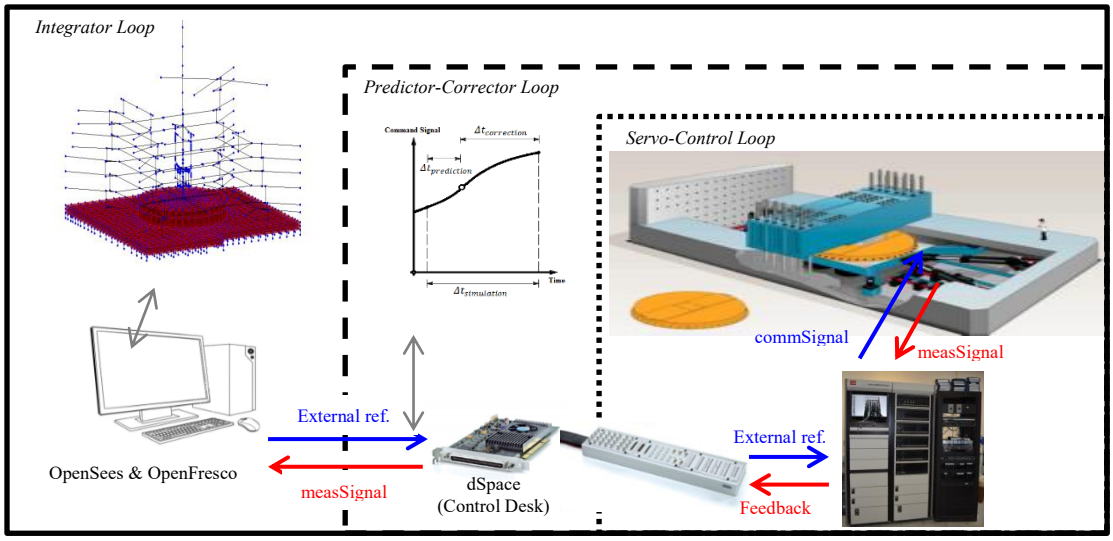

Figure 3-7 Hybrid simulation configuration

3-3-2-1 OpenSees and OpenSeesSP

OpenSees, the Open System for Earthquake Engineering Simulation, is a software framework for simulating applications in earthquake engineering using finite element methods, developed in 1997 by PEER (Pacific Earthquake Engineering Research Center). The use of OpenSees as the computational driver in hybrid simulation provides advanced capabilities for modeling and analyzing the nonlinear response of structural systems using a wide range of material models, elements, and solution algorithms. OpenSees is designed for parallel computing (OpenSees*SP*) to allow for scalable simulations on high-performance computing platforms [5].

Using OpenSees*SP* in hybrid simulation provides the ability to expand to more complex nonlinear numerical models with many degrees of freedom and execute them at a faster rate by using parallel computation. When generating a parallel application on a computational machine with *n* processors, a single processor (P0) is running the main interpreter and processing commands from the main input script while the other processors are running subdomain objects [6]. On the first execution of the analyze() command in the TCL script the model is partitioned, that is, the elements are split and distributed among *n-1* processors to solve the system of equations in parallel [7]. While using OpenSeesSP, the computational model needs to be suitable for parallel processing. Specifically, for hybrid simulation experimental element related computations must remain on the main processor (P0) in order to maintain communication with the real-time DSP in the experimental facility. This can be achieved by calling a recently developed partition function and setting the partition for the experimental element to P0 (main processor) before the first call of the analyze() command. The deployment of the MUMPS (MUltifrontal Massively Parallel sparse direct Solver) [8] solver in OpenSees*SP* also increased the speed of solving the system of equations of the hybrid model considered in this research. The

middleware OpenFresco (discussed next) makes this software readily adaptable for hybrid simulation.

3-3-2-2 OpenFresco

The OpenFresco (Open-source Framework for Experimental Setup and Control) software framework is a middleware used to connect the finite element model with the SRMD control and data acquisition systems [9]. OpenFresco standardizes the deployment of hybrid simulation and extends its capabilities to applications with advanced numerical techniques by providing an interface for different software and laboratory equipment [9]. A new experimental bearing element was developed in OpenFresco that is able to transfer three translational and three rotational degrees of freedom that can be applied to the experimental substructure using SRMD. In addition, this new experimental bearing element provides the user-selectable option to either transfer axial deformation or axial force to the test specimen. Due to the high axial stiffness of the bearings being tested, force control is preferred in the vertical direction. This enables 3-D testing that can capture the coupled vertical-horizontal behavior of large scale seismic isolation bearings with variability in axial force due to overturning moment of the structural system and vertical ground excitation.

3-3-2-3 Real-Time Predictor-Corrector

The SRMD control system operates at a rate of 1000 Hz, updating the actuator commands and getting feedback signals from sensors measuring the current displacement and force state of the platen. For smooth control and movement of the platen, the commands to the actuators from the hybrid model should be updated at an identical rate. However, the numerical portion of the hybrid simulation is often times not running in a real-time environment and could

thus require variable calculation times that randomly exceed the allowed time (a fraction of the integration time step size) to calculate new target values for the control system. Therefore, a real-time predictor-corrector algorithm is deployed to generate smooth command signals updated at the same rate as the control system base clock frequency while receiving displacement targets from the numerical model at a non-deterministic rate.

The dSpace Control Desk environment allows running real-time applications generated from Simulink and Stateflow models. Simulink is a block library tool for modeling, simulating, and analyzing dynamic systems. Combined with Simulink Coder (formerly Real-Time Workshop) in the MATLAB environment it can generate C code for the real-time implementation of systems [10]. Stateflow is an interactive design and simulation tool for event-driven systems. All these tools are used to create the event-driven real-time Predictor-Corrector algorithm used for continuous hybrid simulation [11, 12]. While receiving displacements from the numerical model, a polynomial is fitted to the displacement commands to generate a continuous command signal at the desired rate. The order of the fitted polynomial can simply be changed in the state-flow coder diagram (see Figure 3-8) before executing a hybrid test. For these simulations, second order polynomials were selected for displacements, velocities and accelerations. To synchronize the nondeterministic execution of the OpenSees*SP*/OpenFresco analysis with the determinist execution of the control system, the predictor-corrector algorithm performs the following tasks: 1) while the analysis software solves the equations of motion for the new target displacement, the pc-algorithm generates command displacements based on polynomial forward prediction; 2) once the new target displacement has been received, the pc-algorithm switches into the correction mode where it generates command displacements driving the platen response towards the new target displacement; 3) if the new target displacement is not

received within 60% of the simulation time step size, the pc-algorithm gradually slows down the command displacements until the new target displacement is received [12]. Therefore, in order to achieve a real-time execution of the hybrid test without any slowdowns, the OpenSees*SP* analysis software needs to compute a new target displacement in less than 6 msec. To reduce communication delays between OpenFresco and the pc-algorithm, the execution of the predictor-corrector finite state machine as shown in Figure 3-8 was up-sampled by a factor of 10. This means that the prediction-correction tasks and the pulling of OpenFresco communication flags are performed at a frequency of 10 kHz instead of 1 kHz which enables a smoother and faster operation of the synchronization performed by the pc-algorithm. Predictor-corrector states were monitored and recorded for all hybrid tests at the simulation time step interval of 1 msec. No slowdowns were encountered and on average the pc-algorithm performed 3 msec of prediction and 7 msec of correction.

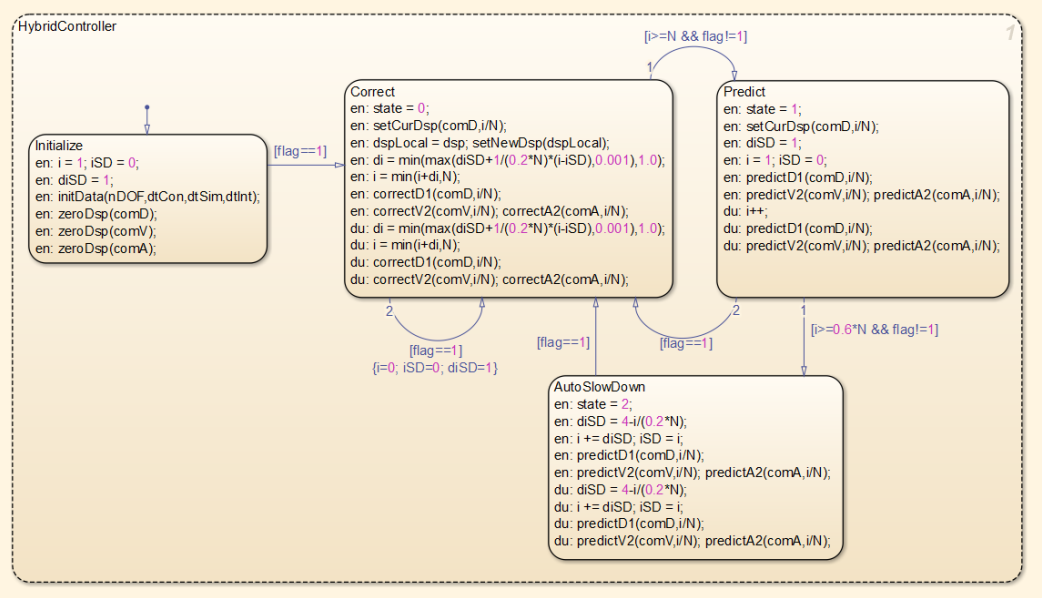

Figure 3-8 Predictor-corrector algorithm in Stateflow [12]

3-4 Implementation of Digital Communication Network using SCRAMNet+

For real-time testing, communication needs to be fast and reliable among the various components. To enable real-time testing and eliminate previously encountered problems with synchronization, delays, and noise caused by D/A and A/D conversions, the SRMD control system was upgraded with a SCRAMNet+ interface that provides complete digital communication, thus eliminating any D/A and A/D conversions. Continuous communication of commands and feedback with the SRMD controller was achieved using the architecture shown in Figure 3-9. The architecture includes a computational driver, the SRMD control system and a real-time digital signal processor using xPC Target communicating through SCRAMNet+ (Shared Common Random Access Memory Network).

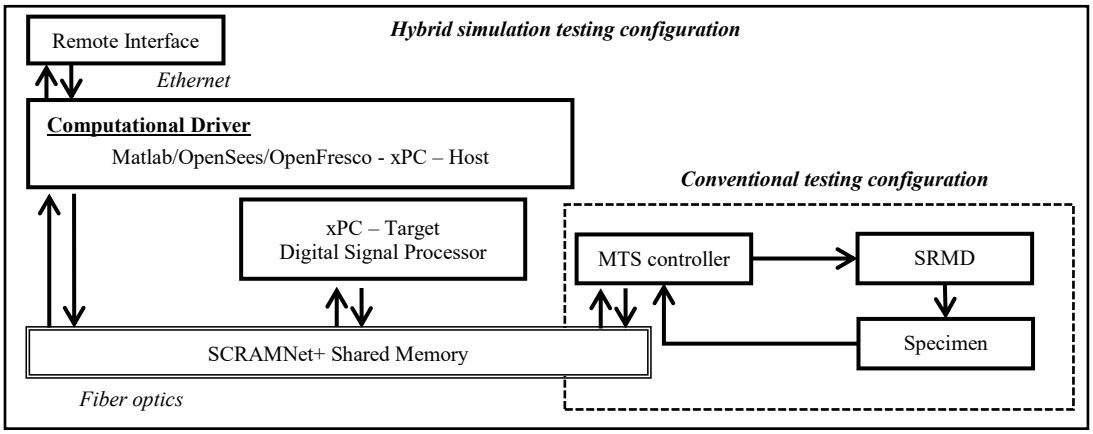

Figure 3-9 Hybrid simulation hardware configuration using SCRAMNet+ and xPC

SCRAMNet+ (Shared Common Random Access Memory Network) is a shared memory network with ultra-low latency digital communication between different nodes. It was deployed here in an effort to enable real-time testing through this fast digital communication between the

different hardware components of the hybrid testing system. SCRAMNet+ equips each computer on the network with its own memory card with a local copy of the shared memory connected via fiber optic cables. Any memory changes made by any one computer on the network are replicated on all the other computers on the network within nanoseconds [13]. The SCRAMNet+ memory cards are connected via high-speed fiber optic cables. The SCRAMNet+ serial ring network is implemented by running a paired fiber optic cable from the transmitter connector pair (T_x) of one node to the receiver connector pair (R_x) of the next node and then repeating this for every node until all the nodes are connected as in Figure 3-10. This implementation provides almost instantaneous communication between the SRMD control system, the xPC Host, and the xPC Target machines. A memory map has been pre-defined to allocate reserved memory partitions on the SCRAMNet+ for reading and writing of data from the xPC and SRMD controller nodes (Table 3-4). The command signals must have the same units as the SRMD machine's internal units which are inch for displacement, deg for rotation, US ton for force and US ton-ft. for moment.

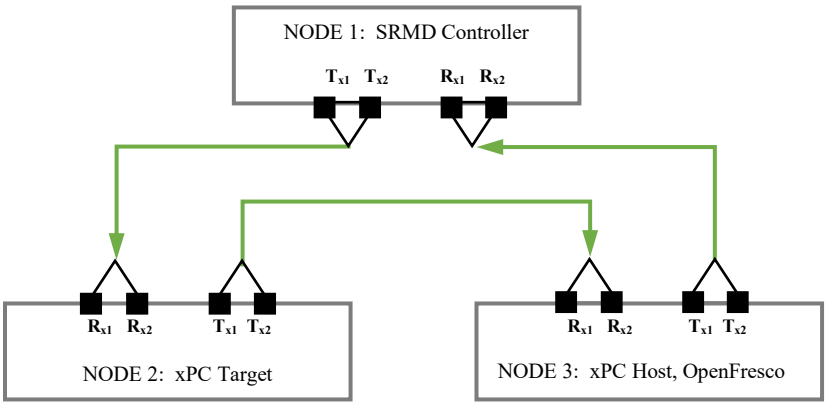

Figure 3-10 SCRAMNet+ serial ring network at the SRMD laboratory

Table 3-4 SCRAMNet+ memory map

Location	***Source***	***Description***
1	xPC	Longitudinal Reference
2	xPC	Lateral Reference
3	xPC	Vertical Reference
4	xPC	Roll Reference
5	xPC	Pitch Reference
6	xPC	Yaw Reference
7	xPC	Compression Reference
8 ... 8+NSCRU-1	xPC (NSCRU = 8)	User SCRAMNet+ inputs
64 ... 64+NSCOU-1	SRMD (NSCOU = 48)	User SCRAMNet+ outputs

To accommodate other potential future system configurations, user selectable channels (readouts) from the SRMD were added to the SCRAMNet+ memory map. Up to 48 user selectable channels from the SRMD can be written to the SCRAMNet+ memory and made available to other nodes on the network ring including the DSP (Figure 3-11). These data channels include the measured feedback signals required for the hybrid simulation or they can be used as an additional data acquisition system synchronized with the xPC host-target environment in other potential applications.

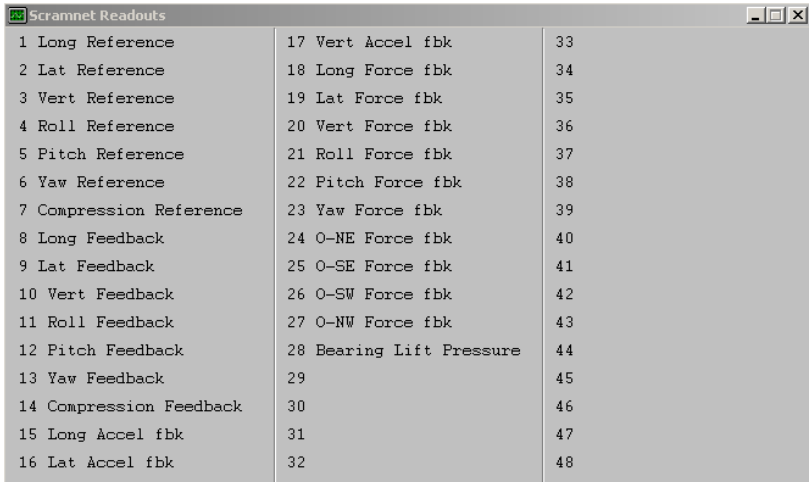

Figure 3-11 SRMD SCRAMNet+ readout map.

To generate the real-time signals for the SRMD control system using SCRAMNet+ network, Simulink Real-Time was used in the test setup instead of previously used system of dSpace and Control Desk. The xPC Target operating system is a digital signal processing tool that enables communication of programmable Simulink and Stateflow models to physical systems and execute them in real time on PC-compatible hardware [10]. In this high performance host-target prototyping environment, the host computer runs the numerical analysis model while the target computer is running a real-time kernel essentially converting a regular PC into a digital signal processor that operates in hard real-time. During a hybrid simulation, the digital control signals generated by the predictor-corrector algorithm running on xPC Target are written into pre-allocated memory locations on the SCRAMNet+ memory ring and are thus almost instantaneously made available for the SRMD control system to process.

After implementation of SCRAMNet+ and xPC Target, the *Hybrid Controller* was modified for digital communication between different components. As can be seen from Figure 3-12 the Simulink block on the top left reads the command signals (longitudinal and lateral displacements and vertical force) from OpenFresco and the block on the bottom left reads the

feedback signals (displacements, accelerations, and forces of the platen) from the SRMD control system based on the predefined memory map. Similarly, the block on the top right writes reference commands (longitudinal and lateral displacements and vertical force) to the SRMD controller and the block on the bottom right writes feedback signals (isolator shear forces) to OpenFresco.

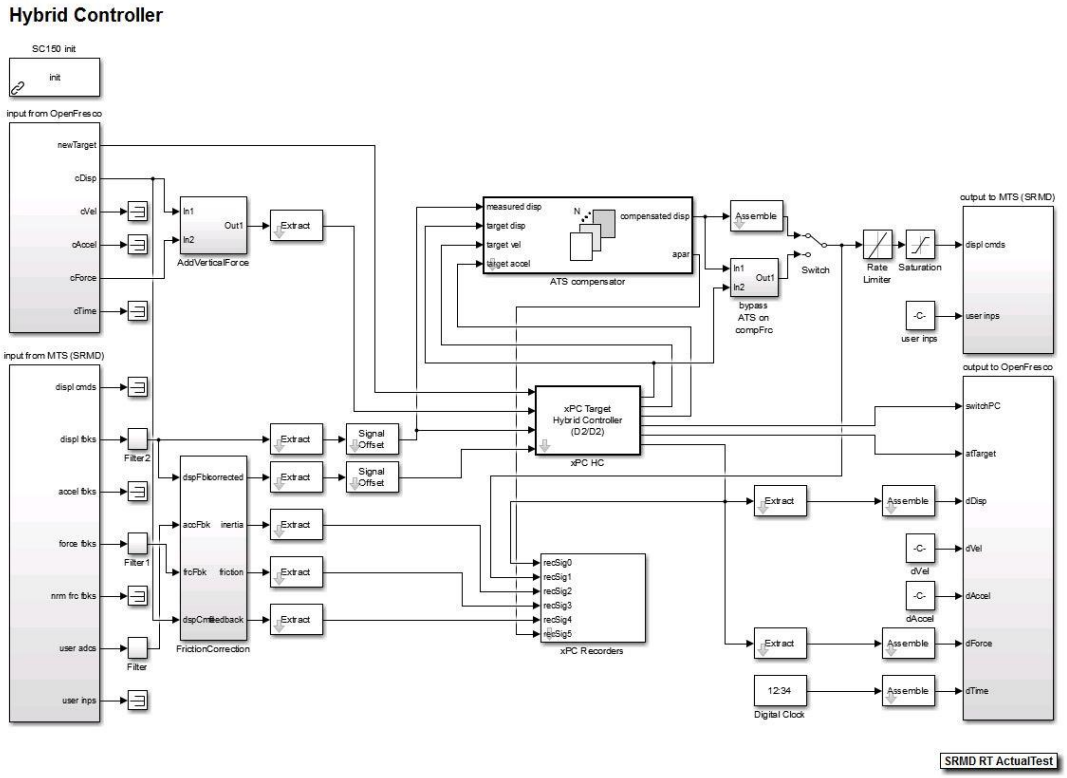

Figure 3-12 Hybrid Controller configuration in Simulink using SCRAMNET+ and xPC Target

3-5 Delay Compensation

Delay is an important characteristic of any experimental loading system and one of the main parameters that can determine the acceptable rate of testing in hybrid simulation tests. In general, delay is the time difference between the command signal and its measured response. Delays typically fall into three main categories of communication delays, computational time

delays, and loading system delays [14]. To assess system delays in the SRMD for the different platen degrees of freedom during a hybrid simulation, cross correlation functions and minimization of RMS (root mean square) errors between measured and commanded signals were used. The maximum of the cross correlation between these signals indicates the time delay that these two signals are best aligned [15].

The SRMD was estimated to have about 60 msec of delay in the measured displacement response compared to a command from its internal function generator. This delay is mainly due to a lag in the response of the hydraulic actuators driven by the four-stage poppet valve assembly. Proper delay compensation is required to perform fast hybrid simulation tests and potentially enable real-time testing and that requires more advanced control strategies such as using feed-forward control and adaptive delay compensation to minimize the delays. Different delay compensation strategies used throughout this project are described here. An effective delay compensation strategy can consist of one or more of these approaches combined to achieve acceptable results.

3-5-1 Constant Delay for each DOF

One approach to compensate for delays is to compensate for a constant delay value for each DOF. In this approach, the delay values were measured prior the actual test and compensated accordingly during the hybrid simulation tests using Simulink. In this method, once the command signal generated by predictor-corrector algorithm reaches its target value, the *atTarget* flag will be triggered after the specified delay to read displacements and forces (measured signals) and the integrator will use them to advance to the next integration time step.

It is possible to have different delays for each DOF in multi-DOF systems since control gains are calibrated independently. Compensating by a single time value for all DOFs may result in the actuators moving out of sync and exciting the higher modes in the system, especially in real-time testing and should be avoided. Also, in the SRMD facility, the vertical DOF is controlled in force control mode, while the other DOFs are controlled in displacement control mode. Thus, there can be large differences in the delay for the vertical DOF in comparison with the other two horizontal DOFs. Even the two horizontal displacement DOFs have been observed to have different delay times. A Simulink subsystem was implemented in the *Hybrid Controller* model to compensate for proper delay value in each DOF, as shown in Figure 3-13.

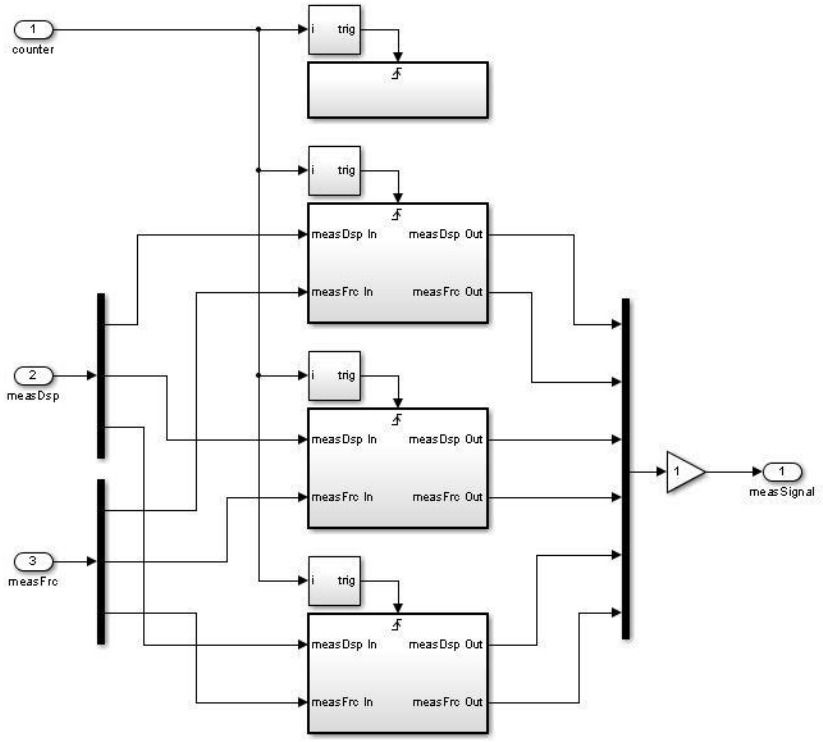

Figure 3-13 Delay model in Simulink

3-5-2 Feed-forward Control

To reduce delay in the test system, a more advanced control strategy available within the SRMD control system such as adding feed-forward (FF) control was also used. In the FF control strategy, the time derivative of the command signal is multiplied by the user supplied FF gain, and added directly to the valve command signal. Basically, the command signal is trying to predict the next value by using the current velocity to get ahead of current command signal. Including FF gain in the control system provided a significant performance improvement in terms of delays in the two horizontal directions; see Figure 3-14. Unfortunately, this FF gain was not helpful in vertical direction because the control system in vertical direction is based on a cascade control loop where the inner loop is in displacement control and the outer loop is in force control. Although this control strategy can reduce the delay, it can be problematic especially for higher frequency signals where FF control tends to create overshoots. Special caution is required when the controller is using this compensator.

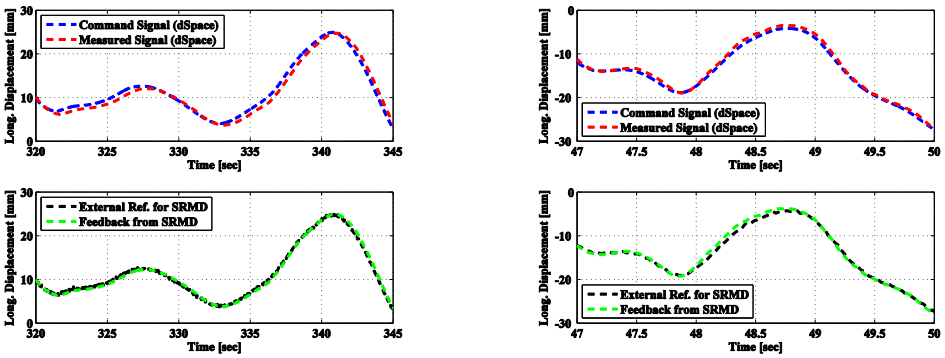

(a) (b)

Figure 3-14 Tracking signal for delay: (a) no FF and (b) with FF

3-5-3 Adaptive Time Series (ATS) Compensator

An adaptive actuator delay compensation scheme called the adaptive time series (ATS) compensator developed by Chae et. al [16] was used to further minimize the delays and improve the actuator tracking in the SRMD response. This adaptive delay compensation method predicts a time-advanced command signal to compensate for delay. Using a second order adaptive compensator system, the compensated input actuator displacement (u^c) in each DOF is calculated from actuator target displacement (x^t) using Eq. 3-4 at each time step (k).

$$u_k^c = a_{0k}x_k^t + a_{1k}\dot{x}_k^t + a_{2k}\ddot{x}_k^t \tag{3-4}$$

where the three adaptive gains (a_0, a_1, and a_2) are continuously updated at the control system frequency using the least squares method for a predefined period of time ($q\Delta t$) between the measured displacement (x^m) and compensated displacement of the actuators for each DOF to minimize control errors.

To apply the ATS compensator to the SRMD, two minor modifications were made. First, the algorithm was extended to perform adaptive delay compensation individually for all degrees of freedom of the SRMD. Second, the ATS was modified to utilize reference velocities and accelerations computed directly from the predictor-corrector algorithm using command signal data instead of computing them by differentiating measured reference displacements. Since the predictor-corrector algorithm utilizes polynomials for extrapolation and interpolation, it was possible to directly differentiate the displacement polynomials to obtain velocity and acceleration polynomials. This modification produced more accurate and clean velocity and acceleration references with significantly reduced noise compared to the original implementation using measured feedback directly.

A Simulink block of the ATS originally developed by Chae et al. [16] was added into the *Hybrid Controller* Simulink model and adaptive gain margins were calibrated prior to performing a real-time hybrid simulation to ensure stability and proper delay compensation. After its implementation, it was found that the ATS compensator used with digital SCRAMNet+ communication was able to reduce the average delay in the SRMD from 60 msec down to about 5 msec, which would make real-time testing feasible. The ATS compensator was originally developed and validated for systems using displacement control; however, the vertical degree of freedom of the SRMD is usually controlled in force. It was found that the ATS was not as effective in compensating for delay in the bearing axial degree of freedom during real-time hybrid tests. This was likely due to the higher frequency content in these signals. However, use of the ATS compensator in slower hybrid simulations resulted in better tracking of axial forces in vertical direction.

Threshold values for triggering the three ATS compensators were set to 0.005 in., 0.005 in., and 1094 ton for longitudinal displacement, lateral displacement and axial force respectively. Initial values for the ATS adaptive gains, permissible gain ranges and rate of change for these gains are required input values for the ATS compensator. Table 3-5 summarize values used in this research program.

Table 3-5 ATS coefficients setup

Coefficients	**Initial values**	**Range**	**Maximum rate of change**
a_0	1.0	0.7-1.05	2
a_1	0.030	0.0-0.070	0.05
a_2	0.00045	0.0-0.0018	0.001

Figure 3-15 shows the adaptive change of the gains (a_0, a_1, and a_2) for the longitudinal degree of freedom for one of the real-time hybrid simulations. The a_0-gain compensates for over or under shoot. As can be seen from the figure the gain tended to be less than one over large portions of the hybrid simulation, meaning that there was more compensation necessary for overshoot than undershoot. This is due to the FF control that tends to create overshoot as was described earlier. The a_1-gain corresponds directly to the delay compensation. As can be seen from the figure, the ATS adaptively compensated for delays between 0 and 60 msec over the course of the hybrid simulation. The a_2-gain is the higher order term and function of the delay compensation square. All these three gains reach the preset limits in few instances during this simulation. The limits were set to avoid large changes in parameters that could lead to instabilities.

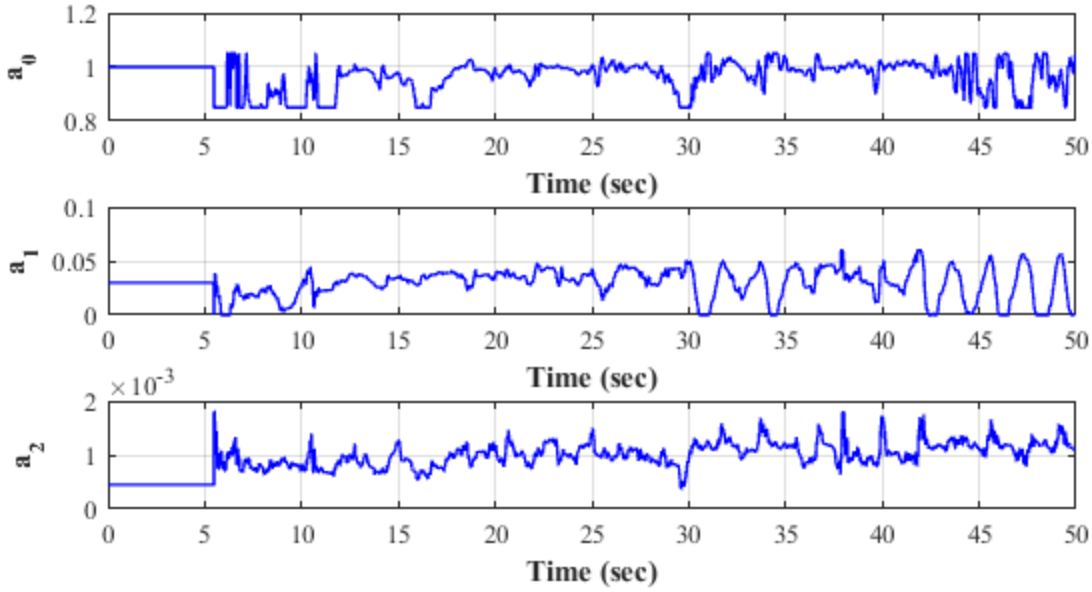

Figure 3-15 Adaptive change of ATS compensator gains during a hybrid simulation

3-6 Rate and Accuracy of Hybrid Tests

The rate of testing in hybrid simulation tests is primarily governed by the computation time of the numerical model, and total delay in the system including communication and loading system delays. In hybrid simulation tests conducted here, the numerical portion of the response was computed using a high-performance computer with parallel processing capabilities achieving computation times that were sufficiently fast to enable real-time testing. On the other hand, implementation of the digital communication network using SCRAMNet+ led to almost instantaneous communication (less than 1 msec delay) between the different components of the hybrid test setup. Combination of FF control and ATS delay compensation was able to eliminate most of the remaining delays in the system necessary for real-time and near real-time hybrid tests.

To assess accuracy and performance of a hybrid simulation test with regard to experimental errors different measures can be used. Average time delay, difference between the command and measured signal, and the tracking indicator (TI) based on actuator tracking in each signal were considered in this research program [17, 18]. Sample cases for the highest rate of testing achieved for 2-D and 3-D excitation and corresponding performance measures are presented here. These rates were selected to ensure stability and accuracy of the hybrid simulation tests. To demonstrate some of these measures applied to evaluate delays, sample results are presented for hybrid simulations. More details on the test program are provided in Chapter 5.

Run # 8 was a developmental run (empty table run) with only FF control (no ATS delay compensation) and was executed in real-time. Average delays of this simulation were 17 and 18

msec. Figure 3-16 shows the displacement response of this simulation as well as different error indicators. Normalized displacement errors are up to 8 and 12% in longitudinal and lateral direction respectively. Normalized TI in longitudinal and lateral direction are around 30 and 40 % at the end of the test. Based on these provided results, it became apparent that reliable and accurate real-time hybrid testing can not be achieved using FF control only on the SRMD.

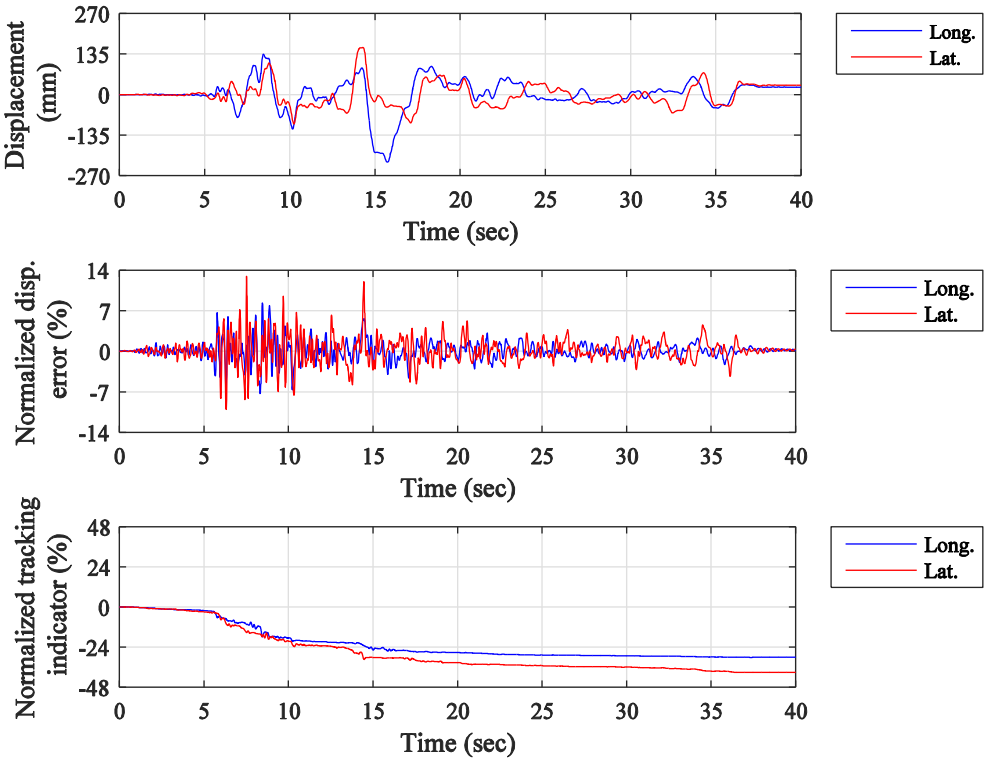

Figure 3-16 Command signals and corresponding experimental error indicators (with FF and no ATS) – Run # 8 – 2D – real-time

Run # 42 was a hybrid simulation test at the design hazard level with two horizontal components of the ground motion and executed in real-time with using FF control and ATS compensators. Average delays of 6.3 and 3.8 msec were measured in longitudinal and lateral direction respectively. Figure 3-17 shows the displacement response of this simulation as well as different error indicators. Normalized displacement errors are about 4% in both longitudinal and lateral direction. Normalized TI in longitudinal and lateral direction are 21 and 17% at the end of

the test. These results demonstrated that an accurate real-time hybrid testing could be achieved by employing FF control and ATS compensator for 2-D hybrid tests.

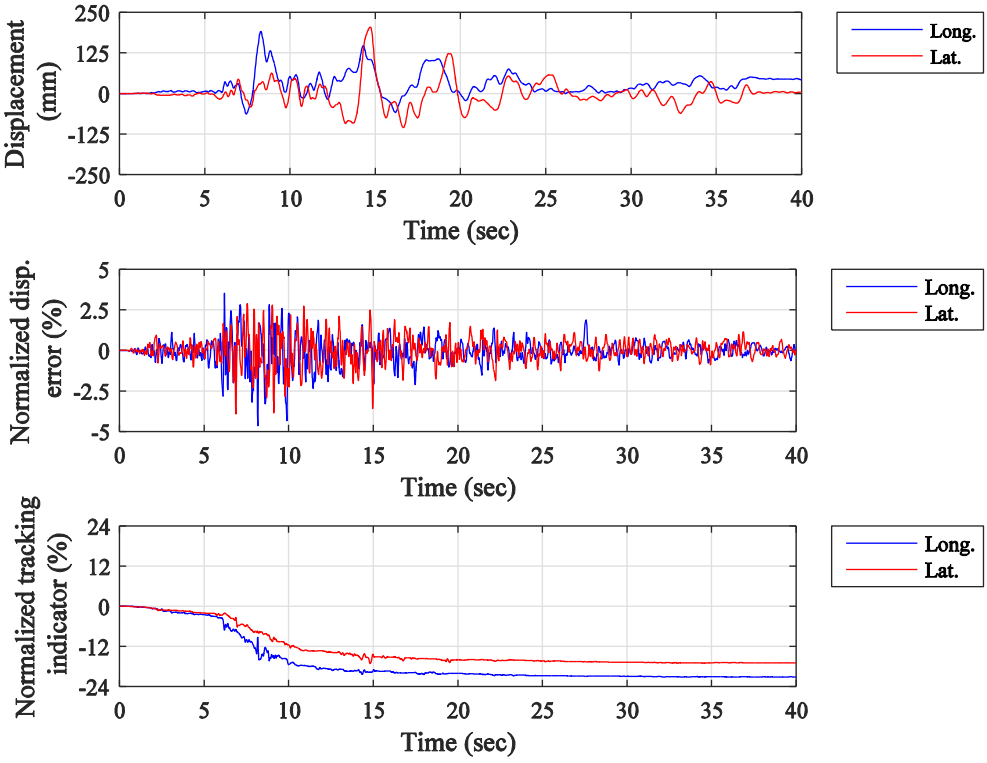

Figure 3-17 Command signals and corresponding experimental error indicators (with FF and ATS) – Run # 42 – 2D – real-time

Run # 166 was a hybrid simulation test at design hazard level with two horizontal components of the ground motion and as well as controlling vertical force due overturning effects and executed 2x slower than real-time. Both FF control and ATS delay compensator were used in this simulation. Average delays are 1, 2, and 0 msec in longitudinal, lateral and axial direction respectively. Figure 3-18 shows the displacement response of this simulation as well as different error indicators. Normalized displacements/force errors are less than 1% in horizontal displacements and 5% in for axial force. Normalized TI is less than 10% for horizontal displacement and around 40% for axial force at the end of the test. For 2-D excitation while

simulating overturning effect in axial direction, testing rate of 2x time slower than real-time simulations provided the fastest while accurate simulation.

Unfortunately, 3-D hybrid tests (controlling the vertical force due vertical excitation and overturning effect on the bearing as well as horizontal displacements) could not be carried out in real-time or near real-time because delay compensation techniques were not able to improve tracking performance for the high frequency vertical forces to guarantee both stability and accuracy. This is partly due to the type of actuator used in vertical direction at SRMD. For 3-D excitation tests, rate of testing 10x slower than real-time is the fastest testing rate to have a reliable and accurate simulation results based on error measures (see Figure 3-19).

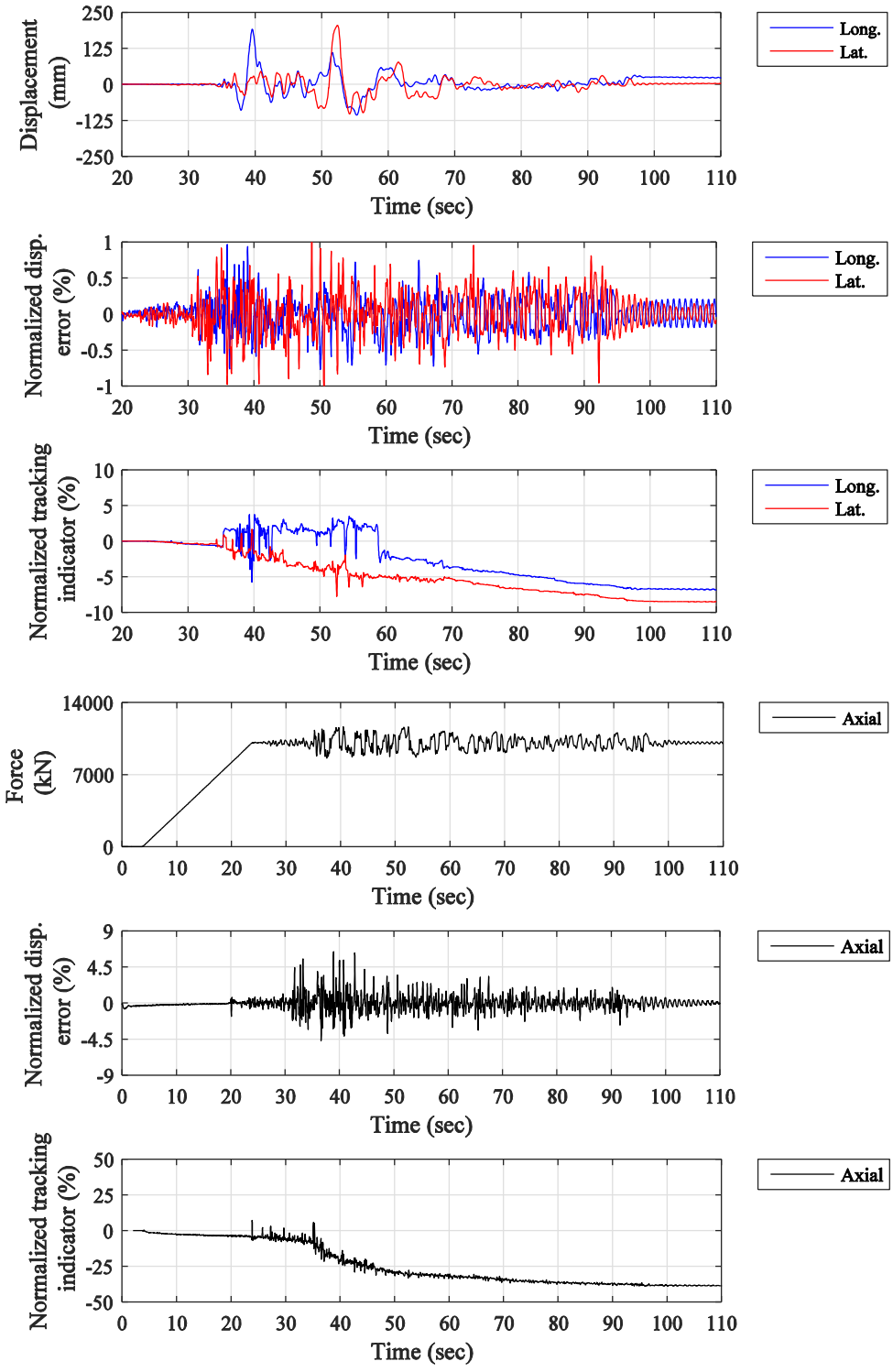

Figure 3-18 Command signals and corresponding experimental error indicators – Run # 166 – 3D – 2x slower

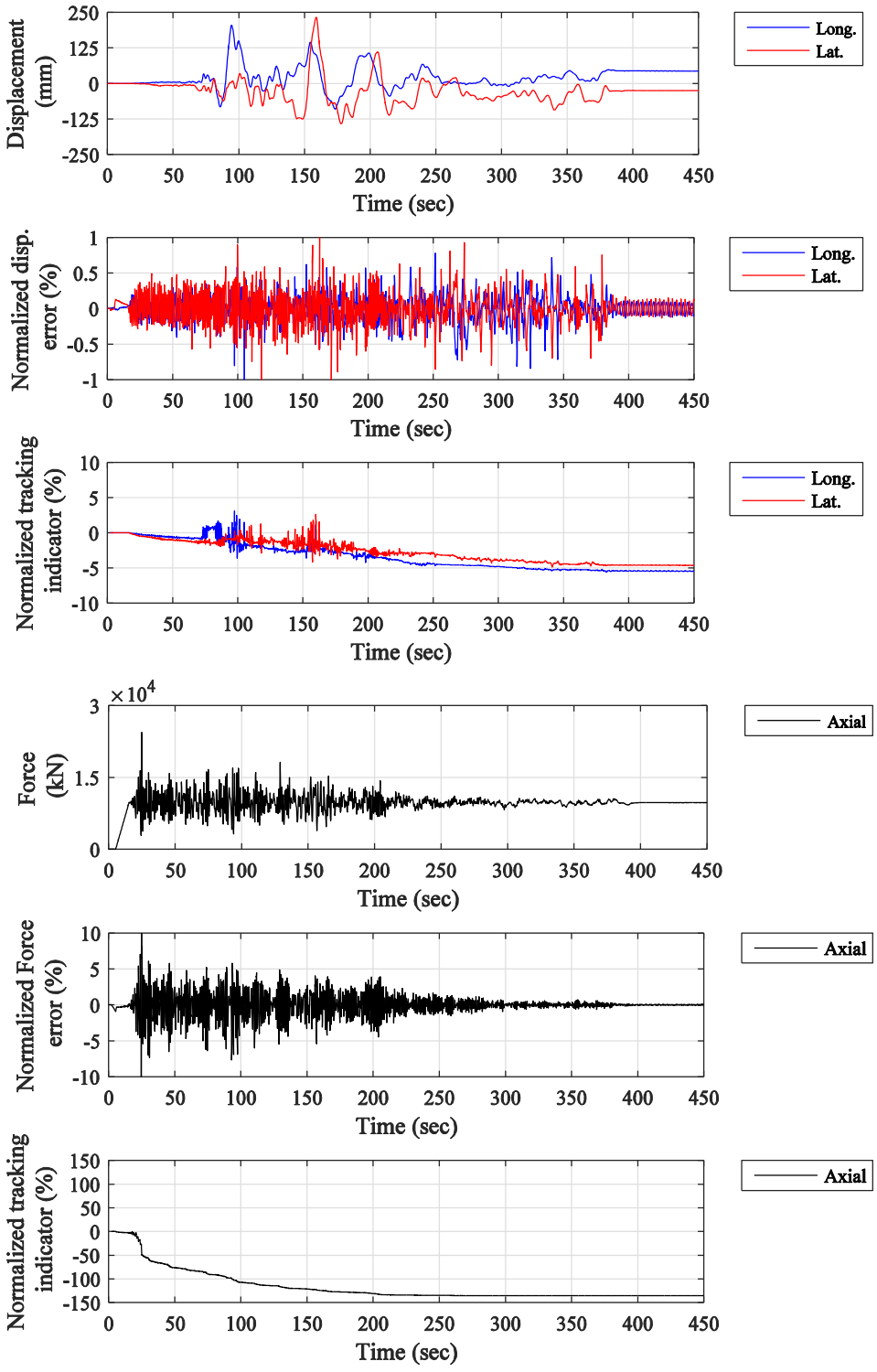

Figure 3-19 Command signals and corresponding experimental error indicators – Run # 157 – 3D – real-time

3-7 Compensation for Friction and Inertia Forces

Feedback forces in the SRMD controller were obtained from uniaxial load cells on the actuators. While an empty table run should ideally provide zero shear force readings, large forces on the order of 2,000 kN have been observed during fast tests with significant accelerations. This is mainly due to inertia forces of the platen mass and friction due to the platen sliding on the vertical actuators and outrigger supports. During hybrid test, prior to sending the measured shear force signals in the SRMD controller as restoring forces to the hybrid model corrections were required to remove inertia and friction forces from these signals. While it is desirable to have a load cell right beneath the bearing to directly measure the actual shear forces in the bearing, this would have been difficult and very costly considering the magnitudes and multiple components of the forces that need to be measured. In standard cyclic characterization testing of devices on the SRMD, these effects are corrected during post-test analysis. Most often the correction is performed by subtracting the measured forces from an empty table run of the same input motion.

Two different models were developed and used to correct for friction and inertia forces during hybrid simulation tests conducted here. Model 1 is an empirical model to predict the inertia and friction forces in the SRMD machine while Model 2 uses system identification techniques to calculate different system properties to model inertia and friction forces.

3-7-1 Model 1: Empirical Model for Inertia and Friction Forces of the SRMD

In this model, the effective mass of the set-up and the accelerations of the table in each direction was estimated and provided by the operator. The effective mass of the table can change

for different set-ups and is provided by operator of the SRMD. Bare weight of the machine for this specific test set-up was measured to be 1226.8 kN. To calculate the inertia force, accelerations were calculated through the predictor-corrector algorithm to obtain a smoother signal and then multiplied by the provided effective mass.

Previous studies of the SRMD have identified the dependence of the friction force values with velocity as shown in Figure 3-20 and Table 3-6. In addition, the friction forces have been found to be dependent on the direction of sliding; e.g., the longitudinal and lateral directions indicate different friction values. Two different assumptions can be made to estimate the friction forces.

1. Use the square root of sums of squares (SRSS) of both (longitudinal and lateral direction) velocities to calculate the peak velocity dependent friction force and then distribute them based on their magnitude, neglecting the dependence on the direction; and
2. Calculating the corresponding friction force for each horizontal DOF based on its own velocity.

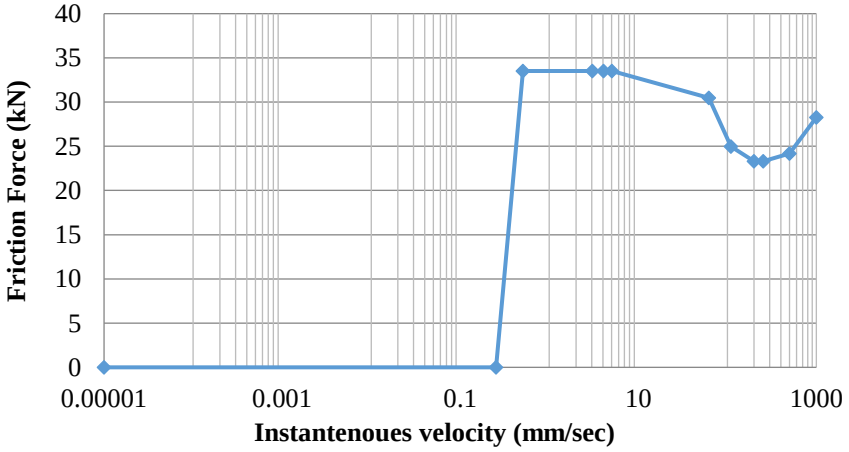

Figure 3-20 Friction force for different instantaneous velocity values

Table 3-6 Approximate friction force versus instantaneous velocity

Instantaneous velocity (mm/sec)	*Friction force (kN)*
0.0	0.0
0.3	0.0
0.5	33.5
3.0	33.5
4.1	33.5
5.1	33.5
62.0	30.5
110.0	25.0
199.9	23.3
254.0	23.3
500.1	24.2
1000.0	28.3

Based on several experiments with empty table and applying the force correction to zero out the force, the second approach was found to be more appropriate in correcting for friction. Calculation of velocity and the application of any filter in displacement will add additional delays in the signal. It was first attempted to calculate velocity directly from the measured table displacements and/or accelerations, but the resulting signal turned out to have significant noise. Alternatively, the velocity was calculated based on the command signal sent to the controller from Simulink. However, the command is not guaranteed to be in phase with the actual motion of the table due to displacement tracking errors. To make sure that friction correction is applied with proper delay compensation, some empty table runs were first examined in the expected range of velocity. First, a few parameters were set, including the velocity at which to cap the maximum friction force. In order to simplify the model, a cap was assumed below a certain threshold velocity since the static friction force was not possible to capture. Also, to avoid large

jumps in the force feedback, especially at displacement reversals when the velocity changes its sign, the friction force was set to zero below another threshold value. This is also beneficial during free vibration at the end of the experiment when the velocity is oscillating and large changes in the friction force could cause high-frequency noise feedback in the measured signals sent back to the hybrid model.

Note that when one-directional testing is performed in the laboratory, velocity from the other DOF should be set to absolute zero. The reason for this is because the noise in the calculated velocity can be very large even though the displacement is small. This large velocity noise in the perpendicular direction will change the calculation of the friction force, leading to erroneous compensation for friction due to the velocity.

A study by Shortreed et al. [19] demonstrated that there is also another source for friction force, which depends on the vertical load in the machine. Movement of the platen will involve nine different friction surfaces, eight on outrigger actuator contact surfaces and one for the four vertical actuators beneath the table platen, see Figure 3-21. This vertical load dependent friction force is a function of the direction of motion, outrigger forces, overall vertical load, and lift pressure. Based on the expected vertical load on the bearing during the hybrid simulations, constant single values can be calculated for different directions. Variation of this portion of the friction force were found to be negligible for these tests and were not included.

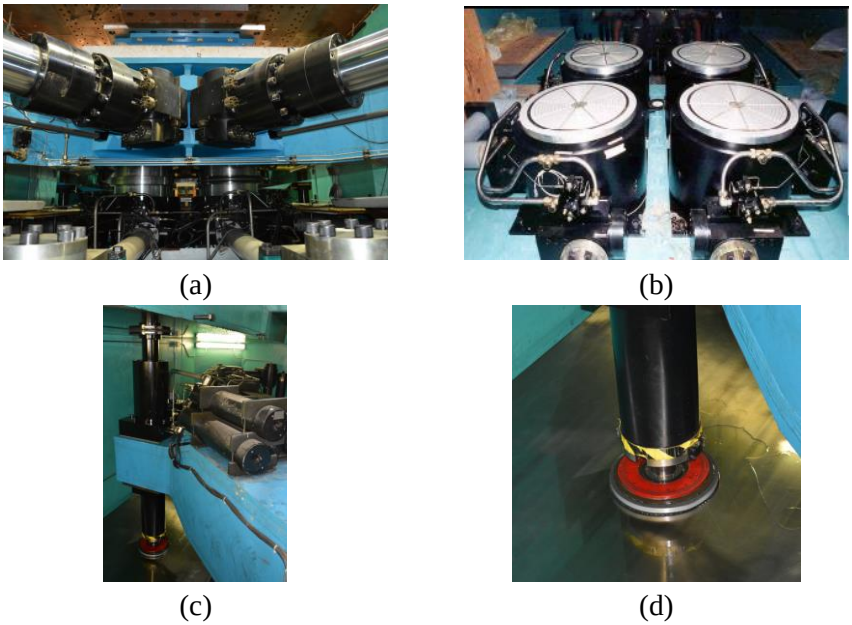

(a) (b)

(c) (d)

Figure 3-21 Machine contact surfaces: (a) and (b) vertical actuators; (c) and (d) outriggers

3-7-2 Model 2: Inertia and Friction Force model using System Identification Techniques

In 2008, O. Ozcelik et al, studied and verified the applicability of parameter identification approaches to model the mechanical subsystem of the Large High Performance Outdoor Shake Table at UC San Diego [20]. Using a similar approach, a model for correction of inertia and friction forces for the SRMD was calibrated using system identification techniques. Inertia forces due to the table platen were calculated based on the calibrated effective mass of the setup consisting of specimen, platen, and moving actuator parts in each of the three translational degrees of freedom, and the measured accelerations in each direction. Accelerations were measured with accelerometers placed on the table platen.

Previous studies of the SRMD friction force model have identified the dependence of the friction force on velocity as well as the direction of sliding [19]. In this model, it was assumed

that friction forces consisted of a combination of static and dynamic components. Static friction is a constant friction value that changes sign based on the direction of sliding. The dynamic portion of the friction force is assumed to be linearly proportional to the velocity of sliding (sliding velocity exponent = 1).

To identify friction and inertia parameters in an empty table run, measured force ($F_{measured}$) are recorded using actuator load cells and horizontal accelerations ($\ddot{u}$) are recorded using accelerometers on the table platen. Feedback velocity ($\dot{u}$) was calculated from measured displacements using actuator displacement transducers. The unknown parameters are effective mass (m_e), static friction force ($F_{Static_Friction}$), dynamic friction force ($F_{Dynamic_Friction}$) and any offset (d) in the force measurements. With these assumptions, the following equilibrium equation (Eq. 3-5) was derived for horizontal forces in both longitudinal and lateral direction for an empty table run.

$$F_{measured} = m_e\ddot{u} + F_{Static_Friction}sign(\dot{u}) + F_{Dynamic_Friction}\dot{u}^{\alpha} + d \ (\alpha=1) \quad (3\text{-}5)$$

Using system identification techniques, a linear least squares model with linear constraint was fitted for the given data sets (empty table runs) independently for both longitudinal and lateral direction to calculate the unknown model parameters. It should be noted here that assuming a nonlinear dependency on sliding velocity for the dynamic friction component did not significantly improve the estimation of friction forces in the system (i.e. sliding velocity exponent $0.1 < \alpha < 2$). Also, the experimental setup used for testing of different types of bearings was different therefore effective masses for these setups were different while the friction behavior was assumed to be the same. Table 3-7 shows the calculated parameters for the inertia and friction force correction model.

Table 3-7 Parameters calculated for resisting force correction

Force correction model parameters	***Longitudinal***	***Lateral***	***Vertical***
Effective mass [kN/g] -Unison and EQS test setup	1111.79	1145.77	1111.79
Effective mass [kN/g] - EPS test setup	982.97	1001.38	982.97
Static Friction Force [kN]	5.1	8.6	-
Dynamic Friction Force [kN-sec/cm]	0.00716	0.0087	-

Once inertia and friction parameters were calculated, the force correction model was implemented into the *Hybrid Controller* Simulink model. In this model, longitudinal and lateral velocities are calculated based on feedback displacements (instead of commanded displacements) of the platen to ensure that they are in phase with the actual motion of the platen. Readings from accelerometers located on the table platen were also used for the inertia force correction. To make sure that force corrections were applied with the proper phase, empty table runs were first examined producing velocities in the range that was expected for the hybrid tests. Same as the previous model, to avoid rapid changes in the force feedback, especially at displacement reversals when the velocity can fluctuate in sign due to noise, the friction force was set to zero below a threshold velocity (0.05 in/sec). The force correction model, schematically shown in Figure 3-23, was calibrated by attempting to reduce the measured force to zero during empty table runs.

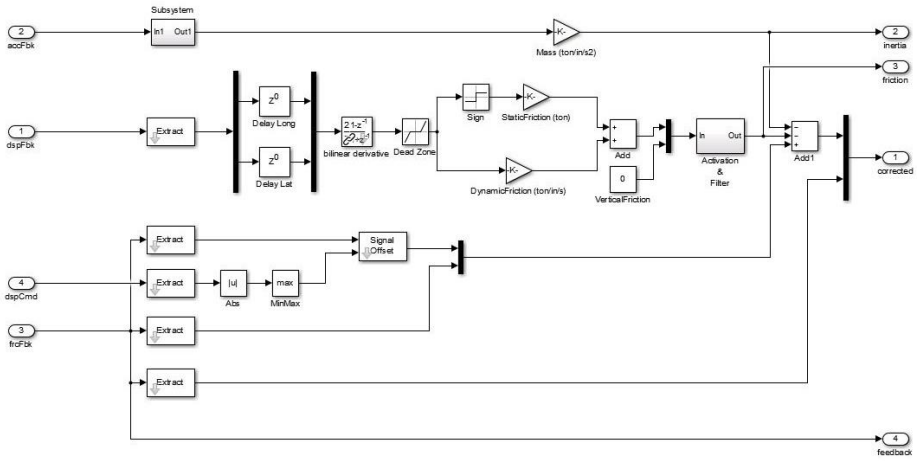

Figure 3-22 Model schematic to correct for friction, inertia and offset using friction model

Figure 3-23 shows an example of a correction procedure for an empty table. Ideally, there should be zero residual force after correction for inertia and friction. As shown, the residual force is mostly below 10 KN (~ 0.011 % of the longitudinal force capacity) which is well within the expected range of force accuracy of the SRMD.

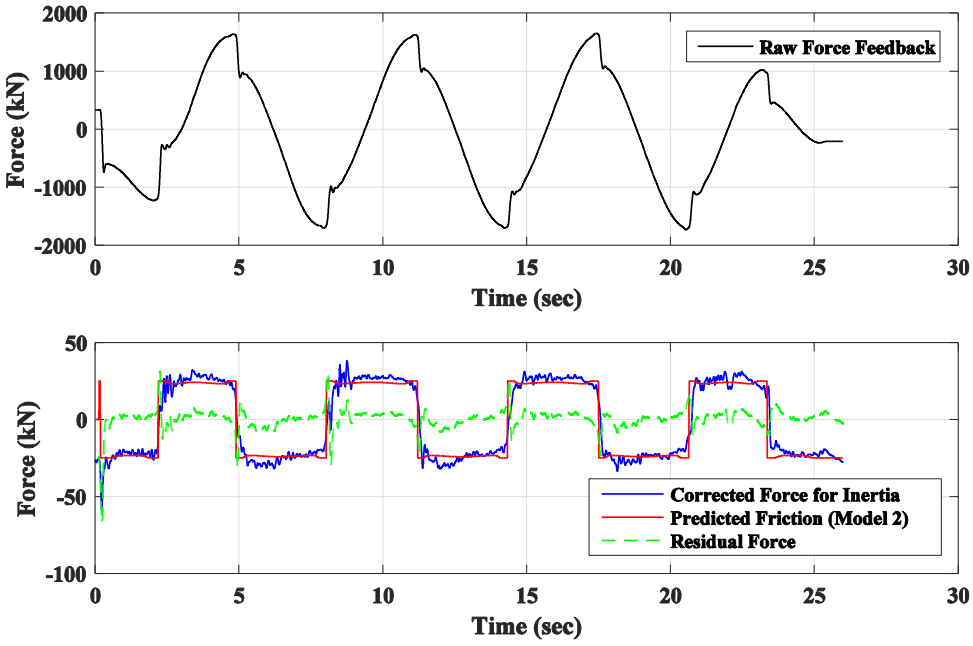

Figure 3-23 Sample correction of feedback forces (longitudinal direction)

3-8 Preparation for Hybrid Simulation Test

Before executing a hybrid simulation test, few additional features were implemented in the system to ensure safe testing and accuracy of the feedback signal to be used in the hybrid model.

3-8-1 Limiter Settings for Magnitude and Rate

Magnitude limits (*magnlimits*) are set based on (1) the capacity of the specimen and testing machine, (2) predicted unstable response of the numerical model based on numerical simulation, and (3) the limits that the SRMD machine operator and researchers have specified on the machine's control system to make sure that the command signals from the Simulink Predictor-Corrector model do not exceed certain values. These limits are implemented in the Simulink model and are necessary for safety reasons as both the equipment and the specimen can be damaged at certain levels. Typically, longitudinal and lateral displacement and vertical force are the DOFs that are controlled in a hybrid test of a bearing with the SRMD. Typical displacement and force limits used in these tests are listed in Table 3-8.

Table 3-8 Magnitude limits for different degrees of freedom

	Full Stroke/Capacity	***magnlimit***
Longitudinal Displacement	±1219.2 mm	±787.4 mm
Lateral Displacement	±609.6 mm	±533.4 mm
Vertical Force	79476.6* kN	[+31115 and -31.115] kN

* Compression is positive and tension is negative for the machine.

Velocity limits (*ratelimits*) are also important for the safety of the laboratory equipment, which caps the maximum rate at which the command signal can be increased each time step. If

this rate cap is reached during the test, a command signal will continue to increase at the maximum allowable rate with constant velocity until it is able to catch up to the signal, which often occurs during load reversal. This value should be set slightly larger than the maximum expected velocity during the test, and it can be an effective safety measure if the simulation becomes unstable and provides an excessively large command. Typical *ratelimits* used in these tests are as follows:

- Longitudinal and Lateral displacement: 2540 mm/sec
- Vertical force: 17,780 kN/sec

Note that these *ratelimits* need to be modified when the testing rate (Simulation Time Step/Integration Time Step) is changed. Implementation of the magnitude and rate limiters on the command signals are schematically shown in Figure 3-24.

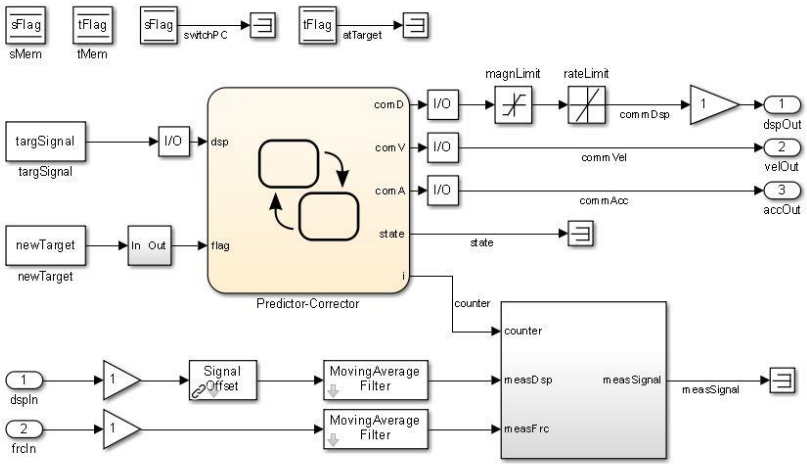

Figure 3-24 Applying the limits on the command signals

3-8-2 Initial Offset due to Drifting

Based on observations during testing with the SRMD, it was found that there is some drifting of the horizontal forces before the actual earthquake motion starts during a hybrid

simulation. To remove the force offset due to drifting on the actuator, a threshold (0.002 in.) on both horizontal displacement commands has been added to the force correction model. Once one of the command signals passes this threshold, the control system will take the average force over 10 samples and then offset the horizontal force feedback signal based on this value.

3-8-3 Special Setting for Testing of Triple Friction Pendulum Bearings

Testing pendulum bearings in horizontal direction requires significant movement of the table platen in the vertical direction due to the geometry of these bearings. In other words, once the slider inside the bearing starts to move up as it slides sideways on the concave surfaces, the table platen needs to move down to accommodate the increase in height of the bearing while maintaining the desired axial load. In case of poor tracking of the vertical displacement of the system, the axial force on the bearing will likely have poor tracking as well. This may result in a different horizontal response of the bearing due to the coupling between the vertical and horizontal bearing response. Efforts to improve the tracking of the axial force for pendulum type of bearings are discussed next.

- **Vertical Displacement**

As previously mentioned, the SRMD operates in force control in the vertical direction. The SRMD control system was programmed to take into account the vertical displacement during testing of single friction pendulum bearings. An optional observer in the SRMD controller takes a single value for effective curvature of the bearing and considers that curvature to help track the vertical displacement of the bearing while maintaining the commanded axial force on

the bearing (Figure 3-25). However, in the case of triple friction pendulum bearings, the effective curvature changes for the different sliding stages and should thus be adjusted based on the current horizontal displacement amplitudes.

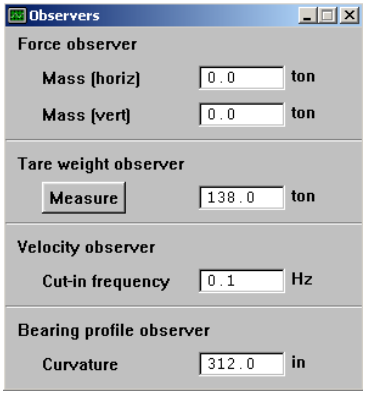

Figure 3-25 Optional observers available in the SRMD controller

If the required displacement of the bearing in vertical direction can be calculated accurately based on the horizontal displacements of the bearing, controlling the vertical displacement through the external reference will result in better tracking of the commanded axial force on the bearing (because of the cascade control loop, both axial force on the bearing and vertical deformation of the bearing can be sent as command signals to the control system). For the triple friction pendulum bearing, the relationship between the vertical and horizontal displacements becomes quite involved due to the fact that the bearing slides on different stages not only during the loading but also the unloading phases. A simple lookup table to predict the vertical displacement for certain horizontal displacement will not work because the behavior is path-dependent.

- **Force Normalization**

The horizontal response of friction pendulum bearings strongly depends on the axial force of the bearing. During 1-D and 2-D hybrid simulations with a constant axial force on the

bearing, it was observed that the SRMD controller could not maintain that constant axial force very accurately. Significant axial force fluctuations occurred mostly at horizontal displacement turnaround points during fast and real-time hybrid simulations. To compensate for these erroneous fluctuations of the axial force, the Simulink model included a force correction feature such that the horizontal shear forces of the bearing were first normalized by the instantaneous measured axial force on the bearing and then multiplied by the target axial force on the bearing.

3-9 Summary of Hybrid Infrastructure

As described in this chapter, several hardware and software components as well as correction and compensation procedures are necessary to conduct hybrid simulations with the SRMD. Figure 3-26 summarizes the different components and their line of communication with each other. The numerical model is programmed in OpenSees*SP* to solve the governing equations of motion at each integration time step for the hybrid model. OpenSees*SP* calculates new target displacement values for the next time step and sends these to all numerical elements as well as the experimental element in OpenFresco which generates the desired deformations and loads on the isolator test specimen. OpenFresco transforms the target signals from global degrees of freedom to basic element degrees of freedom and then communicates with the xPC Target machine running the Simulink predictor-corrector model. As described, this Simulink model running in real time is able to generate smooth command signals by writing digital signals to SCRAMNet+ memory each 1 msec using a predictor-corrector algorithm within the simulation time step. Next, the SRMD real-time controller reads these command signals as external reference signals and commands the motion of the table platen accordingly.

At the end of each simulation time step when the target displacement is reached by the SRMD, force and displacement measurements of each desired degree of freedom are obtained and then sent back to the numerical model. These response quantities are also referred to as feedback signals. These feedback forces not only consist of restoring forces in the physical seismic isolation bearing but also include inertia and friction forces of the platen. A shear force observer was instead implemented by measuring platen degree of freedom forces through the actuator uniaxial load cells and subtracting inertia and friction forces before sending them back to the hybrid model. This correction of the feedback forces was implemented within the Simulink real-time model described earlier. Once the numerical simulation receives the restoring forces from both the numerical and experimental elements, the analysis proceeds to the next integration time step.

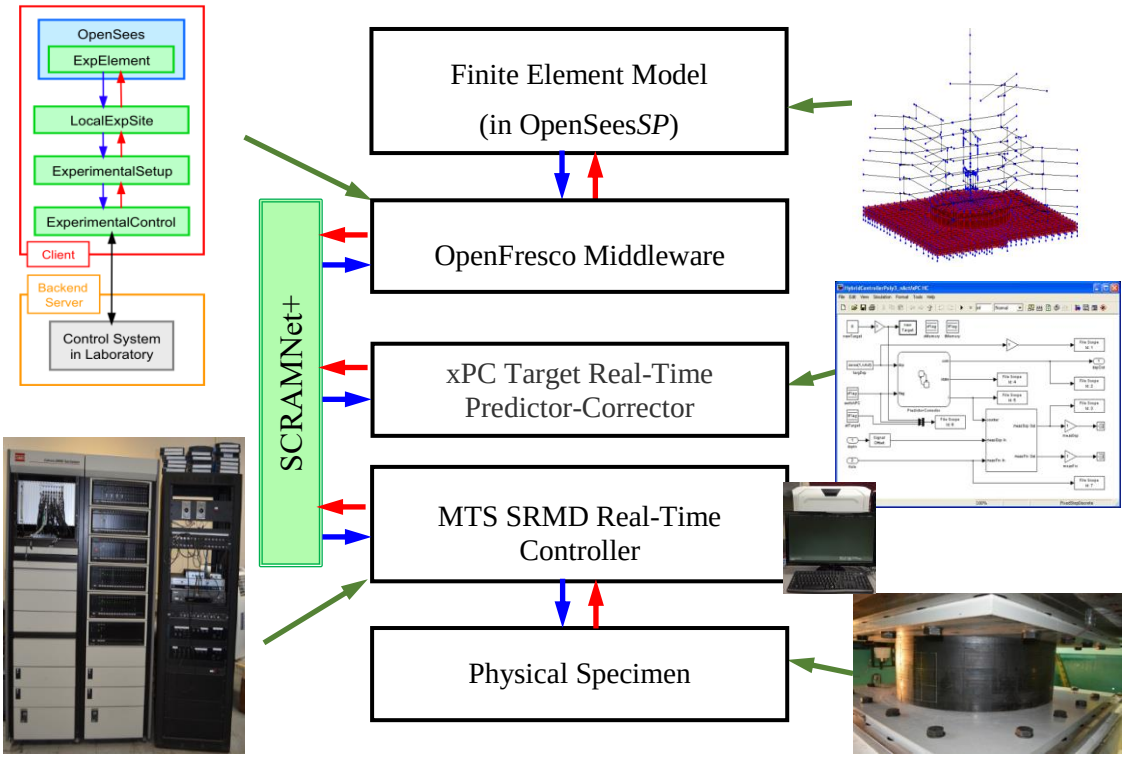

Figure 3-26 Schematic of the test set-up using SCRAMNet+ and xPC Target

3-10 Conclusions

This chapter described the adaptation of a full-scale bearing test machine to conduct real-time or near real-time hybrid simulations to study the dynamic response of isolated structures under realistic earthquake excitations. This research program confirms that real-time hybrid simulation can be a viable testing method to experimentally assess the behavior of large isolators at full-scale. The real-time hybrid simulations of structural systems with several thousand degrees of freedom were made possible by integrating high performance parallel computing approaches to execute the numerical analyses.

Challenges encountered in achieving reliable simulation results for these large scale dynamic tests such as compensation and correction for delay, inertia forces, and friction forces in the experimental setup were addressed. Despite the lack of a load cell to directly measure the experimental bearing forces, reliable feedback forces were obtained by measuring forces from actuator load cells and correcting them on-the-fly for machine friction and inertia force effects. To this end, a new model for inertia and friction force correction was developed, implemented and then calibrated for different test setups using system identification techniques. A SCRAMNet+ network providing fast digital communication between different hardware components of the hybrid test system was successfully implemented in an effort to enable real-time hybrid tests at the SRMD testing facility.

During the experimental test program, the tracking performance (in terms of delays) was significantly improved by employing the Adaptive Time Series delay compensator and using feedforward-control in the SRMD control system. Employing these advanced delay compensation techniques enabled real-time hybrid testing for 1-D and 2-D excitations

(controlling one or two horizontal displacement degrees of freedom). It was determined that it is currently not possible to conduct 3-D real-time hybrid simulations with the SRMD due to insufficient vertical tracking performance. To achieve acceptable performance and accuracy in the force controlled vertical DOF a hybrid simulation should be performed at a minimum 10x-slower than real time under 3-D earthquake excitations.

It is recommended to further improve the tracking performance of the SRMD machine for any future hybrid simulations performed on this testing system. It is apparent that real-time or near-real-time hybrid simulations of seismic isolation systems can more closely capture the true behavior of the isolators by applying realistic load combinations. Strategies developed to further minimize tracking errors and improve control in horizontal but more importantly vertical direction can lead to new applications of hybrid simulations for large scale bearings.

References

[1] UCSD (2014): Caltrans seismic response modification device (SRMD) test facility. <available online at: http://structures.ucsd.edu/node/62>.

[2] Schellenberg, A. H., Sarebanha, A., Schoettler, M. J., Mosqueda, G., Benzoni, G., and Mahin, S. A. (2015): Hybrid Simulation of Seismic Isolation Systems Applied to an APR-1400 Nuclear Power Plant. Technical Report PEER 2015/05 Pacific Earthquake Engineering Research Center, University of California, Berkeley, Berkeley, CA.

[3] Sarebanha, A., Schellenberg, A., Schoettler, M., Mosqueda, G., and Mahin, S. (2017): Hybrid Simulation of Full Scale Seismic Isolation Bearings Using the Caltrans SRMD Test Facility. 16WCEE, Santiago, Chile.

[4] dSpace (2013): dSPACE GmbH.

[5] OpenSees (2014): Open system for earthquake engineering simulation (Version 2.4.4) [computer software]. <available online at: http://opensees.berkeley.edu/>.

[6] McKenna, F. T. (1997): Object-oriented finite element programming: frameworks for analysis, algorithms and parallel computing.

[7] McKenna, F., and Fenves, G. L. (2007): Using the OpenSees Interpreter on Parallel Computers. NEESit.

[8] Amestoy, P. R., Duff, I. S., L'Excellent, J.-Y., and Koster, J. (2001): A Fully Asynchronous Multifrontal Solver Using Distributed Dynamic Scheduling. SIAM Journal on Matrix Analysis and Applications, 23 (1), 15-41.

[9] OpenFresco (2014): Open-source framework for experimental setup and control (Version 2.7) [computer software]. <available online at: http://openfresco.berkeley.edu/>.

[10] Mathworks (2013): MathWorks – Real-Time Workshop. <available online at: https://www.mathworks.com/matlabcentral/linkexchange/links/752-mathworks-real-timeworkshop>.

[11] Mosqueda, G., Stojadinović, B., and Mahin, S. A. (2005): Implementation and accuracy of continuous hybrid simulation with geographically distributed substructures. Technical Report EERC 2005-02, Earthquake Engineering Research Center, University of California, Berkeley, Berkeley, CA.

[12] Schellenberg, A. H., Mahin, S. A., and Fenves, G. L. (2009): Advanced Implementation of Hybrid Simulation. Technical Report PEER 2009/104 Pacific Earthquake Engineering Research Center, University of California, Berkeley, Berkeley, CA.

[13] SCRAMNet+ Network (2000): Technical Description Document. Systran Corporation.

[14] Hashemi, M. J. (2013): Collapse simulation of multi-story buildings through hybrid testing with substructuring techniques. Ph.D. dissertation, Dept. of Civil and Environmental Engineering, The State University of New York, University at Buffalo, Buffalo, NY.

[15] Bendat, J., and Piersol, A. (2013): Engineering Applications of Correlation and Spectral Analysis. New York, NY.

[16] Chae, Y., Kazemibidokhti, K., and Ricles, J. M. (2013): Adaptive time series compensator for delay compensation of servo-hydraulic actuator systems for real-time hybrid simulation. Earthquake Engineering & Structural Dynamics, 42 (11), 1697-1715.

[17] Ahmadizadeh, M., Mosqueda, G., and Reinhorn, A. M. (2008): Compensation of actuator delay and dynamics for real-time hybrid structural simulation. Earthquake Engineering & Structural Dynamics, 37 (1), 21-42.

[18] Mercan, O. (2007): Analytical and experimental studies on large scale real-time pseudodynamic testing. Ph.D. dissertation, Dept. of Civil and Environmental Engineering, Lehigh Univ., Bethlehem, Pa.

[19] Shortreed, J. S., Seible, F., Filiatrault, A., and Benzoni, G. (2001): Characterization and testing of the Caltrans Seismic Response Modification Device Test System. 359 (1786), 1829-1850.

[20] Ozcelik, O., Luco, J. E., Conte, J. P., Trombetti, T. L., and Restrepo, J. I. (2008): Experimental characterization, modeling and identification of the NEES-UCSD shake table mechanical system. Earthquake Engineering & Structural Dynamics, 37 (2), 243-264.

Chapter 4 Hybrid Simulation of Seismically Isolated Nuclear Power Plant using Full-Scale Bearing

4-1 Introduction

Hybrid simulation combines numerical and experimental modeling approaches to investigate the behavior of a structural system under different loading conditions. Numerical portions include components with behavior that is well understood and can be modeled reliably. Experimental portions include parts of the structure that are highly nonlinear or difficult to model. This chapters describes the numerical models, physical specimens, test setup configuration and different instrumentations used in this research program to experimentally asses the seismic performance of seismically isolated NPP under different level of earthquake shakings.

4-2 Analytical Model of Seismically Isolated Nuclear Power Plant

The prototype structure is an Archetype Nuclear Test (ANT) model of seismically isolated 1,400 MW Advanced Power Reactor (APR1400) plant provided by KEPCO E&C (Figure 4-1). The ANT model represents a simplified version of the APR1400 nuclear power plant design and is the basis for research conducted herein. Total weight of nuclear island (NI) including NI mat, nuclear reactor, its containment building, and auxiliary building is 4,730 MN. The isolation system has 486 bearings supporting the superstructure with an average design axial load of 9,733 kN on each bearing. Table 4-1 list the modal frequencies for the first 7 modes of the isolated structure.

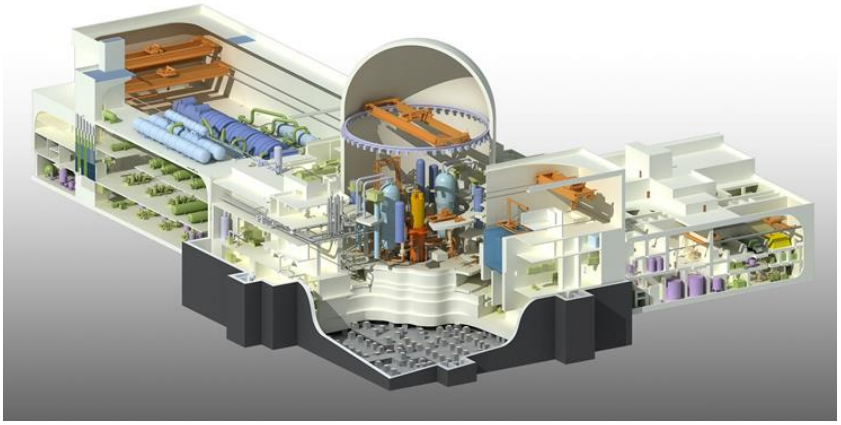

Figure 4-1 Perspective overview of APR1400 nuclear power plant – courtesy of KEPCO E&C

Table 4-1 Modal frequencies of the isolated NPP model

Mode	*Frequency (Hz)*	*Direction*
1	0.477	Isolation – Horizontal X Translation
2	0.477	Isolation – Horizontal Y Translation
3	0.711	Isolation – Torsion
4	3.539	RCB - Horizontal Translation
5	3.546	RCB - Horizontal Translation
6	7.023	ACB - Horizontal Translation
7	7.521	ACB - Horizontal Translation

4-2-1 Different Models of the Isolation System

Three variations of the seismically isolated ANT model were provided by KEPCO E&C. The three models consist of the same plant superstructure, but use three different approaches to model the seismic isolation plane. These three models use one-bearing equivalent, five-bearing equivalent and 486 bearing with different base mat foundations to accommodate these configurations (Figure 4-2).

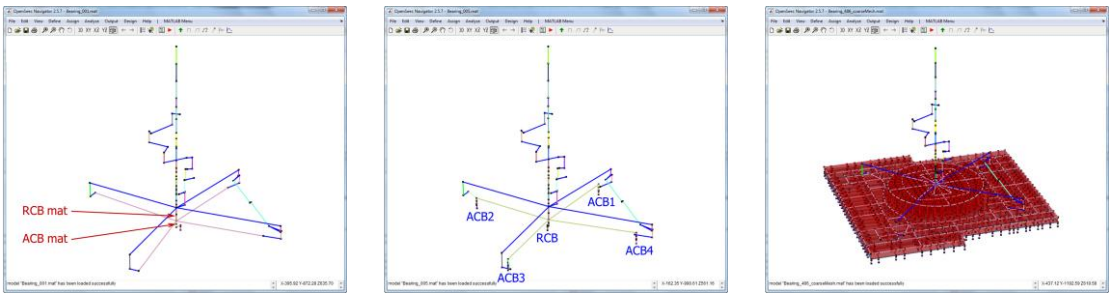

(a) (b) (c)

Figure 4-2 Different ANT models: (a) One-bearing equivalent (b) five-bearing equivalent and (c) 486 bearing model in OpenSees [1]

The first and simplest model utilizes one equivalent bearing element to represent the entire isolation plane. The second model consists of five bearings where each one of them

represents a group of bearings under four sections of the auxiliary complex buildings (ACB) and one central bearing under reactor containment building (RCB) section. The third and most complex model includes all 486 bearings in the isolation plane. In the first two models, the base mat foundation beneath the RCB and the mat foundation are modeled using equivalent beam element while in the model with 486 bearings the base mat is modeled using solid elements. More details on the three analytical models can be found in Shao et. al [1].

Each of these models are important in the experimental (Chapter 4 and 5) and numerical (Chapter 6) studies conducted throughout this dissertation in terms of speed of execution of the numerical model and capturing complex response behavior of the structure. The one-bearing equivalent model can represent the global behavior of the power plant quite well but cannot capture torsional response and overturning effects on the behavior of the individual isolator while the other two models can capture these behaviors. On the other hand, one- and five-bearing equivalent model are much faster to execute numerically considering their fewer DOFs and the mat foundation modeled using beam elements instead of solid elements. Fast execution time of the numerical portion is one of the essential key parameters to achieve real-time and fast hybrid simulation testing. For the hybrid simulation tests discussed in Chapter 4 and 5, all three models were used. The resposne of isolation system in the one-bearing model will be entirely determined by the experimental test specimen whereas in the other two models the reposne of the isolation system will be mostly dictated by the numerical isolators. In these two models, the local bearing reposnose under realistic loading could be captured accurately using the experimental bearing and it can be used to study potential limiations of the analytical bearing elements. For the five-bearing equivalent model, the experimental element was assigned to represent either the group of bearings under the RCB or the group of bearings under ACB1 (the north-east quadrant

of the ACB) and with the 486-bearing model the experimental element was assigned to the isolator in the northeast corner of the nuclear island mat.

4-3 Different Types of Bearings

Three bearing manufacturers produced full-scale test specimens based on preliminary analytical studies of the ANT model. The resulting specimens had significantly different design and ultimate displacement capacities. The specimens included two lead plug rubber bearings (LPRB), two friction sliding bearings with a flat sliding surface and compression springs (EQSB), and two sets of triple friction pendulum bearings (TFPB). A summary of design properties is provided in Table 4-2.

Table 4-2 Summary of design properties of the isolation bearings

Isolation bearing	Design displacement, D_d (mm)	Lateral force at D_d (kN)	Q_d (kN)
Unison eTech (LPRB)	210	1,900	1,010
ESCO RTS (EQSB)	152	2,920	1,090
EPS (TFPB)	584	1,510	730

For brevity, the remaining discussions will focus only on the LPRB manufactured by Unison eTech. This type of bearing was the main focus of this dissertation. Detailed results for all the bearings can be found in Schellenberg et al. [2].

4-3-1 Test Specimens: LPRB

Two LPRB manufactured by Unison eTech were tested in characterization and hybrid tests. These bearings were 1,520 mm in diameter and had four 200-mm diameter lead cores, see

Figure 4-3. Thirty rubber layers with a 7-mm thickness resulted in a total rubber thickness of 210 mm. These were sandwiched between 29 steel plates also with 7-mm thickness and 60-mm thick end plates giving the bearing a total height of 533 mm. Characteristic strength and stiffness properties are provided in Table 4-3. A design shear strain of 100% produced a design displacement capacity of 210 mm.

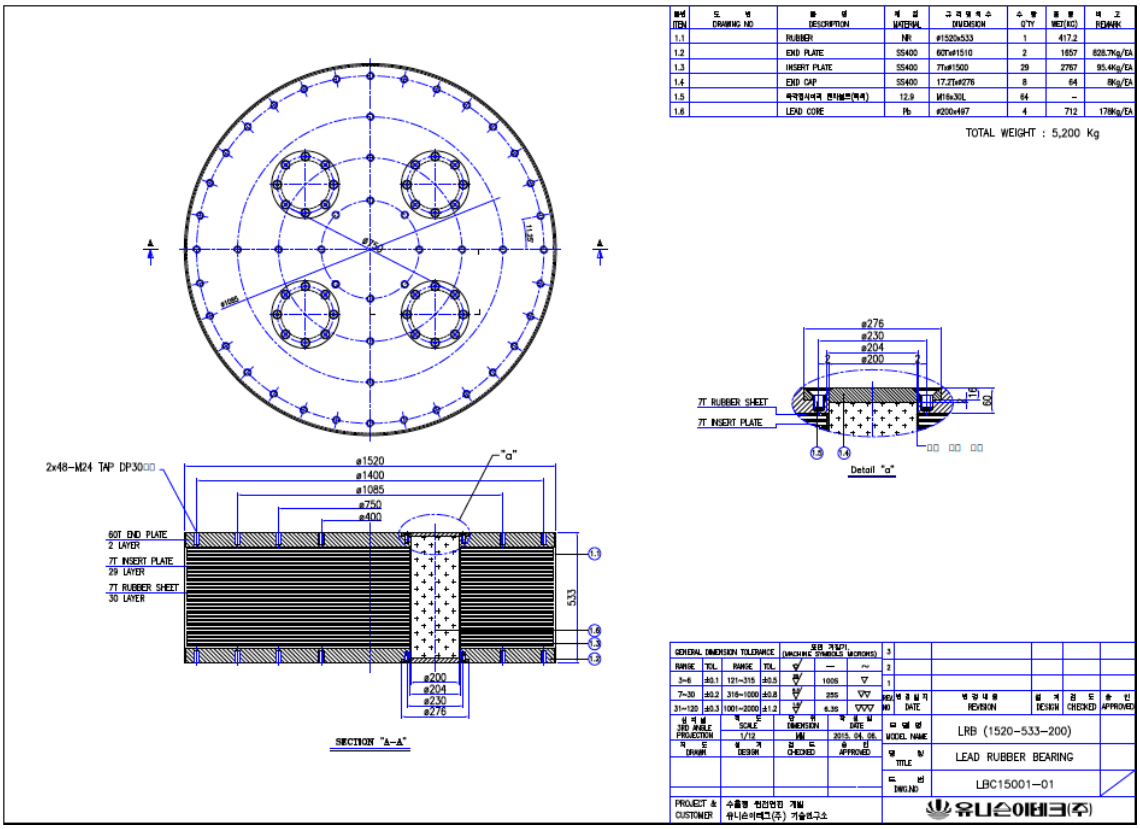

Figure 4-3 LPRB specifications provided by Unison eTech

Table 4-3 LPRB design properties

Design Properties					
Vertical stiffness (K_v)	12,896 kN/mm	Second slope stiffness (K_2)	4.2 kN/mm	Equivalent stiffness (K_{eq})	9.0 kN/mm
Initial stiffness (K_1)	545 kN/mm	Characteristic strength (Q_d)	1,010 kN	Equivalent damping ratio (H_{eq})	0.335

Quality control test data was provided by the manufacturer as shown in Figure 4-4. The axial load applied during this test was 21,350 kN, a factor of 2.2 times the design compression load. The measured axial force-displacement response for a LPRB is shown in Figure 4-5. There is a pronounced change in axial stiffness that occurs around the design axial load. This characteristic and the hysteretic damping are important considerations for the axial load fluctuations caused by vertical excitation and overturning.

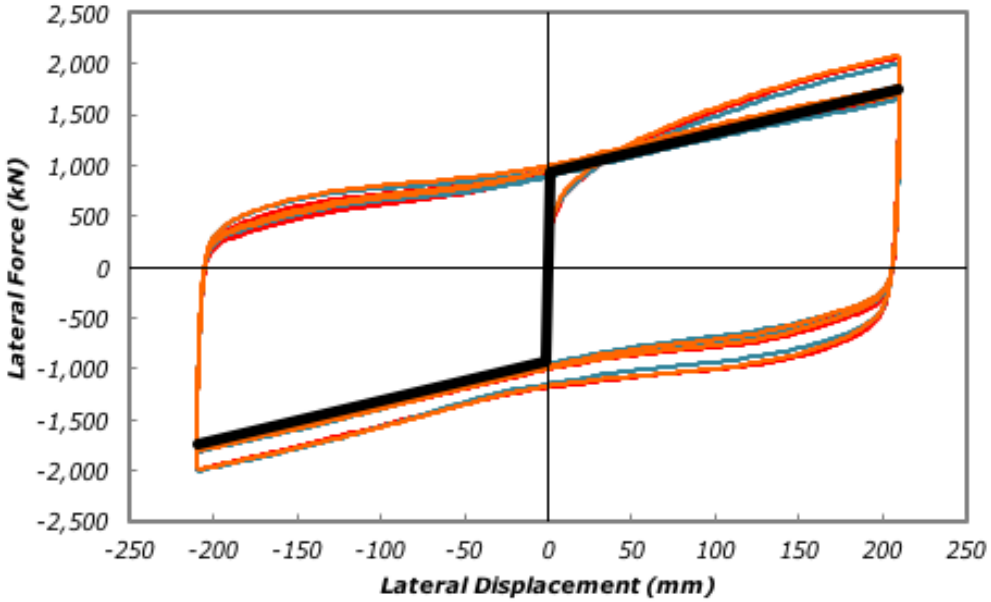

Figure 4-4 LPRB lateral quality control test and design envelope

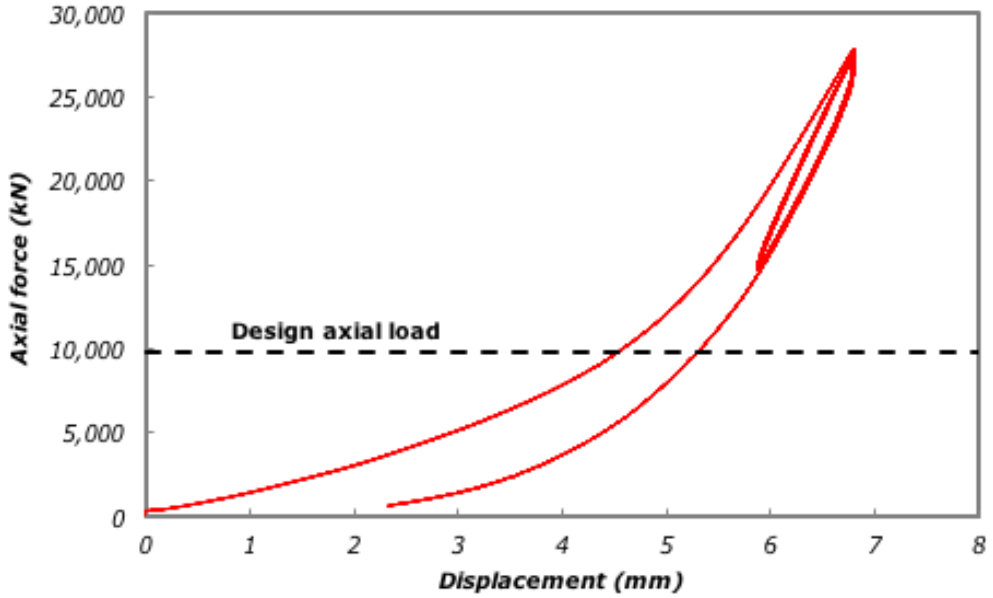

Figure 4-5 LPRB axial quality control test

Before conduction hybrid simulation test, properties of the analytical bearing models were updated based on characterization tests of the isolators. These included horizontal, vertical, rotational stiffness values as well as yield strength of the lead cores and equivalent vertical damping. Updated properties of the bearing obtained from these tests is summarized in Table 4-4. More details on the characterization tests can be found in Schellenberg et. al. [2].

Table 4-4 Updated bearing properties prior to hybrid tests

Bearing Properties					
Initial stiffness (K_1)	263.6 kN/mm	Characteristic strength (Q_d)	1,387 kN	Effective vertical stiffness	5,100 kN/mm
Second slope stiffness (K_2)	6.3 kN/mm	Equivalent stiffness (K_{eq})	12.66 kN/mm	Equivalent vertical viscous damping ratio	3.25 %

4-4 Test Setup Configuration

A system of concrete spacers blocks (bolted to the platen) and a system of steel spacers (bolted to the cross beam) were utilized to install the isolators into the test machine. The concrete

spacer blocks were aligned, leveled, grouted, and then post-tensioned (through high-strength 38-mm-diameter threaded rods) to the platen. The steel spacers and upper adapting plate were aligned to the cross beam and bolted using high-strength 38-mm-diameter A325 bolts. The position of the lower adapting plate was established relative to the upper adapting plate assembly. The lower adapting plate was grouted and then post-tensioned (through high-strength 38-mm-diameter threaded rods) to the platen. An overview of the basic test set-up used in this testing program is shown in Figure 4-6.

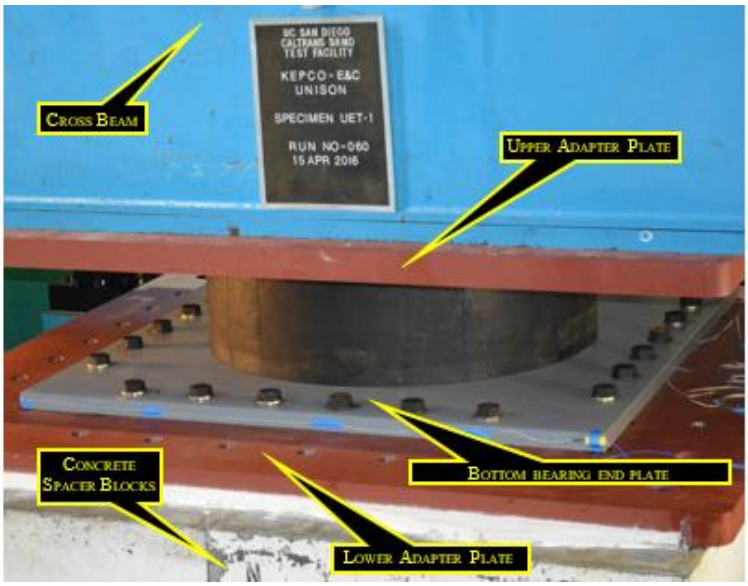

Figure 4-6 Overview of the typical test set-up

4-4-1 Recorded Data and Instrumentations

Different signals were measured and recorded during each test. Horizontal force readouts on the SRMD test system are obtained by means of four load cells mounted at the interface between the platen and horizontal actuators. Vertical force readouts are obtained by means of pressure cells on the four vertical actuators and the eight outrigger actuators. The position of the platen is measured using displacement transducers on the four horizontal actuators and the four

vertical actuators. Each millisecond, the data recorders calculate the x, y, and z displacement components, and each force component is combined in order to provide three forces (longitudinal, lateral, and vertical) and three moments (roll, pitch, and yaw) acting on the platen. Accelerometers are installed on the platen, within the top surface plate for acceleration measurements in x, y, and z directions. A typical list of channels recorded for tests on isolation bearings is provided in Table 4-5.

Linear voltage displacement transducers (LVDTs) were used to measure vertical deformations of the bearing. Vertical displacement feedback of the table is not the same as vertical deformation of the bearing because of the flexibility of the cross beam, see Figure 4-7. Configuration for these LVDTs is shown is Figure 4-8. These LVDTs were placed in four corners as close as practical to the LPRB bearing. In order to obtain a more reliable measurement of the vertical deformation of the bearing; especially for calculation of the vertical stiffness of the bearings; average values of the four displacement transducers at each corner of the bearing were considered.

Video and audio recordings were obtained of all testing stages via three color cameras. Video captured through this camera helped to understand the behavior of the bearing, and in case of failure it helped identify the failure mechanism.

Thermocouples installed in the Unison eTech bearings were monitored by a separate data acquisition system. In preparation for testing, holes were drilled in the top end caps of the lead cores and thermocouples, inserted between 20 and 25 mm. Neither a precise depth nor contact with the lead was discernable considering the small diameter hole provided for the wire thermocouple.

Table 4-5 Typically recorded channel list

Channel number	***Channel***	***Units***
1	Long. reference	in.
2	Lat. reference	in.
3	Long. feedback	in.
4	Lat. deedback	in.
5	Vert. feedback	in.
6	Roll feedback	°
7	Pitch feedback	°
8	Yaw feedback	°
9	Long. force fbk	U.S. ton
10	Lat. force fbk	U.S. ton
11	Vert. force fbk	U.S. ton
12	Roll force fbk	Ton-ft
13	Pitch force fbk	Ton-ft
14	Yaw force fbk	Ton-ft
15	Compression force fbk	U.S. ton
16	V-NE force fbk	U.S. ton
17	V-SE force fbk	U.S. ton
18	V-NW force fbk	U.S. ton
19	V-SW force fbk	U.S. ton
20	O-NE force fbk	U.S. ton
21	O-SE force fbk	U.S. ton
22	O-NW force fbk	U.S. ton
23	O-SW force fbk	U.S. ton
24	AXNE accel fbk	*g*
25	AYNE accel fbk	*g*
26	AYNW accel fbk	*g*
27	AZNE accel fbk	*g*
28	NE disp.	in.
29	SE disp.	in.
30	NW disp.	in.
31	SW disp.	in.

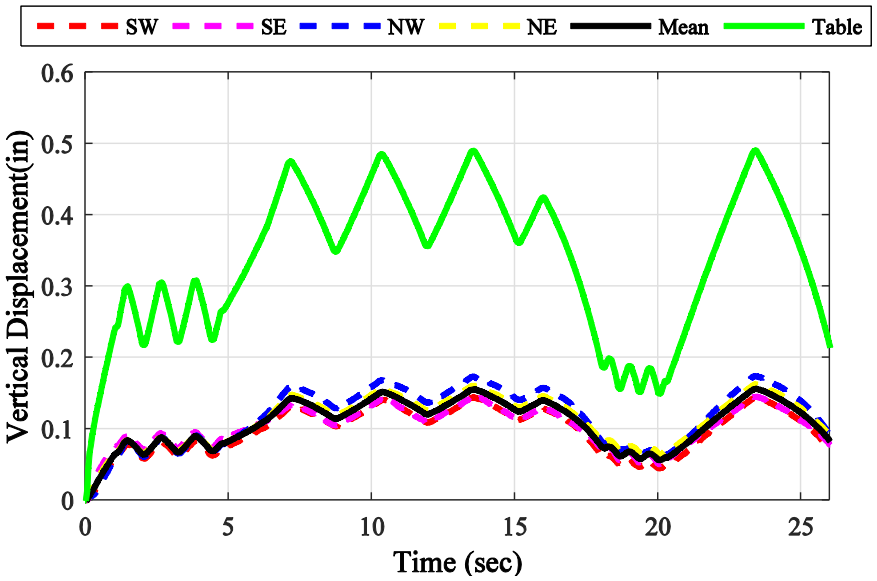

Figure 4-7 Vertical displacement of the SRMD and LVDTs

Figure 4-8 LVDTs used to measure vertical deformation of the bearings

4-4-2 Data acquisition systems

For all the hybrid simulation tests, data was simultaneously recorded on four different machines that were part of the overall testing system including: analysis machine (high performance PC), real-time xPC Target machine (or dSpace Control Desk), MTS SRMD Controller, and an additional data acquisition machine.

Nodal and element response quantities for the entire OpenSees model were recorded on the computing machine. Because the analysis model was a hybrid model consisting of numerical as well as one experimental element, measured response quantities included the experimental

element. OpenFresco was deployed on the analysis machine allowing control and data acquisition quantities to be recorded through the SCRAMNet experimental control object. Response quantities in OpenSees and OpenFresco were recorded at the integration time step interval of 0.01 seconds, providing a frequency resolution of up to 50 Hz.

Secondly, data was recorded on the real-time xPC Target machine where the predictor-corrector algorithms were executed for time synchronization. All the commanded and measured data that passed through the predictor-corrector was recorded at a sampling rate of 1 kHz, which is identical to the MTS SRMD real-time digital controller sampling rate. In order to confirm the correct operation of the event-driven predictor-corrector algorithm and the inertia force and friction correction algorithm, it was necessary to record data at such a high sampling rate.

The third and fourth machine that recorded data during each hybrid simulation was the digital SRMD controller and the aforementioned standalone machine that monitored thermocouples. For the majority of the hybrid tests, the data acquisition rate on the SRMD controller was set at 50 Hz. Synchronization of the standalone data acquisition system with the primary data acquisition system is achieved by comparison of a common signal recorded on both systems. Since heat generation and dissipation is a fairly slow process, temperature data was recorded at a low sampling rate of 1 Hz on the standalone DAQ system.

Multiple simulation runs were conducted to study and improve the performance of the overall hybrid test system. Recorded data in different data acquisition system were essential to ensure each component is working properly. These runs are considered developmental and crucial for the success of the test program. Results for these tests are reported in Schellenberg et. al. [2].

References

[1] Shao, B., Schellenberg, A. H., Schoettler, M. J., and Mahin, S. A. (2016): Numerical Analysis of Seismic Isolation Systems applied to an Archetype Nuclear Test (ANT) Power Plant under varied Seismic Conditions and Aircraft Impact Loading. Technical Report PEER, Pacific Earthquake Engineering Research Center, University of California, Berkeley, Berkeley, CA.

[2] Schellenberg, A. H., Sarebanha, A., Schoettler, M. J., Shao, B., Mosqueda, G., and Mahin, S. A. (2016): Hybrid Simulation of Seismic Isolation Systems applied to an Archetype Nuclear Test (ANT) Power Plant under Design Level Excitation. PEER.

Chapter 5 Seismic Response of NPP Isolated with LPRB

5-1 Introduction

Results from hybrid simulations conducted on NPP seismically isolated with lead plug rubber bearings (LPRB) are reported for different loading scenarios. The complex nonlinear behavior of the full-scale seismic isolation bearings (i.e. vertical-horizontal coupling due to overturning or 3-D seismic excitation) was captured experimentally and its interaction with the numerical model of the superstructure was studied to evaluate system level and in-structure response. Description of the isolated nuclear power plant, numerical model of the superstructure, full scale bearing specimens, and test setup used in these tests are described in Chapter 3 and 4.

5-2 Hybrid Simulation Test Plan

The full set of all hybrid simulation scenarios conducted on the LPRB bearings is presented in Table 5-1. This table summarizes the test number, model discretization, ground motion components considered, the test rate, ground motion scale factor, bearing specimen, and laboratory testing notes which describe the necessary steps taken to achieve successful testing. A list of hybrid simulation runs on the LPRB bearings that are discussed and compared here is presented in Table 5-2. The test rate is the time scale factor that describes by how much the duration of the test was extended to slow down the simulation and minimize the effects of delays. Due to the performance capabilities of the SRMD, not all scenarios could be executed in real-time. This was primarily due to vertical actuator response resulting in slower execution times in 3-D tests to compensate for the delays. The complete set of tests performed, including development tests and hybrid simulation are reported in Schellenberg et. al [1]. Details on used ground motion in these hybrid simulation (selection and scaling) are presented in Shao et al. [2].

Table 5-1 Hybrid simulation tests conducted on LPRB bearings (Unison eTech)

LPRB test no.	*Model*	*Components*	*Test rate*	*Ground motion scale factor*	*Bearing*	*Notes*
34	1-bearing equivalent	1D	real-time	1.0	UET-1	Development ; Note 1
35	1-bearing equivalent	1D	real-time	1.0	UET-1	Development ; Note 2
36	1-bearing equivalent	1D	real-time	1.0	UET-1	Development ; Note 3
37	1-bearing equivalent	1D	real-time	1.0	UET-1	Development ; Note 4
38	1-bearing equivalent	1D	real-time	1.0	UET-1	
39	1-bearing equivalent	1D	real-time	1.0	UET-1	Development ; Note 5
71	1-bearing equivalent	1D	real-time	1.0	UET-1	Updates stiffness parameters
55	1-bearing equivalent	1D	2	1.0	UET-1	
40	1-bearing equivalent	2D	real-time	1.0	UET-1	Development ; Note 6

1. **Force feedback factor was zero. The command signal to SRMD was based only on the analytical bearing's response.**
2. **Investigation of system delays: OpenSees delay of 15 msec and xPC delay of 12 msec.**
3. **Investigation of system delays: Modified ATS gains. Resulted in more overshoot and additional delay.**
4. **Feedforward gain was added on Longitudinal degree of freedom (0.08). xPC delay of 8 msec.**
5. **Feedforward gain was modified on Longitudinal degree of freedom (0.12). xPC delay of 5 msec. but tracking and overshoot were worse than run 38.**
6. **Bidirectional tuning: Feedforward gain was implement in Longitudinal (0.08) and Lateral (0.04). Delays were 6 msec Longitudinal and 4 msec Lateral.**

Table 5-1 (Continued) Hybrid tests conducted on the LPRB bearings (Unison eTech)

41	1-bearing equivalent	2D	real-time	1.0	UET-1	Development; Note 7
42	1-bearing equivalent	2D	real-time	1.0	UET-1	Note 8
43	1-bearing equivalent	2D	real-time	1.0	UET-1	Corrected ScramNet memory mapping. Note 9
44	1-bearing equivalent	2D	real-time	1.0	UET-1	Development; Note 1, 9, and 10
45	1-bearing equivalent	2D	real-time	1.0	UET-1	Note 9
56	1-bearing equivalent	2D	2	1.0	UET-1	
46	1-bearing equivalent	3D	real-time	1.0	UET-1	
57	1-bearing equivalent	3D	10	1.0	UET-1	
164	1-bearing equivalent	3D (2/3V)	10	1.0	UET-2	Note 11
48	5-bearing equivalent	1D	real-time	1.0	UET-1	center location; Unstable
49	5-bearing equivalent	1D	real-time	1.0	UET-1	center location; Development; Note 12

7. **Bidirectional tuning: Feedforward gain was implement in Longitudinal (0.08) and Lateral (0.05). Delays were 6 msec Longitudinal and 4 msec Lateral. Tracking was much better.**
8. **Slower execution time may have been caused by sampling rate, which seems to cause a problem because SRMD control system works on 1000 Hz but the upFactor might result in a problem syncing the flags and DAQ signals that likely operate at 1024, 2048 or 4096 Hz.**
9. **Bidirectional test, but with vertical control sent from OpenFresco.**
10. **Bypassed ATS on compression force command.**
11. **Vertical ground motion component used a new spectral matched record with a 2/3 factor.**
12. **Modified the application of gravity load before testing. ATS did not work with this.**

Table 5-1 (Continued) Hybrid tests conducted on the LPRB bearings (Unison eTech)

50	5-bearing equivalent	1D	real-time	1.0	UET-1	center location
51	5-bearing equivalent	2D	real-time	1.0	UET-1	center location
52	5-bearing equivalent	1D	real-time	1.0	UET-1	corner location
53	5-bearing equivalent	2D	real-time	1.0	UET-1	corner location
165	5-bearing equivalent	1D	2	1.0	UET-2	corner location
166	5-bearing equivalent	2D	2	1.0	UET-2	corner location
178	5-bearing equivalent	2D	2	1.0	UET-2	corner location; Unstable; Note 13
54	5-bearing equivalent	3D	10	1.0	UET-1	corner location; Note 14
167	5-bearing equivalent	3D (2/3V)	10	1.0	UET-2	corner location
172	486-bearing	2D	15	1.0	UET-2	
171	486-bearing	3D (2/3V)	15	1.0	UET-2	
174	1-bearing equivalent	2D	real-time	0.67	UET-2	
173	1-bearing equivalent	2D	real-time	-	UET-2	AIA
60	1-bearing equivalent	1D	-	1.0	UET-1	Real-time displ. feedback (Run 55)
61	1-bearing equivalent	2D	-	1.0	UET-1	Real-time displ. feedback (Run 56)

13. Changed analytical bearing model to LeadRubber-X.

14. Upper limit on compression force (23,130 kN) was reached. Seemed that the target was not much higher.

Table 5-2 Matrix of run numbers for hybrid simulation comparisons

Unison eTech Bearing			
1-D vs. 2-D	***Influence of Test Rate***	***Influence of Vertical Excitation***	***Influence of Model Discretization***
38 vs. 42 (real time) 55 vs. 56 (2x slower)	38 vs. 55 (1-D) 42 vs. 56 (2-D) 46 vs. 57 (3-D)	56 vs. 57 (2x vs. 10x)	56 vs. 166 vs. 172 (2-D) 164 vs. 167 vs. 171 (3-D)

Results presented here focus on the structural responses recorded by OpenSees and OpenFresco. For each comparison, the behavior of the experimentally tested isolator is presented in terms of displacement and force demands and the in-structure response is presented in terms of floor response spectra. For the isolator specimen, hysteresis loops in longitudinal and lateral directions, the horizontal displacement orbit and the shear force interaction surface are provided. For the plant superstructure, floor response spectra are provided at three different elevations in the reactor containment building (RCB), the internal structure (INS), and the auxiliary complex building (ACB) (as shown in Figure 5-1). The response spectra for the input ground motions are also included. The elastic response spectra were generated by analyzing 2 DOF linear-elastic systems with 5% damping and the reported spectral quantities are vector norms of the response quantities in the two horizontal directions.

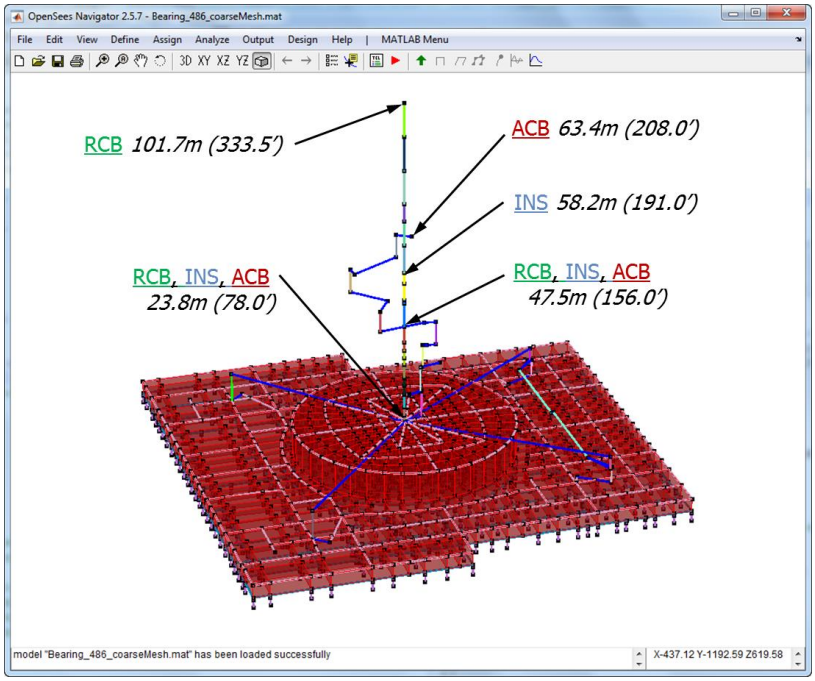

Figure 5-1 Superstructure result output locations

5-3 Results of Hybrid Simulation with LPRB

In the sections that follow, results from the hybrid simulations are compared to evaluate the effects of testing parameters on the simulation results. A key objective is to evaluate the importance of real-time testing with multiple components of excitation and the effects on simulations results.

5-3-1 Comparison of 1-D and 2-D Horizontal Inputs

5-3-1-1 Runs 38 and 42 (real time)

Figure 5-2 presents a comparison of the hysteresis loops for a 1-D longitudinal hybrid simulation (Run 38) with a 2-D bidirectional hybrid simulation (Run 42). The 1-bearing equivalent ANT model was used and the hybrid simulations were executed in real time. As can

be seen from the figure, the maximum longitudinal displacement demand from the 1-D test is 167 mm, which is smaller than the 191 mm demand from the 2-D test which was expected (Typically to consider bi-directional effects of earthquake excitations, demand may be estimated by combining unidirectional maxima in a combination of 100 and 30 % using linear static results). From the longitudinal hysteresis loop of the 2-D test, shear-force fluctuations are obvious in many places, caused by the perpendicular lateral deformation. Furthermore, the hysteresis loops of the 2-D test become narrower more quickly compared to the 1-D test. This reduction of the yield force over time is caused by the increase of the temperature in the four lead cores. In the 2-D test, the lead cores heated up faster because of the increased work (see Figure 5-3) that is being done due to bidirectional motion, hence the observed narrowing of the hysteresis loops. The maximum shear force in the 1-D test is 2,340 kN and 2,414 kN in the 2-D test. For the 2-D test, the shear-force interaction surface is mostly circular except for two distinct loops. The reason for the shear-force interaction surface having two loops that are outside the circular yield surface is that there are two clear instances where the LPRB responds in the post-yield range, once in the longitudinal positive direction and once in the lateral positive direction.

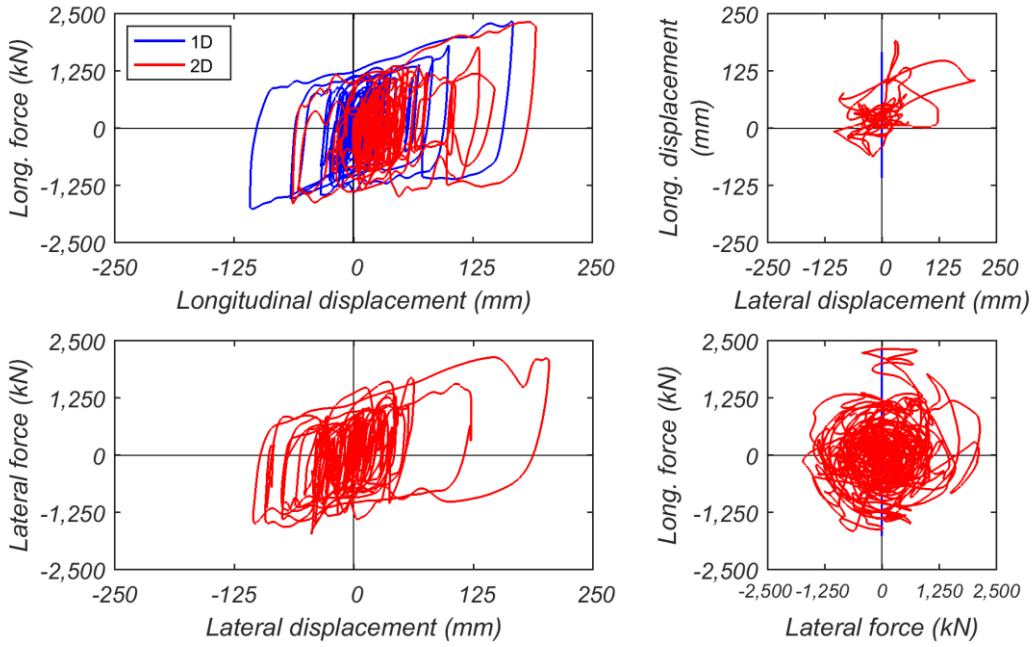

Figure 5-2 Comparison of bearing response to 1-D and 2-D analyses (real-time)

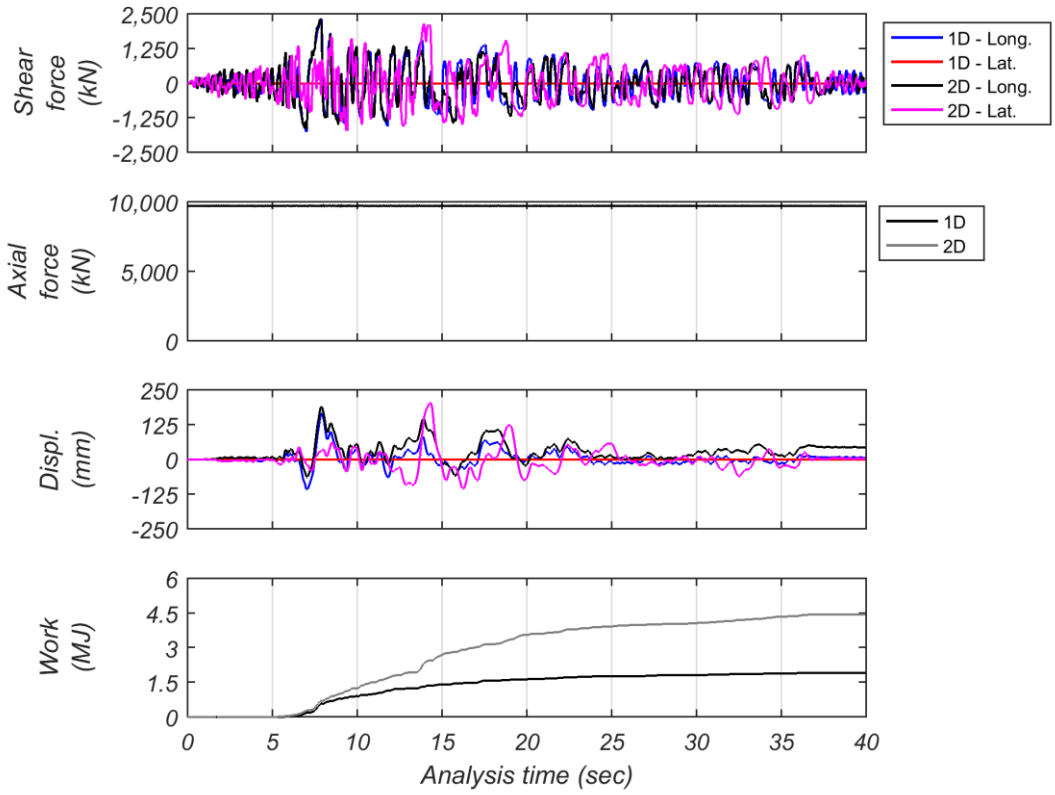

Figure 5-3 Comparison of bearing response to 1-D and 2-D analyses (real-time)

Figure 5-4 shows floor response spectra for the RCB, INS, and ACB. Generally, the floor response spectra from the 1-D and 2-D test are nearly identical with the exception of the high frequency spectral acceleration peak for the INS. Peaks can be identified in the spectra at several distinct frequencies. For the RCB, the largest spike in the floor spectra reaches 3.2*g* and occurs at ~3.8 Hz, which corresponds to the first horizontal mode of vibration of the RCB. A much lower spike of ~1.4*g* is observed between 7.5–9 Hz, which is due to the interaction of the RCB with the INS and ACB. Similarly, in the floor response spectra of the INS the main spike can be identified at ~8.0 Hz reaching a spectral acceleration of 1.8*g*. This spike corresponds to the first-mode frequency of the INS. In the floor response spectra of the ACB the main spike can be identified at ~7.5 Hz reaching a spectral acceleration of 2.1*g*. This spike corresponds to the first- and second-mode frequencies of the ACB. Finally, for all the floor spectra in all three superstructures there are two smaller humps between 1.2-1.7 Hz and around 2.5 Hz. The first one corresponds to an effective isolation frequency with the isolator responding somewhere in between the linear-elastic and nonlinear range and the second one corresponds to the isolator responding in its linear-elastic range.

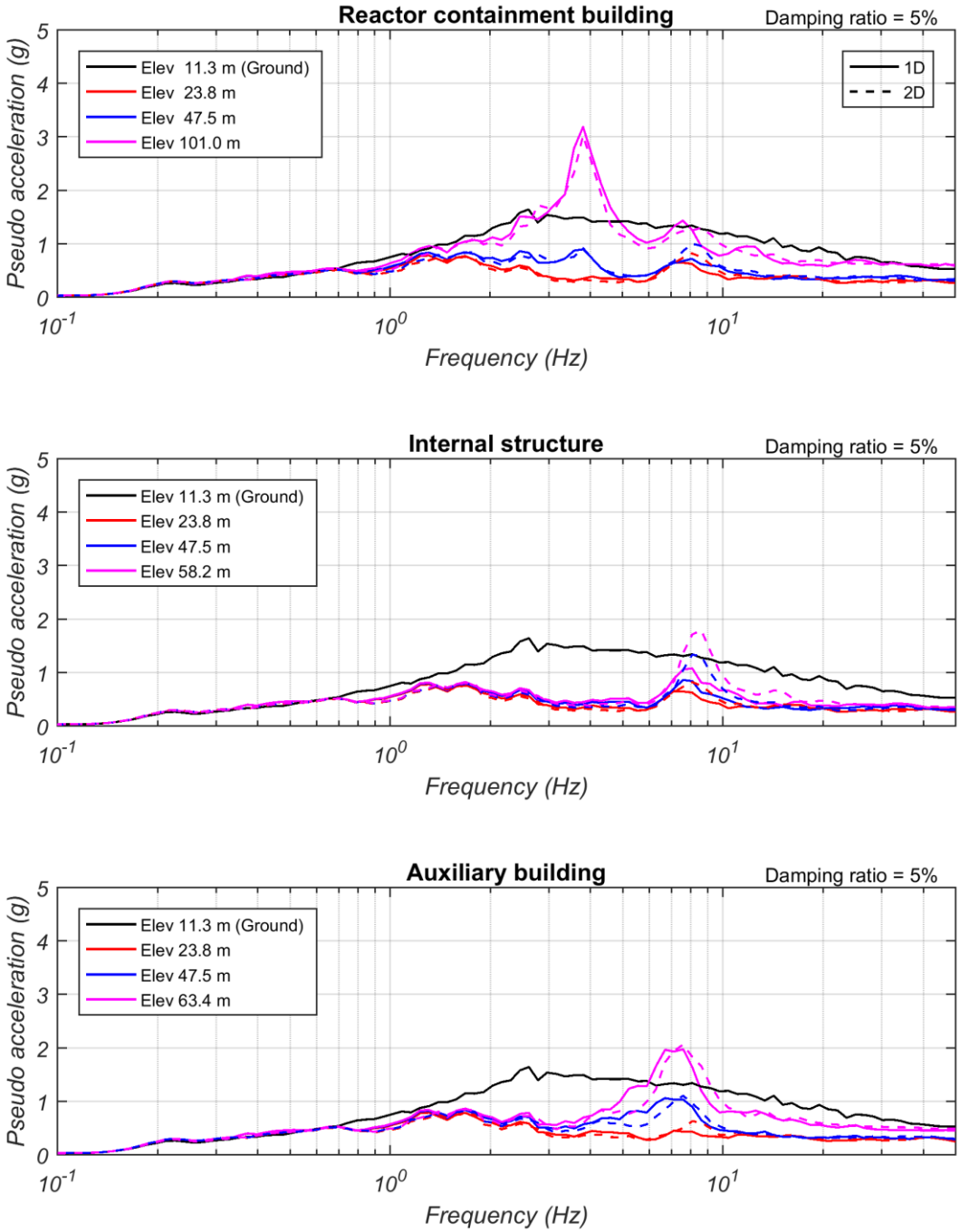

Figure 5-4 Response spectra comparison of 1-D and 2-D analyses (real-time)

Considering that for the 2-D test the yield strength of the lead cores reduces more and faster than in the 1-D test and given that due to bidirectional movement the hysteresis loops are more rounded in the 2-D tests, one would expect the floor response spectra to be lower in the 2-

D test than in the 1-D test. However, this is not evident from the floor response spectra results; on the contrary, for the INS floor response spectra the spectral acceleration peaks around 9 Hz are larger in the 2-D test than the 1-D test. This counterintuitive behavior is caused by experimental errors which were fairly large in these two real-time hybrid simulations, because not all of the system delay could be compensated for and an average delay of approximately 8.5 msec remained for the 1-D test and 5 msec for the 2-D test. Comparing Fourier amplitude plots of the displacement errors (Figure 5-5), one can identify amplitude spikes around 8 Hz for the 2-D test which are not present in the 1-D test. It was concluded that even though average delays were less in the 2-D test, the displacement errors, especially at higher frequencies, were larger than in the 1-D test. This behavior, which is caused by the SRMD was the reason for the counterintuitive results observed in the floor response spectra.

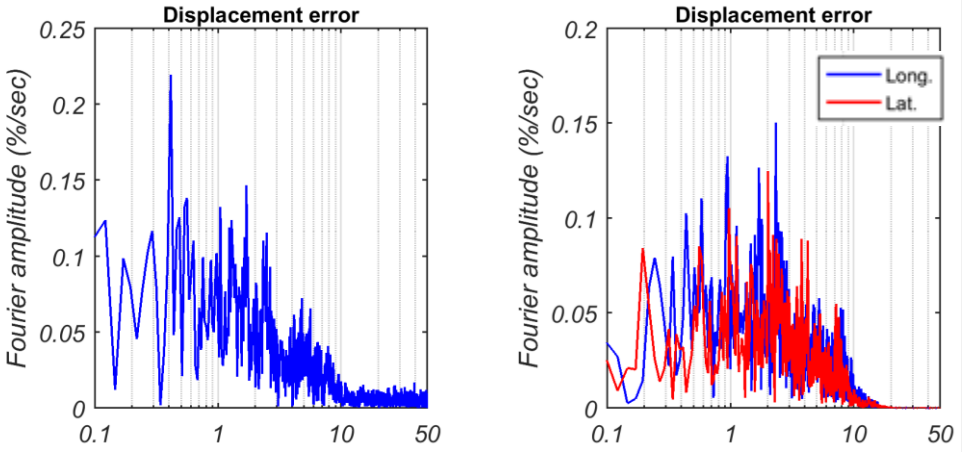

(a) Run 38 (b) Run 42

Figure 5-5 Fourier amplitude of displacement error in Run 38 and 42

Finally, it is important to observe that for most elevations, the peak floor accelerations are around 0.25*g*, which is a reduction by a factor of two from the peak ground acceleration (PGA).

5-3-1-2 Runs 55 and 56 (2x-slower)

Figure 5-6 and Figure 5-7 compare the 1-D (Run 55) to 2-D (Run 56) results for the 1-bearing equivalent ANT model which was executed 2x-slower than real time. As can be seen, the maximum longitudinal displacement demand from the 1-D test is 149 mm, which is identical to the 149 mm demand from the 2-D test. Similar to the real-time hybrid simulations that were compared before, the longitudinal hysteresis loop of the 2-D test show shear-force fluctuations caused by the perpendicular lateral deformation. Furthermore, the hysteresis loops of the 2-D test become narrower more quickly than the ones of the 1-D test. The maximum shear force in the 1-D test is 2,215 kN and 2,235 kN in the 2-D test. Similar to the real-time test, for the 2-D test the shear-force interaction surface is mostly circular except for two distinct loops.

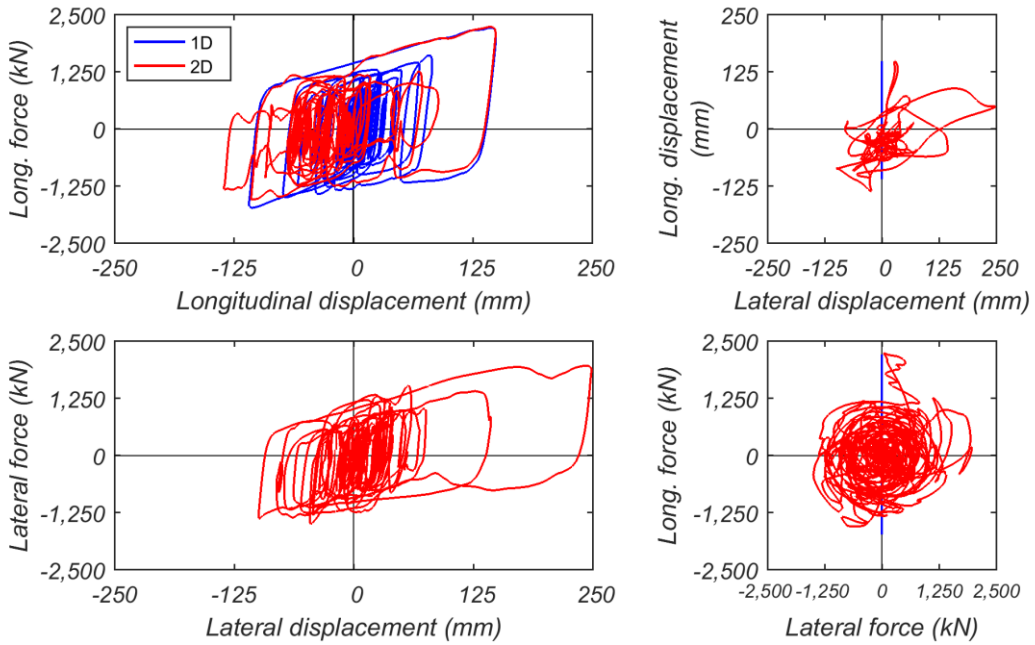

Figure 5-6 Comparison of bearing response to 1-D and 2-D analyses (2x slower)

Figure 5-7 compares the floor response spectra for the 2x-slower than real-time test; note that there is a distinct difference in the size of the spectral acceleration spikes between the 1-D

and 2-D tests for all the superstructure components. While the peaks occur around the same frequencies, the spectral accelerations in the 2-D test are clearly smaller than in the 1-D test. For the 2-D test the spectral amplitude at the first-mode frequency of the RCB is 2.6*g*, whereas the one from the 1-D test is 2.8*g*. Similarly, the spectral amplitude at the first-mode frequency of the INS is 0.7*g* for the 2-D test and 0.8*g* for the 1-D test. For the ACB, the spectral amplitude at the first-mode frequency is 0.9*g* for the 2-D test and 1.3*g* for the 1-D test. Finally, the same trend can be observed for the two smaller humps between 1.2-1.7 Hz and around 2.5 Hz. As previously mentioned, the first corresponds to an effective isolation frequency with the isolator responding somewhere in between the linear-elastic and nonlinear range and the second one corresponds to the isolator responding in its linear-elastic range. At both of those frequencies the spectral accelerations from the 2-D test are again smaller than the ones from the 1-D test. So it is clear that overall less acceleration is transmitted to all the superstructure components in the 2-D test than the 1-D test for two reasons:

1. As described earlier, the yield strength of the lead cores decreases more and at a faster in the 2-D test compared to the 1-D test. A smaller characteristic strength of the isolator means that less shear force and hence less acceleration is being transmitted into the superstructure.
2. The bidirectional movement in the 2-D test produces more rounded hysteresis loops than the unidirectional movement in the 1-D test. A more rounded hysteresis loop causes less abrupt changes in shear force that could cause acceleration spikes.

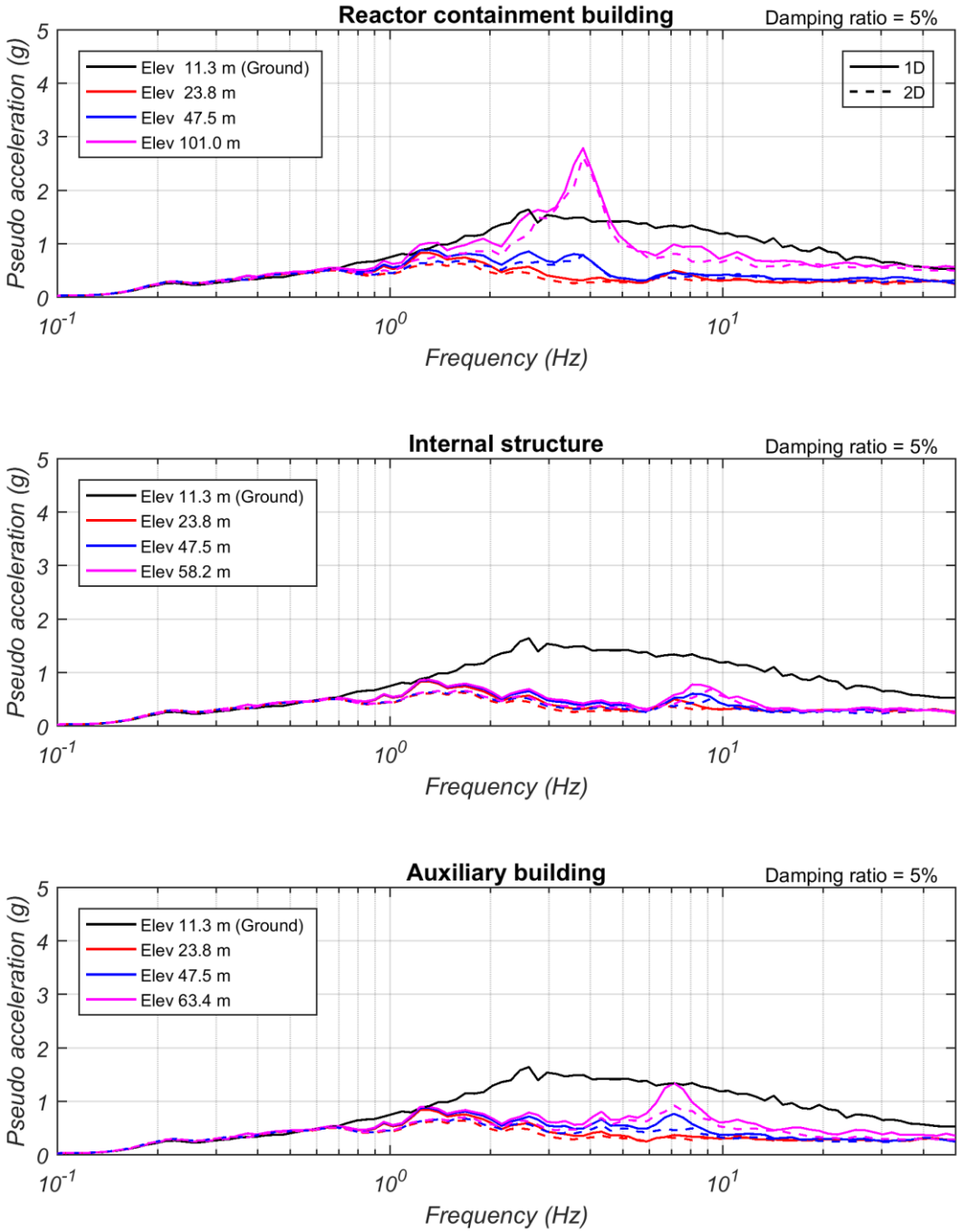

Figure 5-7 Response spectra comparison of 1-D and 2-D analyses (2x slower)

5-3-2 Influence of Test Rate

5-3-2-1 Runs 38 and 55 (1-D)

Figure 5-8 and Figure 5-9 compare the hybrid test results for two different rates of testing. The 1-bearing equivalent model was used to perform 1-D hybrid simulations in real time (Run 38) and 2x-slower than real time (Run 55). As can be seen from Figure 5-8, the maximum longitudinal displacement demand from the real-time test is 167 mm, which is larger than the 149 mm demand from the 2x-slower test. Comparing the hysteresis loops, it can also be seen that shear-force fluctuations in the real-time test are more pronounced than in the 2x-slower test. This behavior can most likely be attributed to two effects. The first is that the dynamic effects in terms of inertia and friction forces in the test setup and specimen are playing a more important role in the real-time test. The second reason is that the experimental errors were noticeably larger in the real-time test compared to the 2x-slower test. Even though the work done in these two hybrid tests should be identical, it seems that the yield force reduction of the lead cores initially occurs a bit faster in the real-time test than the 2x-slower test. Eventually, towards the end of the motion the widths of the two hysteresis loops are nearly identical. However, the seemingly narrower hysteresis loop at the beginning of the motion is more likely also caused by the larger dynamic effects in the real-time test as described before. The maximum shear force in the real-time test is 2,340 kN, which is larger than the 2,215 kN shear force in the 2x-slower than real-time test. It can be concluded that the faster (real-time) execution of the hybrid simulation has a moderate effect on the hysteresis loops of the LPRB, mostly caused by inertia force effects.

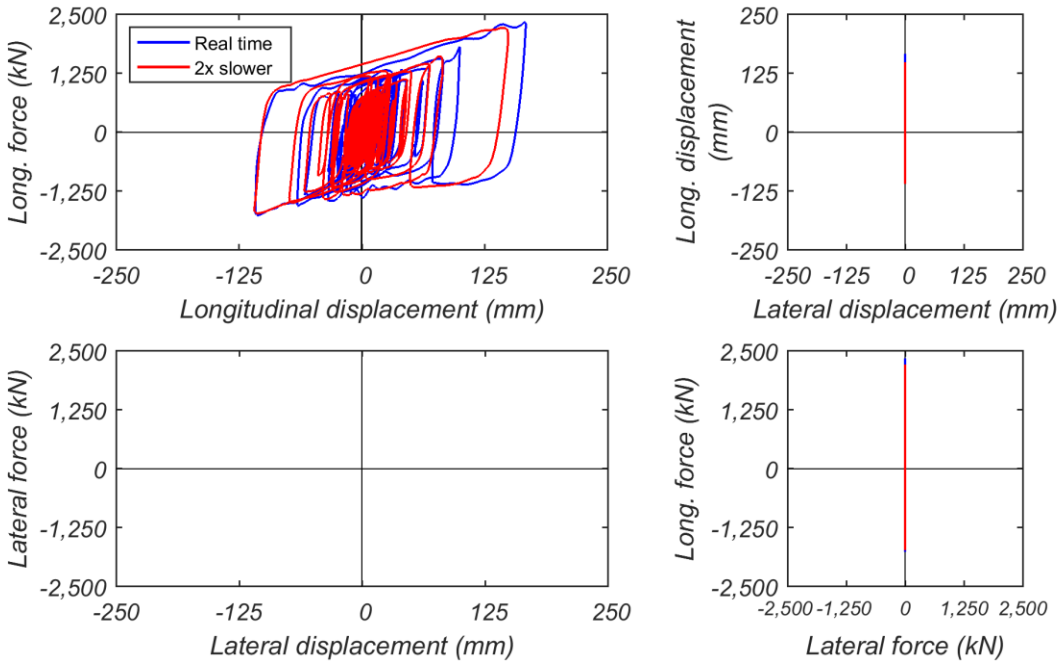

Figure 5-8 Comparison of bearing response to test rate (1-D)

Figure 5-9 compares the response spectra for the real-time and 2x-slower than real-time hybrid tests. For frequencies above 3 Hz, the response spectra for the RCB, INS, and ACB are consistently greater for the real-time hybrid simulation than the 2x-slower hybrid simulation. The real-time hybrid simulation clearly generated more high-frequency excitations that were transmitted through the LPRB bearing into the superstructures. As explained before, this behavior can be attributed to the greater dynamic effects and larger experimental errors in the test system experienced during real-time testing. Comparing Fourier amplitude of the displacement errors and force feedbacks as well as error monitors for the two tests (Figure 5-5), it can be seen that tracking performance was considerably reduced in the real-time test versus the 2x-slower test. In addition, all the error monitors show approximately half the errors in the 2x-slower test as compared to the real-time test. Average delays in the real-time test were estimated around 8.5 msec, whereas in the 2x-slower test they were around 2.9 msec. It is impossible to separate those two effects, but it seems that in the real-time hybrid simulation the experimental

errors played a more important role on the behavior of the superstructures in terms of floor response spectra than the dynamic effects. Further investigation of these results and additional simulations are necessary to confirm this conclusion.

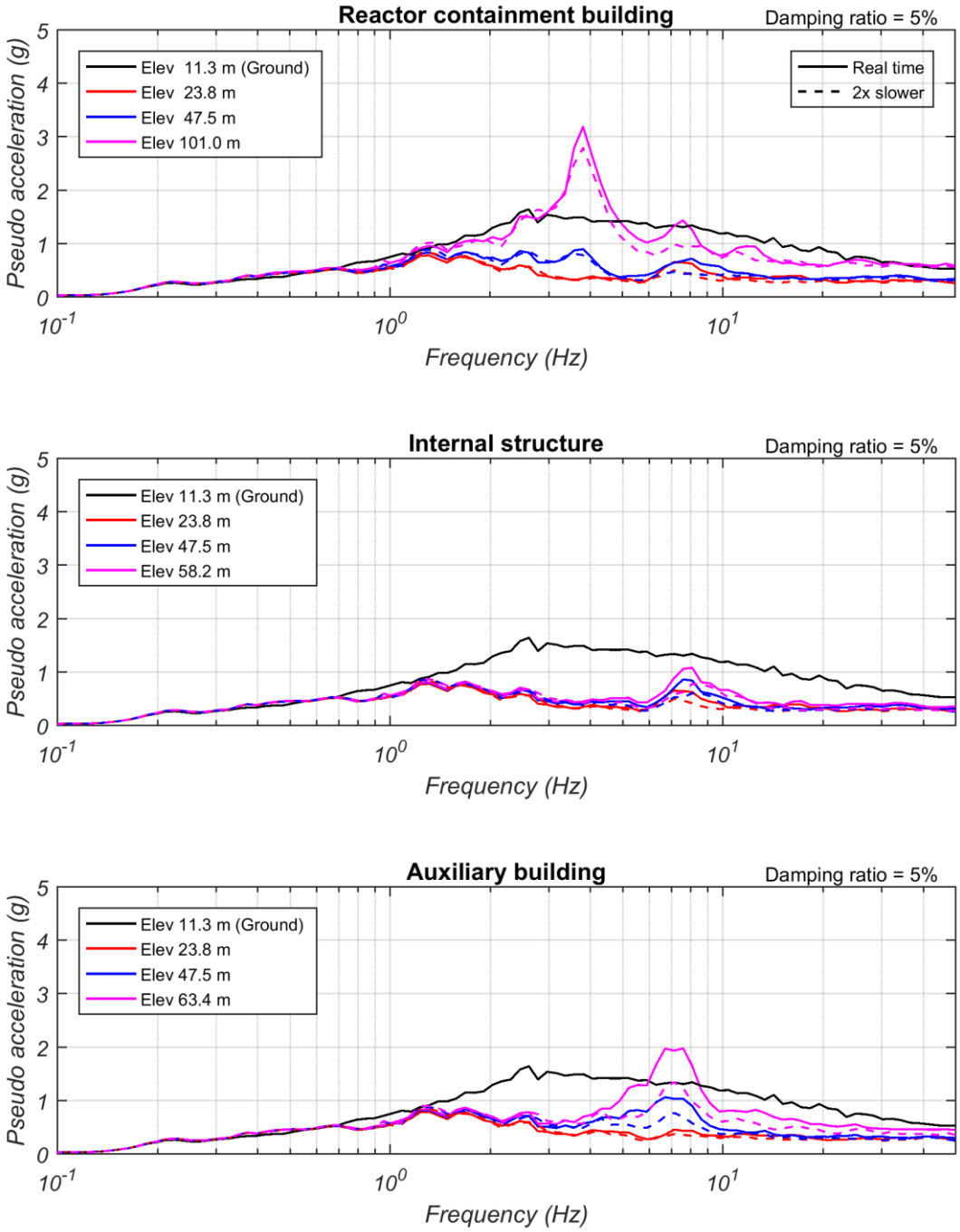

Figure 5-9 Response spectra comparison to test rate (1-D)

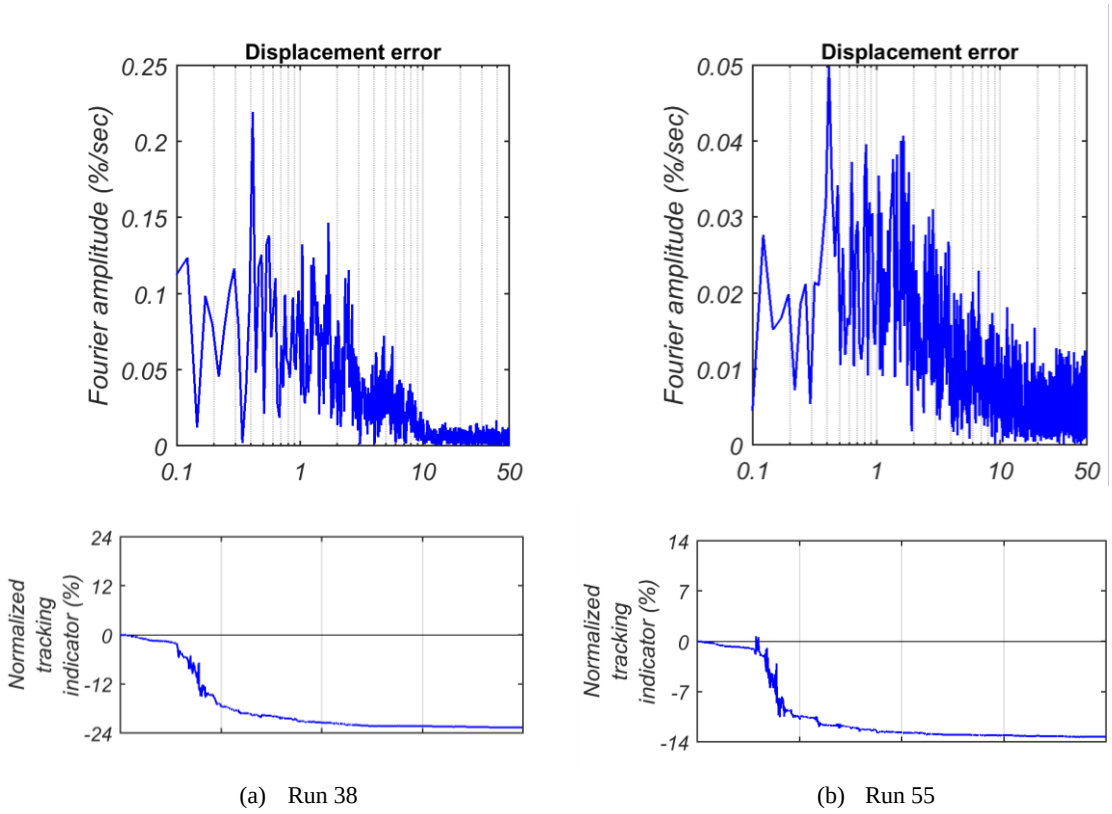

(a) Run 38 (b) Run 55

Figure 5-10 Fourier amplitude of displacement error (top) and normalized tracking indicator (bottom) in run 38 (a) and run 55 (b)

5-3-2-2 Runs 42 and 56 (2-D)

Figure 5-11 presents a comparison of the hysteresis loops for a real-time hybrid simulation (Run 42) with a 2x-slower hybrid simulation (Run 56). The 1-bearing equivalent ANT model was used and the hybrid simulations were conducted with 2-D input. As can be seen from the figure, the maximum displacement demand from the real-time test is 230 mm, which is smaller than the 254 mm demand from the 2x-slower test. Comparing the hysteresis loops, it can once again be seen that shear-force fluctuations in the real-time test are more pronounced than in the 2x-slower test. However, this is less obvious than in the 1-D tests because shear-force fluctuations in one direction, evident in the hysteresis loops, are also caused by perpendicular motion in the other direction. From the hysteresis loop comparison in longitudinal direction, it

can be seen that the loops for the real-time test are shifted to the right as compared to the 2x-slower test. This response produced larger positive displacement demands and a positive instead of a negative residual displacement (2 in for real-time vs. -0.5 in for 2x-slower test). At this point it is unclear why this occurred for the 2-D real-time hybrid test. Comparing the 1-D versus 2-D longitudinal hysteresis loops for the real-time hybrid simulations in Figure 5-2 the same observation can be made; that is, the longitudinal hysteresis loops for the 2-D real-time test (Run 42) are shifted to the right. Because parts of the hybrid testing system had to be restarted right before conducting Run 42 due to a software issue, the most likely cause for this behavior are shear force conditions that were present in the testing system at the start of the hybrid simulation.

The comparison of the shear-force interaction surfaces in Figure 5-11 show that typically the shear-forces in the real-time test are larger than in the 2x-slower test. The maximum shear force in the real-time test is 2,414 kN, which is larger than the 2,235 kN shear force in the 2x-slower than real-time test. This behavior is again mostly caused by inertia force effects in the test setup and test specimen. Hence, the same conclusion can be made for the 2-D tests as for the 1-D tests. The real-time execution of a hybrid simulation has a moderate effect on the hysteresis loops of the LPRB and these effects are mostly caused by inertia forces in the test setup and specimen. The additional inertia force effects tend to increase the LPRB's maximum resisting force.

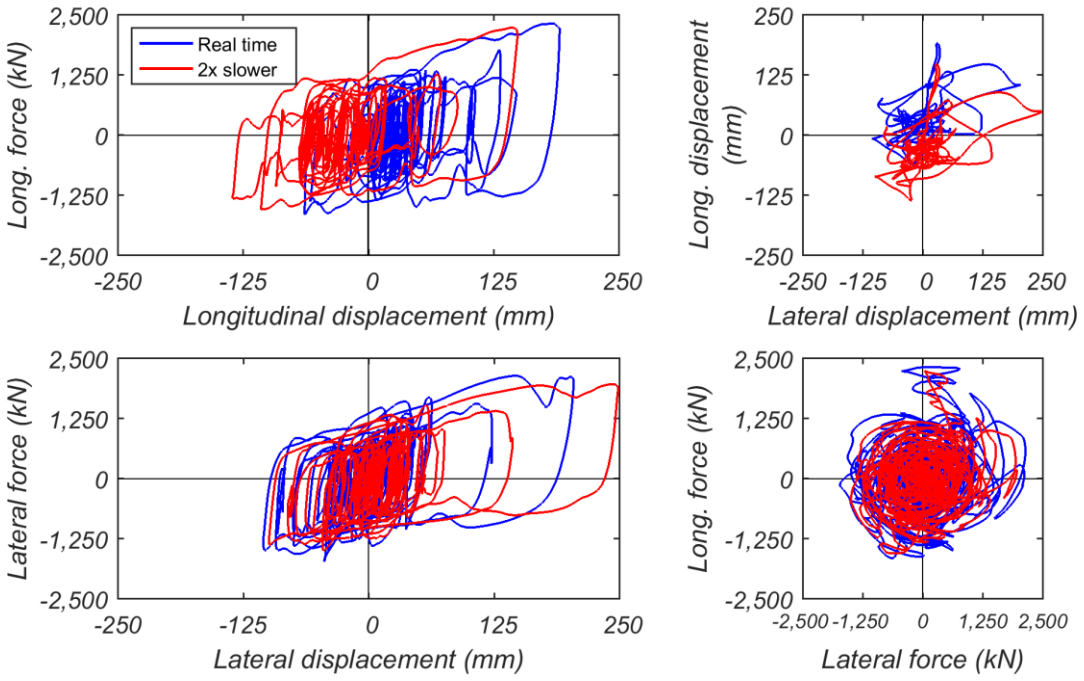

Figure 5-11 Comparison of bearing response to test rate (2-D)

Figure 5-12 compares the response spectra for the real-time and 2x-slower than real-time tests for hybrid simulations with 2-D ground motion input. For frequencies above 2 Hz, the response spectra for the RCB, INS, and ACB are consistently greater for the real-time hybrid simulation than for the 2x-slower hybrid simulation. The real-time hybrid simulation clearly generated more high-frequency excitations that were transmitted through the LPRB bearing into the superstructures. For the real-time test, the spectral amplitude at the first-mode frequency of the RCB is 4.1*g*, whereas the one from the 2x-slower test is 3.3*g*. Similarly, the spectral amplitude at the first-mode frequency of the INS is 1.8*g* for the real-time test and 0.7*g* for the 2x-slower test. For the ACB, the spectral amplitude at the first-mode frequency is 2.7*g* for the real-time test and 1.1*g* for the 2x-slower test. As explained before, these differences can be attributed to the greater dynamic effects and larger experimental errors in the test system experienced during real-time testing.

Comparing Fourier amplitude of the displacement errors as well as error monitor for the two tests (Figure 5-15), it can be seen that the achieved overall tracking performance was fairly similar in the real-time test and the 2x-slower test. Average delays in the real-time test were 6.3 msec in longitudinal and 3.8 msec in lateral direction, whereas in the 2x-slower test they were 3.0 msec in the longitudinal and 5.0 msec in the lateral direction. However, the Fourier amplitudes of the displacement error have a clear peak around 8 – 9 Hz for the real-time test that is not present in the 2x-slower test. The difference in spectral amplitudes is most pronounced around 8 – 9 Hz (corresponding to first-mode frequency for ACB and INS), which could indicate that the vertical-horizontal coupling of the LPRB also contributed to the increase in the floor spectra peaks. It seems that the SRMD had more difficulties in maintaining the constant axial design load on the bearing during the real-time hybrid simulations (especially the 2-D real-time hybrid simulations).

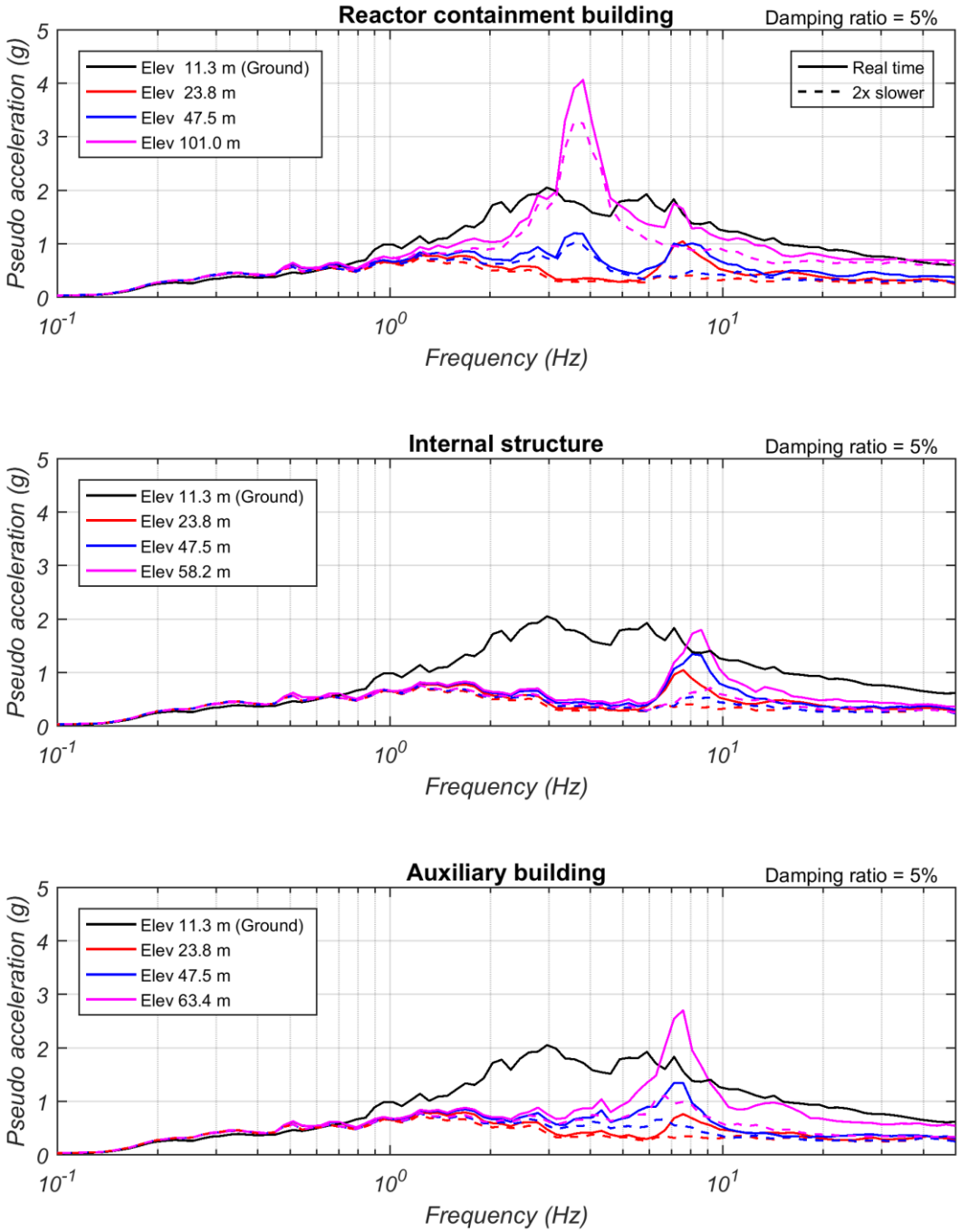

Figure 5-12 Response spectra comparison to test rate (2-D)

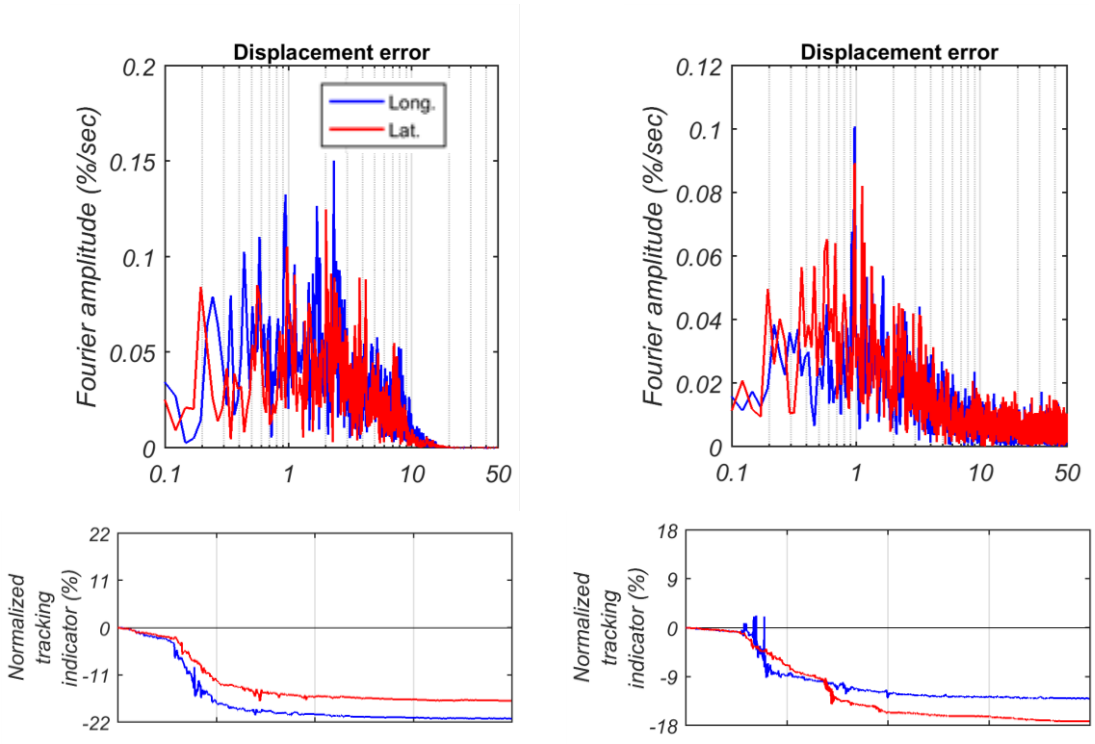

(a) Run 42 (b) Run 56

Figure 5-13 Fourier amplitude of displacement error (top) and normalized tracking indicator (bottom) in run 42 (a) and 56 (b)

5-3-2-3 Runs 46 and 57 (3-D)

Figure 5-14 presents a comparison of the hysteresis loops for a real-time hybrid simulation (Run 46) with a 10x-slower hybrid simulation (Run 57). The 1-bearing equivalent ANT model was used and the hybrid simulations were conducted with 3-D ground motion input. As can be seen from the figure, the maximum displacement demand from the real-time test is 240 mm, which is smaller than the 254 mm demand from the 10x-slower test. Comparing the hysteresis loops, it can once again be seen that shear-force fluctuations in the real-time test are more pronounced than in the 10x-slower test. The comparison of the shear-force interaction surfaces shows that typically the shear-forces in the real-time test are larger than in the 10x-slower test. The maximum shear force in the real-time test is 2,355 kN, which is considerably

larger than the 2,058 kN shear force in the 10x-slower than real-time test. This behavior is again mostly caused by inertia force effects in the test setup and test specimen which are basically nonexistent in the 10x-slower test. Hence, the same conclusion can be made for the 3-D tests as for the 1-D and 2-D tests. The real-time execution of a hybrid simulation has a moderate effect on the hysteresis loops of the LPRB and these effects are mostly caused by inertia forces in the test setup and specimen. The additional inertia force effects tend to increase the LPRB's maximum resisting force.

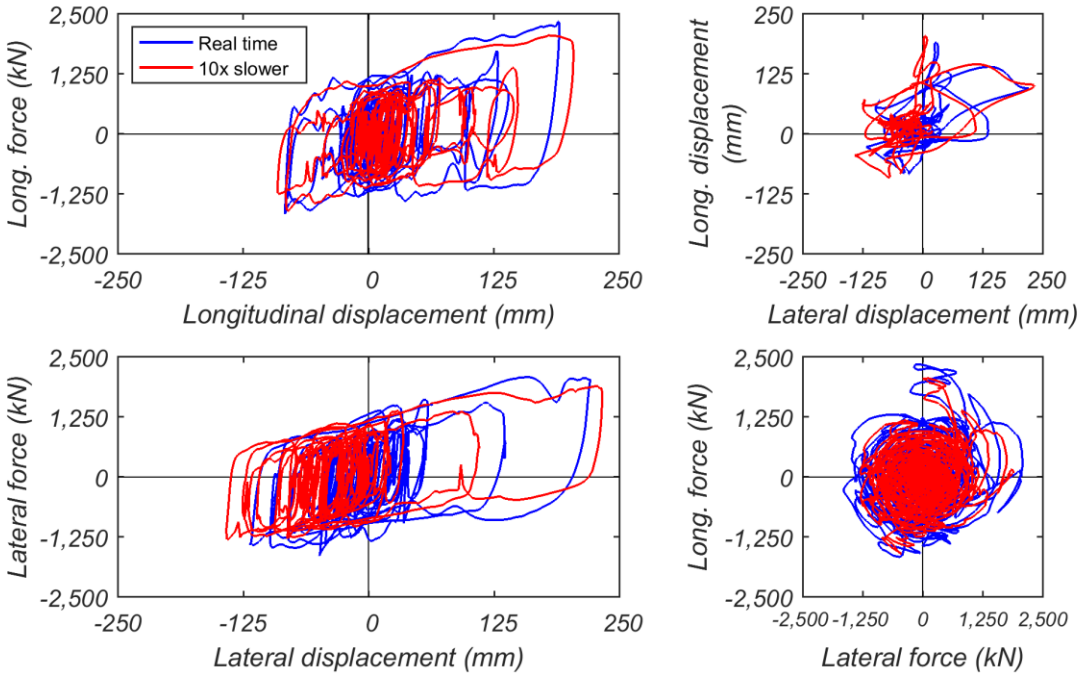

Figure 5-14 Comparison of bearing response to test rate (3-D)

Figure 5-15 compares the response spectra for the real-time and 10x-slower than real-time tests for hybrid simulations with 3-D ground motion input. For the real-time test the spectral amplitude at the first-mode frequency of the RCB is 3.7*g*, whereas the one from the 10x-slower test is 3.0*g*. The spectral amplitude at the first-mode frequency of the INS is 1.5*g* for the real-time test and is 1.6*g* for the 10x-slower test. For the ACB the spectral amplitude at the first-mode

frequency is 2.6*g* for the real-time test and 2.5*g* for the 10x-slower test. It can be seen that around the first mode frequency of the RCB spectral amplitudes are greater for the real-time hybrid simulation than for the 10x-slower hybrid simulation. However, for the INS and the ACB they are nearly identical in both tests. In addition, a new peak in the floor spectra of the INS and ACB can be identified between 15 – 16 Hz (corresponding to higher mode frequencies of the superstructure). This new peak that was not present in the 1-D and 2-D hybrid simulations is caused by the vertical-horizontal coupling of the LPRB and will be discussed in more detail in the next section.

It is very important to note here that the 3-D real-time hybrid simulation (Run 46) had very poor tracking performance for the vertical force controlled degree of freedom. The vertical response of the SRMD machine had considerable lag with the force feedback signal at 90 – 180 degrees out of phase with the force command. In addition, the force feedback was also overshooting by up to 50% in certain instances. This inaccurate response of the SRMD in the vertical direction, especially at higher frequencies, is caused by several issues. Firstly, as described in Chapter 3, the vertical actuators are hydrostatic actuators controlled by a four-stage poppet valve assembly. The vertical actuators do not track as accurately and cannot respond as fast leading to amplitude overshoot and phase roll-off at higher frequencies. Secondly, the control of the vertical degree of freedom is using a cascade controller with the inner loop being in displacement control and the main outer loop being in force control. Force control of servo-hydraulic actuators is very challenging and tracking performance for force controlled actuators is typically not as good as for actuators in displacement control. Given these difficulties it is not surprising that it was not possible to perform 3-D real-time hybrid simulations with the SRMD.

Nevertheless, it was very valuable to try to run a few 3-D real-time hybrid simulations to determine machine performance and assess limitations for these kinds of tests.

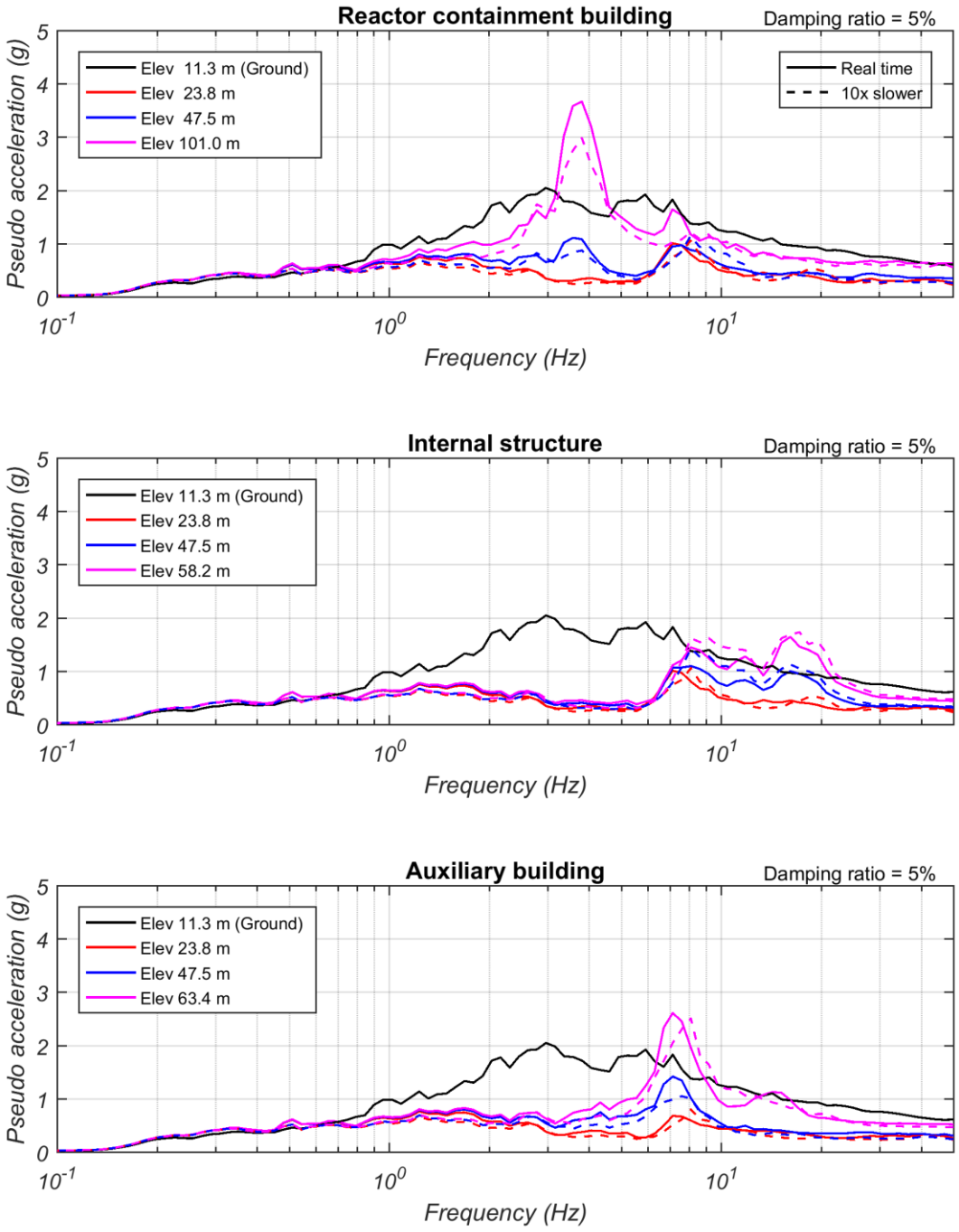

Figure 5-15 Response spectra comparison to test rate (3-D)

Finally, it is also important to assess vertical tracking performance for the 10x-slower hybrid simulation. Overall performance was much better than in the real-time test, but the average delay for the vertical DOF was still 4.8 msec in the OpenSees analysis, which means that the actual delay in the control system was 48 msec (10x more). In addition, there was still a small amount of overshoot happening. To achieve acceptable performance and accuracy in the force controlled vertical DOF a hybrid simulation should be performed at a minimum 10x-slower than real time. It was concluded that it is currently not possible to conduct 3-D real-time hybrid simulations with the SRMD due to insufficient vertical tracking performance. Therefore, results from Run 46 are not considered sufficiently accurate and should not be used in making any conclusions related to the isolated power plant behavior. However, they provide valuable insight in terms of assessing machine performance and limitations.

5-3-3 Influence of Vertical Excitation

5-3-3-1 Runs 56 and 57 (2x- vs. 10x-slower)

Figure 5-16 compares the hysteresis loops obtained from a hybrid simulation without vertical excitation (Run 56) and with vertical excitation (Run 57). The 1-bearing equivalent ANT model was used and the hybrid simulations were conducted 2x-slower than real time (Run56) and 10x slower than real time (Run 57). The hysteresis loops in longitudinal and lateral directions, the horizontal displacement orbits, and the shear-force interaction surfaces are fairly similar except for displacement offsets in both longitudinal and lateral directions. Close observation of the plots demonstrates that the results from the test including vertical excitation show small higher frequency (~10 Hz) shear-force oscillations that are not present in the results from the test without vertical excitation. The oscillations are most noticeable in the lateral

hysteresis loop but can also be seen in the longitudinal hysteresis loop in a few locations on the negative shear-force side. Other differences, especially the different displacement offsets are likely caused by the two different testing rates. Nevertheless, the shear-force oscillations clearly demonstrate the vertical–horizontal coupling that occurs in LPRBs. As the bearing displaces sideways in horizontal direction and the axial force fluctuates (between 3000 kN and 24,500 kN) due to the vertical ground motion input, the shear resistance of the bearing fluctuates as well.

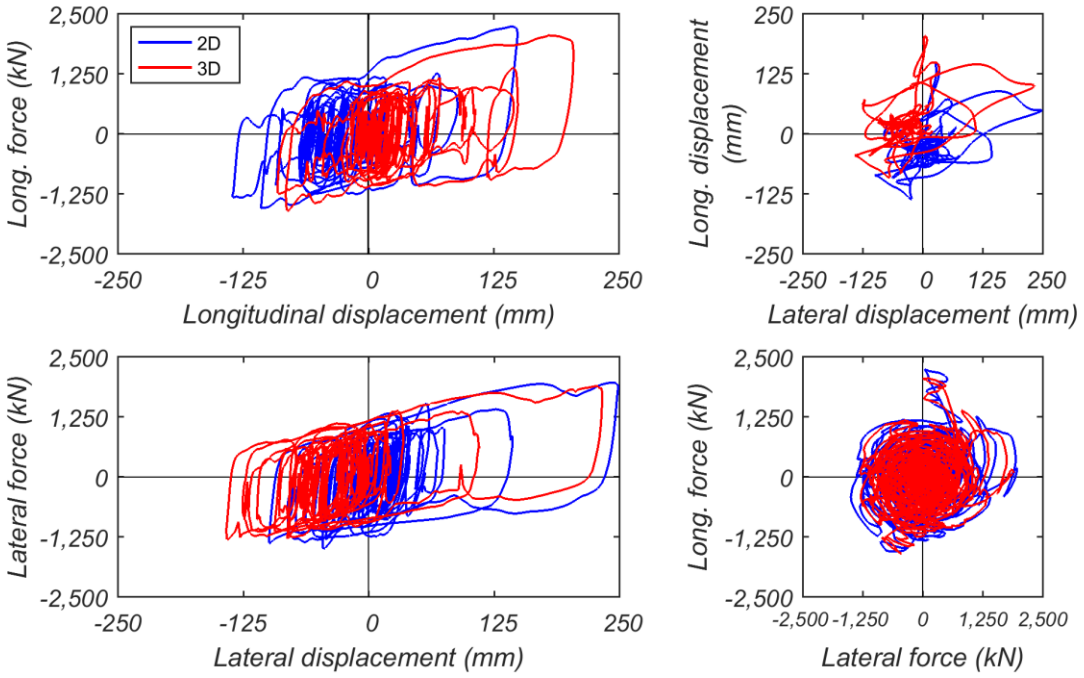

Figure 5-16 Comparison of bearing response to a ground motion with and without vertical excitation (2x vs. 10x slower)

Comparing the floor response spectra for the hybrid simulations with and without vertical excitation (see Figure 5-17), there is a very distinct difference in the size of the spectral acceleration spikes between the two tests. While the peaks occur around the same frequencies, the spectral accelerations from the test including vertical excitation are significantly larger. The differences are most pronounced at the higher frequencies for the INS and ACB. For the INS, the peak spectral acceleration for the test without vertical excitation is 0.7g, whereas the one from

the test including vertical acceleration spikes up to 1.6*g*. The spikes occur at a frequency of ~8.5 Hz, which is very close to the fundamental vertical frequency of the plant superstructure at about 10 Hz. As mentioned in the previous section, the LPRB exhibits vertical–horizontal coupling; this effect becomes most apparent in the floor response spectra, whereas it was barely noticeable in the hysteresis loop plots.

Because the vertical frequency of oscillation is around 10 Hz, the shear-force oscillations caused by the coupling also occurred at around 10 Hz. The first-mode horizontal frequency of the INS is around 8 Hz, which is very close to the vertical frequency of the superstructure. Similarly, the first mode frequency of the ACB is around 7.5 Hz which is also very close to the vertical frequency of the superstructure; hence, the spectral acceleration for the ACB spikes from 1.1*g* for the test without vertical input, up to 2.5*g* for the test with vertical input. On the other hand, the first-mode frequency of the RCB at 3.7 Hz is well separated from the vertical frequency. Hence, the floor response spectra of the RCB are much less influenced by this effect.

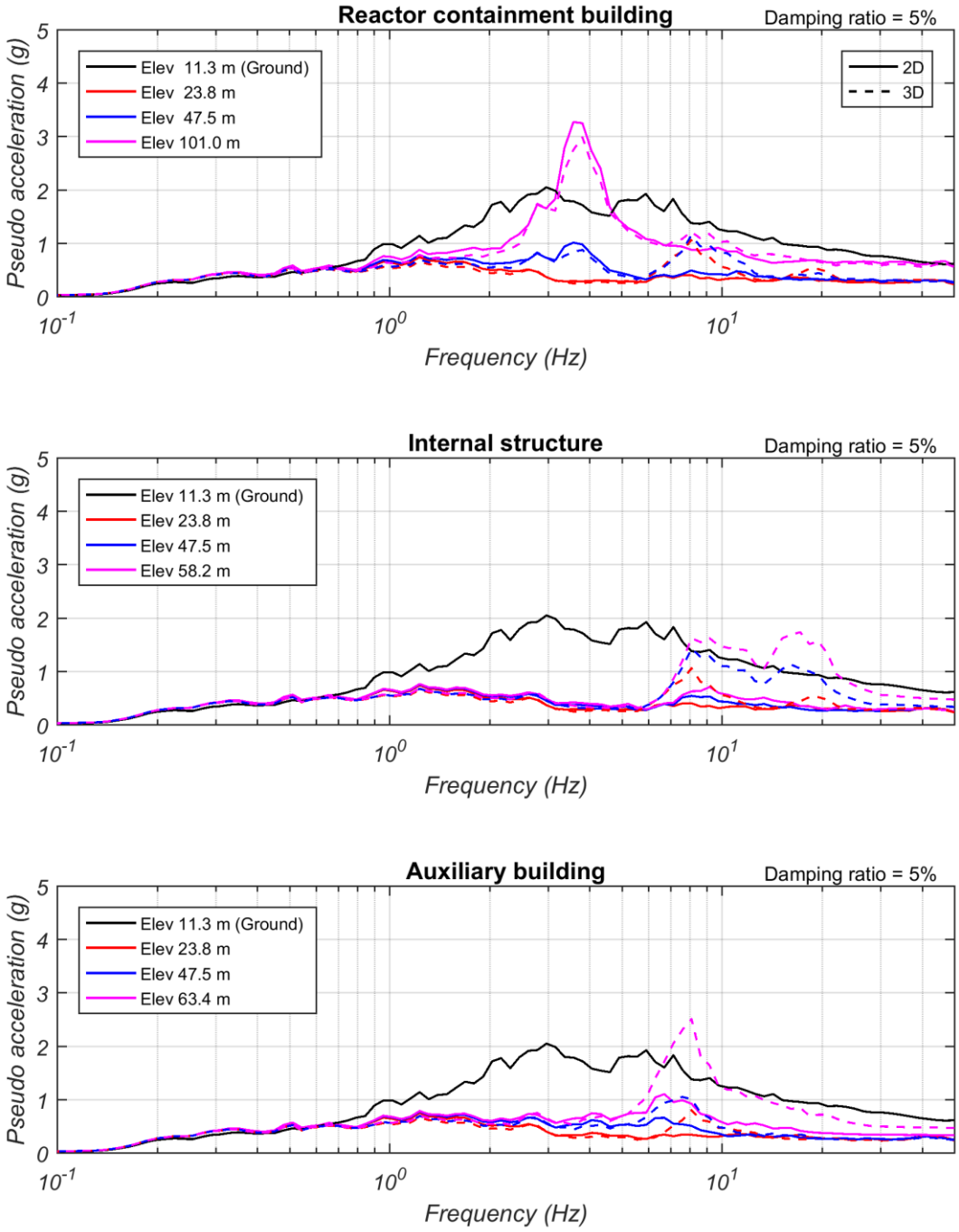

Figure 5-17 Response spectra comparison to a ground motion with and without vertical excitation (2x vs. 10x slower)

5-3-4 Variation due to Different Bearing Discretization Models

5-3-4-1 Runs 56, 166, and 172 (2-D)

Figure 5-18 and Figure 5-19 compare test results from three different hybrid models subjected to 2-D ground motion input. In the first test (Run 56), the 1-bearing equivalent model was used and the hybrid simulation was executed 2x-slower than real-time. In the second test (Run 166), the 5-bearing equivalent model was used with the experimental bearing located under the north-east quadrant of the ACB and the hybrid simulation was also executed 2x-slower than real time. Lastly, in the third test (Run 172) the 486-bearing model was used with the experimental bearing located in the north-east corner of the ACB and the hybrid simulation was executed 15x-slower than real time. The different execution speeds as well as the different locations of the experimental bearing make it somewhat difficult to compare the three models and determine what the effects of the model discretization alone are.

As observed in Figure 5-18, the hysteresis loops in longitudinal and lateral directions, the horizontal displacement orbits, and the shear-force interaction surfaces match fairly well for the 5-bearing equivalent model and the 486-bearing model. However, the isolator response of the 1-bearing equivalent model is somewhat different than the isolator response from the other two models. The 1-bearing equivalent model produced an isolator displacement demand of 254 mm, the 5-bearing equivalent model had an isolator displacement demand of 215 mm, and the 486-bearing model had a similar displacement demand of 204 mm. There are two main reasons that the 1-bearing equivalent model experienced a different response than the other two hybrid models. First, the isolator response in the 1-bearing model was entirely determined by the experimental test specimen, whereas in the other two models the response of the experimental

isolator was mostly dictated by the numerical isolators. Second, for both the 5-bearing equivalent model and the 486-bearing model, the experimental isolator represented a corner location where the isolator is affected by overturning effects. In contrast, for the 1-bearing equivalent model no overturning effects were captured. From these results, it is obvious that the analytical isolator model used in the 5-bearing equivalent model and the 486-bearing model could not capture all the complexities of the experimental response. It is concluded that for hybrid simulations where analytical bearings are used to model some portion of the isolation plane, improved analytical isolator models are necessary, and more effort should be taken during testing to iteratively tune the parameters of improved analytical isolator models as more data becomes available. Additionally, means to further increase computation speeds for the 486-bearing model are needed to perform hybrid simulations at 2x-slower than real time testing rates instead of 15x-slower than real time testing rates.

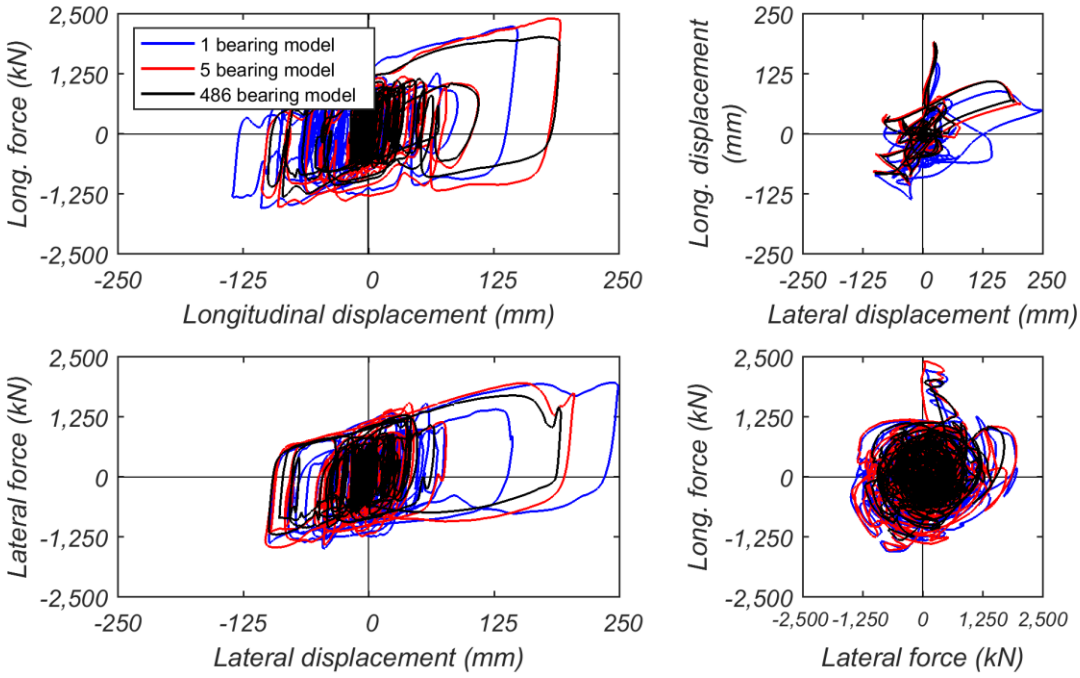

Figure 5-18 Comparison of bearing responses to bearing layout discretization (2-D)

Comparing the floor response spectra in Figure 5-19 results in similar conclusions to those drawn in the previous paragraph. The 5-bearing equivalent model and the 486-bearing model produced floor response spectra for the INS and the ACB that match quite well, while the ones from the 1-bearing equivalent model are significantly smaller. In addition, for the floor response spectra of the ACB a frequency shift occurred of the main spectral acceleration peak around the fundamental period of the ACB. For the 1-bearing equivalent model, the main spectral acceleration peak occurred at a frequency of 3.7 Hz, but for the 5-bearing equivalent model and the 486-bearing model the peak shifted to a frequency of about 3 Hz. At this point it is unclear why this shift was so large. Further investigation of this phenomenon is necessary to determine the cause.

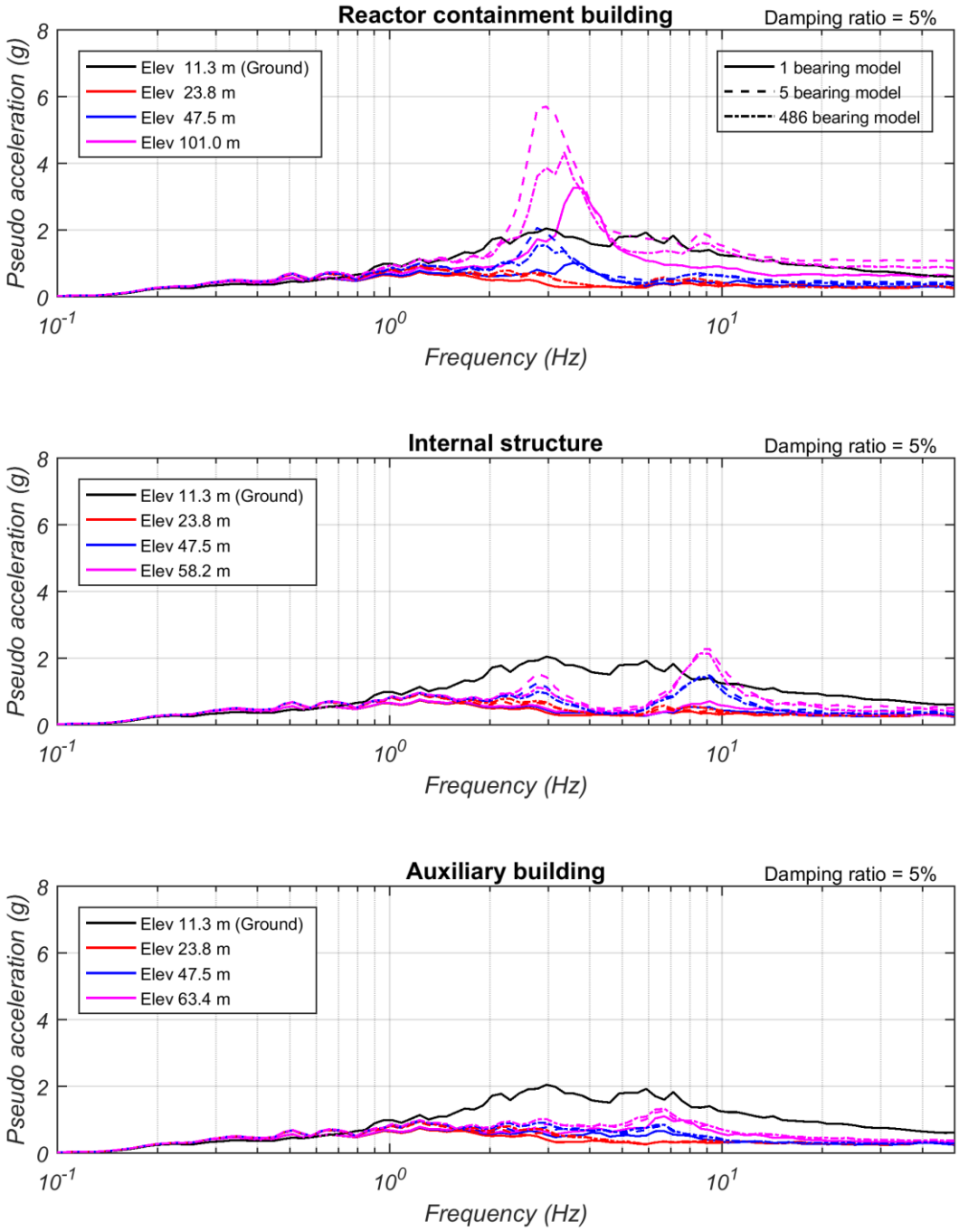

Figure 5-19 Response spectra comparison to bearing layout discretization (2-D)

5-3-4-2 Runs 164, 167, and 171 (3-D)

Figure 5-20 and Figure 5-21 compare test results from three different hybrid models subjected to 3-D ground motion input. In the first test (Run 164), the 1-bearing equivalent model

was used and the hybrid simulation was executed 10x-slower than real-time. In the second test (Run 167), the 5-bearing equivalent model was used with the experimental bearing located under the north-east quadrant of the ACB and the hybrid simulation was also executed 10x-slower than real time. Lastly, in the third test (Run 171) the 486-bearing model was used with the experimental bearing located in the north-east corner of the ACB and the hybrid simulation was executed 15x-slower than real time. As in the previous comparison, the different execution speeds as well as different locations of the experimental bearing make it somewhat difficult to compare the three models and determine what the effects of the model discretization alone are.

As can be seen from Figure 5-20, the hysteresis loops in longitudinal and lateral directions, the horizontal displacement orbits, and the shear-force interaction surfaces match fairly well for the 5-bearing equivalent model and the 486-bearing model, but they do not agree well with the 1-bearing equivalent model. In these 3-D hybrid simulations, the 1-bearing equivalent model produced an isolator displacement demand of 259 mm, the 5-bearing equivalent model reached an isolator displacement demand of 216 mm, and the 486-bearing model had a similar displacement demand of 204 mm. The two main reasons for the discrepancies in the 1-bearing equivalent model response were discussed previously. It should be noted that in these tests, the axial load variations in the 1-bearing equivalent model in the test specimen are only due to vertical ground motion input only while the other two models are capturing overturning effects as well. From these results, it is evident that the analytical isolator model used in the 5-bearing equivalent model and the 486-bearing model is not an accurate presentation of the actual bearing behavior. It is concluded that for hybrid simulations where analytical bearings are used to model some portion of the isolation plane, improved analytical

isolator models are necessary, and time is required during testing to iteratively update the parameters of such analytical isolator models.

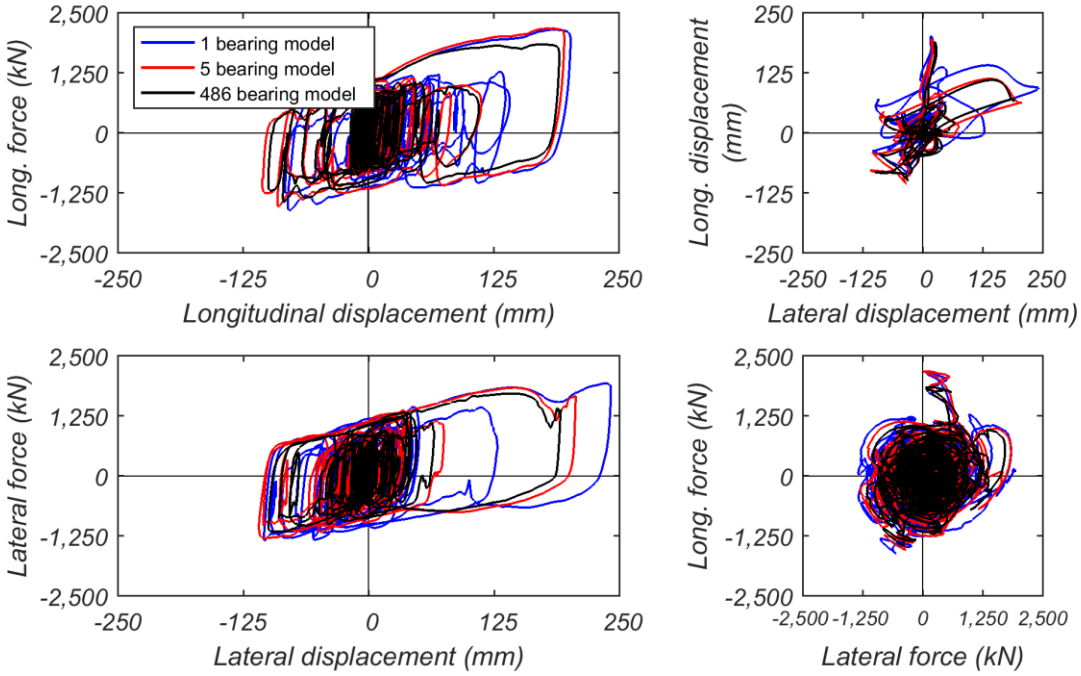

Figure 5-20 Comparison of bearing responses to bearing layout discretization (3-D)

Comparing the floor response spectra in Figure 5-21 results in similar conclusions to those drawn in the previous section.

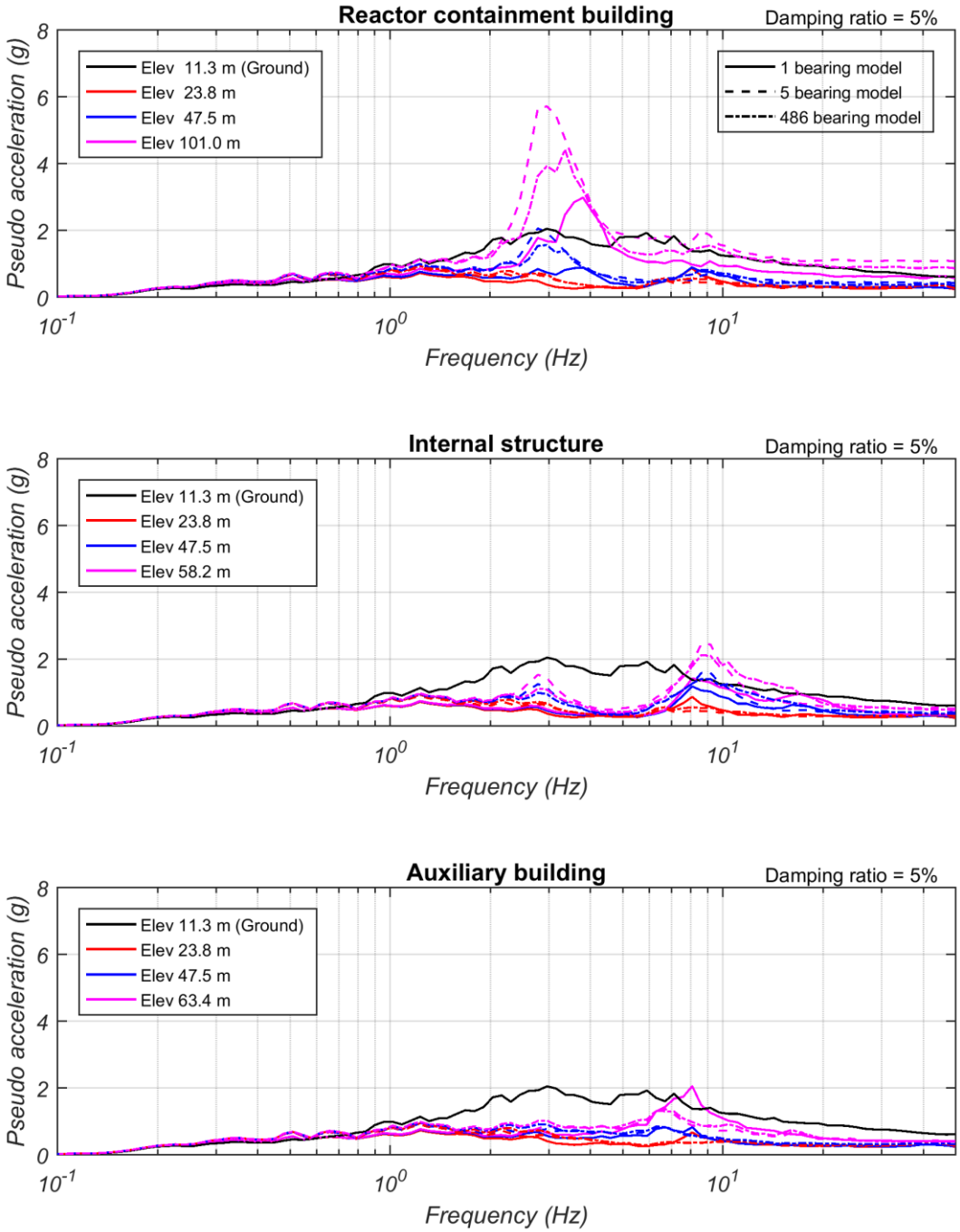

Figure 5-21 Response spectra comparison to bearing layout discretization (3-D)

5-3-5 Bearing Failure Test

Test 253 was performed to characterize the behavior of the LPRB beyond its design level through an elliptical input motion targeting a maximum 580% shear strain. The bearing failed at

approximately 899 mm longitudinal displacement, see Figure 5-22. The peak longitudinal shear force corresponds with 428% shear strain at failure, a factor of 4.3 times the design shear strain. This failure was mainly due to bond failure between the rubber and steel shim (see Figure 5-23) at a very large shear strain.

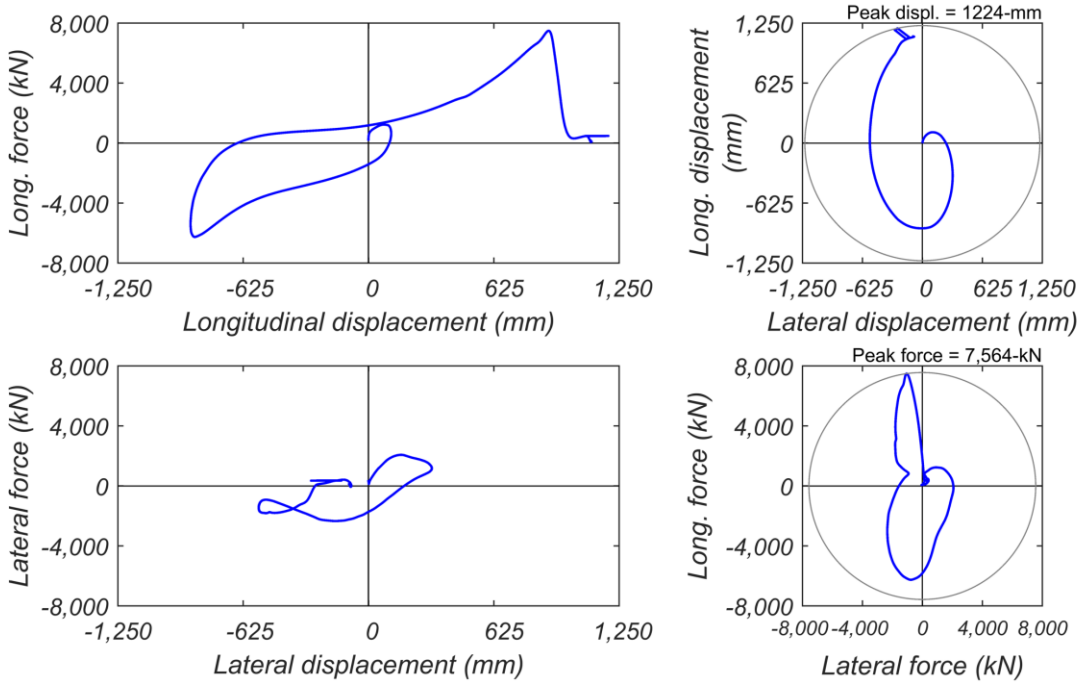

Figure 5-22 Bearing hysteretic response during failure test of UET-2: Run 183 with 16,259 kN axial load

a) (b)

Figure 5-23 Failure of the LPRB (UET-2): (a) deformed bearing under 400% shear strain, (b) ruptured bearing

5-4 Conclusion

The seismic response of seismically isolated NPP structures was examined using hybrid simulation. Different hybrid models were used to examine the behavior of the LPRB bearing and effects on superstructure response.

Overall, the seismically isolated NPP behaved as expected. Base shears and floor accelerations were generally reduced substantially compared to what might be expected for a fixed-base structure (here observed by comparison of floor spectra). However, the tests were able to identify specific differences associated with different bearings, loading conditions, and earthquake excitations.

The performance and accuracy of several different hybrid models of the nuclear power plant structure were assessed. It is concluded that the hybrid model that used one equivalent experimental bearing to represent all the bearings under the plant performed very well in terms of execution speed and accurate results were obtained from 1-D and 2-D tests. However, this model was not able to simulate overturning from the plant superstructure or capture the resulting axial load fluctuations in the bearings. The hybrid model where one equivalent experimental bearing represents one of five bearing groups also performed very well in terms of execution speed. With this model, it was possible to capture and study the effect of axial force fluctuations in the test bearing due to overturning. However, the accuracy of the response of this model is somewhat dependent on the fidelity and accuracy of the analytical bearing elements used to represent the other four bearing groups. The efficacy of the hybrid model where the experimental bearing represents one individual bearing out of all the bearings in the isolation system was limited. In the experimental bearing, the local bearing response under realistic loading was

captured accurately which was able to identify limitations of analytical bearing elements. However, the response of the overall isolation system was entirely dictated by the behavior of the analytical bearing elements. The ability to accurately calibrate the analytical bearing behavior to match the experimental bearing behavior was heavily dependent on the fidelity of the numerical model; in addition, it was time consuming to run. Despite employing a high-performance computing platform, the hybrid model could not be analyzed in real time. A 15x-slower than real-time execution was the fastest hybrid simulation that could be achieved for this model.

Heat generation in the LPRB was larger during 2-D testing than during 1-D testing, causing the yield strength of the lead cores to decrease faster, and leading to larger displacement demands in the hybrid tests. At least 2-D hybrid simulations should be performed to capture bearing demands accurately. Two-dimensional versus 1-D testing also affected floor response spectra, with the 1-D tests significantly overestimating spectral accelerations.

The real-time execution of the hybrid simulations had a moderate effect on the hysteresis loops of the LPRB in comparison to tests 2x times slower than real-time. These changes were mostly caused by inertia force effects.

The LPRB showed substantial vertical–horizontal coupling behavior. Vertical force fluctuations due to overturning effects did not influence significantly the behavior of the LPRB. While conducting 3-D tests did not affect bearing displacement demands in comparison to 2-D tests, it had a major effect on floor response spectra. It is essential to include vertical ground motion input in hybrid testing to accurately predict floor response spectra. Neglecting vertical excitation can significantly underestimate horizontal spectral accelerations around the vertical frequency of the isolated plant.

References

[1] Schellenberg, A. H., Sarebanha, A., Schoettler, M. J., Shao, B., Mosqueda, G., and Mahin, S. A. (2016): Hybrid Simulation of Seismic Isolation Systems applied to an Archetype Nuclear Test (ANT) Power Plant under Design Level Excitation. PEER,

[2] Shao, B., Schellenberg, A. H., Schoettler, M. J., and Mahin, S. A. (2016): Numerical Analysis of Seismic Isolation Systems applied to an Archetype Nuclear Test (ANT) Power Plant under varied Seismic Conditions and Aircraft Impact Loading. Technical Report PEER, Pacific Earthquake Engineering Research Center, University of California, Berkeley, Berkeley, CA.

Chapter 6 Seismic Response of Base Isolated Nuclear Power Plants Considering Impact to Moat Walls

6-1 Introduction

In the U.S., design provisions for nuclear facilities limit the displacement of the seismic isolation system by a stop or moat wall, that is intended to prevent failure of the bearings [1]. Design guidelines aim to prevent impact by specifying a required minimum clearance to stop (CS) with a low annual frequency of exceedance. For example, ASCE 4 [2] requires a CS no less than the 90th percentile displacement demands corresponding to Beyond Design Basis Earthquake (BDBE). Use of a CS below the specified value requires analysis to demonstrate that impact will not result in unacceptable performance of the NPPs. Importantly, the consequences of impact or procedures to mitigate these effects have not been examined for NPPs. In this chapter, a moat wall model suitable for parametric studies is proposed to capture the impact

forces and effects on the isolated NPP. The moat wall model is applied to simplified isolated plant model and variable characteristics of the isolation hardware and moat wall properties are considered to capture parameters that influence impact response. A more detailed model for isolated NPP is presented and studied in the following chapter.

6-2 Simplified Model of Nuclear Power Plant

This study focuses on modeling the effects of moat wall impact on seismic response of base isolated NPPs. A simplified superstructure model is considered for the NPP, consisting of a lumped-mass stick model for 1-D horizontal earthquake shaking. The model of the NPP and the design of the isolation system is largely based on current design efforts for a standardized isolated APR1400 plant model. The dynamic properties of the model listed in Table 6-1 are similar to the reactor containment building (RCB) of the APR1400 [3-5]. This model was found suitable for these studies as it could capture some higher mode effects in the superstructure that can be excited by the impact force. The mass of the structure and the secondary systems were lumped at discrete locations at select levels (Figure 6-1). The weight of the structure consisting of the representative RCB is 70,000 tons and the total weight of the structure is 118,000 tons considering the base mat above the isolation system. The thickness of the base mat is 3 m and assumed to be rigid in this model. The isolation system model includes three isolators beneath each of the structural stick model connections to the foundation. For this study considering only the shear behavior of the bearings, each was modeled as a bilinear hysteretic horizontal spring. Modeling parameters considered for the isolation system are provided in Table 6-2.

Throughout this study, the response is evaluated at an elevation near the ground level, which is at an elevation of about 23m considering the basement depth. This location is examined

to compare the various model configurations considered. The structural model was implemented in OpenSees [6] to make it more conducive to numerous parametric studies and take advantage of its large element library for modeling complex and nonlinear behavior of the structure including impact. As discussed next, a moat wall model is proposed and added to the NPP to capture the impact forces at large displacements.

Table 6-1 Modal frequencies for isolated simplified NPP (2-D)

Mode	***Frequency (Hz)***	***Direction***
1	0.50	Isolation – Horizontal Translation
2	1.58	Isolation – Vertical Translation
3	4.27	RCB - Horizontal Translation

Table 6-2 Properties of the entire isolation system using Lead Rubber Bearings (LRB)

Bearing model parameters			
Effective stiffness (K_{eff})	1187.65 ton/cm	Post elastic stiffness (K_2)	572.01 ton/cm
Lead yield force (Q)	12928.30 ton	Initial stiffness (K_1)	5720.1 ton/cm
Yield Displacement (D_y)	2.51 cm	Yield force (F_y)	14364.8 ton

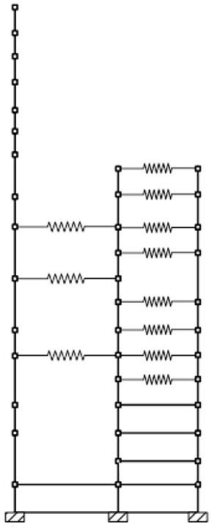

Figure 6-1 Lumped mass model for RCB

6-3 Moat Wall Model

The seismic design of isolated NPPs with a CS below the specified value will require analysis considering impact to the moat wall or stop. A moat wall model for impact analysis is proposed in efforts towards developing the necessary tools to examine the consequences of impact on the NPP. The stop can be constructed in the form of a moat wall around the basement of the NPP with this study considering only 1-D horizontal response. Modeling of the moat wall as the stop requires consideration of the reinforced concrete wall and soil backfill resistance in the structural model as well as localized impact behavior. While previous studies have examined impact for regular buildings both experimentally [7, 8] and numerically [9, 10], the impact behavior of a NPP can have different characteristics due to its potential size scale [11]. The thickness of the base mat and moat walls considered here are loosely based on preliminary designs for the seismically isolated APR1400 with parameters varied to capture a wider range of behaviors. Figure 6-2 shows a schematic of the basement isolation level of the considered NPP and the surrounding moat wall with dimensions considered in this study. The approach taken to develop the moat wall impact model is based on past experimental studies on impact at smaller scales, previous analytical work, and supplementary finite element analysis to gain insight on impact between a massive wall and structure as considered here. In this study aimed at studying the effects of seismic pounding in NPPs, different (CS) values were assumed to examine the effect of this parameter.

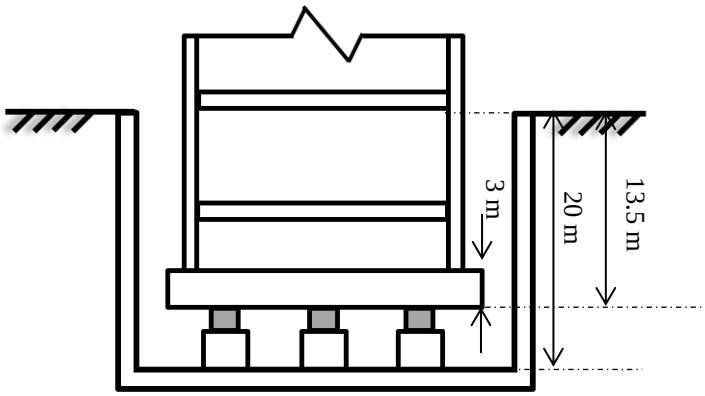

Figure 6-2 Schematic view of NPP with moat wall and backfill soil

Studies of pounding in base isolated structures has been mainly analytical with various approaches used to model contact based on small scale experimental verification [12]. Parameters for modeling the behavior of the moat wall with soil backfill under impact forces at the scale considered here is limited in the literature, particularly for the case of large contact areas. To gain insight and better estimate the properties of the moat wall under impact forces, finite element analysis were performed using LS-Dyna [13]. Impact between the slab and the moat wall was examined in detail by modeling a unit width (1 ft. [0.3048 m]) of the slab and moat wall while assuming different impact velocities to the slab. It should be noted that the backfill soil was not included in these detailed finite element simulations since the primary purpose was to examine the contact interface. This structural model was composed of the structural components and the contact surface as described below.

1. *Moat wall and mat foundation*: In the finite element analysis, the moat wall was modeled as a reinforced concrete wall with solid elements for concrete with constant stress element formulation and beam elements for reinforcement bars. The material models MAT_WINFRITH_CONCRTE (084/085) and MAT_PLASTIC_ KINEMATIC (003) were used to model concrete and steel respectively. To constrain

the reinforcement bars into the concrete, the *Lagrange in Solid* constraint was used. It should be noted that in cases where the concrete undergoes severe damage, this method may not be suitable. Modeling details for the moat wall such as dimensions, material properties, and reinforcements are described in detail in the next section.

2. *Impact between the base mat and moat wall*: Structural poundings can be modeled numerically by defining contact between colliding structural objects. One approach to model contact in LS-DYNA is to use penalty base approach. In this case, when a penetration is detected, a force proportional to the indentation depth is applied to resist and ultimately eliminate the penetration [13]. The default penalty stiffness at the contact interface depends on the element volume, contact segment area, and material properties. The *CONTACT_AUTOMATIC_SURFACE_TO_SURFACE contact card in LS-Dyna was used here to model the impact between the base mat and the moat wall.

The LS-DYNA simulation results were primarily used to understand the behavior of the moat wall and develop a macro model considering impact. These analyses indicate the deformation due to impact of a moat wall at this scale and configuration does not follow the previous assumption of modeling the moat wall as a cantilever column with non-linear behavior concentrated at its base due to an impact forces modeled as a transverse point load [10]. Therefore, a new model was proposed to be able to capture the observed behavior of the moat wall with a larger impact surface as observed in the finite element simulations (Figure 6-3). The macro model consists of a Hertz damped spring model for the impact interface, elastic beams and nonlinear rotational springs modeling the moat wall force-deformation behavior, and springs to capture the backfill soil contributions. This macro element has an elastic section along the height

of the moat with non-linear rotational springs at the base, top and bottom contact points of the thick mat foundation. The rotational springs are placed where non-linear behavior of the moat is expected as indicated by the deformed shape and largest strains observed in the finite element simulations. Two circles at different elevations represent the masses of the moat wall and the backfill soil and are connected using compression only springs.

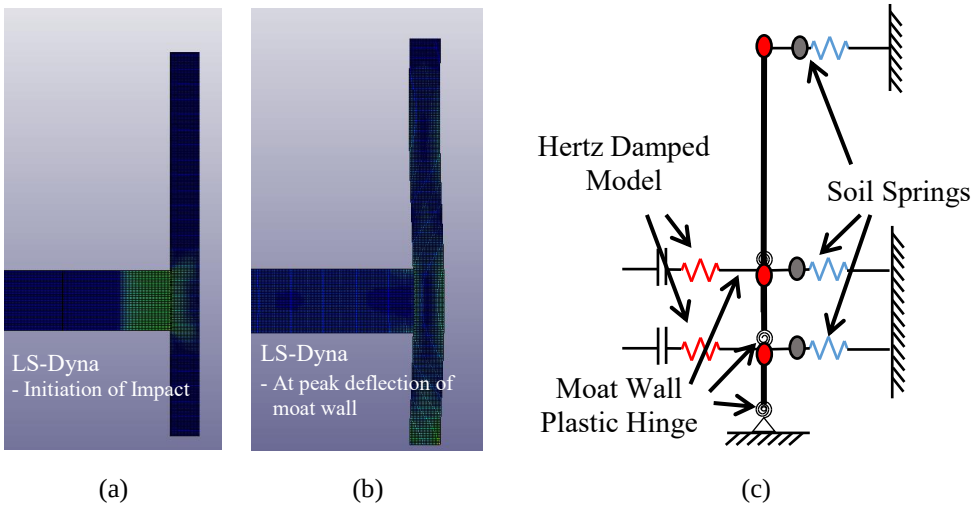

(a) (b) (c)

Figure 6-3 Slab and moat wall deformed shape modeled in LS-Dyna (a and b), and proposed macro model to capture impact in OpenSees (c)

For the parametric studies investigating the effects of impact, the components of the macro element were modeled using existing elements in OpenSees and are listed below. A macro element was implemented on each side of the simplified NPP 2D model to capture the effects of impact to the moat wall. Details on modeling assumptions are described in the sections that follow.

6-3-1 Moat wall

For this study, the moat wall was assumed to be 20 m (63 ft.) in height by 1.524 m (5 ft.) thick, and 48.7m (160 ft.) wide which surrounds the base mat of the isolated structure at the

specified clearance. To consider the potential for damage to the wall, the nonlinear behavior was estimated assuming confined concrete for the core material ($f_c' = 34\ Mpa$) and grade 60 steel reinforcement. The longitudinal reinforcement ratio (ρ_s) was assumed to be 0.075 and shear reinforcement at 0.0762 m (3 in.) spacing was considered. The moment-rotation behavior for the assumed wall section is shown in Figure 6-4. This moment rotation behavior was used to model nonlinear rotational springs used in the OpenSees model to capture the response of plastic hinges along the height of the moat wall. The mass of the moat wall was distributed on three nodes along the height of moat wall based on their tributary lengths. In OpenSees, *elasticBeamColumn* elements were used with *zerolength* rotational springs elements at locations with largest bending strains to capture plastic hinging behavior.

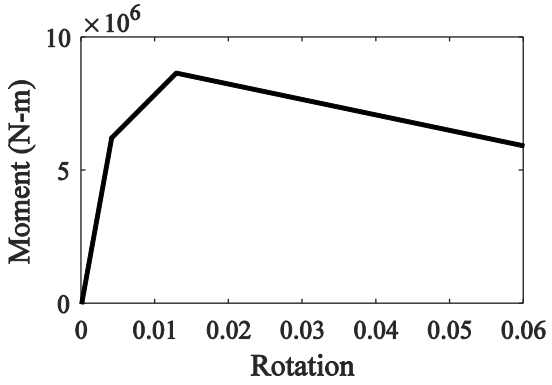

Figure 6-4 Moment rotation for 0.3048 m (1 ft.) width of the wall

6-3-2 Soil Model

The backfill soil was modeled using the Hyperbolic Force Displacement (HFD) model developed by Duncan and Mokwa [14] and Shamsabadi et al. [15]. In OpenSees, the *HyperbolicGapMaterial* model based on the HFD was used in the backfill soil springs. These elements require the ultimate passive resistance, initial stiffness, and unloading/reloading

stiffness of the soil. The resisting force (F) in the HFD model for a given displacement *x* with initial stiffness (K_{max}) and maximum passive resistance (F_{ult}) is given by

$$F(x) = \frac{x}{\frac{1}{K_{max}} + R_f \frac{x}{F_{ult}}} \qquad (6-1)$$

Past numerical studies and experimental tests on bridge abutments with backfill soil were found to be relevant to modeling the backfill soil for this study. A study by Wilson and Elgamal [16] tested a series of large scale abutments with different heights and reported the non-linear force displacement of the backfill soil under passive condition for different soil properties. The properties for Soil Type T2 used in these experimental tests were selected to represent the stiff backfill soil with following properties including: angle of friction, $\Phi = 46°$; soil density, $\gamma = 20.6$ kN/m^3; cohesion, c = 14 kPa; and elastic modulus, E = 40000 kN/m^2. It should be noted that NPPs located on rock sites may have stiffer soil conditions and this will be examined through parameter variations presented later.

Wilson [17] reports the maximum stiffness and ultimate passive force of the soil for varying heights of an abutment wall and for different soil types. Tests were conducted for eight different heights of abutments up to 5 m. The reported data from these large scale experimental tests was used to extrapolate the properties of the soil representative of the 20 m deep moat wall. A logarithmic and a parabolic fit were assumed based on the available range of data. These properties were then used to calculate the stiffness and ultimate force of the backfill soil for given height of the moat wall. Figure 6-5 shows the maximum stiffness and ultimate force of the backfill soil measured from experiments and the extrapolated values for the HFD model at different moat wall heights. A spot check is conducted later to verify that the extrapolation is reasonable.

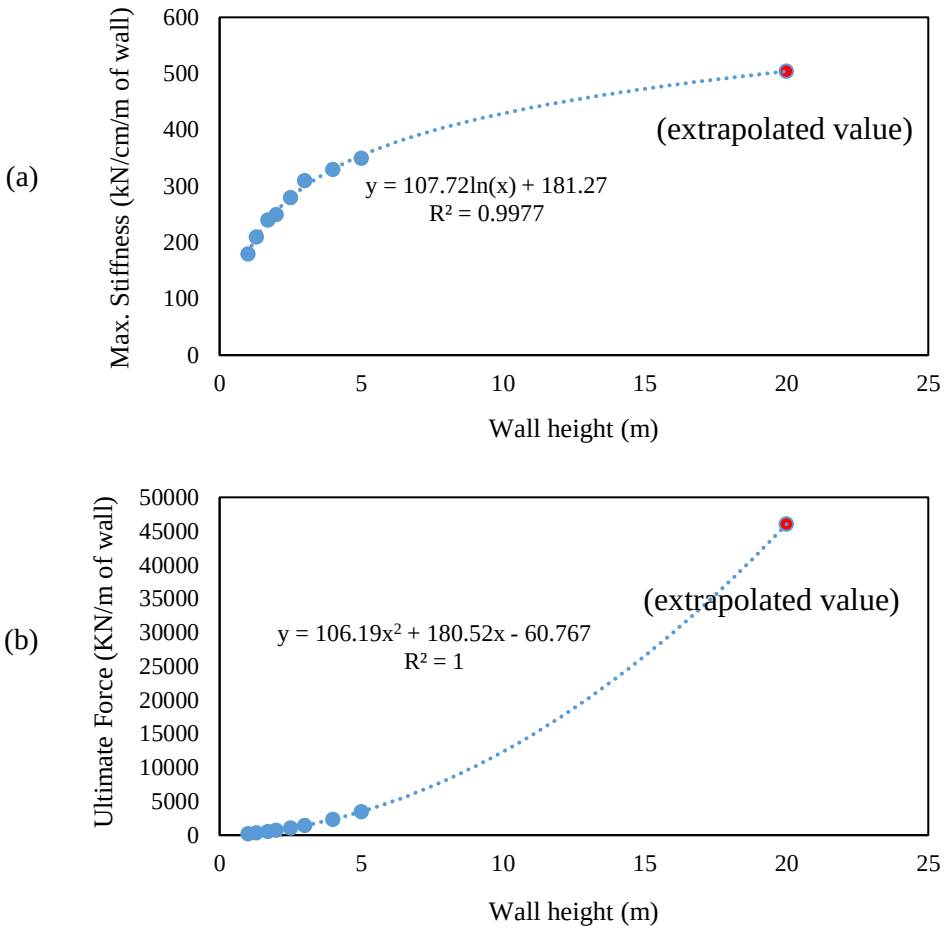

Figure 6-5 (a) Maximum stiffness and (b) ultimate force for HFD model (Soil type: T2)

The total ultimate force was divided within the soil spring in the moat wall macro model using linear shape functions at each horizontal degree of freedom that captures the tributary length and pressure increase with soil depth (Figure 6-6). It should be noted that to calculate the ultimate force for each spring, the shape function was multiplied by the increments of ultimate force. The calculated parameters for OpenSees model are listed in Table 6-3.

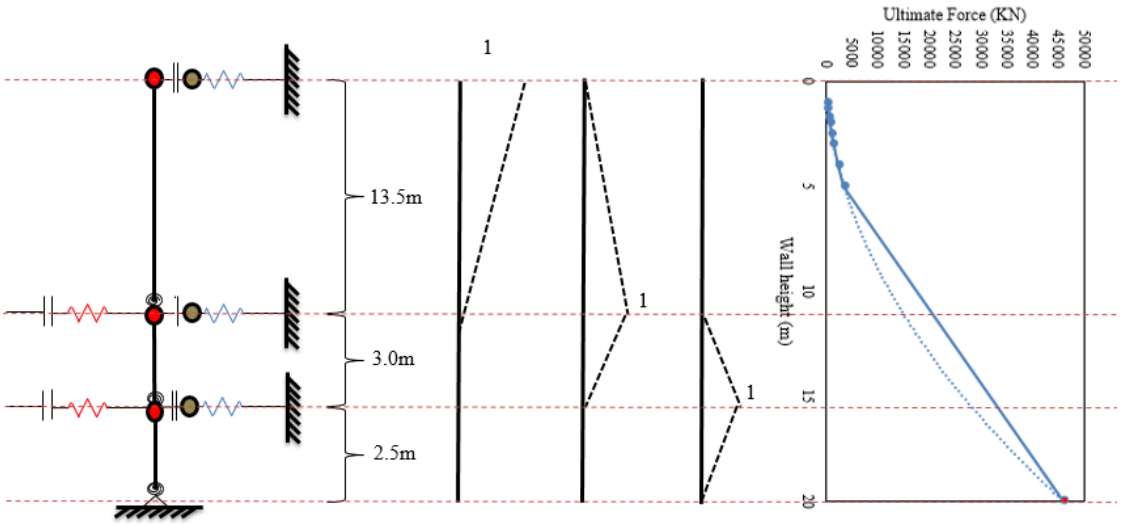

Figure 6-6 Calculation of corresponding ultimate forces for soil spring

Table 6-3 Calculated parameters for unit width soil springs in OpenSees

K_{max} (kN/cm/m of wall)	
All three springs	492.40
F_{ult} (kN/m of wall)	
Top spring	7813.07
Middle spring	19581.10
Bottom spring	10153.34
Total Force	37547.52

- Unloading/reloading stiffness (K_{ur}) = ($10\times K_{max}$)
- Failure ratio (R_f =1.0)

Rankine's theory [18] was used to calculate the ultimate passive soil strength and compare to the extrapolated values above for total ultimate force of the backfill soil. Rankine's theory only requires the soil friction angel (Φ) to calculate Rankine's coefficient (K_p) to be used in calculation of the ultimate passive force of the backfill soil given by:

$$K_p = \tan^2\left(45 + \frac{\Phi}{2}\right) = \frac{1+\sin\Phi}{1-\sin\Phi} = 8.4344 \qquad (6-2)$$

$$P_p = \frac{1}{2}K_p \times \gamma \times H^2 = 34749.9\ {}^{kN}/_{m} \qquad (6-3)$$

There is an 8% difference between the passive ultimate force of the backfill soil estimated using Rankine's method and the value extrapolated for a 20 m deep wall indicating this approach is reasonable.

The three soil springs in the moat wall were modeled using the force-displacement relationships in Eq. 6-1 and the parameters listed in Table 6-3. Note that a large displacement is required to reach the ultimate passive force of the backfill soil and form a failure plane. The required displacement to mobilize the entire soil on the failure plane for the backfill soil is much larger than maximum expected penetration of about 0.609m [2 ft.]). An area with thickness of 0.609 m and 20 m height (same as height of the moat wall) per width of the wall was conservatively assumed as dynamic soil mass and distributed based on tributary lengths of each node along moat wall's height (Figure 6-7). It will be shown later that the effective soil mass does not have much influence on the impact effects on the superstructure.

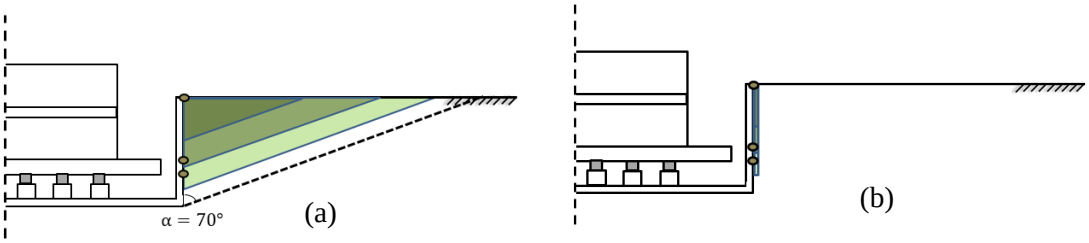

Figure 6-7 Dynamic soil mass consideration - (a) passive failure plane and (b) 0.609m assumed thickness for soil mass

6-3-3 Impact Model

Modeling of the impact interface during structural impact has been mainly based on the Hertz model, originally proposed for static contact of two bodies [19]. The contact force is based

on the relative indentation of two bodies considering their elastic properties and geometry. The contact force is captured with a nonlinear spring of stiffness, K_h given by

$$K_h = \frac{4}{3\pi}\left(\frac{1}{\lambda_1+\lambda_2}\right)\sqrt{\frac{R_1R_2}{R_1+R_2}} \qquad (6-4)$$

for two colliding spheres with radius of R_1 and R_2, or

$$K_h = \frac{4}{3\pi}\left(\frac{1}{\lambda_1+\lambda_2}\right)\sqrt{R_1} \qquad (6-5)$$

for a colliding sphere of radius R_1 to a massive plane surface. The parameter λ_i is a material property related to E_i (Modulus of Elasticity) and ν_i (Poisson's Ratio) and calculated as:

$$\lambda_h = \frac{1-\nu_i^2}{\pi\, E_i} \qquad (6-6)$$

In the case of colliding bodies other than spheres, an equivalent sphere radius could be used to calculate the impact stiffness.

The original Hertz contact law predicts the impact force, but does not capture the energy dissipation due to impact. An improved version of the modeled was introduced with a nonlinear damper in conjunction with the Hertz Spring [20] (Figure 6-8). In this model, the contact force is given by:

$$F_c = K_h\delta^{3/2} + \xi\delta^{3/2}\dot{\delta} \qquad (6-7)$$

where $\dot{\delta}$ is penetration velocity and ξ is the damping coefficient and prescribed as a function of the coefficient of restitution (e), hertz stiffness, and penetration velocity as follows:

$$\xi = \frac{8}{5}\frac{K_h(1-e)}{e\dot{\delta}} \qquad (6-8)$$

For implementation in OpenSees, the ImpactMaterial based on an approximation to the Hertz damped model proposed by Muthukumar and DesRoches [20] was used. This model calculates initial and secondary stifnesses for a bilinear spring such that the dissipated energy during a pounding event for the maximum indentation is the same as energy dissipated in the Hertz damped model for the same indentation. Hertz stiffness and damping coefficient were calculated per unit width of the moat wall using equations 6-5 and 6-8. The calculated value for horizontal impact stiffness is about 250 times more than the equivalent stiffness of the moat wall and backfill soil. To calculate the properties of the impact material, coefficient of restitution (e) was assumed to be 0.8 and ratio of yield displacement over maximum displacement (a) was assumed to be 0.1. Also, based on previous studies the maximum indentation into the material was assumed to be 0.254 cm (0.1 in). The calculated impact stiffness of the impact material was divided evenly between the top and bottom impact springs. A limitation of the bilinear model is that if the initially assumed indentation is under-predicted, the impact force will be under-predicted since the model lacks the hardening characteristics at larger displacements.

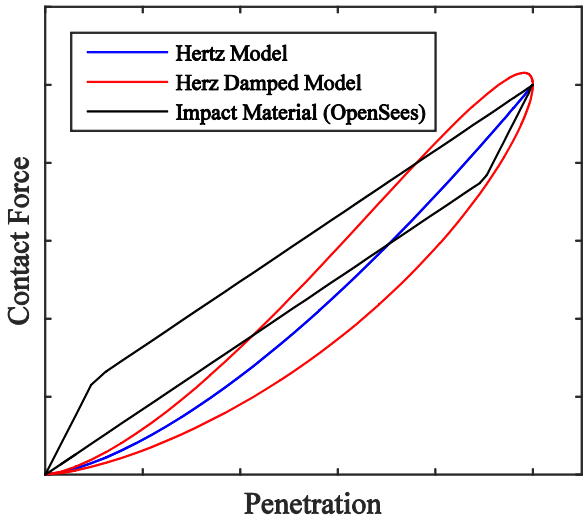

Figure 6-8 Contact force-penetration relation for Hertz, Hertz Damped model and Impact material in OpenSees

6-3-4 Sensitivity Analysis

Sensitivity analysis for modeling parameters of the Hertz stiffness value and effective mass of the concrete moat wall and backfill soil were conducted since there is little guidance on selecting these parameters. Variation in Hertz stiffness over a range of 0.1 to 10 and effective mass range of 0.5 to 10 times of their calculated values were considered. For these various cases, the resulting change in the penetration, acceleration and floor response spectra are presented. These sensitivity studies are mainly intended to examine that the parameters assumed for the impact model are appropriate given the lack of experimental data and identify parameters that should be further evaluated.

6-3-4-1 Hertz Stiffness

Seven different values were considered to study the sensitivity of the structural response to the impact stiffness value. Multipliers of 0.1, 0.2, 0.5, 1.0, 2.0, 5.0, and 10 times were applied on the values calculated for impact stiffness following recommendations for the Hertz model. Results of these simulations under Loma Prieta ground excitation for intensity level of 1.0g and clearance to stop of 0.672m (see section 6-4 for more details) are presented in Figure 6-9 and Figure 6-10.

Figure 6-9 shows the displacement time histories of the base isolation layer for the NPP and the acceleration time histories at ground level in the superstructure around the time of impact for the different values of Hertz impact spring stiffness considered. As shown, a change in the impact stiffness by factors ranging from 0.1 to 10 resulted in ±5% variation in the penetration into the moat wall. This is expected since the Hertz model is intended to capture mainly the local indentation into the material and not the global deformation of the moat wall. These results

indicate that the peak displacements following impact of the superstructure are not sensitive to the assigned value for horizontal impact stiffness. The difference in displacement response from the change of impact stiffness is more pronounced in the subsequent peak in the opposite direction. This can be important due to the potential rebound effect if the structure impacts the opposite side wall. The peak accelerations show slightly more variation in response with the larger stiffness values causing more pronounced higher mode vibrations after the impact as seen in the accelerations.

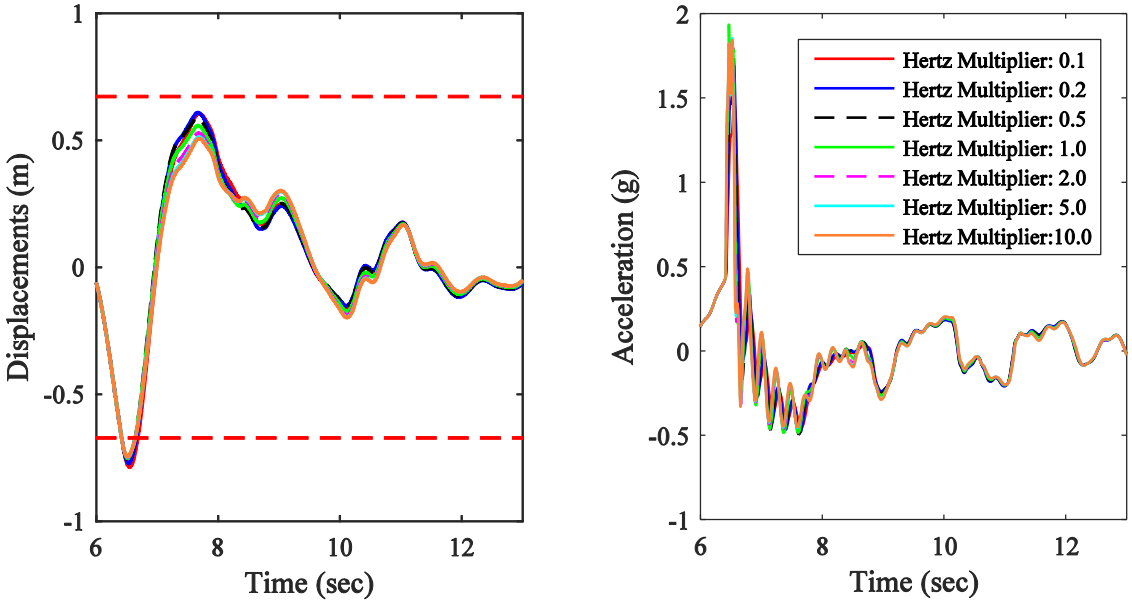

(a) (b)

Figure 6-9 Displacement time histories of the NPP isolation system (a) and acceleration time histories at ground level (b) during and after impact for various impact stiffness values

Figure 6-10 compares the floor response spectra at ground level for the different impact stiffness values considered. Floor response spectra were calculated by analyzing SDOF linear-elastic systems with 5% damping. At frequencies below 3Hz, decreasing the impact stiffness will result in higher spectral acceleration. For higher frequencies, especially around 25Hz corresponding to a higher natural vibration mode in the horizontal direction, increase in floor

response spectra were observed as the impact stiffness was increased. Similar results were observed for other cases considering different ground motions and bearing properties as described in section 6-4.

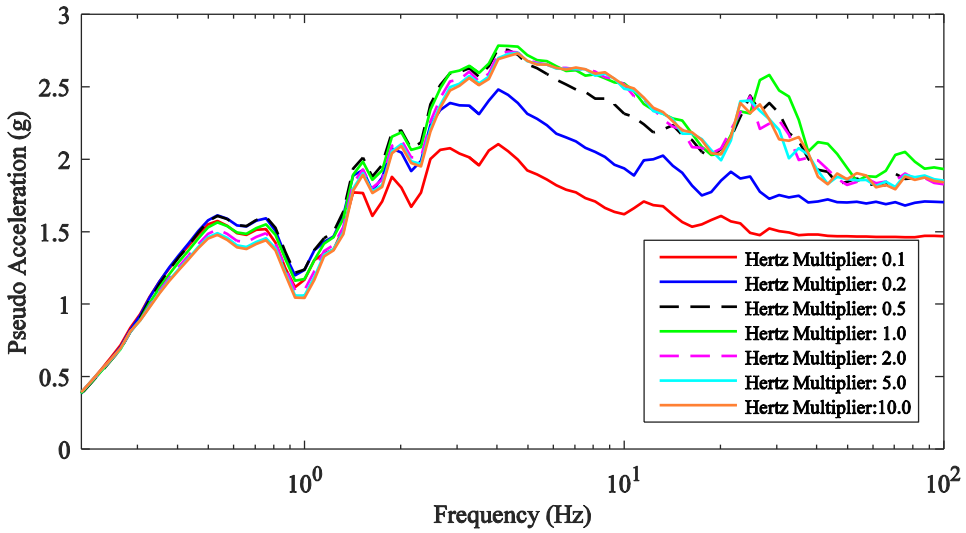

Figure 6-10 Floor response spectra at ground level for various impact stiffness values

6-3-4-2 Mass of Moat Wall and Backfill Soil

Similarly, different values were considered to study the sensitivity of the assumed mass of the moat wall and backfill soil on the response of NPP. These multipliers are 0.5, 1.0, 2.0, 5.0, and 10 times the assigned values for moat wall mass. The assigned mass was originally calculated based on the mass of the concrete wall with 0.6096 m (2 ft.) of backfill soil mass. Results of these simulations under Loma Prieta ground motion for 1.0 g intensity and CS = 0.672 m are presented.

Figure 6-11 shows the displacement time histories of the isolation system and the acceleration at ground level in the superstructure for the considered values of mass for the moat wall and backfill soil during and after the impact. As Figure 6-11 clearly shows, slight variation of mass does not influence the response of the wall or structure. Only when the mass is increased

by a factor of 10 is there a noticeable reduction in the penetration of about ~1cm compared to the nominal case. Increase in the mass also reduced the rebound displacement at the opposite side. Also, assuming 10 times larger mass for moat wall and backfill soil increases the maximum acceleration by a factor of 1.43 and more pronounced high frequency oscillation after the impact. However, increasing the mass led to significant self-vibration of the moat wall excited by its inertial weight and could reduce the effective CS in some cases.

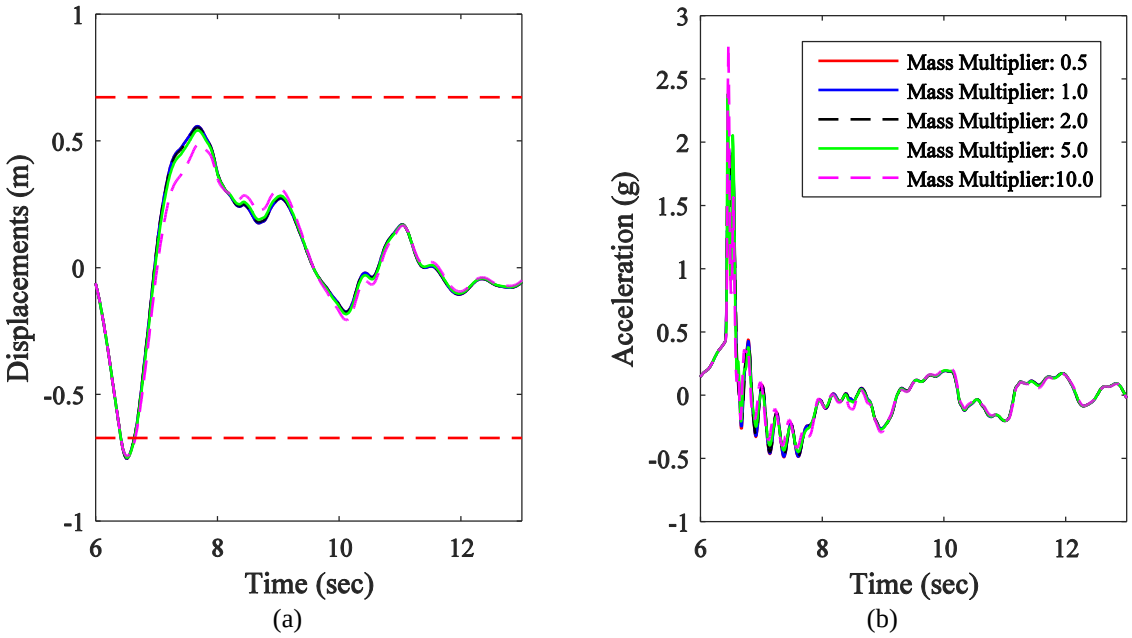

Figure 6-11 Displacement time histories of the base mat of NPP (a) and acceleration time histories at ground level (b)for different assumed for various moat wall and backfill soil mass values

Figure 6-12 shows the floor response spectra for the NPP at ground level. In the low frequency range, there is no significant difference in the spectral floor accelerations. However, for frequencies above 4 Hz, the larger mass resulted in higher spectral accelerations of about 4.2g around 13.2 Hz. Results from different simulations using different ground motions and bearing properties show a similar trend.

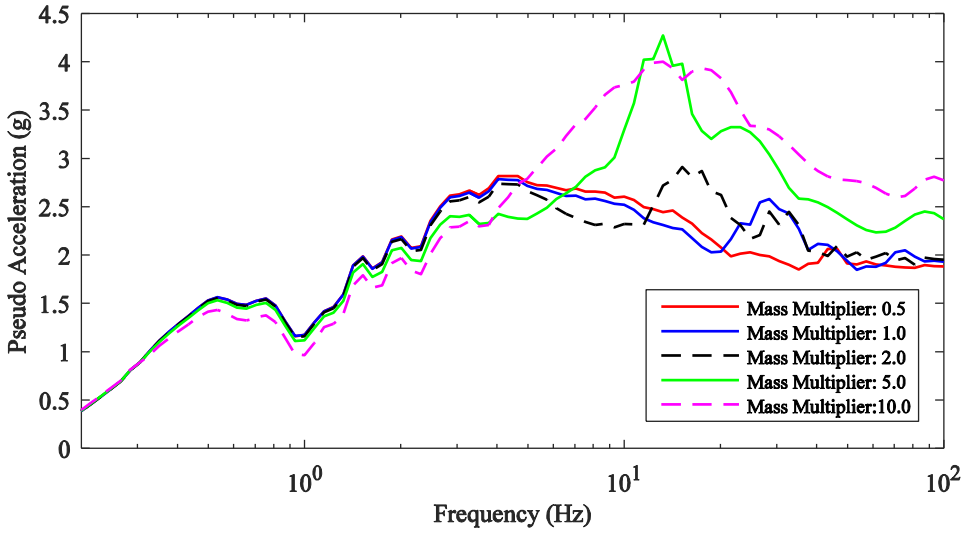

Figure 6-12 Floor response spectra at ground level for various moat wall and backfill soil mass values

6-4 Parametric Study

In order to further study the effects of impact on the seismic response of a NPP, a parametric study was carried out for various modeling and design parameters. These studies are project independent and are meant to provide insight into the sensitivity of modeling assumptions and the potential increased response of NPP considering impact at various velocities. A complete seismic hazard analysis with a suitable set of ground motions was considered beyond the scope of this study. Rather the intent here is to evaluate the proposed moat wall impact model under several ground motions and various modeling parameters to observe the model under a range of conditions. Variations in ground motions, intensity levels, Clearance to Stops, material properties, and different stiffness ratios for the isolators are first considered here. Further variation in moat wall model parameters are considered later.

6-4-1 Ground Motions (GM):

Three pairs of earthquake ground motions were considered and are listed in Table 6-4. These records were obtained from NGA database [21]. The three pairs of records were considered sufficient to observe a variation in bearing behavior.

Table 6-4 Ground motions used in simulations

GM #	*Motion name*	*NGA database name*
1	Chi-Chi	NGA_no_1508_TCU072-E
2		NGA_no_1508_TCU072-N
3	Imperial Valley	NGA_no_180_H-E05140
4		NGA_no_180_H-E05230
5	Loma Prieta	NGA_no_779_LGP000
6		NGA_no_779_LGP090

6-4-2 Intensity Level (IL):

The ground motion records were scaled to match the RG1.60 Revision 2 design response spectrum [22] for DBE (Design Basis Earthquake) motion scaled to 0.5g peak ground acceleration (PGA) without distortion. Also, to examine Beyond Design Basis Earthquake (BDBE) condition, ground motions were scaled by a factor of two which more likely apply to a site with high seismic hazard per NUREG recommendations [2, 23]. Moreover, a third case was considered with PGA of 0.75 g to examine the response of the structure in between DBE and BDBE seismic hazard. Figure 6-13 shows spectral acceleration for different ground motions used for nonlinear response history analysis.

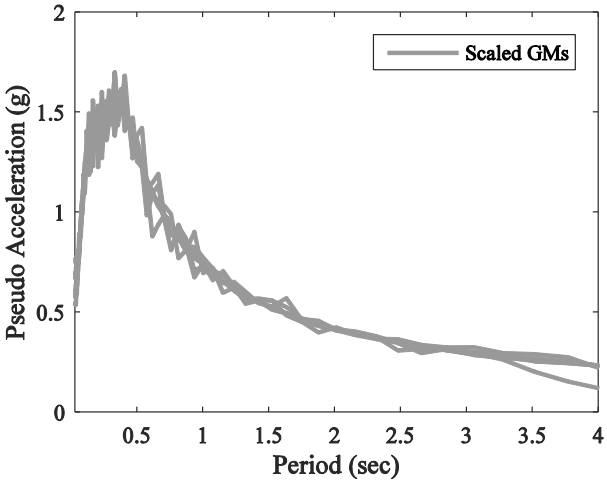

Figure 6-13 Spectral acceleration (5% damping) for different GMs – 0.5g PGA

6-4-3 Clearance to Stop (CS):

ASCE 4 specifies a displacement constraint to be placed no less than 90th percentile BDBE displacement (D_{BD}) along each side of the NPP and the functionality of the isolation system verified to this displacement. An explicit impact analysis is required if the provided CS is less than D_{BD}. A site specific seismic hazard analysis was considered beyond the scope of this study to determine the CS following recommended guidelines. Based on previous analysis of the APR1400, the design displacement D_{BD} was considered to be 224 mm corresponding to 100% shear strain in the elastomeric bearings. Following recommendations in ASCE 4 [2], the CS can be considered as three times the D_{BD}. In total, three values of CS are considered corresponding to 300%, 350 and 400% shear strain in the bearings (Table 6-5). Prototype bearings designed for seismic isolation of the APR1400 were tested at full scale and demonstrated they can reach up to 450% shear strain prior to failure [4, 5, 24].

Table 6-5 Different case considered for Clearance to Stop (CS)

CS/D_d	300 %	350 %	400 %
CS (m)	0.672	0.784	0.909

6-4-4 Bearing Properties:

Measured properties of the isolators were obtained from prototype testing and considered to be the Nominal Values (NV). In order to account for potential variations in properties of the isolators, Lower Bound (LB), and Upper Bound (UB) values were also obtained using conservative property modification factors for LRB based on AASHTO [25] and Constantinou et al. [26]. The adjusted range of properties considered for the bearings and individual property modification factors used are shown in Table 6-6. The total modification factor is given as the multiple of the individual modification factors for each effect considered. ASCE 4 and NUREG specify that the variation of the mechanical properties of the isolation system shall not vary by more than 20% over the life span of the nuclear structure [2, 23], thus this analysis exceeds the allowable variability mainly to observe a wider range of conditions.

Table 6-6 Calculated bounded properties using property modification factors

Prop.	***NV***	***Bound Prop.***	***Property Modification Factor***				
			Total	***Aging***	***Scragging***	***Temperature***	***Material***
K_1 (kN/m)	1870128	LB	1	1	1	1	1
		UB	1.21	1.1	1	1.1	1
f_y (kN)	46954	LB	0.7	1	1	1	0.7
		UB	1.32	1.1	1	1.2	1

Bi-linear models with coupled horizontal behavior represented by a Bouc-wen model [27] were used for the bearings. The secant slope stiffness was selected to give an isolated period of the superstructure of 2.0 sec for design displacement of 0.224 m for lead rubber bearing. The bearing properties were obtained from manufacturers quality control experimental data and modified by the corresponding property modification factors in Table 6-6. Two different cases were considered for the initial stiffness prescribed as a ratio of the second slope stiffness (K_2): 0.1 to represent lead rubber isolators and 0.01 to represent friction type isolators. The same

second slope stiffness was used for both bearing types and resulted in higher initial stiffness (K_1) for friction type bearings.

6-4-5 Case Studies Considered

For each Intensity Level (0.5, 0.75, and 1.0 g) and different isolator properties (LB, NV, and UB), 36 different cases were considered and simulated using the models developed in OpenSees. Table 6-7 shows the parameters for each case considered. In total, 324 different simulations were conducted and the results presented in the sections that follow summarize the 36 cases listed considering the three excitation intensity levels and three sets of bearing properties.

Table 6-7 Cases considered in parametric study

Case #	***GM***	***CS***	***K2/K1***	***Case #***	***GM***	***CS***	***K2/K1***	***Case #***	***GM***	***CS***	***K2/K1***
1	1	300%	0.1	13	3	300%	0.1	25	5	300%	0.1
2			0.01	14			0.01	26			0.01
3		350%	0.1	15		350%	0.1	27		350%	0.1
4			0.01	16			0.01	28			0.01
5		400%	0.1	17		400%	0.1	29		400%	0.1
6			0.01	18			0.01	30			0.01
7	2	300%	0.1	19	4	300%	0.1	31	6	300%	0.1
8			0.01	20			0.01	32			0.01
9		350%	0.1	21		350%	0.1	33		350%	0.1
10			0.01	22			0.01	34			0.01
11		400%	0.1	23		400%	0.1	35		400%	0.1
12			0.01	24			0.01	36			0.01

To gain a better insight into the response of NPP with impact, detailed analysis results are first presented for case 25 with NV bearing properties and ground motion IL of 1.0 g. The displacement demand of the isolation systems is shown in Figure 6-14a and the acceleration response for ground level is shown in Figure 6-14b with and without impact. Data in these figures indicate that the moat wall reduced the actual penetration into the wall by a factor of 2.4

while the acceleration increased by a factor of 3.5. The force-displacement behavior of the isolators is presented in Figure 6-14c and better shows the reduction in maximum displacement. Floor response spectra at ground level shows an increase (up to 6 times) in the floor spectral acceleration to be considered in the design of content within the NPP (Figure 6-14d). Force-deformation for the Hertz impact elements shows that contact only occurred in the negative direction (Figure 6-14e) and the total impact force is about 1.4 times the structure weight. Force-deformation of the backfill soil springs presented in Figure 6-14f absorb about 18% of the impact force in the bottom two soil springs. The top soil springs oscillate due to vibration of the concentrated mass at the top of the moat wall with the forces generated in the top soil springs having a similar amplitude as observed during impact.

6-5 Compiled Results

For the seismic intensity level 0.5 g, no impact occurred between the NPP and the moat wall as expected for design level motions. However, impact was observed for the higher intensity levels, especially when using the LB bearing properties. For intensity level of 0.75 g, 8.3 % of cases with impact were observed for LB which was expected due to the conservatism in design. The ratio of impact cases increased to 72, 38, and 20 % for 1.0 g intensity level with LB, NV, and UB bearing properties, respectively (Figure 6-15). Of interest, 16% of total considered cases experienced impact for NV properties when CS equals to the D_{BD}, noting that only three pairs of ground motions were used here to obtain the D_{BD}.

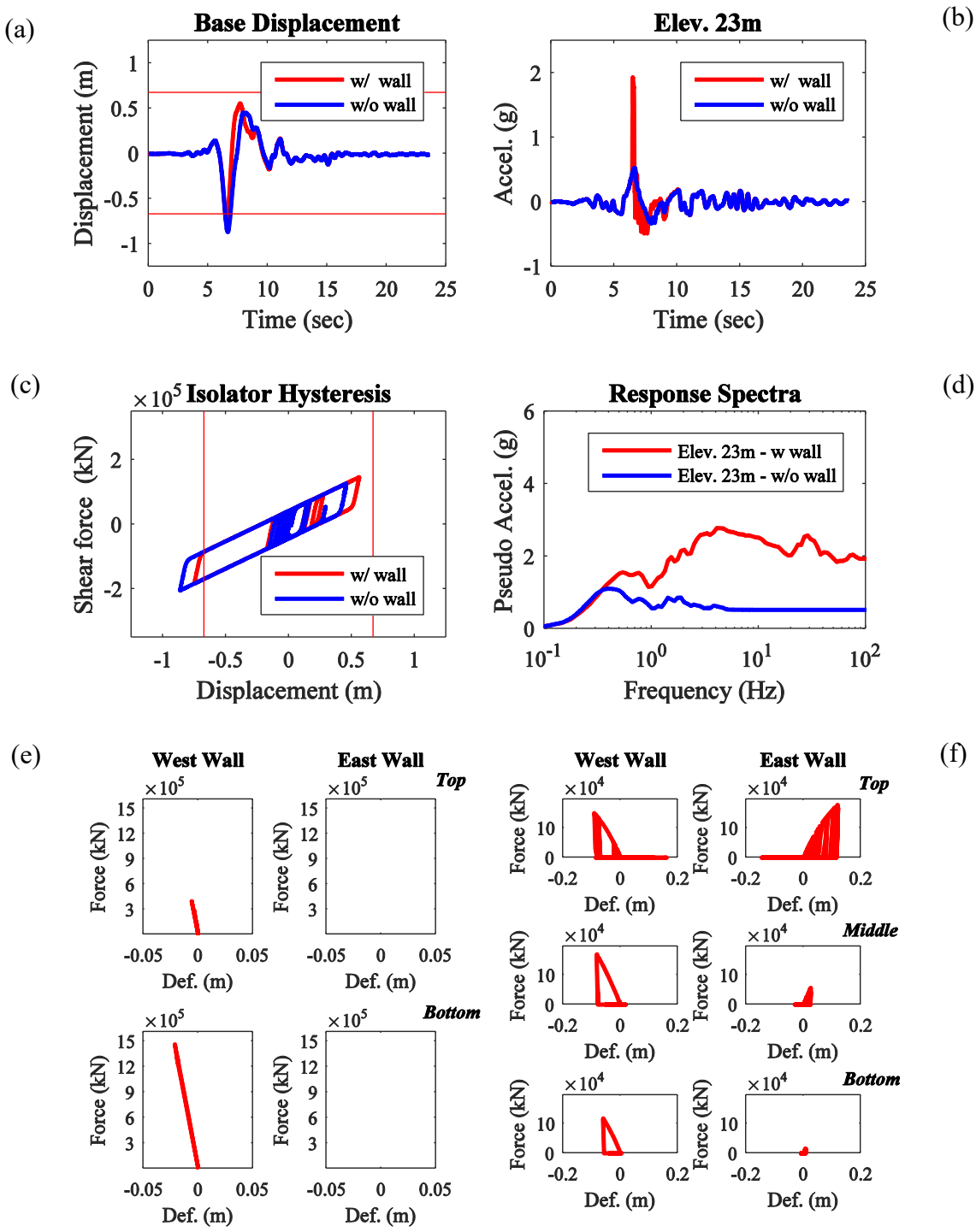

Figure 6-14 GM 5: Loma Prieta, CS: 300 % (0.672 m), IL: 1.0 g, NV, K2/K1 ratio = 0.1 (Case 25) (a) base displacement time history, (b) acceleration at ground level, (c) isolator hysteresis, (d) floor response spectral acceleration at ground level (e) hertz impact force, and (f) backfill soil force-deformation

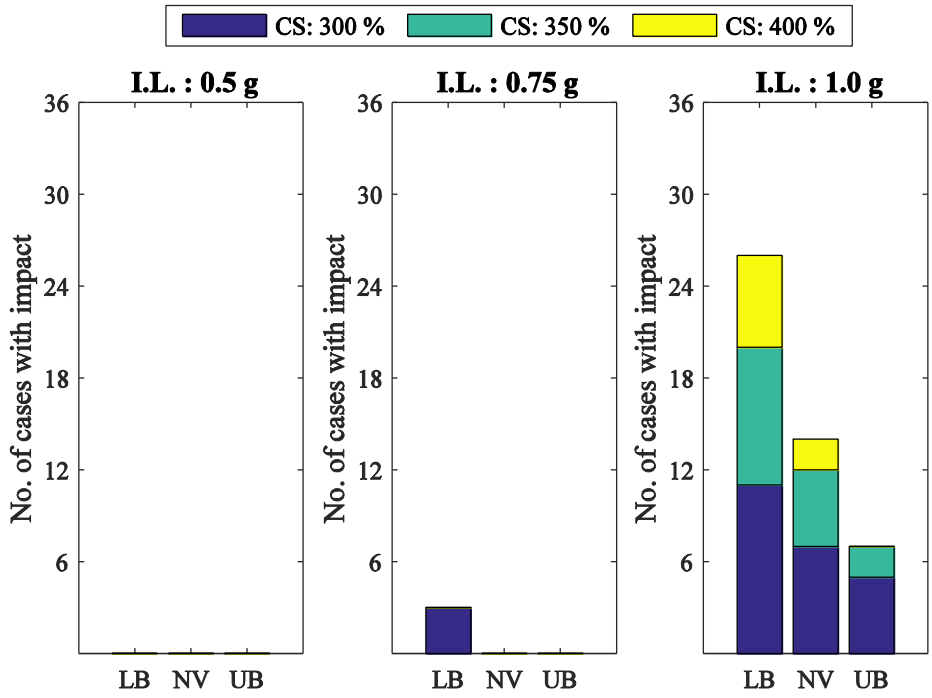

Figure 6-15 Impact cases for different GM Intensity Levels and bearing properties

Displacement demands normalized by CS are presented in Figure 6-16 for all cases considered in this parametric analysis. The simulations were run with and without the moat wall to evaluate the difference in bearing displacement demands. Figure 6-16 indicates by how much the displacements exceed the CS and the effects of the moat wall on reducing these displacement demands. A ratio less than one indicates that the seismic isolation displacement demand was less than the CS and did not impact. For cases where impact did occur, the moat wall and backfill soil as modeled here reduced the displacement demand on the bearings, although there was still significant penetration. In few cases, impact to moat wall resulted in increased displacements in the opposite direction for the isolator compared simulations without a stop (i.e. IL=1.0 – case 25). This increase in displacement is mainly due to the rebound effect of the structure after the first impact, which led to increased displacement demands in the opposite direction.

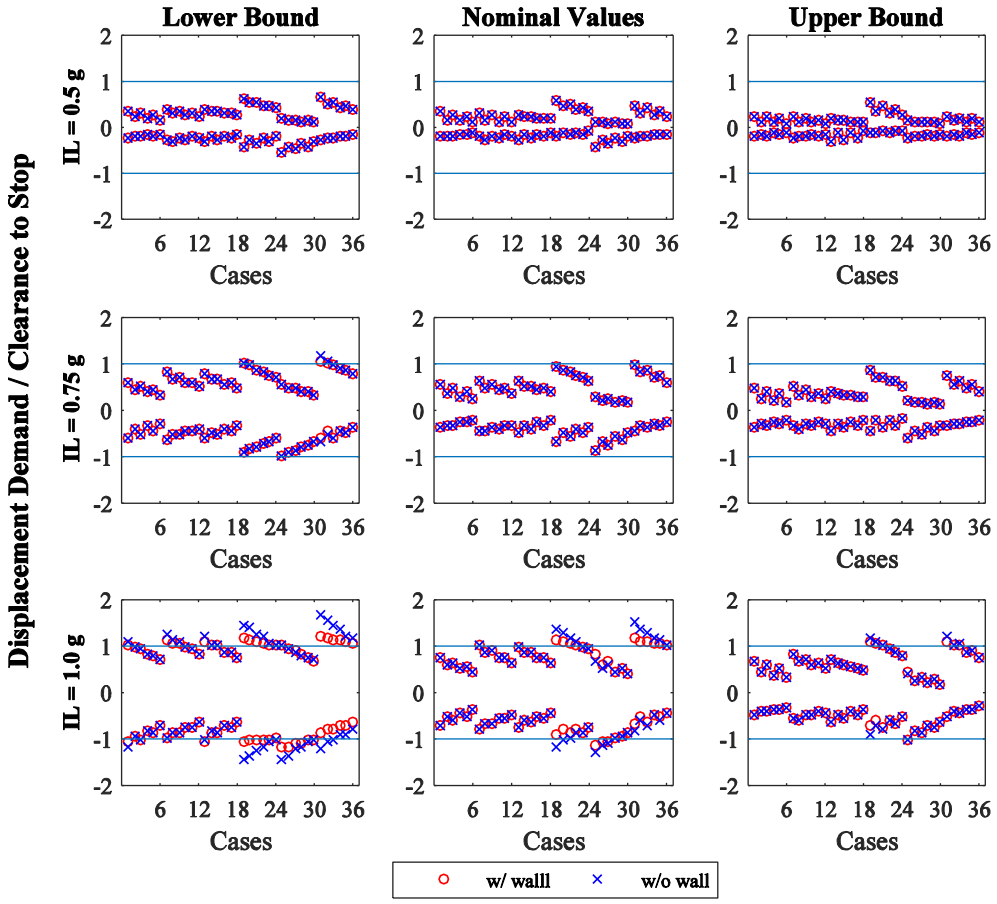

Figure 6-16 Displacement demand normalized by clearance to stop

Consideration of the moat wall and seismic pounding can increase the superstructure response, especially accelerations. Absolute acceleration at the observation point located at ground level is further examined. Figure 6-17 shows the peak absolute acceleration for all cases without and with moat wall (impact) for positive and negative directions. The increase in absolute acceleration can be up to 3.5 times for intensity level of 1.0 g. In some cases, the acceleration increase due to impact in one direction will increase the maximum acceleration in the other direction as well (see cases 18-24 for IL=1.0g – LB).

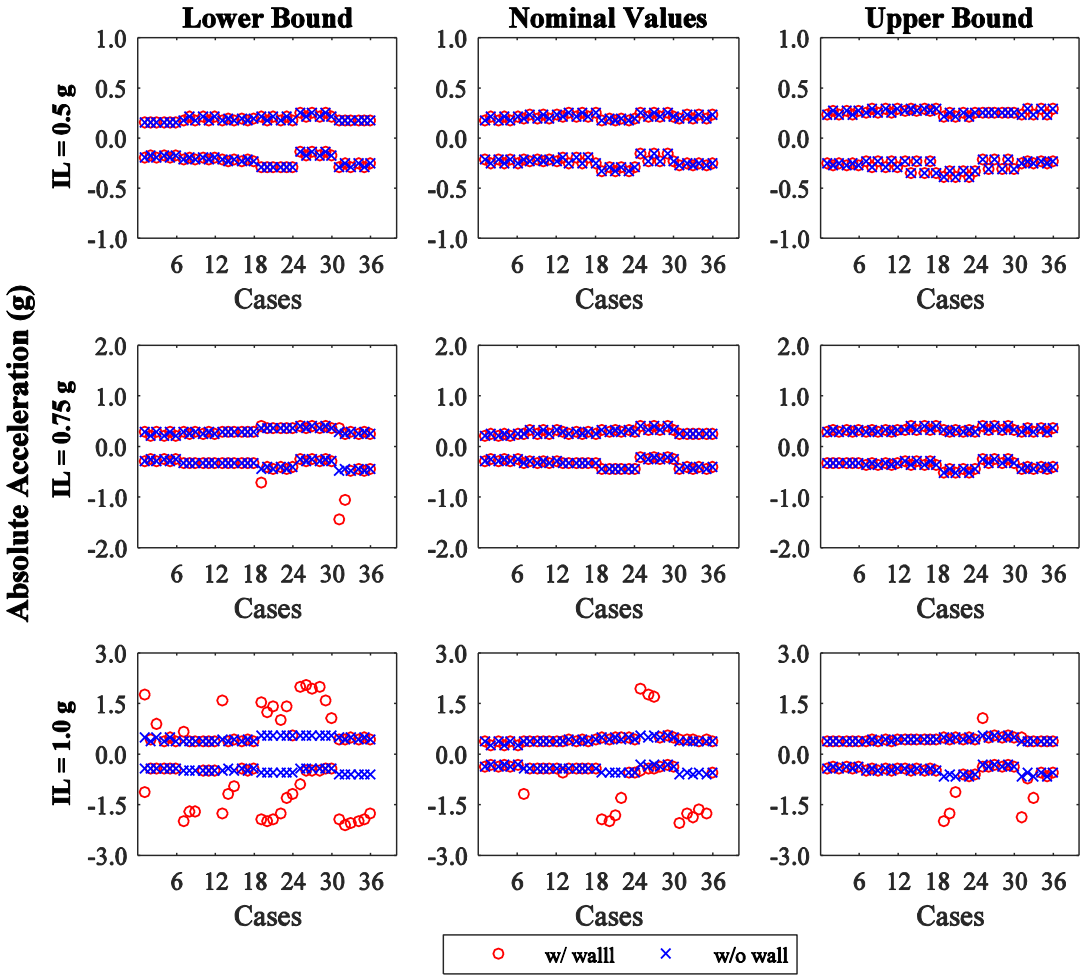

Figure 6-17 Maximum positive and negative acceleration at ground level

6-5-1 Variability on the moat wall and backfill soil properties

Considering the complexity in modeling impact between two large bodies as considered here, the sensitivity in selecting the modeling parameters for the moat wall modeling is further examined. The variation in parameters considered here also provides insight into expected behavior for different conditions such as stiff soil or increasing the size of the moat wall. Different combination of the soil and moat wall properties are considered using various different combinations of stiffness and strength multipliers as listed in Table 6-8. These multipliers were

applied to the estimates obtained earlier for moat wall and soil properties. The parameter range of variability is from 50% to 200% for moat wall properties while soil properties range from 25 % to 400 % due to larger inherent uncertainties in soil properties. Configuration 3 represents the nominal expected properties of the moat wall and backfill soil as used in the previous simulations. Of particular interest, configurations 6 and 7 consider Soil Type B and A per ASCE 7 [28] with 900 and 1800 m/sec shear wave velocities assuming linear elastic soil for the backfill soil. These conditions were considered to assess the response of the moat wall with soft and hard rock condition for the backfill soil while assuming the baseline properties for the moat wall.

Table 6-8 Multiplier on moat wall and soil properties for different configurations

Configuration		***1***	***2***	***3***	***4***	***5***	***6***	***7***
Multipliers	Moat Wall Properties	0.5	0.75	1	1.50	2	1	1
	Backfill Soil Properties	0.25	0.5	1	2	4	Soil Type B	Soil Type A

Figure 6-18 shows the effect of the moat wall variability on the displacement demand ratios and the absolute acceleration at ground level from the base of the NPP for the seven configurations considered under 1.0g excitation. Results from configuration 4 and 5 indicate that stiffening the moat wall and back fill soil (while still assuming compacted soil) only slightly decreases the displacement demand ratio or the amount of penetration into the moat wall. Stiffening the moat wall and soil causes a notable increase in the absolute acceleration at ground level. As an example, for GM4 case 19, 200% and 400 % increase in moat wall and soil stiffness and strength properties will result in a 20 % decrease in displacement penetration from the baseline Config. 3. As a result of this stiffening impact surface, the accelerations response increased by 28%. Compared to simulations with no moat wall, accelerations are increased by 240% and 560% for the baseline Config. 3 and Config. 5 respectively. For GM4 and case 19,

considering Soil Type B and A, the amount of penetration into the moat wall was reduced by almost 50% while the acceleration response was increased by a factor of 3.1 in both configurations compared with the baseline configuration (Config. 3). In cases 19-21 for these two configurations, due to rebound effects the impact in positive direction was followed by an impact in the other direction which caused an additional increase in the acceleration response. A similar behavior was observed for the other ground motions.

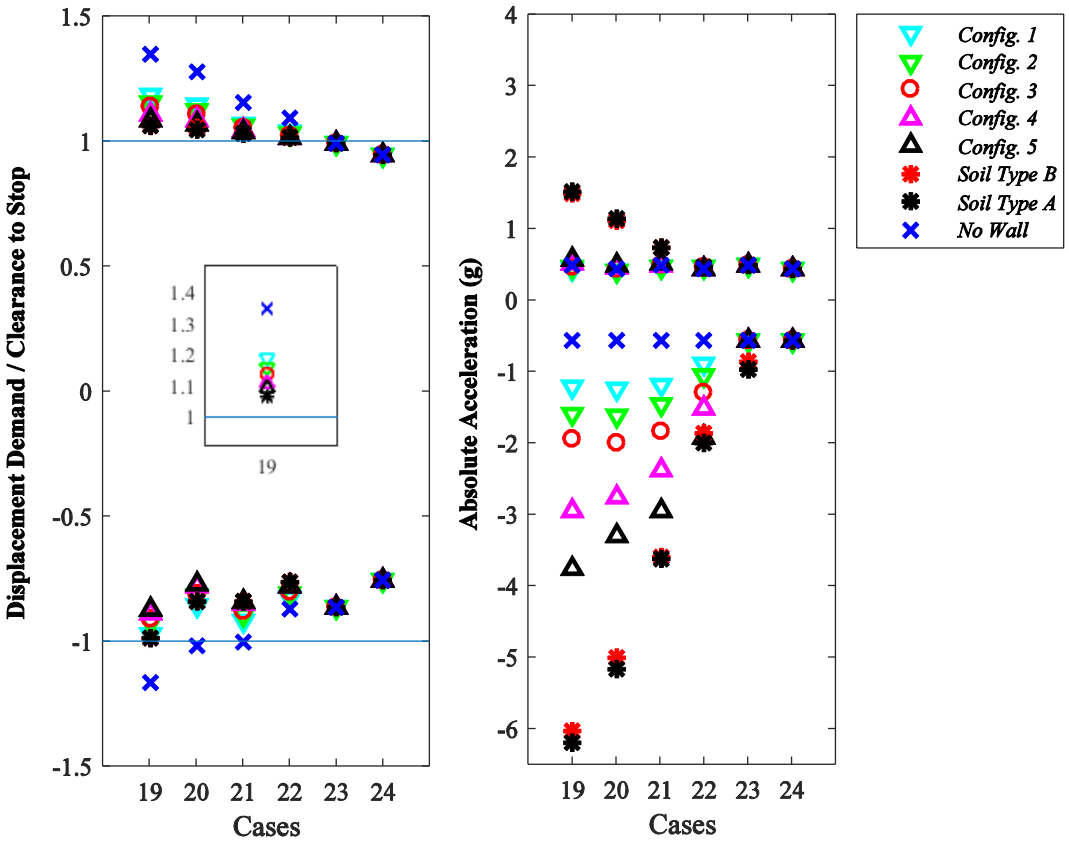

Figure 6-18 Variability in Displacement Demand ratios and Absolute Acceleration at ground level (GM4)

Floor acceleration response spectra were also examined along the height of the NPP for two characteristic bearing properties (K_2/K_1=0.1 for LRB and 0.01 for friction sliding bearing) in order to more directly assess effects on contents. The two stiffness ratios are considered since

they can provide very different results when examining floor response spectra. Before presenting the results for the floor response spectra considering impact to the moat wall, sample results of simulations for the two bearing properties are presented for the same seismic excitation without a moat wall in Figure 6-19. As shown, for frequencies below 1Hz, the spectral acceleration of the isolated NPP with LRB is larger while for higher frequencies the spectral acceleration of the structure with friction type bearings is higher. In particular, around the 1st natural vibration mode of the RCB structure at 4.3 Hz, the amplification of the response is higher for friction type bearing.

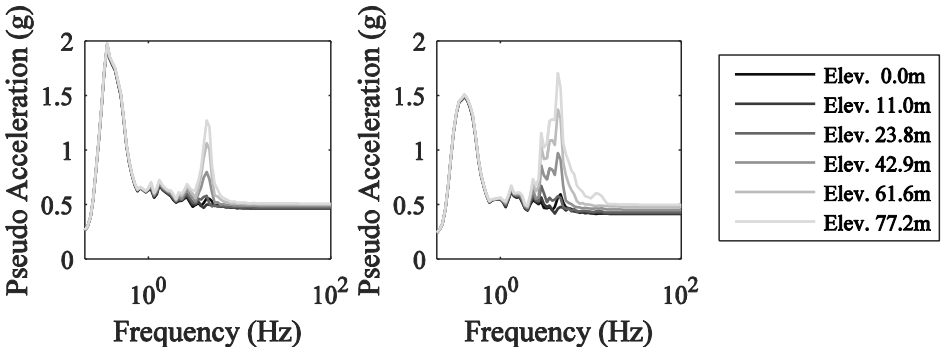

(a) (b)

Figure 6-19 Floor response spectra along the height of NPP – IL=1.0g – GM3 – No Moat Wall - LB – Config. 3 - K2/K1=0.1 (a) and K2/K1=0.01 (b)

Maximum spectral accelerations (frequency range of 0.1 – 100 Hz) for different elevations under 1.0 g intensity earthquake records assuming three different combinations for backfill soil and the moat wall (Config. 1, 3, and 5) are presented in Figure 6-20 and Figure 6-21 for K2/K1 rations of 0.1 and 0.01 respectively assuming LB values (see Table 6-6). It can be seen for cases that impact occurs amplification of spectral acceleration is higher when provided CS is smaller. As clearly shown in the figures, Config. 1 with the more flexible properties for the backfill soil and the moat wall shows relatively smaller difference between the maximum floor spectral acceleration for cases with and without impact. As the properties of the backfill soil and

moat get stiffer (Config. 3 and 5), the difference between floor response spectra's are more pronounced. As described before, increasing the strength and stiffness of the moat wall and soil slightly reduces the penetration into the moat wall while the increase in the acceleration and floor response spectra can be substantial.

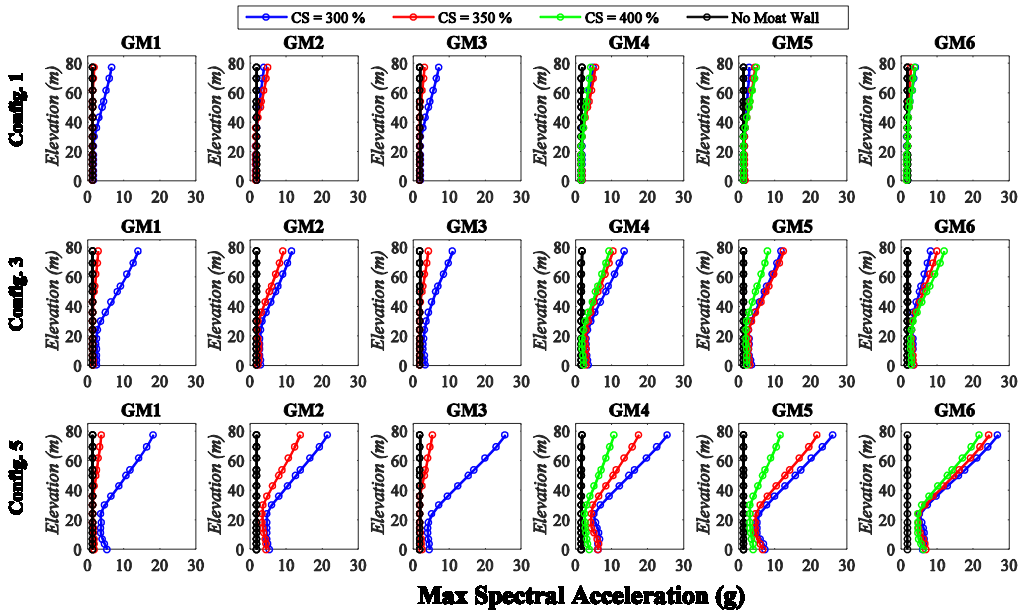

Figure 6-20 Max. spectral acceleration for intensity level 1.0 g – LB – K2/K1=0.1

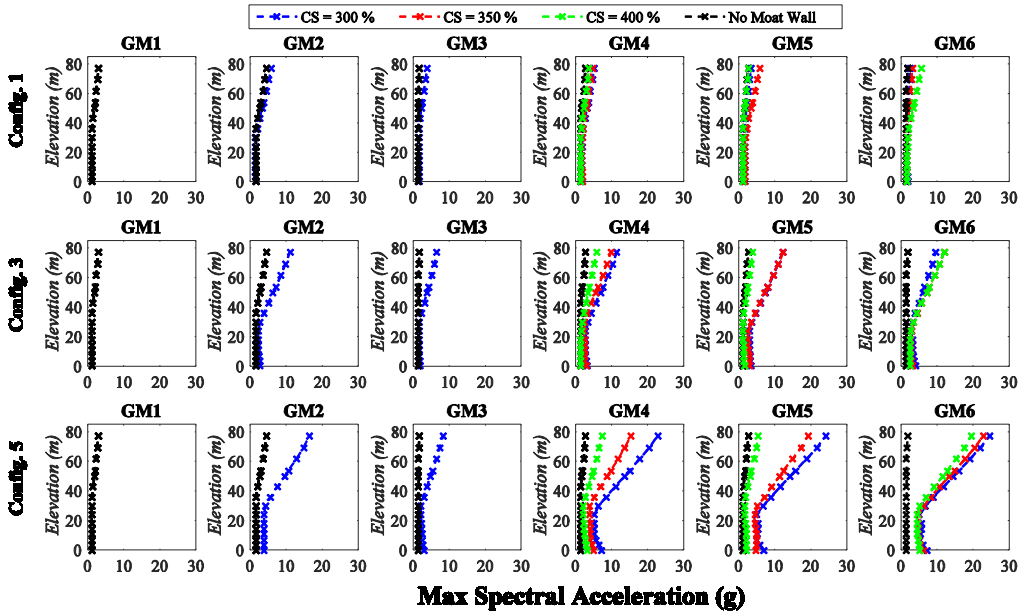

Figure 6-21 Max. spectral acceleration for intensity level 1.0 g – LB – K2/K1=0.01

6-6 Comparison between fixed-base and Isolated NPP with and without Moat wall impact

To evaluate the effectiveness of seismic isolation technology, comparisons between fixed-based and isolated NPP with and without moat wall impact were conducted. Simulations were performed using different ground motions scaled to 1.0g intensity for isolated NPP and range of different intensity level between 0.6 to 1.0 g were considered for fixed-based NPP. In these simulations, nominal values were used for material properties and CS was assumed to be 300% of the bearing's shear strain for six different ground motions and two different post elastic stiffness ratios. Results of these simulation under Imperial Valley ground motion and K2/K1 = 0.1 are presented below.

The displacement demand for isolated NPP without a moat wall is about 0.9 m while the displacement demand for isolated NPP with the moat wall is 0.76 m with a CS of 0.672 m. (Figure 6-22).

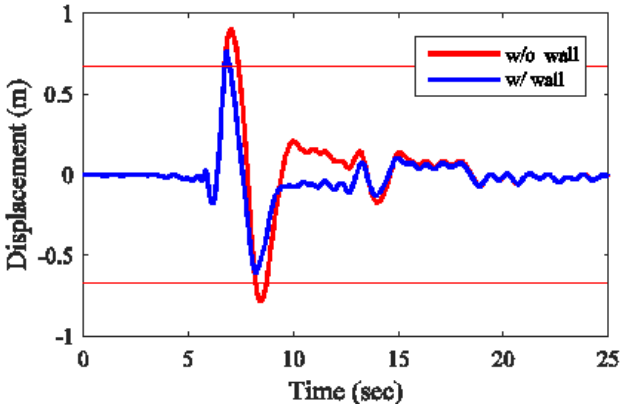

Figure 6-22 Isolator displacement time history

Based on observation of floor response spectra (Figure 6-23), isolated NPP (with and without moat wall) performed better for frequencies above 1.0Hz while the fixed-based structure

has lower spectral acceleration values in lower frequency range under the same level of excitation. This is due to the fact that the 1st natural period of isolated NPP is much larger than the fixed-base NPP and results in higher excitation in lower frequency range. Maximum spectral acceleration in the range plotted for the fixed-base NPP was 6.36g while isolated NPP had the maximum spectral acceleration of 1.34 and 3.76 g with and without moat wall respectively under the same seismic excitation with intensity level of 1.0 g. As shown clearly in the figure, the impact in isolated NPP resulted in higher spectral acceleration in comparison to the response of isolated NPP without moat wall. However, the peak spectral acceleration for the isolated structure was generally smaller than the fixed-base structure even for the cases where there was impact to the moat wall for same intensity level of excitation. This trend mostly applies for frequencies between 10 to 20 Hz which is the primary range of frequency for non-structural components.

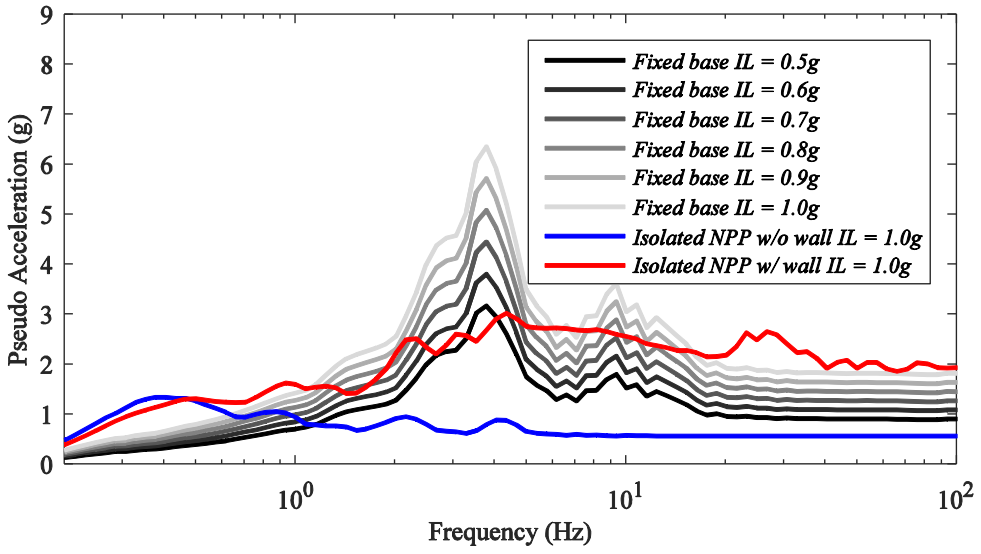

Figure 6-23 Floor response spectra at ground level assuming different intensity level for fixed based NPP vs. isolated NPP with and without a moat wall

6-7 Summary and Conclusion

A simplified modeling approach is presented to consider moat wall impact on the seismic response of isolated NPP. A macro model to capture the impact forces was developed in OpenSees based on past analytical and experimental impact studies combined with observed behavior in finite element model simulations. The moat wall model was then used to examine the NPP response through a series of parametric studies under different seismic intensity levels and various properties for the bearings and moat wall.

While there is some uncertainty in determining effective properties for modeling of impact to the moat wall, a sensitivity analysis on horizontal impact stiffness provided confidence that the estimated impact parameter values are reasonable. More detailed finite element studies could be beneficial to have a better estimate of the impact stiffness and maximum indentation between the two colliding bodies. With respect to the assumed mass for the moat wall and backfill soil, increasing the mass only modestly decreases penetration while causing considerable increase in floor response spectra in frequencies above 4 Hz.

The occurrence and intensity of impact is highly dependent on the assumed bearing properties, and variations in bearing behavior can be obtained from experimental testing to large shear strains. In terms of protection of the seismic isolation system from failure using a stop, the moat wall can limit the displacement demand in the bearings, but there can still be considerable penetration for the isolated NPP considered here. As a result, isolators can undergo displacements larger than their expected maximum displacement limit based on the clearance to stop, indicating the need to test and ensure bearing functionality beyond these limits. As a result of impact, the absolute acceleration was found to increase by factors up to 3.5 at the ground

elevation when compared to a similar simulation without a moat wall. Increase in the moat wall and backfill soil strength and stiffness will decrease the penetration into the moat wall (around 66 % reduction for hardest moat wall and compact backfill soil considered here) but can introduce up to 93 % increase in the maximum absolute acceleration. Increase in the strength and stiffness of the moat wall and the backfill soil can increase displacement demands on the opposite side of impact due to a rebounding effect and may result in a second impact.

It is important to examine the spectral acceleration for frequencies range of interest which affects the non-structural components in NPPs. Bearings with higher initial stiffness (i.e. friction type bearing) generally result in higher spectral acceleration for frequencies above 1Hz along the height of the NPP. Floor response spectral acceleration along the height on the NPP will increase significantly due to impact and this increase in spectral acceleration at ground level for baseline properties of the moat wall and backfill soil and 1.0g intensity could be up to 6 times compared to the case without impact.

For the Simplified NPP, the spectral accelerations in the superstructure for the isolated NPP with and without moat wall impact are generally smaller in comparison to the fixed-base NPP for frequencies between 1.15 to 16 Hz under the same intensity level of excitation. For the conservative Clearance to Stop requirements proposed in NPP design guidelines, impact if it occurs will likely only occur at small velocities. Thus for beyond design basis earthquakes, seismically isolated NPPs are expected to perform much better than a fixed base plant.

References

[1] Kumar, M., and Whittaker, A. S. (2015): On the Calculation of the Clearance to the Hard Stop for Seismically Isolated Nuclear Power Plants." Proc., SMiRT-23.

[2] ASCE (2017): Seismic analysis of safety-related nuclear structures, ASCE/SEI Standard 4. American Society of Civil Engineers, Reston, VA.

[3] Kim, H.-G. (2005): The Design Characteristics of the Advanced Power Reactor 1400. ICONE-13, Beijing, China.

[4] Schellenberg, A. H., Sarebanha, A., Schoettler, M. J., Mosqueda, G., Benzoni, G., and Mahin, S. A. (April 2015): Hybrid Simulation of Seismic Isolation Systems Applied to an APR-1400 Nuclear Power Plant. PEER,

[5] Schellenberg, A. H., Sarebanha, A., Schoettler, M. J., Shao, B., Mosqueda, G., and Mahin, S. A. (August 2016): Hybrid Simulation of Seismic Isolation Systems applied to an Archetype Nuclear Test (ANT) Power Plant under Design Level Excitation. PEER,

[6] OpenSees (2014): Open system for earthquake engineering simulation (Version 2.4.4).

[7] Masroor, A., and Mosqueda, G. (2012): Experimental simulation of base-isolated buildings pounding against moat wall and effects on superstructure response. Earthquake Engineering & Structural Dynamics, 41 (14), 2093-2109.

[8] Sasaki, T., Sato, E., Fukuyama, K., and Kajiwara, K. (2017): Enhancement of Base-isolation based on E-Defense Full-Scale Shake Table Experiments: Dynamic Response of Base-Isolated Building under Impact due to Pounding. 16WCEE, Santiago, Chile.

[9] Komodromos, P., Polycarpou, P. C., Papaloizou, L., and Phocas, M. C. (2007): Response of seismically isolated buildings considering poundings. Earthquake Engineering & Structural Dynamics, 36 (12), 1605-1622.

[10] Masroor, A., and Mosqueda, G. (2013): Impact model for simulation of base isolated buildings impacting flexible moat walls. Earthquake Engineering & Structural Dynamics, 42 (3), 357-376.

[11] Sarebanha, A., Mosqueda, G., Kim, M. K., and Kim, J. H. (2017): "Effects of Moat Wall Impact on the Seismic Response of Base Isolated Nuclear Power Plants." Proc., 16WCEE.

[12] Jankowski, R. (2005): Non-linear viscoelastic modelling of earthquake-induced structural pounding. Earthquake Engineering & Structural Dynamics, 34 (6), 595-611.

[13] LSTC (2011): LS-DYNA, A Program for Nonlinear Dynamic Analysis of Structures in Three Dimensions. Livermore Software Technology Corporation, Livermore, CA

[14] Duncan, M., and Mokwa, R. (2001): Passive earth pressures: theories and tests. Journal of Geotechnical and Geoenvironmental Engineering, 127 (3), 248-257.

[15] Shamsabadi, A., Rollins, K., and Kapuskar, M. (2007): Nonlinear Soil–Abutment–Bridge Structure Interaction for Seismic Performance-Based Design. Journal of Geotechnical and Geoenvironmental Engineering, 133 (6), 707-720.

[16] Wilson, P., and Elgamal, A. (2009): Full-scale shake table investigation of bridge abutment lateral earth pressure. Bulletin of the New Zealand Society for Earthquake Engineering, 42 (1) (2009), 39-46.

[17] Wilson, P. R. (2009): Large scale passive force-displacement and dynamic earth pressure experiments and simulations. Doctoral Dissertation, University of California, San Diego, San Diego, CA.

[18] Terzaghi, K., Peck, R., and Mesri, G. (1996): Soil mechanics in engineering practice, 3rd edition. New York, NY.

[19] Goldsmith, W. (2001): Impact: The Theory and Physical Behavior of Colliding Solids. Dover Publication, New York.

[20] Muthukumar, S., and DesRoches, R. (2006): A Hertz contact model with non-linear damping for pounding simulation. Earthquake Engineering & Structural Dynamics, 35 (7), 811-828.

[21] Ancheta, T. D., Darragh, R. B., Stewart, J. P., Seyhan, E., Silva, W. J., Chiou, B. S. J., Wooddell, K. E., Graves, R. W., Kottke, A. R., Boore, D. M., Kishida, T., and Donahue, J. L. (May 2013): PEER NGA-West2 Database. PEER,

[22] USNRC (2014): Regulatory Guide 1.60 Design Response Spectra for Seismic Design of Nuclear Power Plants. NUREG, United States Nuclear Regulatory Commission, Washington, DC

[23] USNRC (forthcoming): Technical considerations for seismic isolation of nuclear facilities., NUREG-**, Washington, DC.

[24] Kim, J. H., Kim, M. K., and Choi, I. (2017): Experimental Study on the Bidirectional Behavior of a Lead-rubber Bearing. 16WCEE, Santiago, Chile.

[25] AASHTO (2014): Guide Specifications for Seismic Isolation Design. American Association of State Highway and Transportation Officials, Washington, D.C.

[26] Constantinou, M. C., Whittaker, A. S., Kalpakidis, Y., Fenz, D. M., and Warn, G. P. (2007): Performance of Seismic Isolation Hardware under Service and Seismic Loading. MCEER, Buffalo, NY

[27] Casciati, F. (1989): Stochastic Dynamics of Hysteretic Media. Structural safety, 6, 259-269.

[28] ASCE (2010): Minimum Design Loads for Buildings and Other Structure. ASCE/SEI Standard 7, American Society of Civil Engineers, Reston, VA.

Chapter 7 Advanced Modeling of Seismically Isolated Nuclear Power Plant with Impact to Moat Walls

7-1 Introduction

This chapter describes a refined structural model of a NPP based on the seismically isolated APR1400 (see Chapter 5) and its modification for moat wall impact analysis. The simplified NPP model in Chapter 6 served to conduct various studies examining the sensitivity of parameters considered in the impact studies. The model considered here includes a detailed model of the base mat and distribution of isolators in an effort to more accurately assess the seismic response of base isolated NPPs including torsional response. Simulations under uni- and bi-directional horizontal excitations are used to examine the seismic response of base isolated NPPs with pounding to moat wall and its effects on the superstructure response. Results for

impact response parameters including penetration depth, impact velocities, and forces are examined and a simplified methodology to estimate these parameters is proposed.

7-2 Nuclear Power Plant Model

In studies conducted in this chapter, the Archetype Nuclear Test (ANT) model based on the APR 1400 NPP was used for the superstructure [1]. General properties of the ANT model are described in detail in Chapter 3. For the purpose of impact studies presented in this chapter, the ANT model with the 486 lead plug rubber bearing (LPRB) was used here. This 3-D model can capture the torsional response of the NPP, which can be important to study pounding since the corner displacements can increase and initiate impact at a corner. In this model, the base mat was modeled using solid brick elements with fine mesh to better capture the local response of the base mat and the seismic isolation system during impact. Although this model is computationally expensive (compared to the simplified and the other ANT models with a rigid diaphragm for the base mat), the flexibility of the base mat may be important for estimation of the impact forces. Table 7-1 lists the bearing properties for each individual LPRB used in the ANT model. This model was also analyzed in a fixed-base condition to compare with the seismically isolated case with and without impact.

It is important to mention that the dynamic properties of the simplified and detailed ANT models are relatively close for both the isolation system and the Reactor Containment Building (RCB).

Table 7-1 Bilinear bearing model parameters for individual isolators in ANT model

Bearing Properties	
K_{ini} (kN/m)	2524.65
F_y (kN)	936.35
Post-elastic/elastic stiffness ratio	0.0072
Height of rubber (m)	0.21

7-2-1 Modeling of Moat Wall and Backfill Soil

The proposed impact macro element in Chapter 5 was added to the ANT model by introducing 1,240 new nodes and 1,364 elements. These additional nodes surrounded the base mat (Figure 7-1) and every node on the perimeter of the mat foundation was connected through a *gap* element to the impact macro model. The impact model consists of Hertz contact springs, moat wall elements and backfill soil springs (Figure 7-2). Properties of different elements making up the impact macro model were calculated for the tributary length of each impact macro model along the perimeter using properties of a unit of moat wall section as described in Chapter 6.

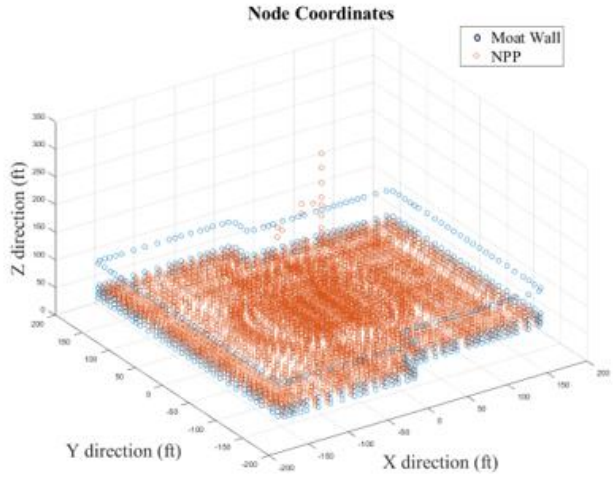

Figure 7-1 NPP and moat wall node coordinates

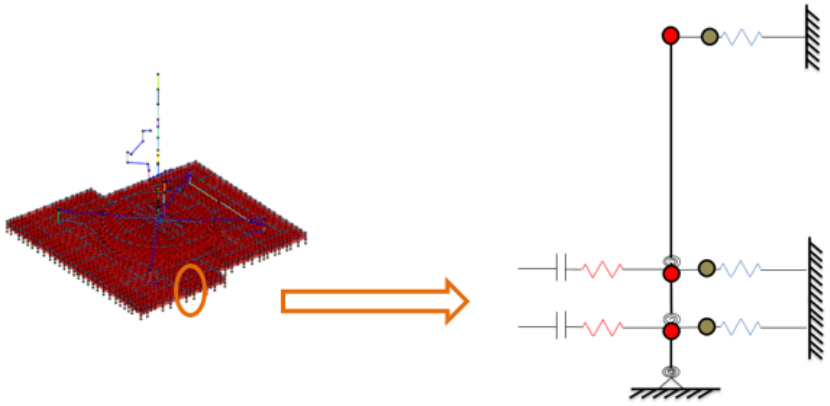

Figure 7-2 Implementation of the impact macro model

- **Hertz Stiffness**

In order to model the contact interface, Hertz stiffness for the impact macro model in Chapter 6 was first calculated following recommendations described in Goldsmith [2]. This method was originally proposed for static contact of two bodies and here it was extended to model the impact between the NPP mat foundation and the moat wall considered as a massive plane and an equivalent sphere. To further evaluate the hertz impact stiffness for this specific application, detailed finite element simulations were performed in LS-Dyna. The same finite element model described in Chapter 6 was used here with more emphasis on the impact force-deformation.

In LS-Dyna, different approaches can be used to model contact between two objects. The most common approach to model contact and calculate contact forces is using a penalty-based approach [3]. Penalty-based contact assumes a series of normal elastic compression only springs between two contacting interfaces to evaluate contact forces. The two contacting interfaces are designated as master and slave surface. The stiffness of these springs between the master and the slave surfaces prevents penetration of master nodes into slave nodes [4-6]. This method uses the size of the contact segment and its material properties to determine the contact spring stiffness by

default. Dynamic impact force results are reported as compressive forces in those aforementioned normal springs. The contact algorithm *CONTACT_AUTOMATIC _SURFACE_TO_SURFACE in LS-Dyna was used to model the impact between the mat foundation and the moat wall.

To study the effect of different contact stiffness values, impact between the NPP mat foundation and the moat wall were simulated in LS-Dyna for different impact velocities and variation in penalty stiffness multiplier. The penalty stiffness multiplier varied over a range of 0.05 to 1 as a scale factor on the default penalty stiffnesses (SFS and SFM [scale factor on default slave and master penalty stiffness] in *CONTACT_AUTOMATIC_SURFACE_ TO_SURFACE card. Figure 7-3 shows the impact force vs. impact deformation (indentation) assuming different contact stiffness multipliers. As seen in the figure, the first peak and high stiffness region of the impact force is due to the deformation in the contact springs while lower stiffness region represents the impact force versus the indentation of the colliding objects, which is of interest in this study. The reported deformation refers to the relative indentation in the moat wall and mat foundation and was measured as the average change in the distance between edges at middle and bottom part of the contact surface for both the moat wall and mat foundation. It should be noted that the reported deformation here doesn't refer to the actual deflection of the moat wall due to flexural bending and shear deformation. During impact, due to the deformation mode of the moat wall, the top of the contact surface disengages before the middle and bottom contact points. Therefore, average indentation at the middle and bottom of the wall were used here.

The contact stiffness should be set to allow minimal penetration between colliding objects while at the same time not inducing contact instabilities due to a large fictitious stiffness

at contact. To extract the desired stiffness from the FEM simulations, a least square fit was used to determine the stiffness parameter for the impact force deformation results of interest (Figure 7-3) in Eq. 7-1:

$$F_{impact} = K_h \times \delta^{1.5} \qquad (7-1)$$

where F_{impact} is impact force recorded in contact springs, K_h is Hertz impact stiffness and δ is indentation in the moat wall and mat foundation. Fitted values for hertz stiffnesses are listed in Table 7-2 for different assumed scale factors in contact stiffness.

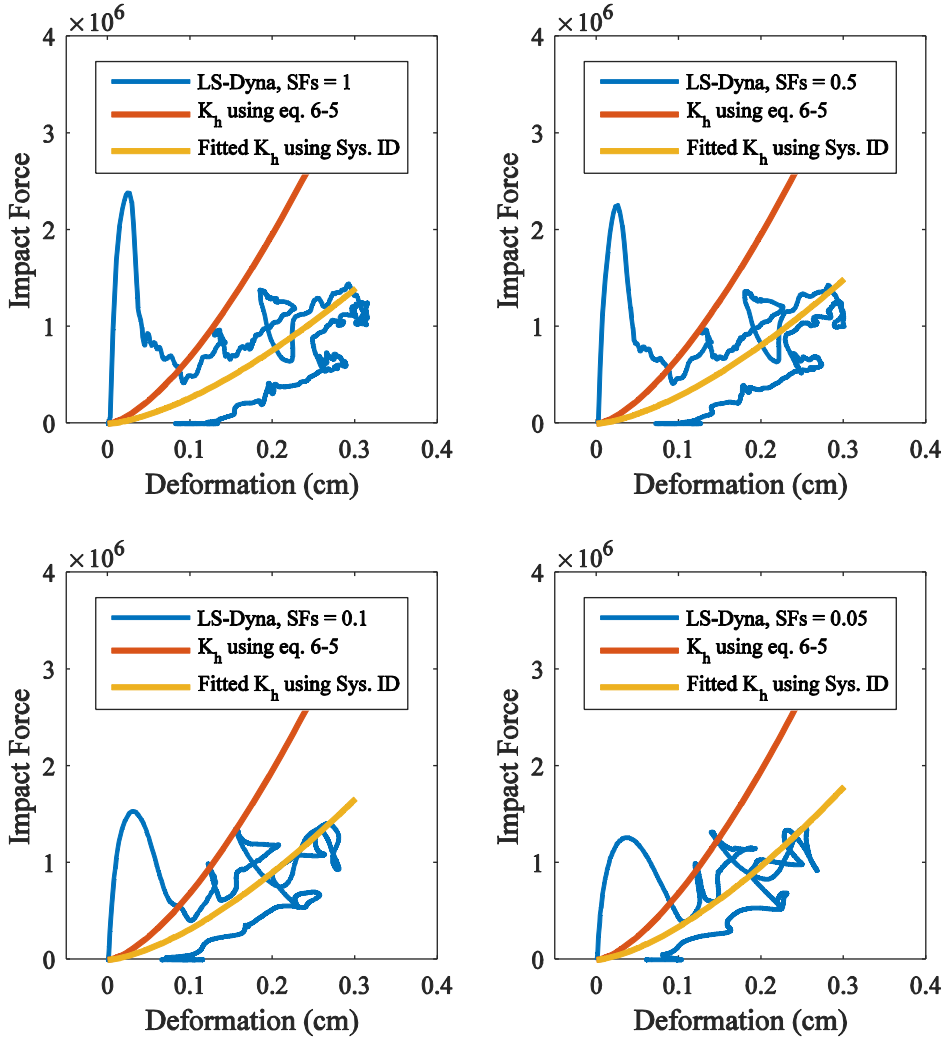

Figure 7-3 Impact force – deformation (indentation) for different scale factors on penalty stiffness using LS-dyna – impact velocity: 0.4572 m/s (1.5 ft./sec)

Table 7-2 Fitted Hertz Stiffness for different scale factors in contact springs

SFS and SFM	***Fitted K_h (N/m3/2)***	***Calculated K_h using Eq. 6-5 ($N/m^{3/2}$)***
1	8.5e+9	2.2e+10
0.5	9.1e+9	
0.1	1.0e+10	
0.05	1.1e+10	

Results from these simulations were used to calibrate the Hertz stiffness parameters used for *ImpactMaterial* in OpenSees. Comparing the calculated stiffness using Goldsmith's equations with the fitted stiffness to the LS-Dyna numerical results showed that all these stiffness values are within the same order of magnitude (LS-Dyna simulations are almost half of the calculated stiffness using Goldsmith's model). Considering the simplicity of the calculation of hertz stiffness using Goldsmith's model, it can be concluded that Goldsmith's model provides a good estimate of the impact stiffness for this considered application noting that is beyond its original intended scope. On the other hand, the LS-Dyna simulation may provide a more realistic value but requires a detailed finite element model as well as computationally expensive analysis.

The hertz stiffness value determined from FEM analysis was used in the proposed macro model to more accurately capture the impact between the NPP and the moat wall. The fitted hertz stiffness for the case SFS and SFM equal to 0.1 was used for modeling impact in OpenSees. Figure 7-4 compares the force deformation of the spring with *ImpactMaterial* based on an approximation to the Hertz Damped model by Muthukumar and DesRoches [7] and calculated results in LS-Dyna. It is worth mentioning that sensitivity analysis performed in Chapter 6 on the hertz impact stiffness showed that the response of the superstructure is not highly sensitive to the assumed values of the hertz stiffness. Also, there are some uncertainty as

to what the initial pulse represents in LS-Dyna and needs to be further investigated and validated using experimental testing.

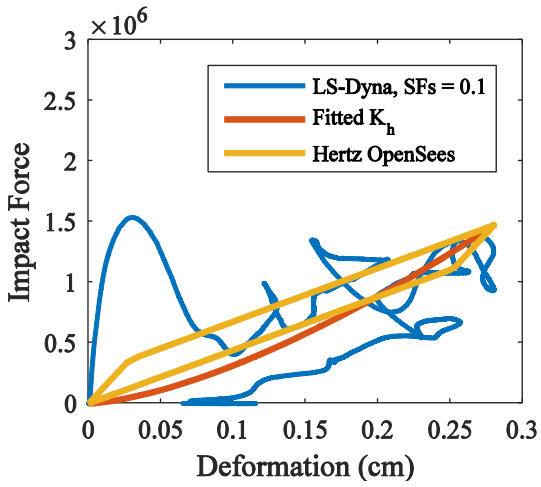

Figure 7-4 Impact force – deformation (indentation) using LS-Dyna, Hertz Damped Model and OpenSees Impact Material

7-3 Numerical Simulations

The refined models of the NPP and moat wall were used to gain a better insight into the effects of impact on structural response. The same structural properties and modeling assumptions for the moat wall and backfill soil as in Chapter 6 are used in these simulations except for the updated Hertz stiffness. Detailed results from different analysis are presented in this section including local behavior of various elements (bearing hysteresis and orbits, impact elements, backfill soil springs, and moat wall elements) as well as floor response spectra for different elevations along the height of RCB. Sample results are shown for the 2-D Loma Prieta record at 1.0g excitation and CS= 0.672 m. Results presented here are representative of the general behavior observed for the simulations conducted.

7-3-1 Sample Results

Figure 7-5 shows the plan view and orientation of the basemat for the structural model. The location of the impact macro elements on west side of the NPP for which detailed results are presented later is identified by the star in the figure.

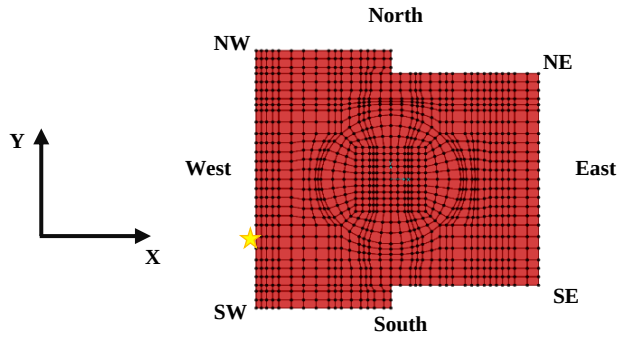

Figure 7-5 ANT Model plane view

- **Bearing Response**

The bearing hysteresis, bi-directional displacement orbits and shear interaction for a center bearing and the four corner bearings are shown in Figure 7-6. Impact occurs once the bearing displacement exceeds the provided CS marked in the figure by the solid red straight lines. The shear force-displacement behavior for different bearings are also presented in Figure 7-6a and 7-6b with maximum shear forces of 3,992 and 4,507 kN in X and Y directions respectively. As shown in the displacement orbit (Figure 7-6c), there are three instances of impact of the NPP to the moat wall, the first at west side, the second at the north side and the third is a partial side impact due to torsion in the NPP. The displacement demands at the corner bearings can be larger than the center bearings due to torsion. The NE corner of the base mat had a second impact in the X-direction due to torsion, while the SE corner had sufficient clearance to the east moat wall. The torsional effects appear to increase after the first impact. The almost solid

circle in the shear interaction plot indicates many cycles of excitation within the initial elastic bearing behavior. These vibrations are related to the initial stiffness of the bearing K_{init} and excites the structure at higher frequencies. The radius of the formed circle is about 935 kN, which corresponds to the yield force of the bearing model.

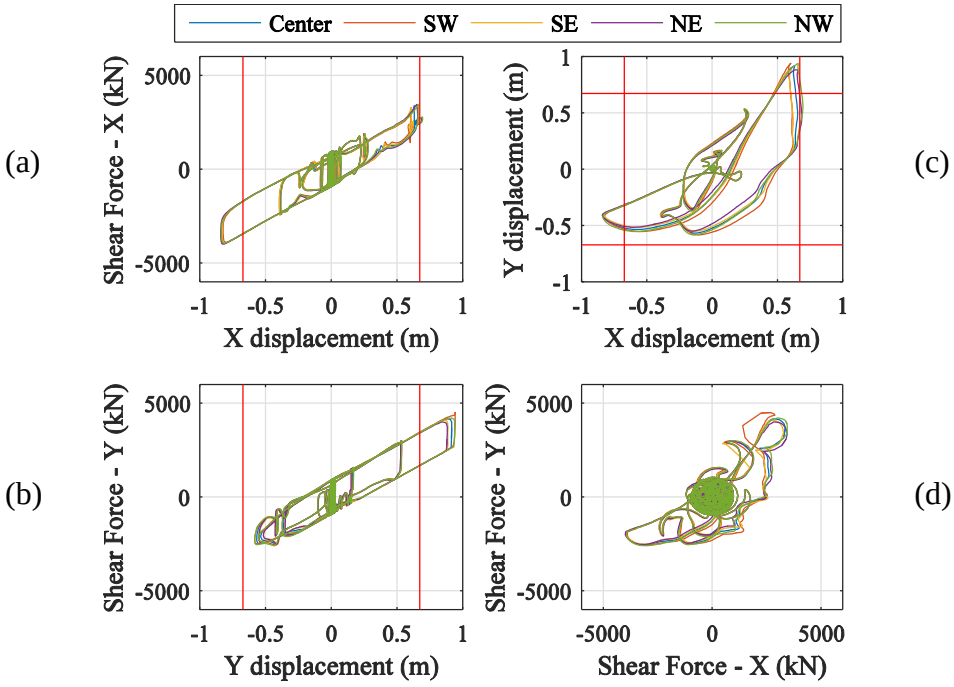

Figure 7-6 Response to 2-D Loma Prieta at 1.0g: (a and b) bearing hysteresis, (c) bearings orbits, and (d) shear interactions

- **Response of Moat Wall Elements**

The response for a set of elements that compose the macro model for a section of the west wall are shown in Figure 7-7. When the NPP displacement exceeds the CS (Figure 7-7a), the impact springs are engaged, resulting in large impact forces. Deformations shown for impact elements include both the gap distance and the indentation into the moat wall (Figure 7-7b). Deformations due to indentation into the moat wall are 2.11 and 4.16 cm for middle and bottom impact springs respectively. It should be noted that the bottom impact spring had higher forces even though they both have same impact properties. At impact, as the forces are transferred to

the moat wall, the moat wall deforms with larger displacements at the location of upper springs. Since the moat wall is fixed at the base, the top impact springs will separate before the bottom springs and lead to larger impact forces in the lower impact spring.

Moat wall response is presented for both the shear forces resistance of the moat wall and the nonlinear rotational springs along the height of the moat wall. Results for shear forces in two different segments of the moat wall are presented in Figure 7-7c. Shear force for the bottom segment represents the moat wall base shear force that is being transferred through the moat wall to the ground. Figure 7-7d shows the response of the corresponding rotational hinges on the moat wall segment. Based on these results, the moat wall reaches its ultimate capacity with significant yielding and residual displacements after impact.

The response of the soil elements behind the moat wall is shown in Figure 7-7e. It can be seen that the top soil spring experiences some excitation before and after impact due to vibration of the node at the top of moat wall. Following the main impact, there are some residual displacements in all the soil springs.

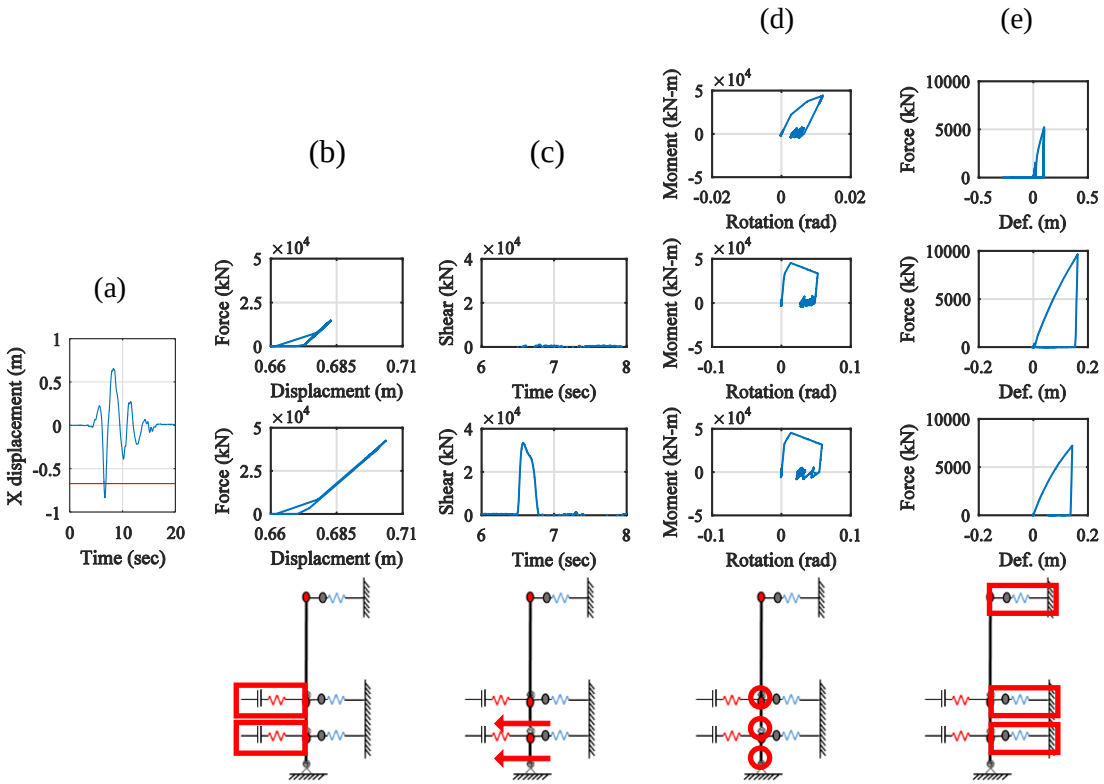

Figure 7-7 Response to 2-D Loma Prieta at 1.0g: (a) base displacement, (b) impact force deformation, (c) moat wall shear force time history, (d) moment rotation of rotational spring, (e) backfill soil force deformation

- **Contribution to Moat Wall Force Resistance**

The total impact forces including contributions from the concrete moat wall and backfill soil springs are presented for the north and west impact of the NPP (Figure 7-8). These total forces were calculated by adding the recorded forces of different components together for every impact macro element along the entire length of wall for the given side. These forces are then normalized by the total weight of the NPP (W = 4,730,292 kN). As Figure 7-8 shows, the shear forces in the concrete moat wall increases rapidly at impact while the compression force from backfill soil increases at a slower rate. This is due to the fact that the soil stiffness is relatively lower than the horizontal stiffness of the moat wall. Therefore, the moat wall has a higher influence on limiting the penetration compared to the backfill soil.

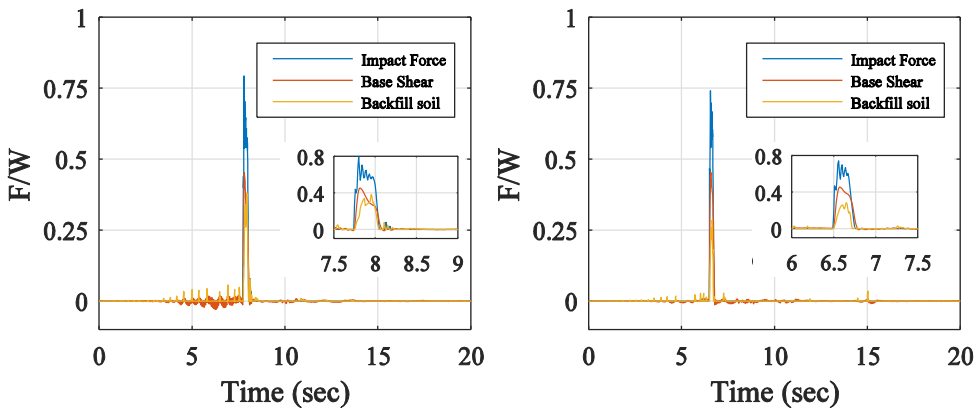

Figure 7-8 Response to 2-D Loma Prieta at 1.0g: total impact force, moat wall base shear, and backfill soil force time history on (a) north and (b) west side of NPP

- **Floor Response Spectra**

Floor response spectra are shown in Figure 7-10 for two different elevations along the height of RCB (see Figure 7-9) and for three different models: Isolated NPPs with and without the moat wall, and the fixed-base condition. Elastic response spectra were generated by analyzing single mass linear-elastic oscillator in the X and Y direction assuming 5% damping. The reported spectral quantities are vector norms of the response quantities in the two horizontal directions. The response spectra for the input ground motions are also included.

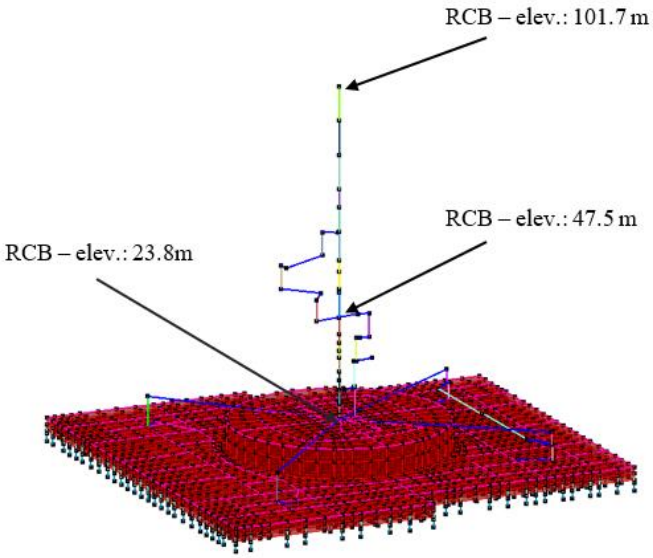

Figure 7-9 Location along elevations of RCB selected to examine floor response spectra

In Figure 7-10, peaks can be identified in the spectra at several distinct frequencies. For the RCB, the largest peak in the floor response spectra occurs at ~3.7 Hz, which corresponds to the first horizontal mode of vibration of the RCB. There is another distinctive frequency around 0.32 Hz, which corresponds to natural frequency of the isolated NPP. For frequencies below 0.5Hz, the spectral acceleration of the fixed-base NPP is lower than the isolated NPP with and without moat wall. This is likely due to the amplification in response of the isolation system at its 1st natural vibration frequency while the fixed-base NPP has a much higher natural frequency. Impact in isolated NPP results in higher spectral acceleration for frequencies above 0.4Hz in comparison to the response of isolated NPP without moat walls. However, the response of the content with natural frequencies above 0.5Hz in the isolated structure without or with the moat wall including impact is expected to be lower than in the fixed-base structure. A similar behavior was observed for the other ground motions.

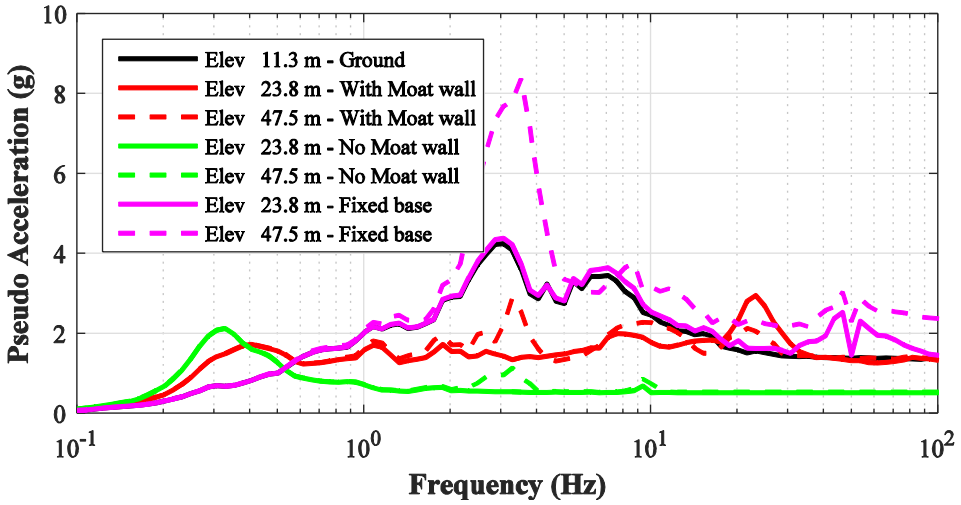

Figure 7-10 Floor response acceleration for RCB at different elevations for fixed-based and isolated NPP with and without moat wall to 2-D Loma Prieta at 1.0g

7-3-2 Torsional Effects

To study the effect of torsion in the response of NPP with a moat wall, a modified model was prepared and analyzed. In this modified model, additional constraints were added to avoid rotation of the NPP under 1-D seismic excitation. Figure 7-11 compares the displacement time histories and bearing orbits of the two models under 1-D seismic excitation using GM3. For the case when torsional response was allowed, it can be seen that due to small eccentricity between center of mass and stiffness (less than 0.1% of the plan dimension of the structure in both horizontal directions) there was a 1.1cm displacement in y direction even though the seismic excitation were only applied in the x-direction.

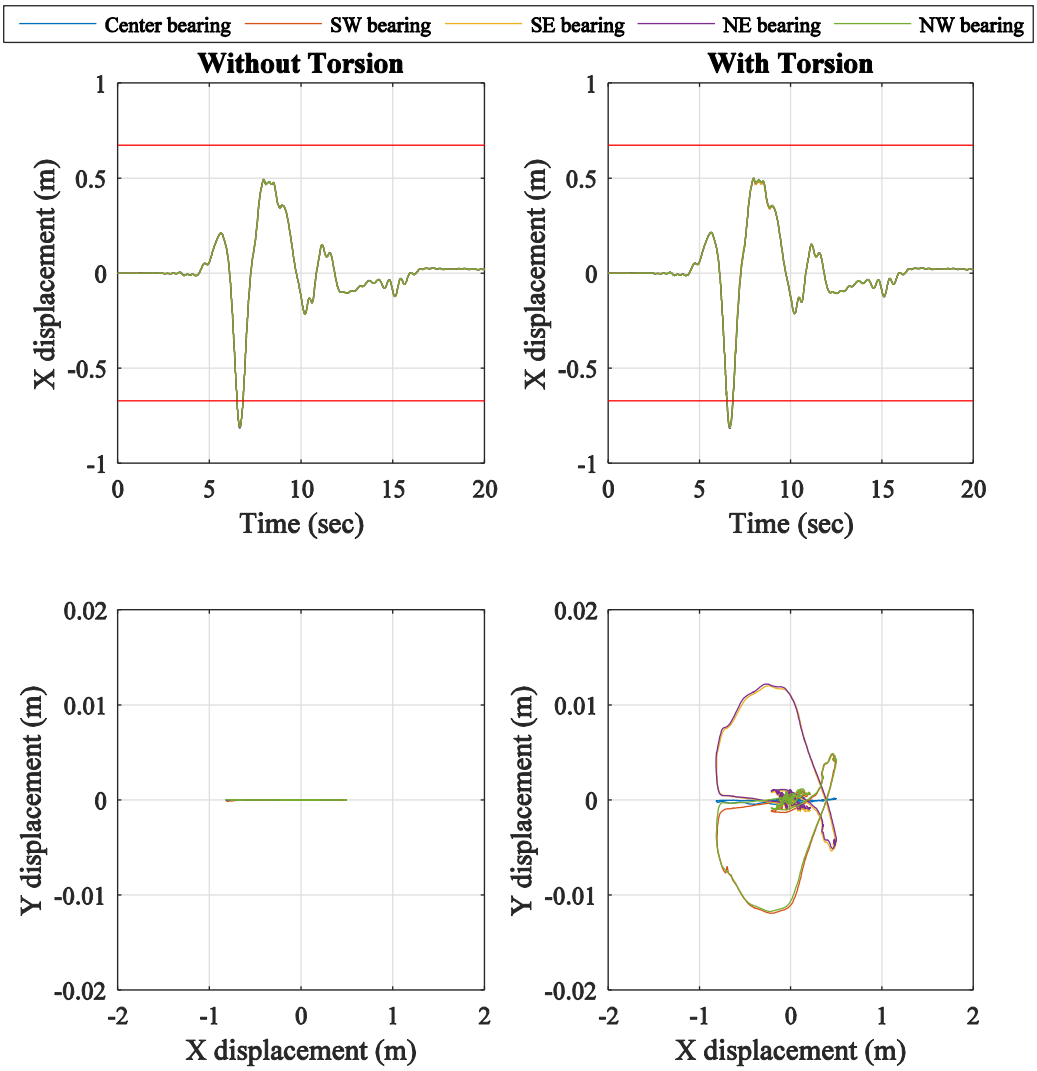

Figure 7-11 Bearings displacements for model with and without torsion, IL:1.0 g – 1-D excitation - Loma Prieta

Comparing different forces at the time of impact, it can be seen that that results are almost identical for the two different models (Figure 7-12). Also, based on observation of the response spectra there is not a significant difference in the response of the two models (Figure 7-13).

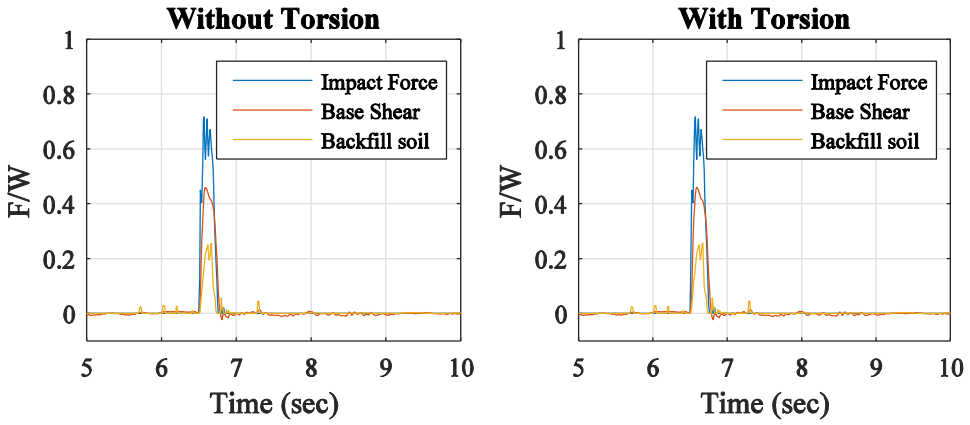

Figure 7-12 Impact, moat wall base shear and backfill soil force comparison for model with and without torsion, IL:1.0 g – 1-D excitation - Loma Prieta

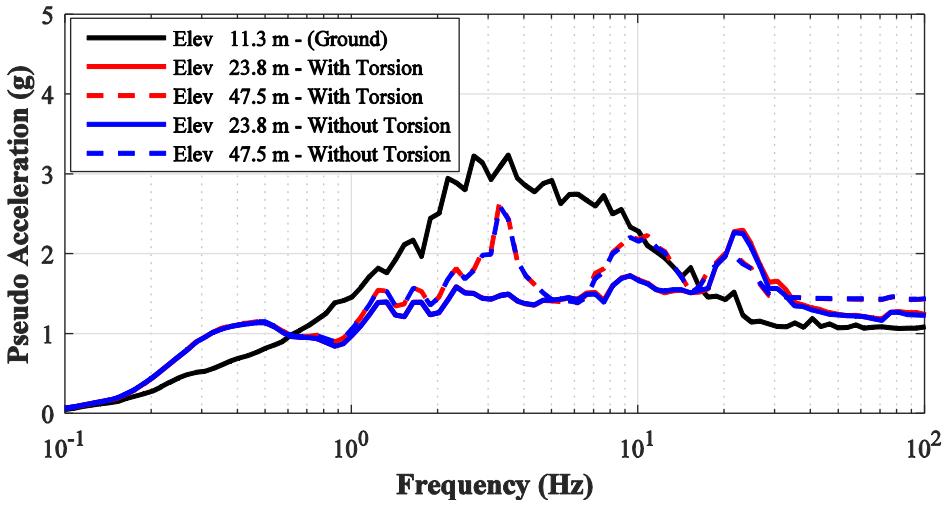

Figure 7-13 Floor response acceleration for RCB at different elevations for model with and without torsion, IL:1.0 g – 1-D excitation – Loma Prieta

It should be noted that even though the effect of torsion on the response is not significant, it is still important to develop and use 3-D models for these analysis since the response of the NPP and bearings is generally different under 2-D ground excitation compare to 1-D excitation. As was observed in Section 7-3-1, impact under 2-D ground excitation appeared to induce torsion in the structure.

7-4 Parametric Study using ANT Model

In order to have a more general understanding of the seismic response of the ANT model considering moat wall impact, simulations were conducted for several ground motions and different modeling parameters. These studies provide insight into the sensitivity of modeling assumptions and the potential increased response of NPP considering impact. Variations in ground motions, intensity levels, and Clearance to Stops (CS) are considered here. The variation of parameters considered here follow a similar approach described in Chapter 6 and summarized briefly here.

Three pairs of earthquakes ground motions: Chi-Chi, Imperial Valley and Loma Prieta earthquake were obtained from NGA database [8] and were considered for these simulations. A total of 6 different cases were considered including three cases of 1-D excitation and three cases of 2-D excitation.

The ground motion records were scaled to match the RG1.60 Revision 2 design response spectrum [9] for DBE (Design Basis Earthquake) motion scaled to 0.5g peak ground acceleration (PGA) without distortion. Also, to examine Beyond Design Basis Earthquake (BDBE) conditions, ground motions were scaled by a factor of two which more likely apply to a site with high seismic hazard NUREG recommendations [10]. Moreover, a third case was considered with PGA of 0.75 g to examine the response of the structure in between DBE and BDBE seismic hazard.

Three different distances were considered for the CS in this parametric study. CS distances were then selected based on the verified maximum shear strain capacity of the rubber and selected to correspond to 300, 350, and 400 % shear strain (Table 7-3). Measured properties

of the isolators were obtained from prototype testing and considered to be the Nominal Values (NV). Different property modification factors were not considered here.

Table 7-3 Different case considered for Clearance to Stop (CS)

CS/D_d	300 %	350 %	400 %
CS (m)	0.672	0.784	0.909

7-4-1 Parameters Considered

A total of 36 different cases were simulated for three different intensity levels (0.5g, 0.75g and 1.0g) under uni- and bi-directional seismic excitations for three different values of clearances to stop and also considering no moat wall. Results are presented for 9 different cases (Table 7-4) for each intensity level. Also, since there was no case of impact to the moat wall for intensity level of 0.5 g (DBE motion) results presented here are only for intensity level of 0.75g and 1.0g (BDBE motion).

Table 7-4 Cases considered for parametric study

Case #	***CHS***	***Ground Motion***
1	0.672 m	Chi-Chi
2	0.672 m	Imperial Valley
3	0.672 m	Loma Prieta
4	0.784 m	Chi-Chi
5	0. 784 m	Imperial Valley
6	0. 784 m	Loma Prieta
7	0.909 m	Chi-Chi
8	0.909 m	Imperial Valley
9	0.909 m	Loma Prieta

7-4-2 Results

- **Displacement Demands**

For all cases considered in this parametric analysis, displacement demands normalized by clearance to stop are presented in Figure 7-14 and Figure 7-15 for intensity level of 0.75g and 1.0g respectively. Also, the same simulations were run without the moat wall to evaluate the change in response due to the effect of moat wall impact. Normalized displacement values less than one indicate that the clearance was sufficient and did not impact. It can be seen that implementation of the moat wall resulted in decrease of the displacement demands even though there is still significant penetration of the basemat into the wall. Reduction of displacement beyond the CS varies between 40% to 80%. It should also be mentioned that comparing the results for 1-D and 2-D excitations, the displacement demand is generally larger during 2-D excitations. This shows the importance of considering 3-D models of NPPs to accurately predict displacement demands.

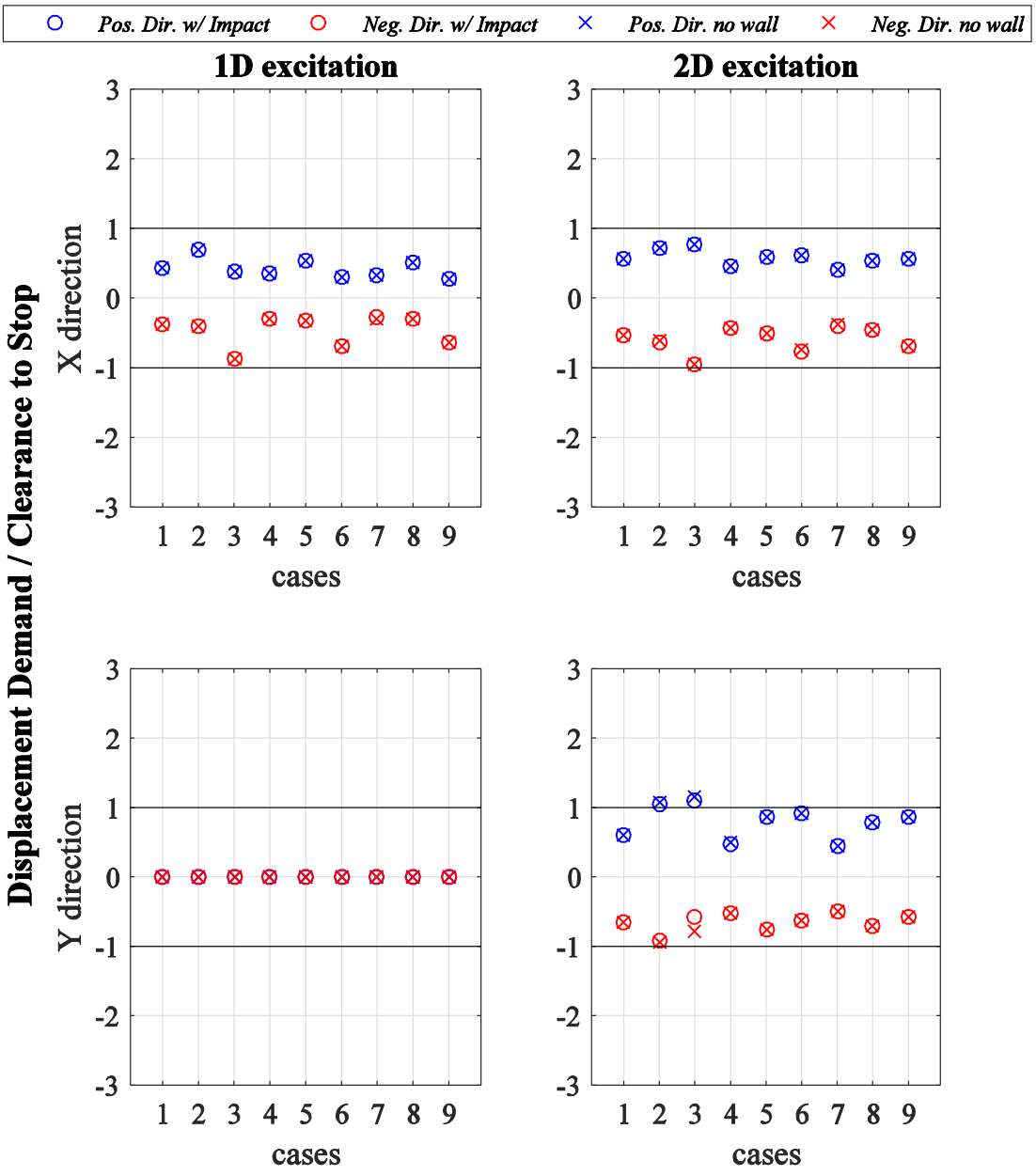

Figure 7-14 Displacement demand over clearance to stop ratio, IL=0.75 g

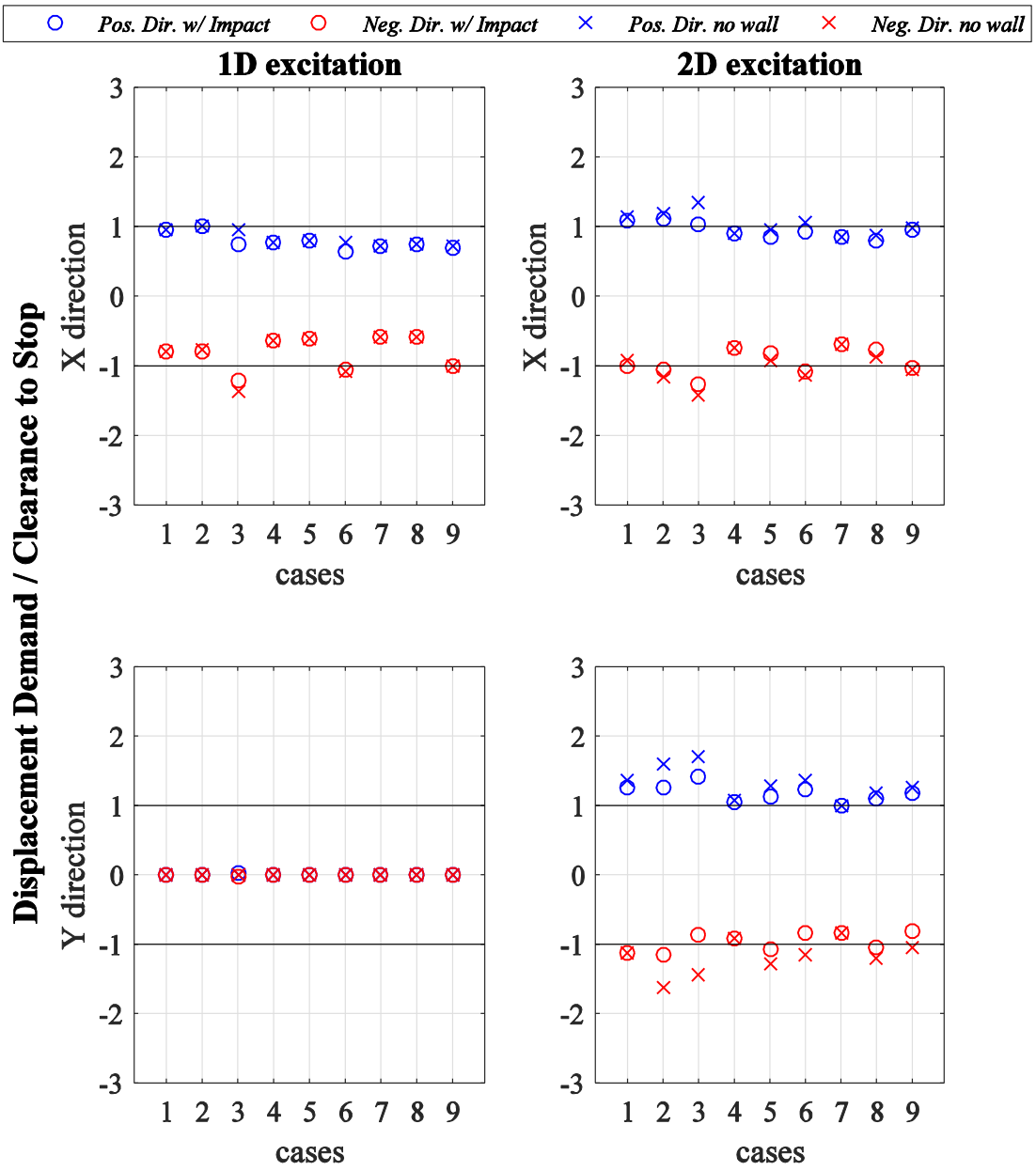

Figure 7-15 Displacement demand over clearance to stop ratio, IL=1.0 g

- **Acceleration**

The most significant concern with seismic pounding is that impact to the moat wall can increase the superstructure response and may lead to damage within the facility. Results for absolute acceleration at elevation 47.5 m are presented for different intensity levels. The following figures show relative acceleration for all cases with and without moat wall (impact

model) for both positive and negative directions. This increase in the acceleration can be up to 2.37 and 2.83 times for intensity level of 0.75 g and 1.0 g (BDBE event) (Figure 7-16 and Figure 7-17).

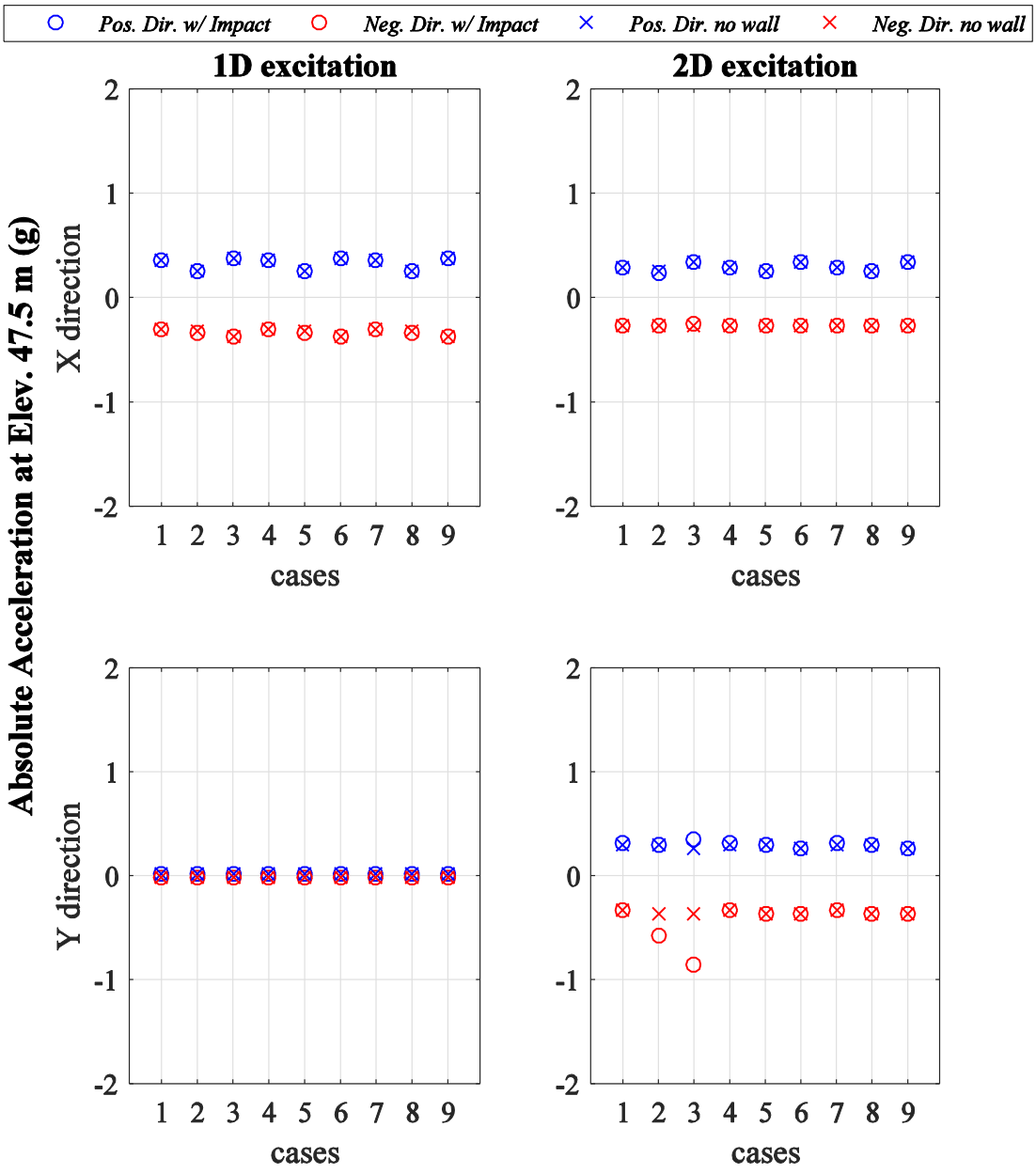

Figure 7-16 Relative acceleration at elev. 47.5 m, IL=0.75 g

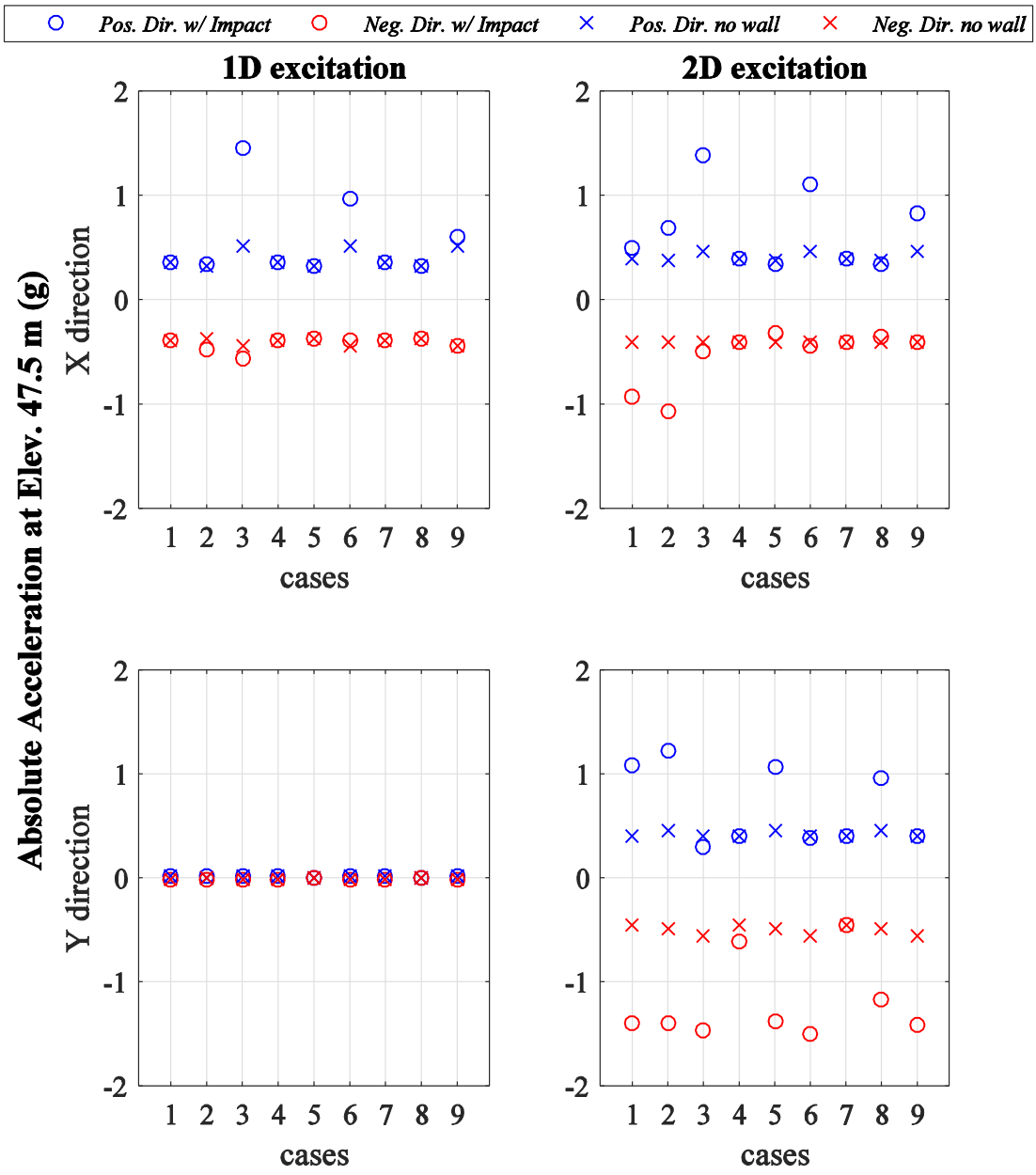

Figure 7-17 Relative acceleration at elev. 47.5 m, IL=1.0 g

7-5 Relations between impact response measures

Results for penetrations, impact velocities and impact forces for all considered simulations are provided in Figure 7-18 to examine the relationship between these impact response parameters [11]. There are clear trends between these parameters, which can be used to

develop a simplified relationship to predict impact response parameters. The shear strength of the moat wall calculated using plastic design and the maximum soil contribution are noted in the figure and described next. An energy based approach is then proposed to develop a conservative relation between the impact response parameters.

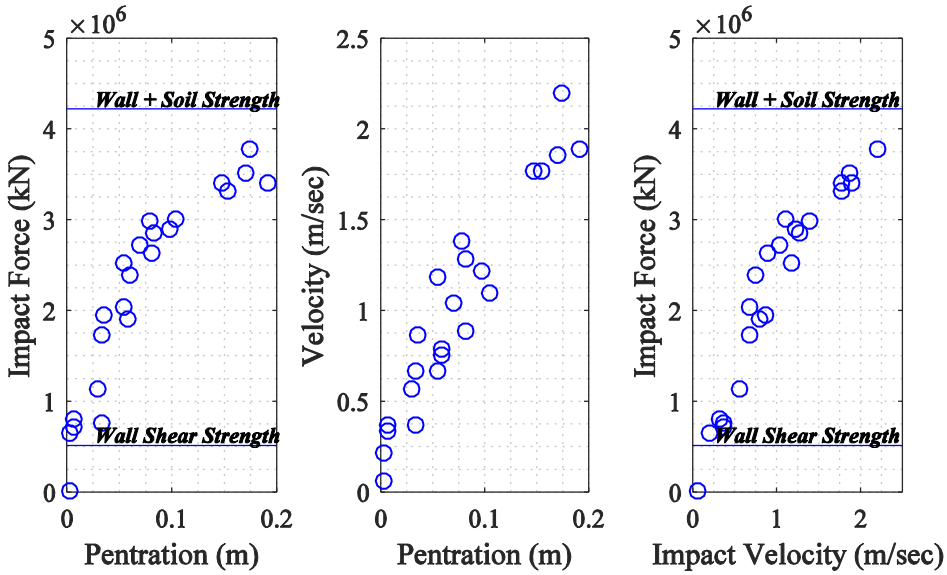

Figure 7-18 Relationships between different impact response parameters

7-5-1 Strength of Moat Wall and Backfill Soil

The shear strength of the moat wall was calculated using plastic design. Two different plastic collapse mechanisms were considered to find the minimum shear capacity of the moat wall (Figure 7-19) with the lowest value corresponding to Scenario 1.

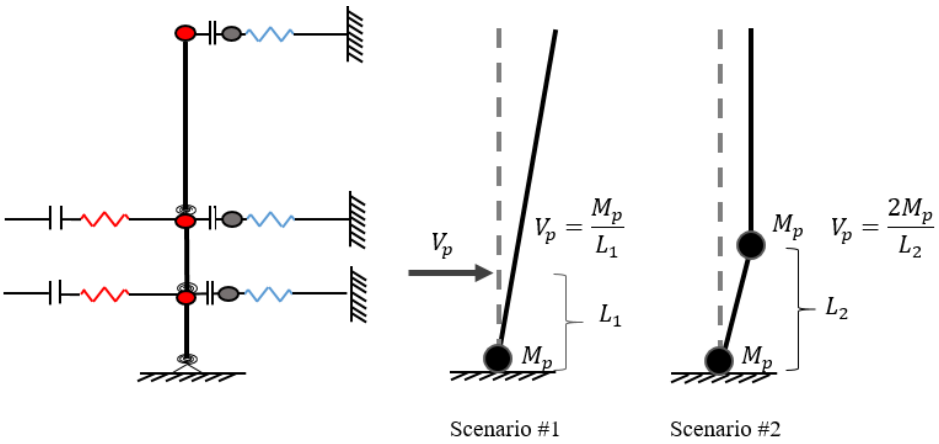

Figure 7-19 Shear strength of the moat wall using plastic design

$$V_p = \min\left(\frac{M_p}{L_1}, \frac{2\times M_p}{L_2}\right) \qquad (7-2)$$

$$= \min\left(\frac{2.81\times10^6}{3.96}, \frac{2\times2.81\times10^6}{5.48}\right) = 7.09\times10^5 kN$$

For backfill soil, the ultimate passive force of the soil was calculated based on total ultimate force of the soil per unit width of the wall. (Table 6-3).

$$F_{soil} = F_{ult}[per\ \ m]\times NPP\ Width \qquad (7-3)$$

$$= 37547.5\times98.75 = 3{,}708{,}005\ kN$$

7-5-2 Estimation of Penetration

A simplified method to estimate penetration into the moat wall based on the moat wall properties and the given impact velocity (v_{imp}) using conservation of energy is proposed. It is assumed that the kinetic energy ($E_{kinetic}$) of the NPP moving as a rigid body before impact transforms to strain and hysteretic energy (E_{strain}) that cause deformation of the moat wall and backfill soil. In this simplified approach, it is assumed that throughout the short duration of impact, there is no additional input energy from ground excitation added into the system and no

energy loss during impact. The total mass of the isolated NPP including basemat and superstructure (m_{NI}) is 482,682 ton. Using conservation of energy:

$$E_{kinetic} = E_{strain} \tag{7-4}$$

$$E_{kinetic} = \frac{1}{2}\, m_{NI}.v_{imp}^2 \tag{7-5}$$

$$E_{strain} = \int F_{moat}.dx \tag{7-6}$$

Assuming an elasto-plastic model for an equivalent resisting spring, the strain energy of the moat wall system can be calculated as the area under the force-deformation curve (Figure 7-20). Since the resistance to the impact is primarily coming from the structural moat wall (Figure 7-12), the maximum force of this equivalent system was assumed to be the shear strength of the wall and the yield displacement (δ_y) was calculated from yielding rotation of the moat wall section to form a plastic hinge in scenario 1 (Figure 7-19).

$$F_{moat\,,max} = V_p = 7.09 \times 10^5 kN \tag{7-7}$$

$$\delta_y = \theta_y \times L_1 = 0.012 \times 3.96\, m = 0.0475\, m \tag{7-8}$$

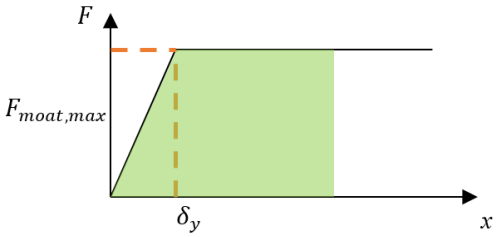

Figure 7-20 Shear strength of the moat wall using plastic design

Based on the energy formulation, penetrations into the moat wall for different impact velocities were calculated and compared with measured values based on numerical simulations

(Figure 7-21). The predicted penetrations using this method provide an approximate upper bound for penetration.

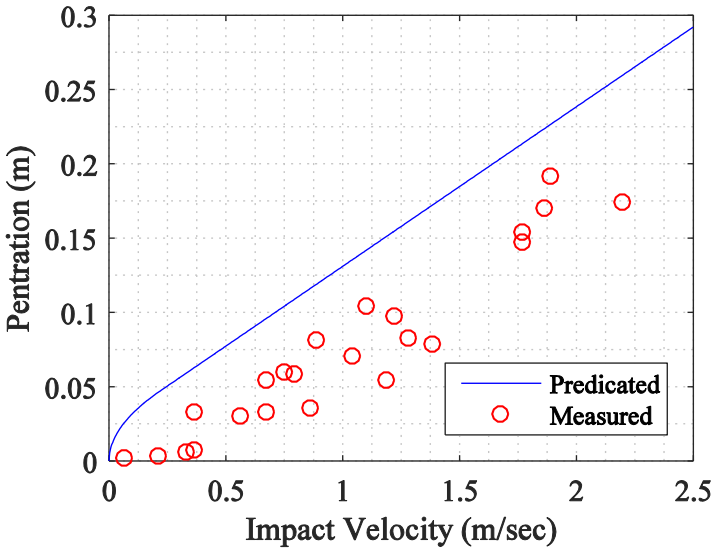

Figure 7-21 Measured and predicted penetrations for different impact velocities

Per ASCE 4-16 [12], if the CS is smaller than specified, the moat wall (stop) should be analyzed and designed for impact loading. In this case, impact velocity may be calculated either by analysis for BDBE ground motions or by assuming cyclic response of the isolated superstructure to the 95 percentile BDBE displacement at a calculated frequency for the isolation system [12]. The simplified method described here will provide an estimate of penetration into the moat wall based on an assumed impact velocity and strength of the moat wall. This can be a useful tool for designers to calculate the expected displacement demand on the isolation system considering moat wall compliance. It should be noted that this simplified approach was developed using a single moat wall system and needs to be examined under a wider set of configurations.

7-6 Summary

A detailed model was used to investigate the seismic response of isolated NPP considering impact to moat walls. The macro element proposed in this dissertation was used to capture the impact force between the NPP and the moat wall.

To more accurately model the Hertz stiffness at impact, results from finite elements simulation results in LS-Dyna were used to examine the stiffness between the mat foundation and the moat wall. The estimation of impact parameters could benefit significantly from validation using experimental tests in future.

In the case of 2-D horizontal earthquake excitation, torsional effects in the ANT model caused slightly different displacement demands especially at corner bearings. Torsion of the base mat could result in amplification of displacements and increase in the probability of impact in NPP. It should be noted that even though the effect of torsion on the response is not significant for the model considered here, it is important to consider use of 3-D models since the response of the NPP and bearings are generally different under 2-D ground excitation in comparison with 1-D excitation.

Based on the assumed properties for the moat wall, penetration can be significant and this additional displacement should be considered in the design of the isolation system. Results for the response of the moat wall showed that the ultimate capacity was reached and led to degradation in strength and residual displacements in the moat wall due to impact. These moat walls may need to be replaced after an extreme event with significant impact velocity.

Comparing the floor response spectra, it can be concluded that the spectral acceleration of the isolated NPP without and with a moat wall including impact are generally lower in

comparison to the fixed-base NPP under the same level of excitation. As a result of impact, the acceleration may increase significantly along the height of the NPP. This increase can be up to 2.83 times of the acceleration response for the NPP without a moat wall for intensity level of 1.0 g corresponding to BDBE events.

It was shown that the influence of the moat wall to limit the displacement demand during the impact is more pronounced than the contribution of the backfill soil. Based on provided results, there were some clear trends between different impact response parameters (impact velocities, impact forces and penetrations), which was used to develop a simplified method to estimate penetration into the moat wall given impact velocity and properties of the moat wall.

References

[1] Shao, B., Schellenberg, A. H., Schoettler, M. J., and Mahin, S. A. (2016): Numerical Analysis of Seismic Isolation Systems applied to an Archetype Nuclear Test (ANT) Power Plant under varied Seismic Conditions and Aircraft Impact Loading. Technical Report PEER, Pacific Earthquake Engineering Research Center, University of California, Berkeley, Berkeley, CA.

[2] Goldsmith, W. (2001): Impact: The Theory and Physical Behavior of Colliding Solids. Dover Publication, New York.

[3] LSTC (2011): LS-DYNA, A Program for Nonlinear Dynamic Analysis of Structures in Three Dimensions. Livermore Software Technology Corporation, Livermore, CA

[4] Mohammed, T. (2011): Reinforced Concrete Structural Members Under Impact Loading. Doctoral Dissertation, University of Toledo, Toledo, OH.

[5] Meo, M., Morris, A. J., Vignjevic, R., and Marengo, G. (2003): Numerical simulations of low-velocity impact on an aircraft sandwich panel. Composite Structures, 62 (3), 353-360.

[6] Farnam, Y., Mohammadi, S., and Shekarchi, M. (2010): Experimental and numerical investigations of low velocity impact behavior of high-performance fiber-reinforced cement based composite. International Journal of Impact Engineering, 37 (2), 220-229.

[7] Muthukumar, S., and DesRoches, R. (2006): A Hertz contact model with non-linear damping for pounding simulation. Earthquake Engineering & Structural Dynamics, 35 (7), 811-828.

[8] Ancheta, T. D., Darragh, R. B., Stewart, J. P., Seyhan, E., Silva, W. J., Chiou, B. S. J., Wooddell, K. E., Graves, R. W., Kottke, A. R., Boore, D. M., Kishida, T., and Donahue, J. L. (May 2013): PEER NGA-West2 Database. PEER, University of California, Berkeley, CA

[9] US-NRC (2014): Regulatory Guide 1.60 Design Response Spectra for Seismic Design of Nuclear Power Plants. NUREG, United States Nuclear Regulatory Commission, Washington, DC.

[10] US-NRC (forthcoming): Technical considerations for seismic isolation of nuclear facilities., NUREG-**, Washington, DC.

[11] Sarebanha, A., Mosqueda, G., Kim, M. K., and Kim, J. H. (2017): Modeling of Moat Wall Compliance during Impact in Seismically Isolated Nuclear Power Plants. SMiRT-24, Busan, Korea.

[12] ASCE (2017): Seismic analysis of safety-related nuclear structures, ASCE/SEI Standard 4. Reston, VA.

Chapter 8 Summary and Conclusion

8-1 Summary of research work performed

Seismic isolation is considered an effective strategy to protect structures from the damaging effects of earthquakes. Especially under strong earthquake shaking, seismic isolation bearings can exhibit complex nonlinear behavior that is dependent on several factors including the axial load, temperature, and strain rate of loading. This complex behavior provides some uncertainty regarding the nonlinear seismic response of isolated structures and requires detailed experimental investigations to fully characterize their behavior. Hybrid simulation can be a cost-effective approach for dynamic testing of structural components at full-scale while capturing the system level structural response through interactions with the numerical model. For seismically isolated structures, the dynamic response depends on the combined characteristics of the ground motion, bearings, and superstructure.

The increased flexibility at the base by introducing isolation system and resulting elongation of the natural vibration period of the structure leads to significant reductions in

acceleration and forces transmitted to the structure above the isolation level at the expense of large displacements in the isolation system at sites of moderate to high seismic hazard. To accommodate these displacements, the isolated structure requires a large horizontal clearance or moat at the basement level. The surrounding moat wall around the clearance is intended to function as a stop to limit isolation system displacements. In the case of an extreme earthquake, there exists the potential for impact of the isolated structure to the moat wall. This impact is of significant concern in critical infrastructures including NPPs due to the potential for increased transfer of forces and amplification in structural response.

The research work presented in this dissertation was focused on: 1) experimental testing of an isolated NPP using hybrid simulation and full scale bearing specimens and 2) numerical study of the seismic response of NPPs considering moat wall impact. This research program confirms that real-time or near real-time hybrid simulation is a viable testing method to experimentally assess the behavior of large isolators at full-scale and in-structure response of these critical structure. Experimental verification of bearing behavior can potentially lead to more use of protective system for critical infrastructures around the world. Numerical modeling of the response of an isolated NPP considering moat wall pounding provided better insights of the response of NPPs under extreme earthquake excitation and could address some of the concerns in using this technology for application in the nuclear industry.

8-2 Novel contributions to knowledge

The first part of dissertation presented in Chapter 3, 4 and 5 and was focused on experimental testing of an isolated NPP using hybrid simulation. In chapter 3, the adaptation of a full-scale bearing test machine to conduct real-time or near real-time hybrid simulations to study

the dynamic response of isolated structures under realistic earthquake excitations. The real-time hybrid simulations of structural systems with several thousand degrees of freedom were made possible by employing high performance parallel computing approaches to execute the numerical analyses.

Challenges encountered in achieving reliable simulation results for these large scale dynamic tests such as compensation and correction for delay, inertia forces, and friction forces in the experimental setup were addressed. Despite the lack of a load cell to directly measure the experimental bearing forces, a new model for inertia and friction force correction was developed, implemented and then calibrated for different test setups using system identification techniques.

Based on results from hybrid simulation tests reported in Chapter 5, the complex nonlinear behavior of the seismic isolation bearings (i.e. vertical-horizontal coupling due to overturning or 3-D seismic excitation) was captured experimentally and its interaction with the numerical model of the superstructure ANT (Archetype Nuclear Test) model based on APR1400 NPP was studied to evaluate system level and in-structure response under different considered scenarios. Base shears and floor accelerations were generally reduced substantially compared to what might be expected for a fixed-base structure and was observed by comparison of floor spectra. These tests were able to identify specific differences associated with different bearings, loading conditions, and earthquake excitations. In an effort to simulate more realistic loading conditions, seismic response of the isolated NPP using three components of earthquake excitations using hybrid simulations were made possible as part of this research program. It was shown that these devices have coupled horizontal-vertical behavior and it is important to include overturning effects and vertical ground motion input in hybrid testing to accurately predict floor response spectra for these critical facilities. Neglecting vertical excitation can significantly

underestimate horizontal spectral accelerations around the vertical frequency of the isolated plant.

The second part of the research, which was covered in Chapters 6 and 7, was focused on the seismic response of isolated NPP considering moat wall impact. A macro model to capture the impact forces was developed based on past analytical and experimental impact studies combined with observed behavior in finite element model simulations. To more accurately model the Hertz stiffness at impact, results from finite elements simulation results in LS-Dyna were used to examine the stiffness between the mat foundation and the moat wall. For the isolated superstructure, two different numerical models, a simplified and a detailed model of NPP, were considered. The proposed moat wall model was used to examine the response of a simplified NPP through a series of parametric studies under different seismic intensity levels and various properties for the bearings and moat wall to provide a better insight on the effects of each of these parameters.

In chapter 7, the proposed macro model was added in a more detailed finite element model of the ANT model. This 3D model was able to more accurately capture response behavior of an isolated NPP under uni- and bi-directional horizonal excitation to examine its seismic response considering pounding to moat wall and its effect on the superstructure. Based on the assumed properties for the moat wall, penetration could be significant and this additional displacement should be considered in the design of the isolation system. A simplified method was proposed to estimate penetration into the moat wall given impact velocity and properties of the moat wall. Comparing the floor response spectra, it was concluded that the spectral acceleration of the isolated NPP without and with a moat wall including impact are generally lower in comparison to the fixed-base NPP under the same level of excitation.

8-3 Recommendation for future research work

The present study provides important contributions to understanding the behavior of seismically isolated NPPs subjected to beyond design basis earthquake shaking. The findings presented here can be complemented with additional research in the following areas. Future research on application of hybrid simulation to experimentally test seismic isolators for use in the nuclear industry is suggested as follows:

- It is recommended to improve the tracking performance of the SRMD test system for any future hybrid simulations performed on this testing system. It was determined that it is currently not possible to conduct 3D real-time hybrid simulations with the SRMD due to insufficient vertical tracking performance. Because it is apparent that real-time or near-real-time hybrid simulations of seismic isolation systems can more closely capture the true behavior of the isolators, it is recommended that strategies be developed to determine how to reduce overall delays currently present in the system to an absolute minimum.
- It is important to develop improved analytical models that more closely captures the true behavior of the bearing specially under extreme earthquake excitations. The ability to accurately calibrate the analytical bearing behavior to match the experimental bearing behavior was heavily dependent on the fidelity of the numerical model; in addition, it was time consuming to run the model with many analytical bearing elements.
- Different types of bearing under extreme loading condition for the application of NPPs can be considered and tested using the hybrid simulation infrastructure developed at the SRMD.

With regards to investigation of the response of seismically isolated NPP considering impact to moat wall, to author's knowledge this is one of the first studies on this topic. This study provided significant insights into this behavior but also revealed several topics that need further study and described below.

- More detailed finite elements analysis is necessary to fully represent the geometry and mass of the colliding structures in order to improve the impact model and important impact parameters for application in critical infrastructures. Continuation of detailed finite element modeling using high fidelity model based on previous and future experimental tests could support studies towards assessing the pounding behavior more accurately.
- Numerical and experimental validations of the proposed simplified guideline to predict the impact response parameters of different structures is necessary. This guideline could help engineers to have better insight into the response of the moat wall and estimate the deformation. This could lead to set of design objectives to find the optimum parameters to limit the penetration into the moat wall and as well as acceptable limits for bearing ultimate displacements.
- Efficient measures to mitigate effects of impact and/or reduce probability of impact could be evaluated such as: introducing rubber bumpers to have more gradual impact between NPP and moat wall structures, modeling hardening of elastomeric bearings using experimental tests results or using bearing with adaptive response behavior such as hardening regime under extreme excitations (e.g. Triple Friction Pendulum).
- Large scale shake table hybrid simulation test will provide valuable insights to better study the seismic response of NPP considering pounding. In these tests, superstructure

could be modeled numerically and part of base mat foundation, moat wall and backfill soil can be tested experimentally in the laboratory.